THÈSE POUR OBTENIR LE GRADE DE DOCTEUR DE L'UNIVERSITE DE MONTPELLIER

En Mathématiques et Modélisation

École doctorale : Information, Structures, Systèmes

Unité de recherche : Institut Montpelliérain Alexander Grothendieck

Simulations numériques pour l'Imagerie par Résonance Magnétique à contraste de phase

Présentée par Thomas Puiseux

Le 28/11/2019

Sous la direction de Franck Nicoud et Simon Mendez

Devant le jury composé de

Franck Nicoud	Professeur, IMAG, Univ. Montpellier	Directeur
Simon Mendez	Chargé de recherche, CNRS, Univ. Montpellier	Co-directeur
Tino Ebbers	Professeur, Linköping University	Rapporteur
Jean-Michel Serfaty	Professeur, CHU de Nantes	Rapporteur
Stéphanie Salmon	Professeure, Université de Reims	Présidente du jury
Monica Sigovan	Chargée de recherche, CNRS, CREATIS Lyon	Examinatrice
Ramiro Moreno	Physicien médical, ALARA Expertise	Co-encadrant

UNIVERSITÉ DE MONTPELLIER

Résumé

L'hémodynamique est aujourd'hui considérée par la communauté médicale comme un marqueur prépondérant dans l'apparition et dans l'évolution de certaines pathologies artérielles (formation d'un caillot sanguin, anévrisme, sténose,...). Sa caractérisation par imagerie médicale est désormais possible grâce à l'Imagerie par Résonance Magnétique, qui présente l'avantage d'être une technique non invasive et non ionisante. Historiquement réservée à l'étude morphologique des organes, les progrès technologiques réalisés cette dernière décennie ont permis de l'adapter à l'évaluation hémodynamique grâce à l'IRM à contraste de phase 3D (ou IRM de flux 4D) [100]. En donnant accès à l'évolution temporelle du champ de vitesse dans les trois directions de l'espace en plus de la morphologie du secteur artériel d'intérêt, cette technique constitue potentiellement un outil de choix en pratique clinique pour la prise en charge et le suivi des patients. Contrairement à l'imagerie de flux 2D utilisée pour mesurer le débit selon une orientation et position de coupe déterminées en cours d'examen, l'imagerie 4D fournit au clinicien la possibilité d'évaluer rétrospectivement de nombreuses quantités utiles au diagnostic à partir d'un examen unique et compréhensible. Par exemple, deux mesures de débit volumique effectuées sur un même volume d'acquisition (aorte et tronc pulmonaire) suffisent en théorie à estimer la sévérité d'une hypertension artérielle.

Outre la simplicité d'analyse des données, il devient possible d'estimer de nouveaux biomarqueurs dérivés du champ de vitesse tels que les contraintes de cisaillement parietales [128], la pression statique [86], ou encore le temps de séjour. S'ils sont difficilement accessibles par les techniques d'imagerie classiques, ces paramètres sont pertinents en terme de diagnostic médical : en modifiant la fonction des cellules endothéliales, la variation temporelle du frottement pariétal (Wall Shear Stress) joue un rôle prépondérant dans la déformation des parois vasculaires responsable de la formation d'anévrismes [110] ; la perte de charge est corrélée à la sévérité d'une sténose artérielle et permet également d'évaluer la nécessité d'une intervention chirurgicale pour remplacer une valve cardiaque. Enfin, il est désormais envisageable grâce à l'IRM de flux 4D de quantifier des marqueurs associés à des phénomènes hémodynamiques complexes tels que l'énergie cinétique turbulente [87], ou la perte de charge due à la production de turbulence [64], qui semblent être impliquées dans le développement de certaines pathologies cardiovasculaires comme la formation de plaque d'athérome ou dans certaines dysfonctions cardiaques [32, 45].

Cependant, la résolution spatio-temporelle limitée accessible en IRM de flux 4D

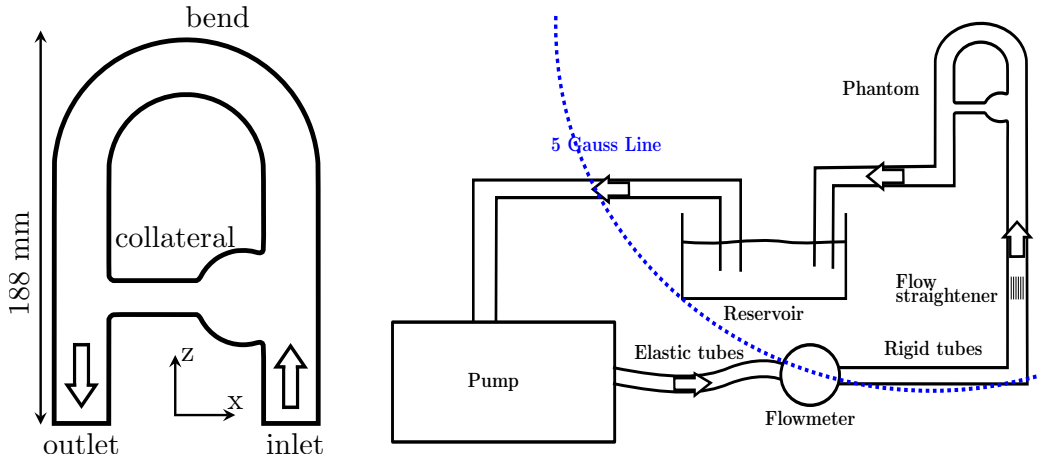

Figure 1: Illustration schématique du banc d'essai expérimental et du fantôme.

(typiquement 2 mm en espace et 0.05 s en temps pour une acquisition thoracique), la dépendance des résultats à la vitesse d'encodage, la présence d'artéfacts expérimentaux ou encore la complexité des séquences et les variabilités inter-constructeurs sont autant de facteurs qui limitent la précision des mesures de flux et la confiance que l'on peut leur accorder [58, 60]. L'erreur de mesure sur le champ de vitesse ne pourra par ailleurs être qu'amplifiée par le calcul d'une quantité dérivée comme le frottement pariétal, pourtant au cœur des applications cliniques. De plus, les complexités intrinsèques au processus d'acquisition en IRM rendent difficilement identifiables les sources d'erreurs de ces mesures (protocole d'acquisition, logiciel, machine). Ces limitations sont autant de freins à l'utilisation intensive de l'IRM de flux 4D en routine clinique ; elles le demeureront tant qu'une méthodologie rationnelle permettant de contrôler in situ la qualité des données hémodynamiques produites n'aura pas été mise en place.

Une méthode alternative consiste à utiliser la simulation numérique par mécanique des fluides (Mécanique des fluides Numériques ou MFN) pour reconstruire l'écoulement 3D compatible à la mesure par IRM. Bien qu'elle repose sur plusieurs hypothèses de modélisation, la MFN couplée aux mesures IRM facilite l'accès à l'intégralité du champ hémodynamique sans les contraintes expérimentales de l'IRM (résolution spatio-temporelle, bruit de mesure, artéfacts). Au regard des bénéfices qu'elle apporte, cette approche a suscité beaucoup d'intérêts dans la communauté médicale et de nombreux développements ont déjà été réalisés à ce jour. Néanmoins, de récentes études ont mis en lumière l'importance prépondérante du choix des paramètres de simulation sur les prédictions de certains marqueurs hémodynamiques [156, 172].

Le premier objectif de cette thèse est de développer une méthodologie permet-

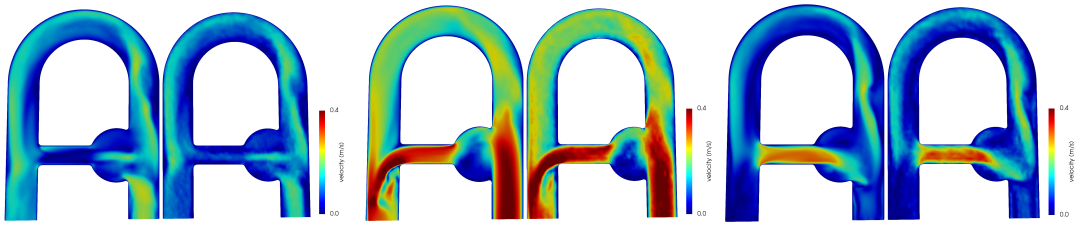

Figure 2: Coupe transverse de la norme du champ de vitesse obtenue par MFN et mesurée par IRM de flux 4D dans le fantôme après post-traitements à trois différents instants dans le cycle (**gauche** début du cycle, **centre**, pic systole et **droite** diastole).

tant l'évaluation systématique des mesures par IRM de flux 4D dans un régime d'écoulement complexe. Pour ce faire, un banc d'essai expérimental muni d'une pompe programmable produisant un écoulement pulsé contrôlé par un débitmètre à ultrason (voir Figure 1) a été développé. L'écoulement est délivré au sein d'un fantôme IRM compatible capable de générer un écoulement typique de ceux observés dans la circulation thoracique (crosse aortique, bifurcation, anévrisme). Les propriétés du fluide et la position des parois rigides du fantôme étant connues au préalable, cette configuration in vitro de s'affranchir d'une multitude de sources d'incertitudes rencontrées physiologiquement (rhéologie du sang, déformation des artères, erreurs de segmentation). L'écoulement résultant mesuré par IRM de flux 4D est ensuite comparé à l'écoulement prédit par un outil de simulation numérique développé à l'IMAG et dédié à la prédiction des écoulements sanguins (YALES2BIO). L'analyse des résultats obtenus permet d'expliquer la majeure partie des différences entre MFN et IRM et de réduire celles-ci par des traitements adaptés (correction de volume partiel, filtrage physique, ré-échantillonnage, ...). La corrélation finalement obtenue (supérieure à 97 %) permet d'établir un écoulement de référence pour le fantôme considéré (voir Figure 2) et de proposer une méthodologie de contrôle qualité utilisable in situ des systèmes IRM de flux 4D.

Dans la deuxième partie de la thèse, la méthodologie développée est utilisée afin d'évaluer différentes méthodes de reconstruction de quantités dérivées du champ de vitesse à partir de mesures IRM. Plusieurs méthodes de reconstruction du frottement pariétal (voir Figure 3) et de la pression (voir Figure 4) sont successivement évaluées et comparées. Dans un premier temps, l'évaluation du frottement pariétal par MFN révèle qu'un raffinement local du maillage est nécessaire pour résoudre raisonnablement la couche limite dans ce régime d'écoulement. De plus, les différentes approches testées fournissent des estimations du frottement très variables et éloignées de la MFN. Au contraire, la reconstruction du champ pression semble très peu sensible aux détails du champ de vitesse mesuré par IRM. De plus la contribution inertielle à la pression semble largement dominer la perte de charge

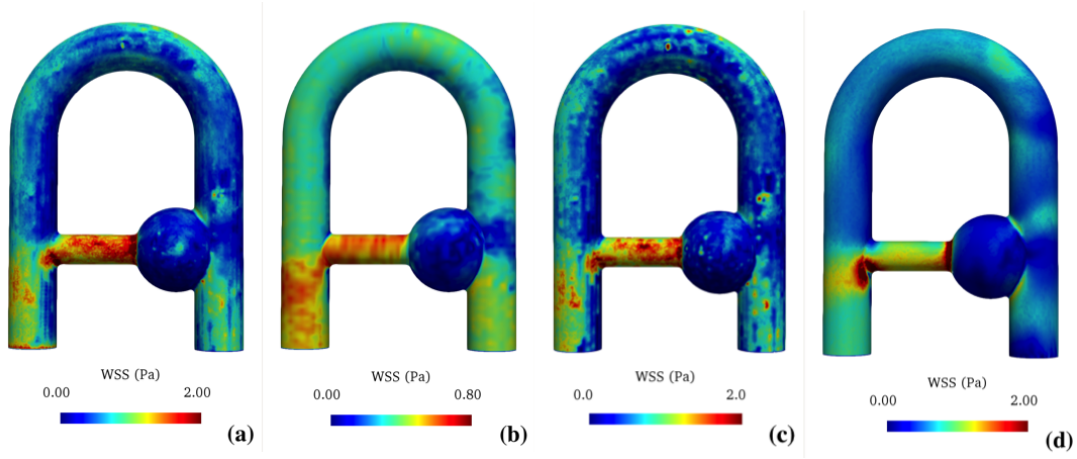

Figure 3: Magnitude du frottement pariétal obtenue en pic systole pour différents algorithmes de reconstruction. (**a**) Approche volume-finis, (**b**) Potters et al., [128], (**c**) Sotelo et al. [142], (**d**) MFN.

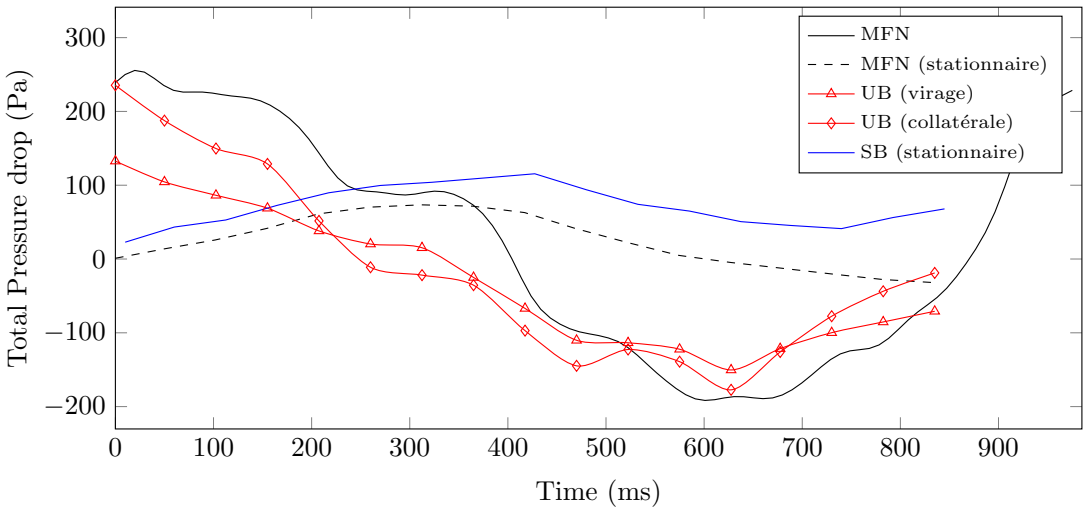

Figure 4: Perte de charge estimée par plusieurs méthodes de reconstruction dans le fantôme. UB : Approche Bernoulli instationnaire, SB : approche Bernoulli simplifiée.

totale dans le fantôme, ce qui suggère qu'une acquisition 2D effectuée à l'entrée du domaine suffit à obtenir une estimation précise des variations de perte de charge.

De nombreuses erreurs de mesures sont dues à l'utilisation de paramètres d'acquisition peu adaptés au type d'imagerie à effectuer (angle de bascule, résolution spatio-temporelle, vitesse d'encodage). Un moyen d'identifier les paramètres causant ces distorsions de la réalité consiste à simuler numériquement le processus d'acquisition en IRM. La dynamique de l'aimantation décrite par les équations de Bloch [17] est au centre de l'acquisition en IRM et constitue le phénomène

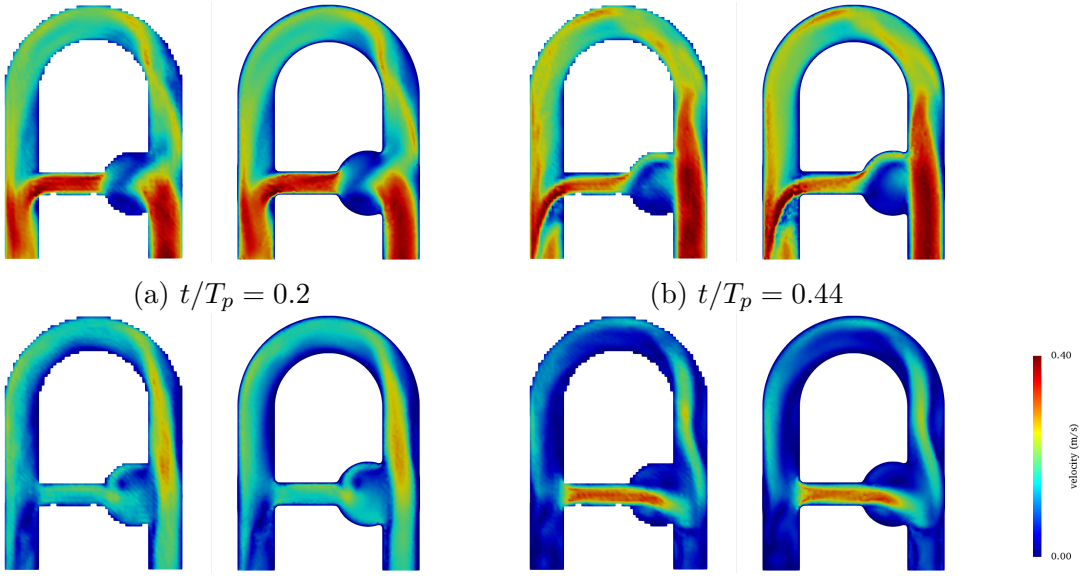

(a) $t/T_p = 0.2$ (b) $t/T_p = 0.44$

(c) $t/T_p = 0.68$ (d) $t/T_p = 0.91$

Figure 5: Coupe transverse de la magnitude du champ de vitesse (**gauche**) simulé par IRM et (**droite**) prédit par MFN à 4 différentes phases dans le cycle.

physique responsable du contraste sur une image en IRM. L'intérêt de telles simulations est alors de pouvoir reconstruire une image synthétique exempte de toute erreur expérimentale propre à la mesure IRM. Un autre intérêt de la simulation d'IRM est de pouvoir distinguer les erreurs dues à un dysfonctionnement machine (aimant permanent, antennes réceptrices, gradients, radio-fréquence, ...) des erreurs logicielles (algorithme de reconstruction, interpolation) ou issues d'un protocole d'acquisition peu adapté au type d'imagerie à effectuer (cœur, carotide, aorte). Afin de prendre en compte le déplacement du fluide dans les simulations, il est nécessaire de coupler l'IRM avec la MFN. Les deux phénomènes mettant en jeu des échelles de temps physique très variées, il est alors complexe de simuler efficacement une telle configuration.

Afin d'aboutir à une évaluation plus complète des données issues des systèmes IRM de flux 4D, le troisième volet de cette thèse présente le développement d'un outil de simulation du processus d'acquisition en IRM. Les étapes principales ainsi que les choix numériques sont développés dans un premier temps. Une méthode de couplage avec la MFN et d'injection de particules permettant de minimiser le coût de calcul est présenté. L'association d'une intégration numérique et d'une formulation semi analytique pour avancer les équations de Bloch est présentée. Par la suite, plusieurs cas de validation sont présentés et les gains associés à cette méthodologie sont quantifiés. Finalement, la méthodologie complète est validée sur le fantôme, le champ de vitesse reconstruit est analysé, et comparé à des

mesures expérimentales (voir Figure 5).

Contents

Chapter 1

Introduction

Chapter contents

1.1 Motivations

With more than 31% of the deaths, cardiovascular diseases (CVDs) are the leading cause of mortality worldwide. Notably, the last three decades have seen an increase

by 6% of the total number of deaths due to cardiovascular disorders [116]. In this respect, research associated with the development of early diagnosis metrics and adapted medical treatments have become a widespread public health issue. Among the many risk factors identified, hemodynamics (dynamics of blood flows) has recurrently proved to be closely related to the onset and evolution of several cardiovascular disorders such as aneurysms, stenoses, or blood clot formation due to thrombosis [14, 48, 109, 110]. Therefore, measurements of the blood flow spatio-temporal distribution could potentially provide useful information on the cardiovascular condition.

Recent technological advances have promoted the development of non-invasive techniques for quantification of hemodynamics. As it provides a comprehensive access to blood flows in-vivo, time-resolved 3D phase-contrast magnetic resonance imaging (or 4D Flow MRI) has gained an increasing interest over the last decades [100]. In one unique exam, 4D Flow MRI opens access to the temporal description of the velocity field in the three spatial directions, as well as the morphology of the region of interest. In this sense, it stands out as a highly relevant tool for diagnosis, patient follow-up and research in CVD. However, this technique suffers from several limitations that can compromise the measurement accuracy and question its relevance for patient diagnosis in clinical practice. This work is part of the current research effort towards a better understanding and control of these limitations.

1.2 Physiology of the cardiovascular system

The cardiovascular system is a closed loop organ system that enables to deliver nutrients, oxygen, hormones, and blood cells to the organs and tissues. The heart acts as a pump that distributes about 5 litres of oxygenated blood into the arterial network, composed by arteries, arterioles and capillaries. The oxygen is then transferred to the tissue and carbon dioxide is carried to the blood. The de-oxygenated blood flows from the venules to the veins, and then back in the heart's right ventricle. The blood filling the right ventricle is ejected into the pulmonary circulation towards the lungs for re-oxygenation by diffusion of oxygen into the blood stream through the alveoli. The re-oxygenated blood is finally sent back into the left ventricle of the heart. The human cardiovascular system is schematically depicted in Figure 1.1.

1.2.1 The heart

The heart splits into two parts to send and collect the blood to the arterial and from the venous circulations, respectively. The de-oxygenated blood flowing from

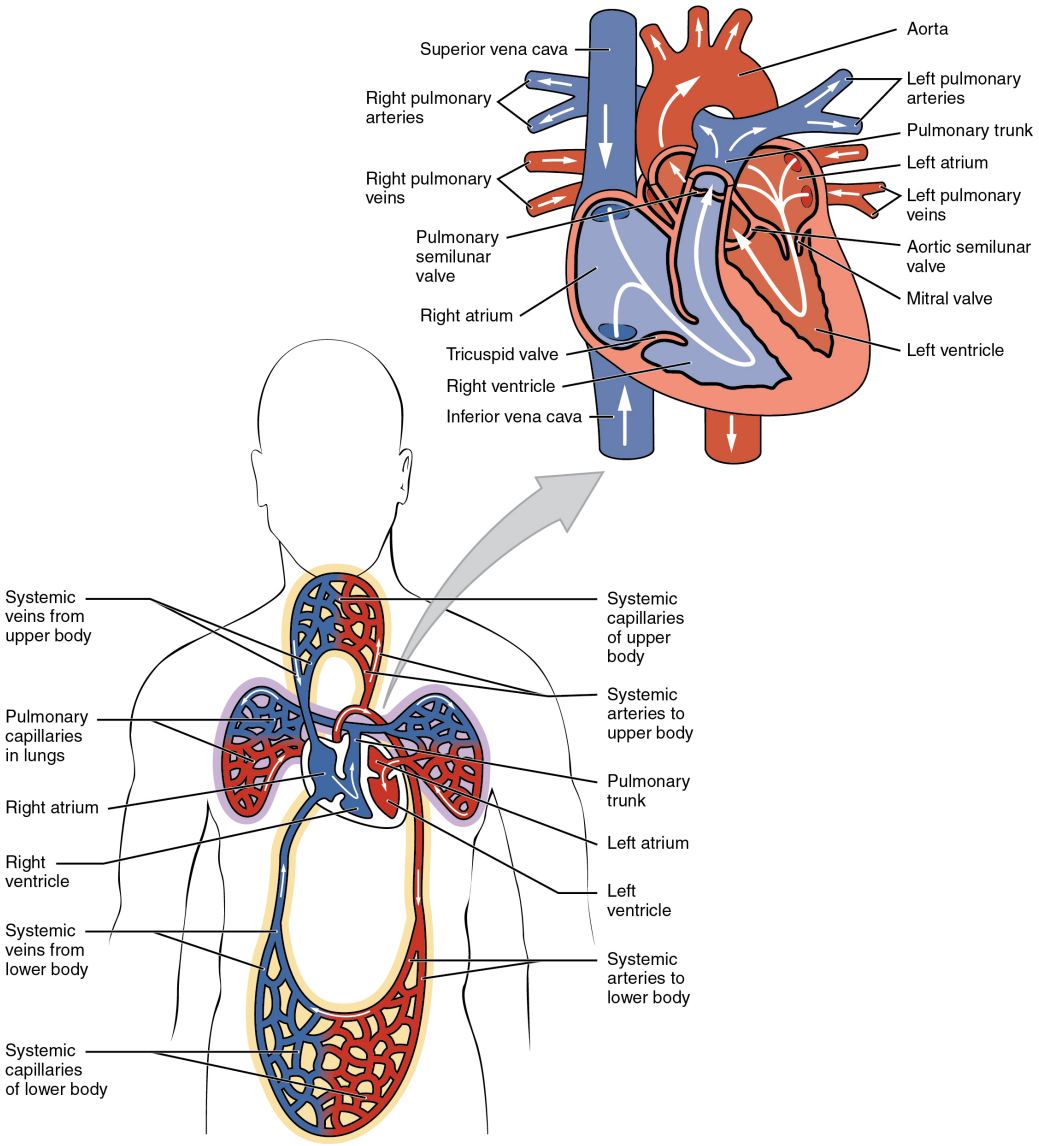

Figure 1.1: Sketch of the cardiovascular system and human heart, taken from [170]. The arterial circulation is coloured in red, and the venous circulation in blue.

the systemic venous circulation is received and stored in the right atrium (RA). The tricuspid valve separates the right atrium from the right ventricle (RV), whose role is to eject the blood towards the pulmonary arteries. Similarly, the oxygenated blood is collected in the left atrium (LA), which is separated from the left ventricle (LV) by the mitral valve. At the LV contraction, the aortic valve opens and the blood is pumped from the LV to the aorta.

1.2.2 The cardiac cycle

A cardiac cycle corresponds to a sequence of events that occur during one heart beat. Each cardiac cycle can be divided into two phases - systole and diastole. The diastole represents the period of time when the heart muscle relaxes. During the diastole, oxygenated blood in the left atrium (LA) progressively fills the left ventricle (LV), while de-oxygenated blood flows from the right atrium (RA) to the right ventricle (RV). During the systolic phase the myocardial muscle contracts to eject the oxygenated blood from the LV through the aorta, as well as the de-oxygenated blood from the RV to the pulmonary system. The human aortic flow rate and pressure signals along a cardiac cycle are presented in Figure 1.2. Most arteries experience large variations of their blood flow waveform and assuming steady flows generally represents a considerable deformation of the reality [53]. From the classical human hemodynamic parameters listed on Table 1.1, the Reynolds number calculated in the ascending aorta and defined as $Re = \frac{2UR}{\nu}$ where U is the bulk velocity, R the vessel radius, and ν the kinematic viscosity, varies within a cardiac cycle in the range $Re \in [0, 4000]$. In steady flow, $Re < 2000$ corresponds to laminar flow regime where flow streamlines remain almost parallel from one to another and the viscous effects dominate while at $Re > 2000$ the transient effects dominate and chaotic unsteady vortices characteristic of turbulent flows may occur. However, when considering a pulsatile flow regime such as that observed in the cardiovascular system, additional turbulent-like features and cycle-to-cycle variations occur during flow deceleration phases [32].

1.2.3 Mechanical structure of the large vessels

The aorta is the largest artery of the body. Connected to the left ventricle, it delivers the oxygenated blood to the systemic circulation. A sketch of the aorta is presented in Figure 1.3a. The aorta is classically divided into two segments: the thoracic and abdominal aorta. The thoracic aorta comprises the ascending aorta that connects to the LV, and the aortic arch that connects to the descending aorta. Three vessels are branched to the aortic arch and supply blood to the upper part of the body (right arm, head, and neck). The abdominal aorta delivers the blood to the inferior members, and splits into the two common iliac arteries.

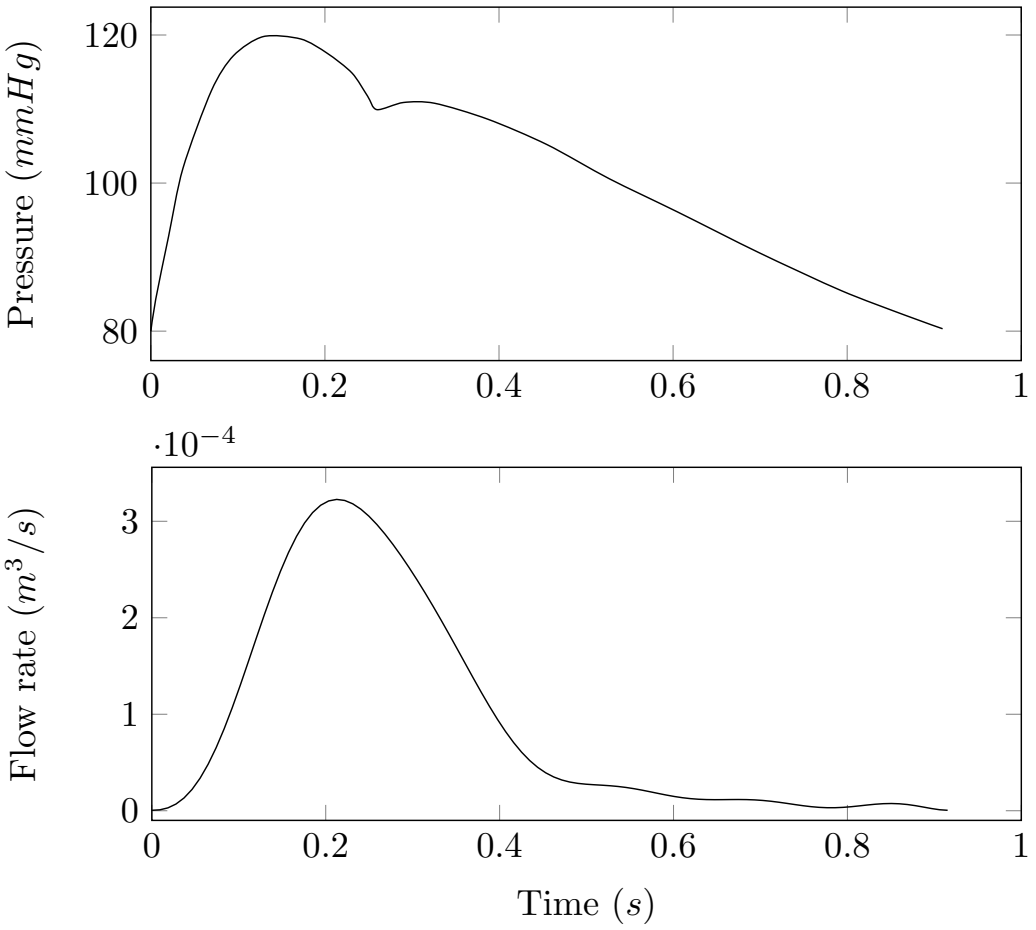

Figure 1.2: Typical healthy human (**top**) static pressure and (**bottom**) flow rate waveforms in the ascending aorta [170].

Table 1.1: Normal range of variations for some classical hemodynamic parameters of the human cardiovascular system.

Parameter	**Range**
heart rate (bpm)	60-100
stroke volume ($ml/beat$)	70-110
ejection fraction (%)	60-72
cardiac output (L/min)	4.0-8.0
blood ventricular velocity (cm/s)	20-25
arterial blood pressure ($mmHg$)	systolic: 10-140, diastolic: 2-8
intra-luminal ascending aortic diameter (mm)	22-36
kinematic blood viscosity (m^2/s)	4.02×10^{-6}

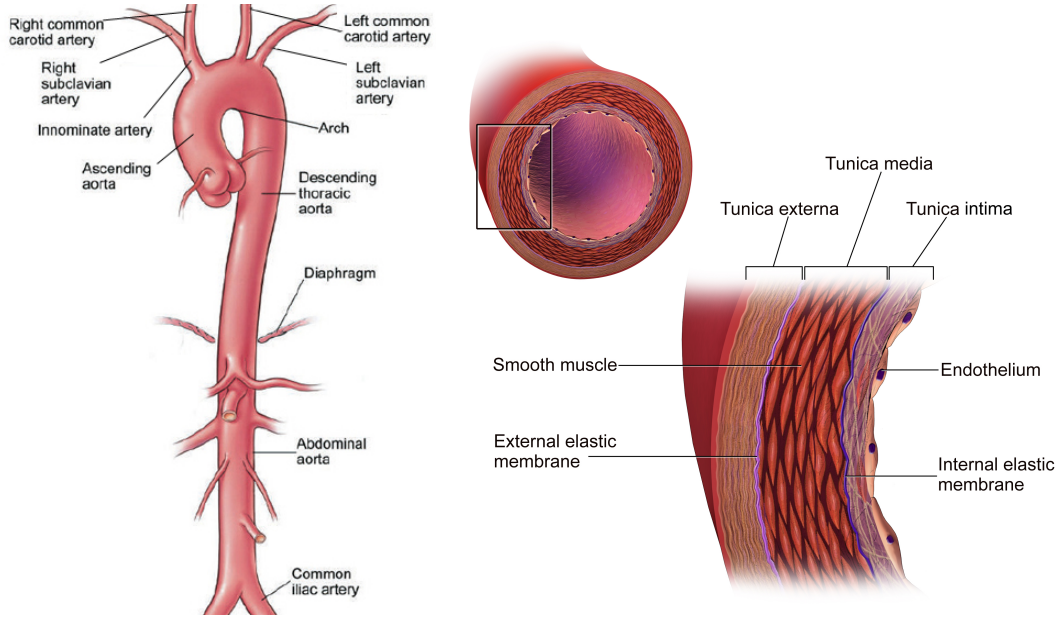

(a) (b)

Figure 1.3: a). Segments of the human aorta. b). Multi-layer composition of the artery walls. Images taken from [2].

As shown in Figure 1.3b, the structure of the arterial walls presents particular mechanical properties to sustain the high blood pressure sent by the heart. The artery wall is basically a multi-layer structure that contains the intima, media and adventitia. While the adventitia contains smooth muscle cells playing only a minor role in the mechanical response of the walls, the media is composed of elastic fibers that absorb the blood pulse wave kinetic energy as it propagates into the vessels. The main role of the media is to maintain the structural rigidity of the vessel by minimizing the arterial deformation. Note that with ageing or arterial diseases, the increase in arterial stiffness can provoke hypertension. The third layer is the intima, which contains collagen fibres and muscles that allow to diffuse nutrients and wastes. The endothelium is an additional thin layer of cells in contact with the blood, whose main functions are to minimize the flow resistance, maintain the vessel wall permeability, and regulate the blood flow. While it acts as a barrier between blood and body tissues, it is selectively permeable to certain chemicals, white blood cells, as well as carbon dioxide. The endothelium is therefore the first blood-wall exchange layer involved in the vessel wall growth, remodelling and regulation of blood coagulation. Endothelial defects are precursors in many arterial diseases.

1.3 The role of hemodynamics in the cardiovascular diseases

Blood mainly contains plasma, platelets, red blood cells and white blood cells which, all together, provide blood with its complex rheology and non-Newtonian properties. These complex features give to blood the specificity to adapt its mechanical response to the surrounding environment (vessel diameter, temperature, stress state). Therefore, understanding the blood flows dynamics at the microscopic level is challenging and remains an active field of research [51, 52, 104, 108**?**]. External factors such as smoking, diabetes, obesity or cholesterol may also impact the blood properties, or deregulate the cardiovascular system. All these elements induce intrinsic changes of the hemodynamics function, which plays a key role in the genesis and evolution of many cardiovascular diseases. Conversely, structural variations such as heart valves defects, chamber geometry, or wall motion impact the hemodynamic response. Because blood flow changes are involved in the process of vascular remodelling and are also impacted by the vascular changes, hemodynamics constitutes a pertinent biomarker to pilot patient diagnosis, follow-ups and could be used as a decision tool to plan surgical treatments. Furthermore, hemodynamics could be used in pilot studies as a tool to evaluate and optimize the design of medical devices in contact with blood [109, 163]. Finally, research-focussed blood flows evaluation in pathological configurations is a promising way to better understand the behaviour of the flow and generate adapted diagnosis metrics.

The mechanisms associated with the formation of atherosclerosis and aneurysms are briefly described as examples to illustrate the clinical interests associated with blood flow measurement.

Atherosclerosis Atherosclerosis is a disease that affects the lumen of the arteries, as well as the arterial wall stiffness. The lumen is narrowed by the subendothelial deposit of plaques made of fat, cholesterol, and other substances found in the blood. The plaque (or atheroma) can damage the arterial wall by increasing its permeability. Also, the lumen narrowing further accelerates the rate of plaque growth. The plaque can detach from the wall and embolize an other vessel, or blood clot could form due to a thrombosis reaction and adhere to the injured site. This can eventually lead to a partial or full obstruction of the vessel (see Fig. 1.4), leading in the worst cases to heart attacks due to the lack of oxygen supply (ischemia).

In atherosclerosis, the vessel obstruction resulting from the plaque deposit accelerates the blood flow locally and therefore introduces higher flow resistance, inducing a local increase of the wall shear stress (WSS). In this sense, the WSS

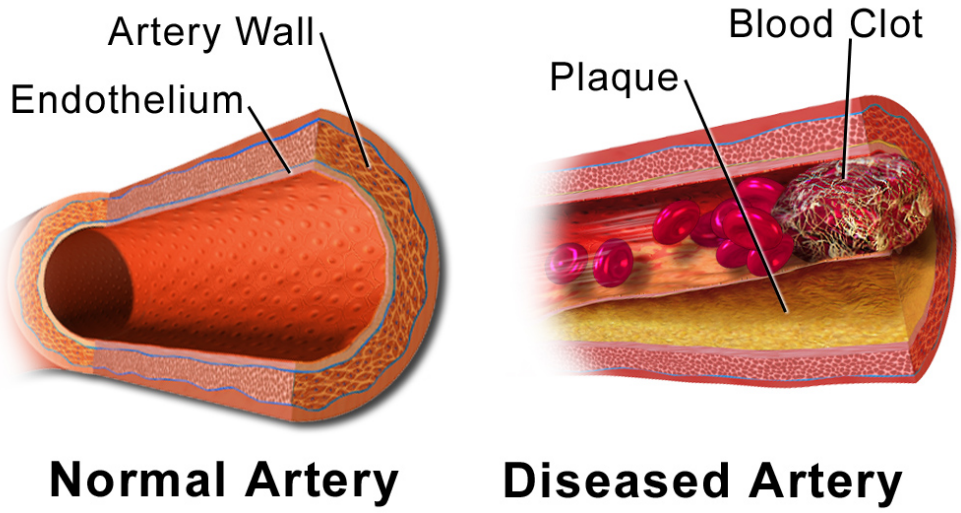

Figure 1.4: Sketch of a normal and embolized artery due to the presence of a plaque and a thrombus [2].

is often used as a biomarker of the arterial stenosis. Moreover, the transstenotic pressure drop is also a common biomarker to assess the severity of the stenosis. Generally speaking, the hemodynamic stress repartition could help surgical repair decision by providing the ideal stenting site deployment [162].

Aneurysm An aneurysm is a localized dilatation of an arterial wall, forming a sac filled with blood. The wall dilatation is accompanied with stretching and tapering. Even if most aneurysms are stable in shape and size, external factors can promote wall weakening and lead to a complete rupture. The rupture provokes an internal bleeding and conducts to death in 75-90% for aneurysms located in the abdominal aorta [5]. The development process of an aneurysm is depicted in Figure 1.5. Nowadays in clinical practice, the only therapeutic criterion to assess the necessity of a surgical intervention is based on a maximum diameter measurement [21]. Multiple factors contribute to the initiation of an aneurysm, including factors affecting the vessel walls and the blood flow. Its evolution and stability highly depend on the stresses (pressure and shear) exerted by the blood flow on the wall. The most classical surgical intervention consists in apposing a stent onto the vessel lumen around the aneurysm neck to deviate the trajectory of the main flow, while creating a stagnation zone in the sac. A decreased saccular velocity reduces the stresses applied on the artery walls, and the stagnation promotes thrombosis formation after the treatment, which helps consolidating the thin artery wall [149].

In this respect, pre and post-operative hemodynamics evaluation could ensure the correct sizing and positioning of the stent. WSS also plays an important role

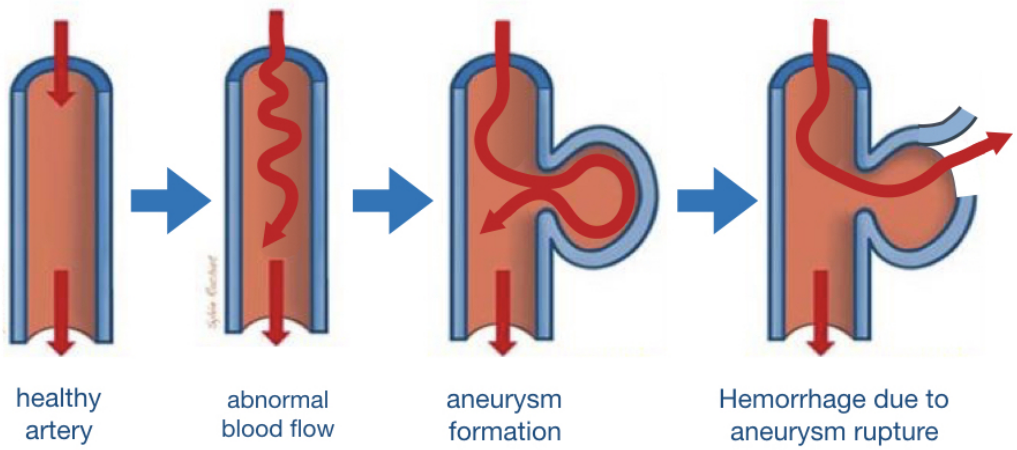

Figure 1.5: Sketch describing the initiation, growth and rupture of an aneurysm.

in aneursym initiation since changes in WSS influence endothelial cell function and thus promote vascular remodelling and vessel dilatation [110]. Some studies demonstrated that regions of high WSS are preferential sites for the development of aneurysms [83], while other found that the aneurysm initiation occurs mainly at low WSS sites [20]. Others markers such as Oscillatory Shear Index, or Spatial WSS gradient were found to impact the aneurysm evolution [83, 110]. While no consensus has been reached about the role it plays in the aneurysmal development, WSS certainly provides useful information to help for the evaluation of aneurysmal evolution, as well as the detection of hotspots.

Other aortic diseases such as aortic coarctation and dissection may be detected by measuring the hemodynamics condition. The pressure gradient and peak velocity at the narrowing site help to measure the severity of the coarctation, and the necessity of a surgical treatment. Aortic dissections could be diagnosed by the presence of regurgitant flow (velocity with inverse direction) in the false lumen. Numerous other congenital heart diseases such as bicuspid aortic valve, single ventricle or Fallot's tetralogy are classically quantified from hemodynamics assessment [44].

1.4 In vivo blood flow measurements

Invasive measurement techniques such as catheterization are simple and robust methods to measure some hemodynamic flow fields. Nowadays, pressure catheterization (introduction of a pressure probe in the artery) is still considered as the clinical gold standard to obtain a direct measurement of the pressure in-vivo and to evaluate the severity of a stenosis. Limited by the risks due to its invasiveness, this procedure is only recommended to treat severe or urgent cases. With the recent

developments in medical imaging techniques, invasive blood flow measurement techniques are progressively replaced by non-invasive measurement techniques such as phase-contrast MRI and Doppler echocardiography, which emerge as the reference blood flow measurement techniques in clinical practice.

1.4.1 Doppler echocardiography

The echocardiography technique benefits from the Doppler effect to estimate the blood velocity or tissues motions in a real-time fashion, with a high temporal resolution. However, an important limitation is that it only gives access to the 1-D velocity component oriented along the ultrasonic beam angle. Speckle tracking [56] or Vector Doppler [121] techniques allow to reconstruct the 2D velocity field by addition of physical constraints to the measurement. Apart from estimating the pressure field using Bernoulli's principle, other hemodynamics quantities are difficult to compute with Doppler-based techniques since the through-plane velocity component is not measured. Figure 1.6a shows a 2D velocity vector map obtained using vector flow Doppler echocardiography mapping in the left heart.

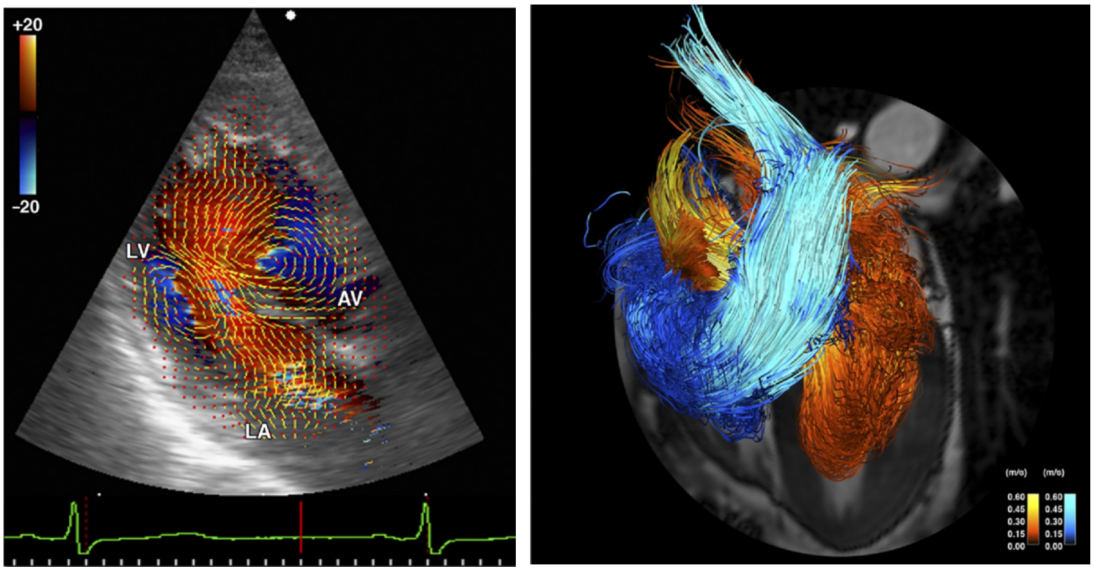

(a) (b)

Figure 1.6: Velocity maps in the heart obtained by a). Vector Doppler echocardiography, and b). phase-contrast MRI. Images are taken from [134].

1.4.2 Phase-Contrast Magnetic Resonance Imaging

Initially developed for visualization of soft tissues, MRI measures the relaxation properties of some specific atoms subjected to high-frequency variations of magnetic

fields. Phase-contrast MRI is a specific class of MRI sequence in which the linear relationship that exists between the phase of the measured signal and the magnetically excited protons velocity is used to reconstruct the blood velocity. Initially developed in 2D [113], it has later been extended to time-resolved 3D imaging [100], referred to as 3D CINE PC-MRI or 4D Flow MRI. A detailed description of the MRI basic operating principles, applications and limitations can be found in Chapter 2.

Briefly, the main advantage of this technique is that it provides in a single exam a comprehensive access to the temporal evolution of the 3D velocity fields as well as the morphology of the arterial region of interest. In this sense, it stands out as a relevant tool to evaluate the hemodynamics fields in-vivo. As compared to 2D CINE PC-MRI, 4D Flow MRI allows to assess the flow field in a fully retrospective fashion. For instance, to measure the flow rate with 2D imaging the user needs to predetermine the position and orientation of a slice. With 4D imaging, the velocity field is first measured in the entire domain so that the slice could be freely positioned afterwards (retrospectively). Moreover, 4D Flow MRI opens access to new hemodynamics biomarkers derived from the velocity field, such as pressure field [86], WSS [128], or residence time, which are pertinent quantities in terms of medical diagnosis but difficult to evaluate with other modalities. Finally, specific 4D Flow MRI sequences have allowed to quantify several biomarkers associated with complex unsteady phenomenon such as turbulent kinetic energy [87] and pressure loss due to turbulent production [64], which were found to be involved in the development of cardiovascular disorders such as atherosclerosis or cardiac malfunctions [31, 45].

While Doppler echocardiography is well suited for rapid diagnosis, PC-MRI generally shows clear advantages for the complete quantification of blood flows.

1.4.3 Limitations

Despite all these advantages, several acquisition parameters can limit the expected accuracy and compromise the MRI measurements reliability [60]. For example, a poor spatial resolution could misrepresent the measured flow near the arterial walls (partial volume effects). Similarly, a poor temporal resolution might provide insufficient flow description, depending on its complexity and pulsatility. Time offsets between space and velocity encoding might also generate motion-induced image artifacts [146]. Also, MRI intrinsically provides a sample average representation of the flow, where the velocity fluctuations are not directly accessible. Moreover, machine-specific variability could affect the measurements depending on both hardware and software settings [58]. Moreover in most of the cases, the measurement errors are at least as much pronounced for quantities that are derived from the velocity field such as the WSS or pulse wave velocity.

1.5 Using numerical simulations to improve diagnosis

Due to the recent increase in computational power, numerical simulation applied to medical research has recently known a widespread development. Since few decades, Computational Fluid Dynamics (CFD) has been thoroughly adapted to blood flows prediction and analysis in the cardiovascular system.

In-silico and in-vitro CFD-based parametric studies are classically performed to isolate some parameters and evaluate their effects on the hemodynamics field [114]. Pilot studies present great interests in the optimization of biomedical devices, and in pre and post operative blood flow assessment [85]. Coupled CFD-MRI studies have sometimes been proposed for validation and verification purposes, either using CFD [59] or MRI [13, 111] as a reference field. Physics-based CFD constraints can also be added to regularize the MRI flow measurements [6, 132].

For in-vivo investigations, CFD can be used as a complementary tool to get in-depth insights into the physiological or pathological cardiovascular flows. To this end, a method consists in coupling CFD with planar MRI flow measurements as boundary conditions to predict the 3D velocity fields within a numerical mesh of the vessel morphology measured with CT or MRI scan.

Although CFD accuracy hinges on model assumptions, it enables to partially bypass some experimental limitations inherent to the MRI acquisition process. The obvious advantage is that CFD has the potential to provide higher spatio-temporal resolutions and to grant an easy access to derived and instantaneous quantities. Therefore, CFD coupled with MR velocity measurements has the potential to provide highly resolved blood flow insights, and will probably further be exploited in the future.

1.5.1 Coupling CFD with PC-MRI

A prerequisite to couple CFD to MRI is to ensure that at some point the two techniques converge towards compatible outcomes. In this respect, considerable efforts have been made to compare and cross-analyse MRI measurements and CFD predictions over the last years. However, as shown in Table 1.2, there is still no consensus on whether or not the two techniques lead to the same outcomes and several limitations are generally pointed out to explain the reported discrepancies. Indeed, some studies conclude that PC-MRI and CFD are in close agreement [13, 77] while others report large discrepancies [70, 84].

As it hinges on many modelling assumptions and numerical approximations, blood flow simulations are generally not exempt from errors. Many studies have

investigated the impact of boundary conditions and numerical strategy on the resulting hemodynamic errors. First, numerous studies highlighted the importance of imposing adequate boundary conditions [114, 130]. Nevertheless, as shown in Table 1.2, idealized velocity profiles (such as blunt, flat, or fully developed profiles) are often prescribed as inlet boundary condition [9, 70, 111, 168], although this may result in erroneous hemodynamic predictions [114]. Moreover, in-vivo simulations may require to account for the wall motions [31], or an a priori knowledge of its mechanical properties (for fluid-structure interactions). However in practice, arterial wall deformations are often neglected [24, 35], which probably leads to misrepresentations of the flow field in the viscous layer, especially for large vessels simulations [37]. Moreover, multiple outlets are commonplace in-vivo, from simple bifurcations (e.g. carotid artery) to entire arterial networks (e.g. pulmonary network). In spite of being a key ingredient driving the flow split between daughter branches, the outflow boundary condition is often reduced to an unrealistic zero pressure condition [29] which constitutes a potential source of errors [70, 72]. Prescribing outflow conditions from measurements (e.g. pressure measurements) could be a way to bypass this restriction, although these latter are certainly not free of errors. For in-vitro models, an alternative way to get a flow split independent of the outlet boundary condition consists in merging the branches in a unique outlet. In this case, flow distribution within the flow domain is driven by the fluid mechanics only and a zero-pressure condition can be prescribed at the outlet.

The complex blood properties require an adapted model to simulate its shear-thinning non-Newtonian behaviour. At the macroscopic level, blood is often assumed to be Newtonian and homogeneous. While this is a reasonable assumption in large arteries such as aorta [55, 123], it may result in erroneous predition for flows experiencing low shear rates (under 100 s^{-1}) [123]. In-vitro simulations with perfectly characterized blood mimicking fluid rheology can be performed to bypass this modelling uncertainty, and to avoid the associated errors.

In addition, making an advised choice of CFD strategy is essential for a reliable hemodynamics prediction. As the typical Reynolds number in the (large) arteries ranges from a few hundreds (laminar) to a few thousands (turbulent), it is important to adopt a CFD strategy that accounts for the turbulence effects during computations. However, this step is often excluded [13, 35]. As solving the whole range of turbulence spectrum generally requires huge computational resources, turbulence modelling strategies are often used to either partially or totally model the velocity fluctuations. Nevertheless, there are still controversies about the proper formulation to model turbulence, and an unsuitable model could significantly affect the flow prediction [87, 111]. Among the large number of existing models, Reynolds Averaged Navier-Stokes (RANS) and Large Eddy

Simulation (LES) are the two recurrent approaches usually adopted in flow solvers. Although more computationally demanding, Large Eddy Simulation has the advantage of capturing the transition to turbulence with no changes of turbulence model parameters and can thus be considered as predictive, whereas Reynolds Averaged Navier-Stokes (RANS) models require parameters adaptations to properly represent transitional flows [73, 98].

Recent CFD challenges also highlighted the large influence of the solver numerics and boundary conditions on the resulting flow patterns [172]. As demonstrated in Valen-Sendstad et al. [156], the discrepancies between different techniques partially come from low-order unconditionally stable implicit schemes proposed as default parameters by several commercial CFD codes, which generate artificial dissipation for robustness purposes. In this sense, a careful validation of the CFD strategy seems important to appreciate the level of errors associated with the modelling assumptions.

1.5.2 Reconstruction of derived quantities from PC-MRI

As already mentioned, the wall shear stress (WSS) is a flow quantity that is often regarded as a biomarker of disorders such as aortic diseases, aneurysm, atherosclerosis, or valve regurgitation. In particular, WSS plays an important role in both aneurysm initiation, growth and rupture, since changes in WSS influence endothelial cell function and thus, promote vascular remodelling and vessel dilatation [110]. Procedures based on different algorithms have been proposed in the literature to reconstruct the WSS [128, 142, 144] from MRI velocity data.

The relative pressure field is also relevant for diagnosis to estimate the severity of a stenosis or a pulmonary hypertension. This quantity can be inferred from velocity measurements and several research works have developed numerical procedures to reconstruct the relative pressure field from MRI [42, 46, 47, 82].

The large number of different approaches proposed in the literature to estimate both WSS and pressure from MRI suggests the importance of a gold standard solution to assess the accuracy and robustness of the proposed methods under realistic complex flow conditions (cf. conditions other than the simple analytic Womersley or Poiseuille flow solutions). Even if Les et al., (2010) [90] found that the WSS computed from CFD does not reach proper convergence with mesh refinements, little attention is generally devoted to ensure that the reference flow variable is correctly converged.

1.5.3 Numerical simulation of PC-MRI

In the hypothesis where a CFD velocity field with limited enough errors is generated, it can be used as the reference field to evaluate the errors that arise

from a direct measurement or when reconstructing a derived hemodynamics field from a 4D Flow MRI acquisition. If the differences between CFD and MRI can be alleviated, one can reasonably assume that the remaining discrepancies are principally due to the MRI acquisition process. Among the many different factors contributing to the MRI velocity error, one can for example mention the dysfunctions induced by defects of the MRI hardware (gradient or radiofrequency coils - see Section 2.2.1) that distort the flow measurement. Furthermore, a set of parameters unsuited to the imaging protocol would also influence the resulting measurements. Indeed, the complex physical principles governing the MR signal acquisition process, the signal processing steps required to reconstruct an MR image, as well as the large variety of user-dependent acquisition parameters are all potential sources of errors that make it generally difficult to precisely identify the reasons for an erroneous measurement.

In this sense, the numerical simulation of the MRI acquisition process could be an efficient way to decompose these modalities in order to identify the sources of errors. It has already proven its usefullness to describe and correct some sources of imaging artifacts [122], as well as to optimize MRI pulse sequences [4]. Moreover, the well-known MR fingerprinting technique [96] is a good illustration of a possible use of MRI simulation to generate a dictionary containing the MR signals of a complete spectrum of tissue properties.

1.5.4 Limitations and scientific challenges

The large variety of possible input options, from the MRI setup (acquisition parameters and post-processing corrections) to the choice of CFD strategy (numerics, modelling assumptions, boundary conditions,...) or the study framework (in-vivo/in-vitro/in-silico), makes it intricate to draw general conclusions about the reported errors in the literature between MRI and CFD outcomes (see Table 1.2). Even in a perfect world where CFD and MRI outcomes would be virtually free of errors, the fundamental differences inherent to MRI and CFD modalities (e.g: high/low resolution in space and time, noise/noiseless data, solution in physical space/k-space filling, etc...) would most probably induce errors relative to the comparison itself.

The complex numerical procedure adopted to compute hemodynamics quantities that are derived from the MRI velocity field (pressure, WSS, pulse wave) are also likely to introduce additional errors, on top of propagating input velocity errors. Indeed, it is expected that quantities such as WSS are very sensitive to velocity measurement errors.

Finally, a clear identification of the MRI sources of discrepancies that remain after corrective post-processing is necessary to further improve quantitative blood

flow measurements in clinical practice. However, the multi-modal MRI acquisition process complicate the identification of the sources of discrepancies.

1.6 Thesis outline and objectives

1.6.1 Objectives

The first objective of this work is then to propose a standardized procedure for comparing MRI and CFD under complex flow conditions. To establish this procedure, a preliminary step is to mitigate the sources of discrepancies coming from each technique separately in order to focus on the errors relevant to the comparison itself.

For this purpose, we designed a fully controllable, reproducible and MRI compatible experiment delivering a blood-mimicking fluid flow within a phantom which gathers topological complexities typical of that observed in-vivo. We have full control of the geometry of the non deformable flow domain and fluid rheology, thus removing classical sources of uncertainties that could be found in-vivo: segmentation errors, wall motion, blood properties. Also, although branching is present within the considered flow domain, there is only one outlet boundary so that a simple zero pressure condition can be safely prescribed. The corresponding flow is predicted by means of a high resolution LES solver, and compared with velocity fields acquired using conventional 4D PC-MRI scans at various spatial resolutions. A quantitative analysis of the differences is then performed to highlight the potential discrepancies induced by a straightforward comparison. Finally, several post-processing steps are encompassed and a generic comparison protocol is proposed to systematically correct for these sources of discrepancies.

Once the standardized procedure established and validated with a proof-of-concept comparison case, the second objective is to use this CFD solution as a reference field to evaluate how the MRI velocity measurement errors propagates when reconstructing derived quantities, such as WSS or pressure field. The accuracy, validity and robustness of different reconstruction algorithms are also tested.

The final objective is to discriminate the source of the observed MRI hemodynamics field errors, and where appropriate, to account or correct them. In this respect, given the complexity of the MRI acquisition process, we aim at developing a 4D Flow MRI acquisition simulation platform to understand and isolate the dominant phenomenon responsible for the errors observed. The interest here is double; the numerical simulation allows to identify the source of measurement errors, but it also can be used to optimize existing PC-MRI protocols and sequences. It is however a long-term objective and this thesis limits to the development of

the MRI simulation framework.

1.6.2 Thesis outline

The second chapter of this thesis first introduces the reader with some fundamental concepts of MRI and the main features of phase-contrast MRI sequences. From these concepts, the experimental limitations that are raised and the most common sources of errors involved in PC-MRI are detailed.

The third chapter describes the numerical framework implemented in the flow solver and presents two validation test cases developed during this thesis.

In the fourth chapter, a CFD-based quality control procedure relevant to the 4D flow MRI technique is developed. This includes all the details about the design of the experimental test bench, the MRI and CFD post-processing steps, and the description of the flow. A proof-of-concept validation of the procedure is presented, results are analysed and conclusions are drawn about the significance and scope of application of this work.

In the fifth chapter, we evaluate the accuracy that can be expected when using MRI data to reconstruct quantities that are derived from the velocity field. Based on our in-vitro CFD framework, and using the CFD as a reference field, we assess and compare the accuracy and robustness of the proposed solution with other existing WSS-reconstruction methods published in the literature. We infer on the reliability of our method and finally come up with general recommendations on the WSS reconstruction from MRI measurements. Then, a very similar approach is developed for the relative pressure reconstruction from MRI velocity measurements. We also assess several pressure reconstruction approaches using the previously developed CFD-based framework. This chapter illustrates an alternative way to use such a reference framework as a benchmark to evaluate and compare different reconstruction approaches.

In the penultimate chapter of this thesis, an in-house 4D Flow MRI acquisition simulator is developed. The algorithm is detailed, and several validation test cases are presented where each part of the full MR velocity reconstruction pipeline are treated incrementally. Finally, 4D Flow MRI simulations of the phantom's experiment are compared with realistic 4D Flow MRI measurements. Conclusions about the significance of the results and possible future developments are finally expressed.

In the last chapter, a retrospective summary of the main results obtained is presented and general conclusions are drawn. Clinical perspectives as well as future research directions are discussed.

Table 1.2: Non-exhaustive review of recent publications comparing 3D PC-MRI to CFD for Newtonian, incompressible flow in a rigid domain under pulsatile regime.

Author, year	**Configuration**	**Compared variables**	**Conclusion of the study**
Miyazaki et al., 2017 [111]	Healthy and double aortic arch	Flow rate Velocity WSS Energy Loss	Moderate correlation for velocity in AAo ($r = 0.53$) and overestimation of flowrate (up to $\varepsilon = 1.87$); poor agreement for WSS and energy loss in AAo
Biglino et al., 2015 [13]	in-vitro normal aorta and TGA	Flow rate Velocity WSS	Flow rate: small discrepancies ($\varepsilon \leq 0.162$, $r^2 \geq 0.86$)
Pahlavian et al., 2015 [70]	Cervical Spinal Subarachnoid space	Velocity	High discrepancies (from 1.4 to 5.6 times greater for MRI through-plane peak velocity magnitudes)
Cibis et al., 2014 [35]	Carotid artery	Flow rate WSS	Good qualitative WSS patterns, WSS magnitude errors up to 30 %, WSS vector angle errors up to 65.6°
Berg et al., 2014 [9]	Intracranial aneurysm	Velocity	Good qualitative agreement, discrepancies for velocity correlation (76.5% of the points have accuracy of more than 80% for MSI)
Van Ooij et al., 2013a and 2013b [157, 158]	in-vitro/vivo intracranial aneurysm	Velocity WSS	High qualitative agreement and high quantitative discrepancies for WSS: $\rho = 0.65$ at peak systole, up to $\varepsilon =$ 27.1% error for velocity magnitudes
Lantz et al., 2013 [87]	in-vivo aorta	Kinetic Energy	Good agreement for peak integrated TKE (13% error for LES , and 51% for RANS $k-\omega$ SST)
Yiallourou et al., 2012 [168]	Cervical spine subarachnoid space	Velocity Flow rate	Overestimation of MRI (error $\geq$ 70% for peak velocity), many visual discrepancies for velocity

DAo: Descending Aorta; AAo: Ascending Aorta; TKE: Turbulent Kinetic Energy; r: Pearson's product moment coefficient; ρ: Spearman's correlation coefficient; MRI-CFD error calculated as: $\varepsilon = \left|\frac{f_{CFD}-f_{MRI}}{f_{MRI}}\right|$ where f is the flow parameter considered. MSI stands for Magnitude Similarity Index [9]. SST: Shear Stress Transport.

Chapter 2

Fundamentals of Magnetic Resonance Imaging

Chapter contents

2.1 Nuclear Magnetic Resonance

Magnetic Resonance imaging is based on the phenomenon of Nuclear Magnetic Resonance (NMR) discovered by Rabi et al. [129] in the 1930's. Then, in 1946, Bloch and Purcell extended this work to liquids and gas and measured the effects of the applied magnetic field on the protons. For this work, they obtained a Nobel Prize in 1952.

The basic principles of NMR arise from the magnetic properties of the protons. An atomic nucleus can be described by a nuclear spin angular momentum $\mathbf{J}$ and a spin quantum number. Only atomic nuclei composed by a odd number of protons and/or odd number of neutrons possess a spin quantum number that is non-zero, and are subjected to Nuclear Magnetic Resonance. A non-zero spin quantum number induces a magnetic moment $\boldsymbol{\mu}$ oriented along the same direction, and that can be expressed as:

$$\boldsymbol{\mu} = \gamma \mathbf{J} \tag{2.1}$$

where γ is a gyromagnetic ratio, a constant specific to each atomic species considered. The hydrogen atom, with a spin quantum number that equals $\pm 1/2$ and a gyromagnetic ratio $\gamma = 267.513 \times 10^6\ rad.s^{-1}.T^{-1}$ is often exploited in NMR as it is the most abundant in the human body. Without any exterior magnetic field, the spins are oriented randomly. In the presence of an external static magnetic field $\mathbf{B}_0$, these spins align according to two lowest energy states, that read:

$$E_{+1/2} = +\frac{1}{2}\gamma B_0 \hbar\ , \qquad E_{-1/2} = -\frac{1}{2}\gamma B_0 \hbar \tag{2.2}$$

where $\hbar$ is the reduced Planck constant. The Boltzmann distribution states that the spins will statistically prefer a parallel orientation ($E_{+1/2}$) rather than an anti parallel orientation ($E_{-1/2}$) since the energetic contribution is more favourable. Moreover, the interaction between the proton's spin and the external magnetic field generates a torque such that:

$$\frac{d\boldsymbol{\mu}}{dt} = \gamma \boldsymbol{\mu} \times \mathbf{B}_0 \tag{2.3}$$

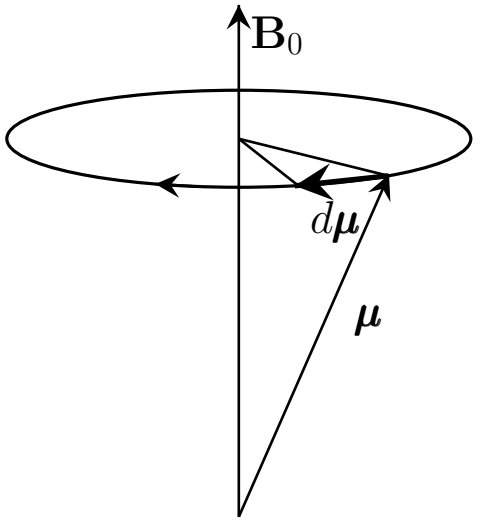

Figure 2.1: Rotation (precession) of the magnetic moment vector μ around the axis of the applied magnetic field $\mathbf{B}_0$. The precession occurs as a response to a torque generated by the interaction between the proton's spins and the external magnetic field.

Note that as a convention, $\mathbf{B}_0$ will be chosen such as $\mathbf{B}_0 = B_0\hat{e}_z$ with $(\hat{e}_x, \hat{e}_y, \hat{e}_z)$ the Cartesian unit vectors. The rotation induced by this torque is called precession and schematically represented in Figure 2.1. The angular frequency of this precession (called Larmor frequency ω_0) is proportional to the external magnetic field such as:

$$\omega_0 = \gamma B_0 \tag{2.4}$$

It is important to note that if $\gamma > 0$ the rotation of the magnetic moment vector follows a left-hand rule about the static field axis and rotates clockwise. Then, the following convention applies: if B_0 is applied along z-axis, then $\mathbf{B}_0 = \frac{\omega_0}{\gamma}\hat{e}_z$ where the angular velocity vector equals $\mathbf{\Omega}_0 = -\omega_0\hat{e}_z$.

Since a huge amount of atoms are considered in the NMR process, the behaviour of a sample of N_s spins included in a volume V can be described at the macroscopic scale, following the classical laws of mechanics by summing the contribution of each magnetic moment:

$$\mathbf{M} = \frac{1}{V}\sum_{i=1}^{N_s}\boldsymbol{\mu}_i \tag{2.5}$$

where $\mathbf{M}$ is the net macroscopic magnetization vector. Following Equation (2.3), if one neglects the interaction of the protons with their environment, the time

evolution of the macroscopic magnetization in a presence of an external static magnetic field $\mathbf{B}_0$ can be expressed as:

$$\frac{d\mathbf{M}}{dt} = \gamma \mathbf{M} \times \mathbf{B_0} \tag{2.6}$$

In classical MRI scan, B_0 ranges from $1.5T$ to $7T$. As a result of the precession induced by $\mathbf{B}_0$, it is possible to express the macroscopic magnetization at thermal equilibrium $\mathbf{M}_0$ as:

$$\mathbf{M}_0 = \frac{\rho_0 \gamma^2 \hbar^2}{4kT} \mathbf{B}_0 \tag{2.7}$$

where ρ_0 is the number of protons per unit volume, k the Boltzmann constant, and T the temperature. Detailed derivation of the thermal equalitibrium magnetization can be found in [65]. This resultant vector $\mathbf{M}_0$ aligns along the field direction $\hat{e}_z$.

2.2 NMR experiment: the Bloch equations

The equations describing the macroscopic evolution of the magnetic response that arise when a set of spins is submitted to an external magnetic field were introduced by Felix Bloch in 1946. This set of spins is called an "isochromat" and defined as an ensemble of spins with the same phase. An NMR experiment basically consists in two steps: a perturbation of the spins from their equilibrium state (excitation), followed by a relaxation where the spins' signature are collected.

2.2.1 Excitation

In the excitation step, an oscillating magnetic field $\mathbf{B}_1$ is applied to disturb the net magnetization from its equilibrium state. This magnetic field called the Radio-Frequency (RF) pulse is applied by a transmit coil transversally to the static field such as $\mathbf{B}_1(t) = B_{1x}(t)\hat{e}_x + B_{1y}(t)\hat{e}_y$, and during a short period of time ($\tau_{\text{rf}} \sim 10\ \mu s$). As a result of an excitation pulse at resonance frequency, the orientation of the net magnetization vector is shifted towards the transverse plane. An RF excitation applied with a frequency $\omega_{\text{rf}} = \omega_1$ can be expressed in the transverse plane with the following complex notation:

$$B_1(t) = B_{1x}(t) + iB_{1y}(t) = B_1^e(t)e^{-i\omega_1 t + \phi} \tag{2.8}$$

where ϕ is the phase of the RF vector, and $B_1^e(t)$ the envelope of the pulse. To characterize the signature of the RF pulse on the system, the flip angle is defined as the amount of rotation accumulated by the magnetization due to an RF pulse. From Eq. 2.4, the flip angle can be defined as:

$$\alpha = \gamma \int_0^{\tau_{\text{rf}}} B_1^e(t)dt \tag{2.9}$$

Typical flip angles are comprised between 0° and 90° for gradient echo sequences while between 90° and 180° for spin echo sequences. Considering a rectangular RF envelope reduces the flip angle to $\alpha = \gamma B_1 \tau_{rf}$. Usually, on modern MR scans, the maximum amplitude of the B_1 field does not exceed 50 μT, and the RF impulse usually lasts few milliseconds.

2.2.2 Relaxation

After the RF pulse, the protons contained in the excited sample start interacting with each other and with their surrounding environment. The magnetization vector relaxes until it recovers its initial longitudinal orientation M_0 (see Eq. 2.7) after a time which is typical of the tissue observed. This is the relaxation. The spin-lattice and spin-spin relaxations may be introduced to characterize the nature of the tissues.

Spin-lattice relaxation The spin-lattice relaxation describes the energy exchanges between the spins and their environment. Its characteristic time (or relaxation time) T_1 corresponds to the time needed for the longitudinal component of the magnetization vector $\mathbf{M} \cdot \hat{e}_z$ to recover 63% of its equilibrium value.

Spin-spin relaxation The spin-spin relaxation describes the magnetization decay in the transverse plane due to the energy exchanges between the spins, themselves, and their environment, and is characterised by the time T_2 (which corresponds to the time needed to relax 37% of the initial transverse magnetization). The steps of a complete NMR experiment are schematically depicted on Figure 2.2.

The spin-spin and spin-lattice relaxation phenomena added in the previous Eq. (2.6) lead to the following Bloch Equation:

$$\frac{d\mathbf{M}}{dt} = \gamma \mathbf{M} \times \mathbf{B} + \frac{M_0 - M_z}{T_1}\hat{e}_z - \frac{M_x}{T_2}\hat{e}_x - \frac{M_y}{T_2}\hat{e}_y \tag{2.10}$$

where $\vec{B} = \vec{B_0} + \vec{B_1}$.

To simplify the Bloch equations, it is common to introduce a rotating frame that rotates clockwise at the Larmor frequency around the z axis of the laboratory frame of reference. The following relation can be used to change the time derivative from the laboratory to rotating frame:

$$\left(\frac{d\mathbf{M}(t)}{dt}\right)_{\mathcal{R}_{lab}} = \left(\frac{d\mathbf{M}(t)}{dt}\right)_{\mathcal{R}_{rot}} + \mathbf{\Omega} \times \mathbf{M}(t) \tag{2.11}$$

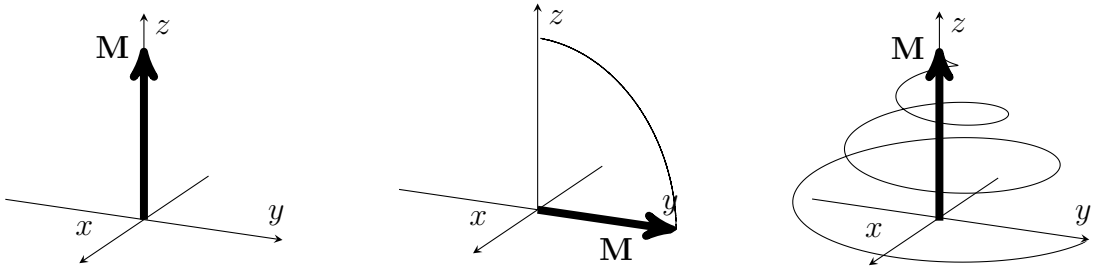

Equilibrium Excitation Relaxation

Figure 2.2: Illustration of an NMR experiment. First, the macroscopic magnetization is aligned with the static magnetic field $\mathbf{B_0} = B_0\hat{e}_z$. A RF pulse is then applied in the transverse plane $\mathbf{B}_1 = B_{1x}\hat{e}_x$. This excitation forces the magnetization vector to align quasi-instantaneously in the transverse plane, orthogonal to the RF pulse axis. After the RF pulse excitation, the magnetization vector recovers its orientation during a phase of relaxation. The duration of this relaxation allows to characterize the material in the region of interest.

where $\Omega = -\omega\hat{e}_z$. Then, the magnetization vector expressed in the rotating frame $\mathbf{M'} = (M_{x'}, M_{y'}, M_{z'})$ reads:

$$\frac{d\mathbf{M'}}{dt} = \gamma\mathbf{M'} \times (\mathbf{B'_1} + \mathbf{B_0} - \frac{\omega}{\gamma}\hat{e}_z) + \frac{M_0 - M_z}{T_1}\hat{e}_z - \frac{M_{x'}}{T_2}\hat{e}_{x'} - \frac{M_{y'}}{T_2}\hat{e}_{y'} \tag{2.12}$$

where $\mathcal{R}_{rot} = (\hat{e}_{x'}, \hat{e}_{y'}, \hat{e}_{z'})$ denotes the unit vectors of the rotating frame of reference. The rotation matrix from the laboratory frame towards the rotating frame reads:

$$\mathbf{R} = \begin{pmatrix} \cos(\omega t) & -\sin(\omega t) & 0 \\ \sin(\omega t) & \cos(\omega t) & 0 \\ 0 & 0 & 1 \end{pmatrix} \tag{2.13}$$

The effective magnetic field corresponds to the magnetic field perceived by an isochromat in the rotating frame, and can be defined as $\mathbf{B_{eff}} = \mathbf{B'_1} + \mathbf{B_0} - \frac{\omega}{\gamma}\hat{e}_z$. Therefore, if $\omega = \omega_0$, the static field contribution is cancelled since $B_0 = \frac{\omega_0}{\gamma}\hat{e}_z$, and therefore $\mathbf{B_{eff}} = \mathbf{B'_1}$.

One can express the complete Bloch equations in the rotating frame of reference using the following matrix notation:

$$\frac{d}{dt}\begin{pmatrix} M_{x'} \\ M_{y'} \\ M_z \end{pmatrix} = \begin{pmatrix} -1/T_2 & \gamma B_z & -\gamma B_{y'} \\ -\gamma B_z & -1/T_2 & \gamma B_{x'} \\ \gamma B_{y'} & -\gamma B_{x'} & -1/T_1 \end{pmatrix}\begin{pmatrix} M'_x \\ M'_y \\ M_z \end{pmatrix} + \begin{pmatrix} 0 \\ 0 \\ M_0/T_1 \end{pmatrix} \tag{2.14}$$

where $B_{x'} = B_{1,x'}$ and $B_{y'} = B_{1,y'}$ represent the RF transmitter magnetic field.

Suppose the RF field is initially applied along the x' axis with a frequency ω_1; it can be expressed in the laboratory frame as:

$$\mathbf{B}_1(t) = B_1(t)\cos(\omega_1 t)\hat{e}_x - B_1(t)\sin(\omega_1 t)\hat{e}_y \tag{2.15}$$

Then, in the rotating frame of reference ($\omega = \omega_0$), it can be expressed as $\mathbf{B}_1'(t) = \mathbf{R}\mathbf{B}_\mathbf{1}(t)$ or:

$$\begin{pmatrix} B_{1,x'} \\ B_{1,y'} \\ B_{1,z} \end{pmatrix} = \begin{pmatrix} \cos(\omega_0 t) & -\sin(\omega_0 t) & 0 \\ \sin(\omega_0 t) & \cos(\omega_0 t) & 0 \\ 0 & 0 & 1 \end{pmatrix} \begin{pmatrix} B_1(t)\cos(\omega_1 t) \\ -B_1(t)\sin(\omega_1 t) \\ 0 \end{pmatrix} \tag{2.16}$$

which simplifies to:

$$\begin{pmatrix} B_{1,x'}(t) \\ B_{1,y'}(t) \\ B_{1,z}(t) \end{pmatrix} = \begin{pmatrix} B_1(t)\cos(\omega_1 - \omega_0)t) \\ -B_1(t)\sin(\omega_1 - \omega_0)t) \\ 0 \end{pmatrix} \tag{2.17}$$

To rotate the spins in the transversal plane, the RF pulse should be applied at the Larmor frequency $\omega_1 = \omega_0$. Therefore the previous expression simplifies to $\mathbf{B}_1(t) = B_1(t)\hat{e}_{x'}$. When the RF is turned on, the relaxation terms in Eq. (2.12) can be ignored since typical values of γB_1 ($\sim 10^3\ rad/s$) are much greater than the decay rates $1/T_1$ and $1/T_2$ ($\sim 1s^{-1}$).

2.3 Analytical solution of the relaxation

After the application of a RF excitation to initially orient the magnetization in the transverse plane, in the presence of a static magnetic field only $\mathbf{B} = B_0\hat{e}_z$ the Bloch equations expressed in the rotating frame of reference simplify to:

$$\begin{aligned} \frac{dM_x'}{dt} &= -\frac{M_x'}{T_2} \\ \frac{dM_y'}{dt} &= -\frac{M_y'}{T_2} \\ \frac{dM_z}{dt} &= -\frac{M_z - M_0}{T_1} \end{aligned} \tag{2.18}$$

Back in the laboratory frame, these equation lead to the following set of analytic solutions:

$$\begin{aligned} M_x(t) &= (M_x(0)\cos(\omega_0 t) + M_y(0)\sin(\omega_0 t))e^{-t/T_2} \\ M_y(t) &= (M_y(0)\cos(\omega_0 t) - M_x(0)\sin(\omega_0 t))e^{-t/T_2} \\ M_z(t) &= (M_z(0) - M_0)e^{-t/T_1} + M_0 \end{aligned} \tag{2.19}$$

where, for the sake of simplicity, $t_0 = 0$ denotes the end of the RF pulse τ_{rf} (i.e: the beginning of the relaxation), and $\mathbf{M}(\infty) = (0, 0, M_0)^T$ the equilibrium magnetization. It is common to express the magnetization as a longitudinal component (M_z) and transverse component using a complex notation $M_{xy} =$

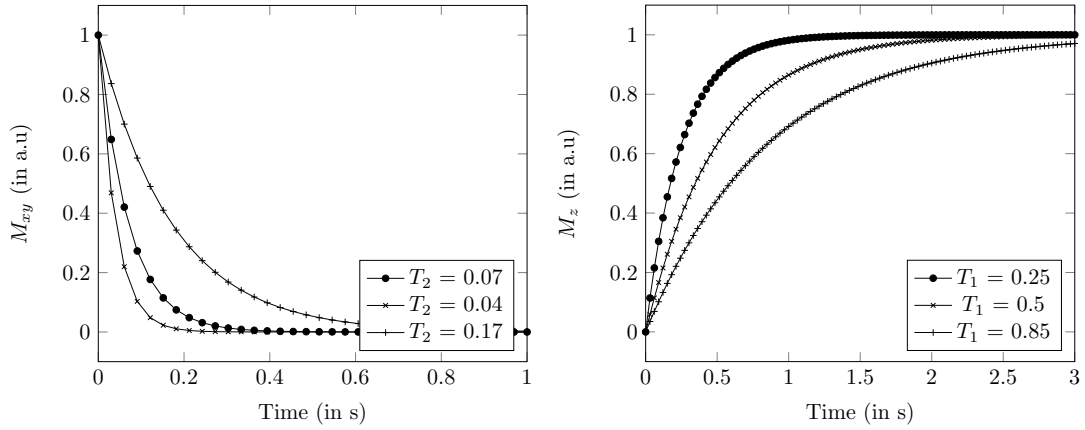

Figure 2.3: Relaxation of the transverse (left) and longitudinal (right) magnetization with initial magnetization $\mathbf{M}(0) = (1.0, 0.0, 0.0)$. First sample ($T_1/T_2$=0.25/0.07) corresponds to relaxation times of fat while $T_1/T_2 = 0.5/0.04$ corresponds to liver and T_1/T_2=0.85/0.17 is for blood at $B_0 = 1.5T$.

$M_x + iM_y$. Moreover, the transverse magnetization at $t = 0$ is often decomposed as $M_{xy}(0) = |M_{xy}(0)|e^{i\phi_0}$, where ϕ_0 is the initial phase shift of the transverse magnetization introduced by the RF excitation. Then, the solution takes the following form:

$$\begin{aligned} M_{xy}(t) &= |M_{xy}(0)|e^{i\phi_0}e^{-i\omega_0 t}e^{-t/T_2} \\ M_z(t) &= (M_z(0) - M_0)e^{-t/T_1} + M_0 \end{aligned} \tag{2.20}$$

Note that the transverse magnetization could also be written as: $M_{xy}(t) = |M_{xy}(t)|e^{i\phi(t)}$ where $|M_{xy}| = |M_{xy}(0)|e^{-t/T_2}$ and $\phi(t) = \phi_0 - \int_0^t \omega dt = \phi_0 - \omega_0 t$ the phase accumulated by the transverse magnetization at time t. The longitudinal and transverse magnetization decays are represented for several tissues in Figure 2.3.

Note that it is also possible to account for the diffusion of the magnetization by solving the Bloch-Torrey equation [155] by adding the diffusion term $\nabla \cdot (D\nabla(\mathbf{M}))$ to Eq. (2.10) where D is the diffusion tensor. The Bloch-Torrey equations are however not treated in this thesis.

2.4 Reception of the signal

2.4.1 Signal detection concepts

The net magnetization resulting from the spin relaxation induces a temporal variation of the magnetic flux Φ, measured through a receiver coil. Consider a sample object which magnetization precesses around its z-axis placed nearby a receiver coil, as depicted in Figure 2.4. According to Faraday's law of induction,

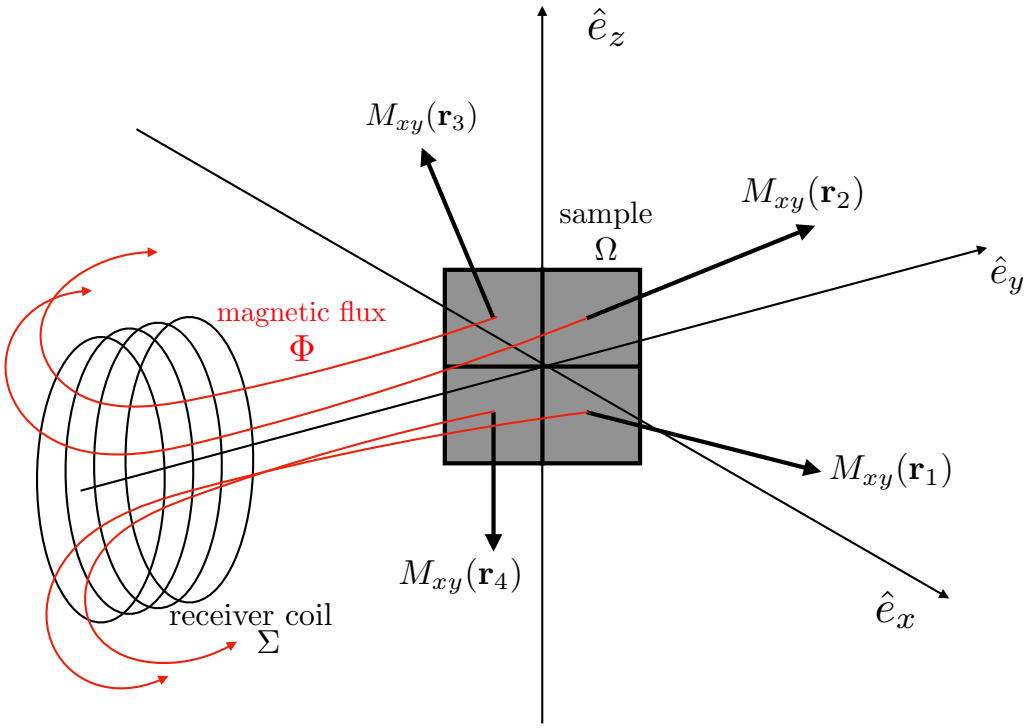

Figure 2.4: Illustration of the magnetic flux induced by a sample composed by four isochromats into a receiver coil.

the rate of change of magnetic flux measured by a receiver coil of surface Σ equals the electromotive force (or voltage) induced in the receiver coil, such as:

$$emf = -\frac{d\Phi}{dt} = -\frac{d}{dt}\iint_{\Sigma} \mathbf{B}^{rec}(\mathbf{r},t)\cdot d\mathbf{S} \tag{2.21}$$

where $\mathbf{B}^{rec}$ is the magnetic field received through the receiver coil and $d\mathbf{S}$ is normal to the coil area and oriented along the positive flux direction. Usually, the detection of this signal is ensured by the RF-coil which is switched from transmitter to receiver. As detailed in Haacke et al. (1999) [65], the magnetic flux detected over a receiver coil can be replaced by the integration over the entire domain of the magnetic field per unit current produced by this coil C^r at position r and due to the magnetization $\mathbf{M}(\mathbf{r},t)$, where a spatial dependence is added. This relation is consistent with the principle of reciprocity. Therefore, the resulting emf induced in a sample of volume Ω (defined as the volume of non-zero magnetization) and detected by the RF-coil could be expressed as:

$$emf = -\frac{d}{dt}\int_{\Omega} \mathbf{M}(\mathbf{r},t)\cdot\mathbf{C}^r(\mathbf{r})d\Omega \tag{2.22}$$

where $\mathbf{C}^r$ is the received magnetic field produced by the receiver coil at all points of non zero magnetization; we often call it the detection sensitivity of the receiver

coil. Given that $M_x = Re(M_{xy})$ and $M_y = Im(M_{xy})$, and recalling the expression of the transverse magnetization given in Eq. 2.20, the time-derivative taken inside the integrand as well as inside the real and imaginary operators leads to the following derivatives:

$$\begin{aligned} \frac{dM_{xy}}{dt} &= -(i\omega_0 + \frac{1}{T_2})|M_{xy}(\mathbf{r},0)|e^{-t/T_2}e^{-i(\omega_0 t - \phi_0)} \\ \frac{dM_z}{dt} &= -\frac{1}{T_1}(M_z(\mathbf{r},0) - M_0)e^{-t/T_1} \end{aligned} \tag{2.23}$$

In the previous equation,$1/T_2$, $1/T_1$ could easily be neglected given that ω_0 is at least 4-5 order larger for classical magnetic field (around 1.5T). Therefore, the z-component vanishing, the time-derivative of the transverse magnetization reduces to:

$$\begin{aligned} \frac{dM_x}{dt} &\approx -\omega_0|M_{xy}(\mathbf{r},0)|e^{-t/T_2}\sin(\omega_0 t - \phi_0) \\ \frac{dM_y}{dt} &\approx -\omega_0|M_{xy}(\mathbf{r},0)|e^{-t/T_2}\cos(\omega_0 t - \phi_0) \end{aligned} \tag{2.24}$$

The previous emf expression (Eq. 2.22) reduces to what is often referred to as the signal $s(t)$:

$$s(t) = \omega_0 \int_\Omega e^{-t/T_2}|M_{xy}(\mathbf{r},0)| \left(C_x^r \sin(\omega_0 t - \phi_0) + C_y^r \cos(\omega_0 t - \phi_0)\right) d\Omega \tag{2.25}$$

Finally, if we note $C_{xy}^r = C_x^r + iC_y^r$ the effective transverse sensitivity of the receiver coil and $C_x^r = |C_{xy}^r|\cos(\phi_r)$ and $C_y^r = |C_{xy}^r|\sin(\phi_r)$ where ϕ_r is the phase of the receiver coil, the signal can be simplified by using simple trigonometric identities. This leads to the following expression in the laboratory frame:

$$s(t) = \omega_0 \int_\Omega e^{-t/T_2}\,|M_{xy}(\mathbf{r},0)| \left|C_{xy}^r\right| \sin\left(\omega_0 t - \phi_0 + \phi_r)\right) d\Omega \tag{2.26}$$

2.4.2 Signal demodulation

A demodulation of the signal is then performed to remove the rapid oscillations at the frequency ω_0. This demodulation is equivalent to viewing the signal in the rotating frame of reference that rotates at frequency ω_0. In practice, the demodulation consists in multiplying $s(t)$ by a sinusoidal signal $\sin(\omega_0 t)$ and to applying a low-pass filter to remove the resulting high frequencies oscillations. The sinusoidal term in Eq. (2.26) $\sin(\omega_0 t - \phi_0 + \phi_r)$ multiplied by $\sin(\omega_0 t)$ together with the trigonometric identity ($\sin a \sin b = \frac{1}{2}(\cos(a-b) - \cos(a+b))$ where $a = \omega_0 t - \phi_0 + \phi_r$ and $b = \omega_0 t$ gives the demodulated signal. Then, a low-pass filter is applied to remove the high frequency component $\cos(a+b)$, resulting in the real channel signal $s_{re}(t)$:

$$s_{re}(t) = \frac{1}{2}\omega_0 \int_\Omega e^{-t/T_2}\,|M_{xy}(\mathbf{r},0)| \left|C_{xy}^r\right| \cos\left(\phi_0 - \phi_r)\right) d\Omega \tag{2.27}$$

Similarly, an imaginary signal can be obtained by multiplying the sinusoidal term in Equation (2.26) by a factor $-\cos(\omega_0 t)$, resulting in s_{im}:

$$s_{im}(t) = \frac{1}{2}\omega_0 \int_\Omega e^{-t/T_2} \left|M_{xy}(\mathbf{r},0)\right| \left|C_{xy}^r\right| \sin\left(\phi_0 - \phi_r\right)) \, d\Omega \tag{2.28}$$

A quadrature detection is finally needed to combine the real and imaginary parts of the signal received by the receiver coil into a complex signal $S(t) = s_{re} + is_{im}$. In practice, two orthogonal coils measure the same precessing magnetization, and this in order to determine the direction of the rotation. The resulting complex demodulated signal is therefore given by:

$$S(t) = s_{re}(t) + is_{im}(t) = \omega_0 \int_\Omega e^{-t/T_2} \left|M_{xy}(\mathbf{r},0)\right| \left|C_{xy}^r\right| e^{i(\phi_0 - \phi_r)} d\Omega \tag{2.29}$$

which in a more condensed form reads:

$$S(t) = \omega_0 \int_\Omega M_{xy}(\mathbf{r},t) C_{xy}^* d\Omega \tag{2.30}$$

where $C_{xy}^* = |C_{xy}|e^{-i\phi_r}$ is the complex conjugate of C_{xy}^r.

2.4.3 Space and time variations of the magnetic field

Note that the previous expression for the signal is valid for time and space constant magnetic fields. However, in practice the z-component of the magnetic fields is space and time varying, such that the Larmor frequency can be expressed (in the laboratory frame) as:

$$\omega(\mathbf{r},t) = \omega_0 + \Delta\omega(\mathbf{r},t) \tag{2.31}$$

where $\Delta\omega$ the frequency shift due to the variations of magnetic field perceived by the sample at position $\mathbf{r}$. In the rotating frame, ω_0 vanishes, then $\omega(\mathbf{r},t) = \Delta\omega(\mathbf{r},t)$. The accumulated phase ϕ of the transverse magnetization at position $\mathbf{r}$ can be expressed in the rotating frame, as:

$$\phi(\mathbf{r},t) = \phi_0 - \int_0^t \omega(\mathbf{r},t')dt' = \phi_0 - \int_0^t \Delta\omega(\mathbf{r},t')dt' \tag{2.32}$$

where it is recalled that $\phi_0 = \phi(0)$ is the phase of the transverse magnetization at the end of the RF pulse ($t = 0$). With this spatio-temporal dependence considered, the transverse magnetization can be rewritten from Eq. 2.20 as:

$$M_{xy}(\mathbf{r},t) = |M_{xy}(\mathbf{r},0)|e^{i\phi_0} e^{-i\int_0^t \Delta\omega(\mathbf{r},t')dt} e^{-t/T_2} \tag{2.33}$$

Then, introducing this spatio-temporal dependence into the signal expressed in Eq. 2.29 leads to:

$$S(t) = \int_\Omega \omega(\mathbf{r},t) M_{xy}(\mathbf{r},t) C_{xy}^* d\Omega \tag{2.34}$$

where $\omega(\mathbf{r},t)$ is largely dominated by the contribution of ω_0, which could be taken outside the integrand and so that Eq. 2.29 is recovered. Note that ω_0 could even be removed, without any loss of information.

2.5 Localization of the signal

One of the main challenge in MRI resides in the spatial localization of the magnetic contribution coming from each isochromat, to the global integrated signal measured by the receiver coil. For that, a spatial encoding is required prior to the signal detection. Spatial encoding involves a key component for the initiation of a MR image: the magnetic field gradients. Magnetic fields gradients denoted by $[G_x, G_y, G_z] = [\frac{dB_z}{dx}, \frac{dB_z}{dy}, \frac{dB_z}{dz}]$ can be applied independently along each of the 3 axes using additional coils, and are used to spatially modify the longitudinal magnetic field strength, and accordingly the Larmor frequency, as follows:

$$\begin{aligned} B_z(\mathbf{r}, t) &= B_0 + \mathbf{G}(t) \cdot \mathbf{r} = B_0 + G_x(t)x + G_y(t)y + G_z(t)z \\ \omega(\mathbf{r}, t) &= \omega_0 + \gamma \mathbf{G}(t) \cdot \mathbf{r} \end{aligned} \tag{2.35}$$

where $\mathbf{r} = (0, 0, 0)$ is defined as the isocentre of the scanner or the centre of the image. The magnetic gradient linearly alters the unique resonance frequency to a continuous bandwidth in order to distinguish the spatial location of signal emitted by the spins. Therefore, three spatial encoding steps are required to encode the three spatial directions. Typical gradients coils are usually designed to produce variations of the magnetic fields that range from 20 to 100 mT/m. In medical imaging, anatomical denominations are usually employed to describe the plane of acquisition. For a human lied down in a MR tunnel, the coronal plane is parallel to the ground; the transverse plane is perpendicular to the ground and separates the head from the feet; the sagittal plane is perpendicular to the ground and separates left from right, as illustrated in Figure 2.5.

2.5.1 Slice selection

Given a 3D volume placed in an MR tunnel, the first step to produce a 2D image (in the xy-plane, by convention) is to locate the position of the image in the direction orthogonal to the slice (along the z-direction). To this end, a slice selective excitation is usually applied to excite exclusively the spins included within the slice. It consists in applying a RF-pulse with a limited bandwidth $\Delta\omega_p$ together with a slice selection gradient G_{ss} along the z-axis to solely excite the spins which resonance frequency is included in the slice of interest, of thickness Δz (as described in Figure 2.6).

Recalling that $\omega(z) = \gamma B_0 + \gamma z G_z$, the frequency bandwidth $\Delta\omega_p$ of the RF-pulse excitation ranges from $\omega(z_0 - \frac{\Delta z}{2}) = \gamma B_0 + \gamma(z_0 - \frac{\Delta z}{2})G_z$ to $\omega(z_0 + \frac{\Delta z}{2}) = \gamma B_0 + \gamma(z_0 + \frac{\Delta z}{2})G_z$. Therefore, a slice selective excitation of thickness Δz centred in z_0 can be obtained by modulating the gradient G_{ss}, such as:

$$\Delta z = \frac{\Delta\omega_p}{\gamma G_{ss}} \tag{2.36}$$

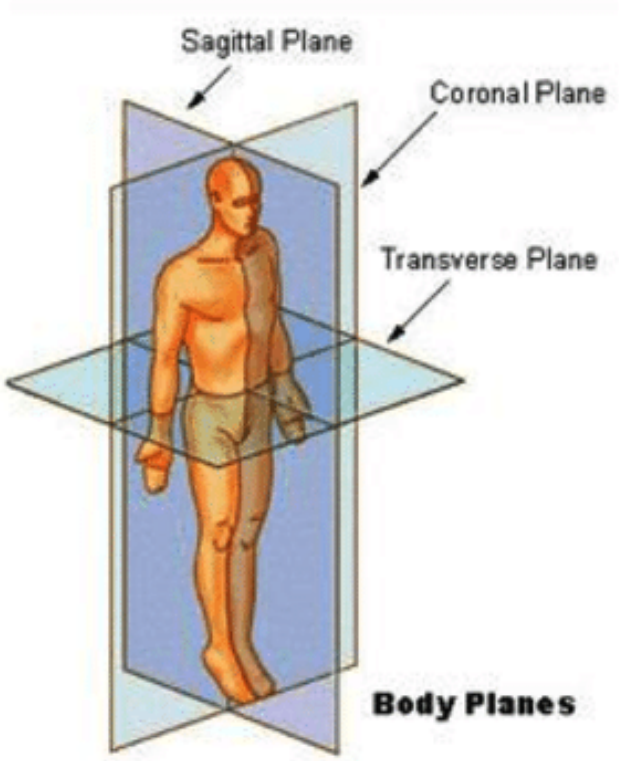

Figure 2.5: Illustration of the three elementary anatomical planes used in medical imaging.

2.5.2 RF pulse shape

Several types of RF pulse shapes can be used depending on the sequence and the object to measure. Hard pulses such as rectangular shapes are efficient but limited to 3D acquisition. Soft pulses (time-varying shape) are usually preferred for selective excitation. One of the most common soft pulses consists in applying a cardinal sine (SINC) shape excitation. The Fourier Transform of the SINC pulse shape with infinite number of lobes results in a perfect rectangular frequency profile, equally exciting the spins located within a slice and leaving the surrounding spins unchanged. In practice, however, a SINC function has a finite duration and therefore does not regularly excite the spins within a given frequency bandwidth. Window functions are usually applied to digitally filter the shape of the pulse by flattening the top of its frequency profile. Moreover, an apodization filter is used truncate the SINC function at its base and avoid exciting the spins located outside the slice thickness. The envelope of a SINC RF-wave can be expressed as:

$$B_1^e(t) = \begin{cases} AW(t)\,\mathrm{sinc}(\frac{\pi t}{t_1}) & \text{if} \quad 0 < t < \tau_{rf} \\ 0 \quad \text{else} \end{cases} \tag{2.37}$$

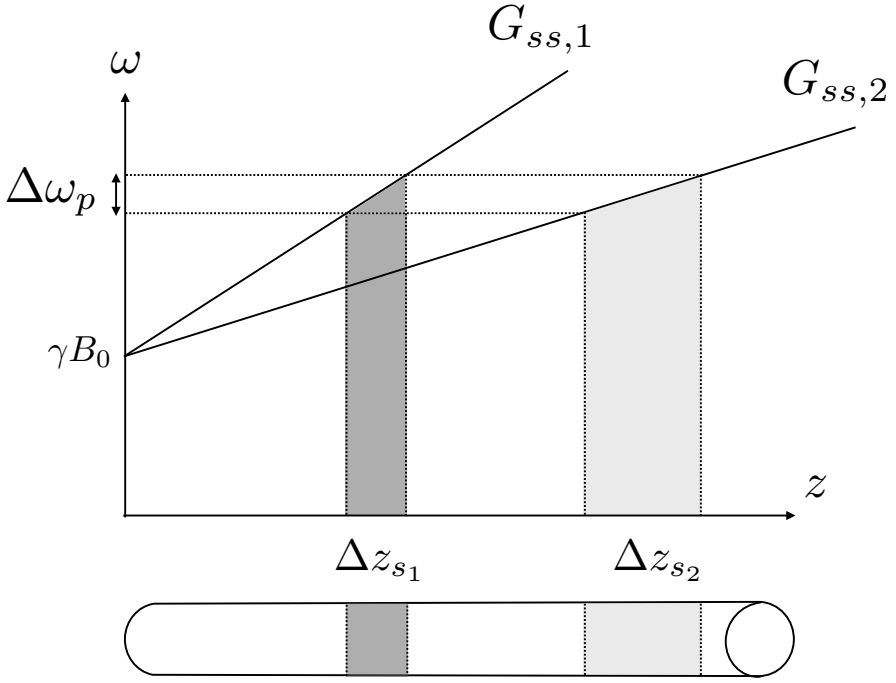

Figure 2.6: Slice-selective excitation. A RF pulse of frequency bandwidth $\Delta\omega_p$ could generate different slice thickness depending on the encoding gradient applied.

where A is the peak RF amplitude, $N = floor(\tau_{rf}/2t_1)$ where N is the number of zero-crossing of the pulse, t_1 is half the width of the central lobe, and $W(t)$ is the window function applied. Usual window functions are:

$$W(t) = \begin{cases} 1, \\ (1-\alpha) + \alpha\cos(\frac{\pi t}{Nt_1}), \\ 0.42 - 0.5\cos(\frac{\pi t}{Nt_1}) + 0.08\cos(\frac{2\pi t}{Nt_1}), \end{cases} \tag{2.38}$$

where the first, second and last lines correspond to no (or rect) window, Hamming ($\alpha = 0.46$) or Hanning ($\alpha = 0.5$) windows, and Blackman windows, respectively. The resulting transverse magnetization obtained for the presented window functions are presented in Figure 2.7. The use of a window function seems necessary to dampen the oscillations that appear at the boundaries of the slice.

2.5.3 Selective excitation pulse design

A typical slice selective excitation sequence is presented in Figure 2.8.

Recalling the relation found in Eq. 2.36, and given a gradient magnitude $G_{ss} = 10mT/m$, the bandwidth necessary to excite a slice of thickness $\Delta z = 7$

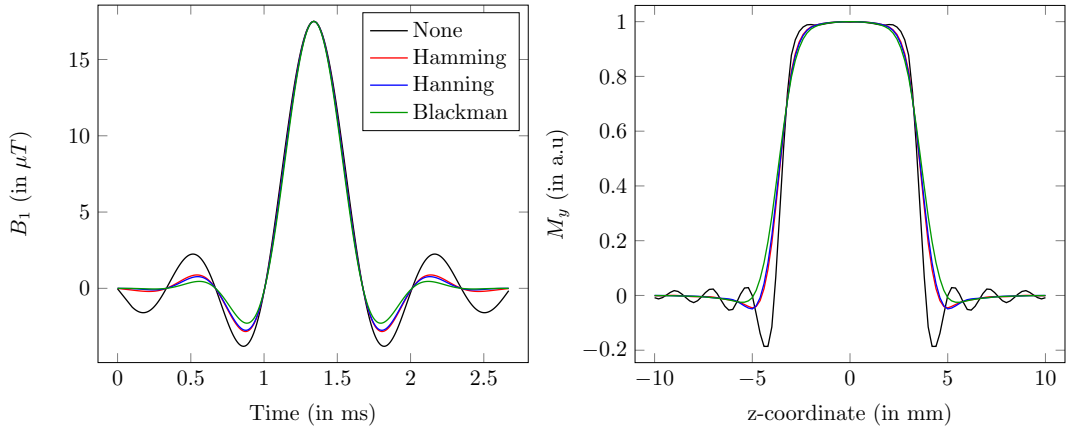

Figure 2.7: **Left** Envelope function of several SINC RF pulse as described in Equation (2.38). **Right** The resulting y-component of the magnetization at the end of the slice selective RF-pulse.

mm is:

$$\Delta f = \frac{1}{2\pi}\gamma G_{ss}\Delta z = 2975 \text{ Hz} \tag{2.39}$$

where $\Delta f = \frac{\Delta\omega_p}{2\pi}$. Moreover, if one considers that the full width at half maximum (FWHM) of the SINC pulse in the frequency domain provides a good approximation of the bandwidth ($\Delta f \simeq \frac{1}{t_1}$), then the duration of the RF pulse can be approximated by: $\tau_{rf} = 2Nt_1 \simeq \frac{4\pi N}{\gamma G_{ss}\Delta z} = 2.68$ ms. Note that looking at FWHM of the magnetization is as expected around $\Delta z = 7mm$ in Figure 2.7.

As the slice selection gradient induces a variation of the frequency of the excited spins through the slice, the phase shift accumulated by the spins should differ by the end of the gradient application. Therefore, a negative gradient with the same magnitude and of duration $\tau_{ss}/2$ is applied to rephase all the spins within the excited slice, as shown in Figure 2.8. After the application of this negative lobe, the excited spins on the slice are refocused and are therefore all with a zero phase. The refocusing gradient is applied for a duration of $\tau_{ss}/2$ since it is assumed that the spins are tipped instantaneously at the centre of the RF pulse. Therefore, the phase is being accumulated from this moment on, when half of the positive lobe slice selection gradient ($\tau_{ss}/2$) remains to apply.

2.5.4 Spatial encoding

After the slice selection (always applied along the z-axis, by convention), to locate each spin within the excited slice, x and y directions are spatially encoded. As for the slice selection, a frequency-encoding gradient (or readout gradient) G_x is applied during τ_x along the x-axis to encode the frequency of the spins. A phase-encoding gradient G_y is also applied for a duration τ_y to spatially encode the phase

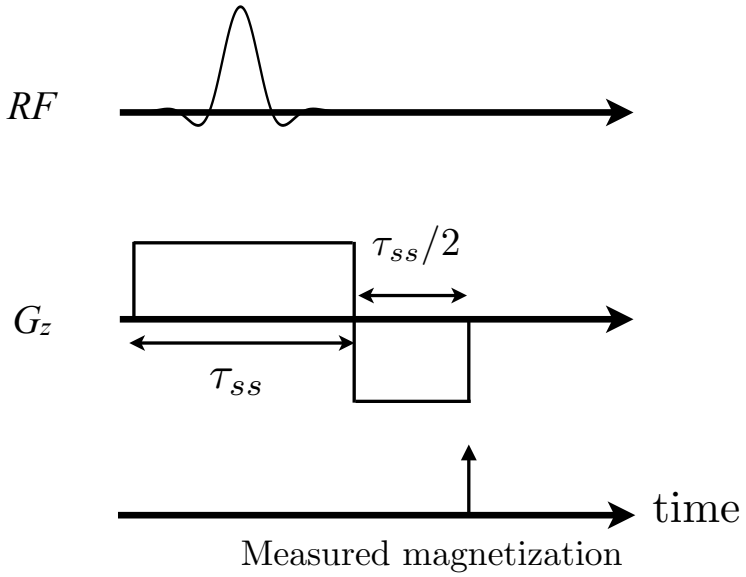

Figure 2.8: 90° flip-angle slice-selective sequence. A negative gradient is applied after the RF-pulse is turned off for refocusing of the transverse magnetization (i.e: to remove the phase shift accumulated over the slice width due to the modification of the frequency by the positive gradient).

of the transverse magnetization along the y-axis. Note that a straightforward approach would be to apply another frequency encoding gradient along the y-axis instead of encoding the phase. Nevertheless, using two frequency encoding gradients would necessarily lead to redundant frequencies between isochromats within a slice. The resulting frequency of an isochromat at location $\mathbf{r}$ can be decomposed as:

$$\omega(\mathbf{r}, t) = \omega_0 + \gamma(G_x(t)x + G_y(t)y) \tag{2.40}$$

where $\Delta B(\mathbf{r}, t) = G_x(t)x + G_y(t)y$. Introducing this expression into the signal measured by the receiver coil as given in Equation (2.34) leads to:

$$S(t) = \omega_0 \int_\Omega C^*_{xy}(\mathbf{r}) \cdot M_{xy}(\mathbf{r}, 0) e^{-t/T_2} e^{-i2\pi(k_x \cdot x + k_y \cdot y)} d\Omega \tag{2.41}$$

where the k-space trajectory is defined as:

$$k_x = \frac{\gamma}{2\pi} \int_0^t G_x(\tau) d\tau \tag{2.42}$$

$$k_y = \frac{\gamma}{2\pi} \int_0^t G_y(\tau) d\tau \tag{2.43}$$

Defining the k-space operators as a spatial frequency (or wave number), Eq. (2.42) shows that the total k-space covered during a time interval is the area under the gradient waveform $\mathbf{G}(t)$. Eq. (2.41) shows that the signal acquired is the

2D Fourier transform of the transverse magnetization weighted by the sensitivity profile of the receiver coil. Recalling that the transverse magnetization can be expressed as a function of the spin density ρ_0 per unit volume (see Eq. (2.7)), it is then possible to rewrite the previous Equation (2.41) as follows:

$$S(k) = \int_{\Omega_k} \rho(\mathbf{r}, T_2) e^{-i2\pi(k_x \cdot x + k_y \cdot y)} dk \tag{2.44}$$

where $\rho(\mathbf{r}, T_2) = \omega_0 \Lambda C_{xy}^* M_{xy}(\mathbf{r}, 0) e^{-t/T_2}$ is an effective spin density, and Λ a constant accounting for the gain factors of the electronic detection system. Note that if the time when the signal acquisition is performed (called echo time TE) is small as compared to T_2, the exponential relaxation term is close to the unit and the dependence of the spin density to T_2 can be removed (i.e: $\rho(\mathbf{r}, T_2)$ becomes $\rho(\mathbf{r})$). Similarly, here the longitudinal relaxation effects were neglected in the signal expression but in the general case, we should write $\rho(\mathbf{r}, T_1, T_2)$.

Finally, taking the inverse Fourier transform of the signal leads to the repartition:

$$\rho(\mathbf{r}) = \int_{\Omega} S(k) e^{+i2\pi(k_x \cdot x + k_y \cdot y)} d\Omega \tag{2.45}$$

Therefore, the spin density is the inverse Fourier transform of the signal acquired over a sample. This relationship represents the key concept exploited in MRI. Sequentially sampling the k-space over a discrete range of frequencies in both phase and frequency encoding directions, and taking the inverse Fourier transform of the resulting discrete signals are the necessary steps to form a 2D image.

2.5.5 k-space coverage

Different k-space trajectories can be adopted to fill the k-space, depending on the amount of signal and pixel width required. The path adopted greatly influences the resulting imaging artefacts. A common and straightforward strategy consists in covering the k-space following a Cartesian trajectory (see Fig. 2.9). First, a phase-encoding gradient is applied to encode the phase of each spin along y direction. Each line is separated by $\Delta k_y = \gamma G_y \Delta t_y$. Between each line increment, n_x columns are filled with sampling interval $\Delta k_x = \gamma G_x \Delta t_x$, where Δt_x and Δt_y are the dwell times of sampling interval along the frequency and phase encoding directions, respectively. Due to the use of a discrete Fourier transform, a sampling constraint to avoid aliasing is to satisfy the Nyquist theorem stating that if a signal sampled with intervals Δx has a spectrum bandwidth in the frequency domain $2k_{x,max}$ greater than $1/\Delta x$, then aliasing would occur. In this sense, the k-space sampling interval Δk_x should be limited to:

$$\begin{aligned} 2k_{x,max} &\leq \frac{1}{\Delta x} \\ \Delta k_x = \frac{2k_{x,max}}{n_x} &\leq \frac{1}{FOV_x} \end{aligned} \tag{2.46}$$

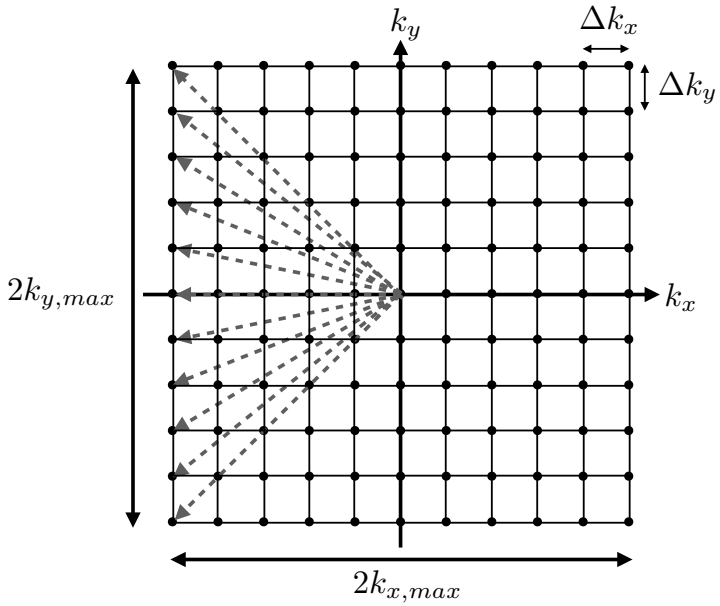

Figure 2.9: Example of a Cartesian k-space trajectory. The k-space is covered from left to right and from top to bottom.

where $FOV = (FOV_x, FOV_y, FOV_z)$ corresponds to the field of view or the image size, and where n_x, n_y is the number of points in the k-space according to readout and phase encoding direction respectively. Note that the previous relation also applies for the y-axis. Other strategies such as radial, spiral or zig-zag k-space trajectories might also be adopted [12].

Note that a large amount of k_x and k_y values are usually required to reconstruct the entire image with a sufficient level of details, and it is common to see k-space matrix size of more than 512×512. However, a larger matrix size would necessarily induce a smaller number of spins per isochromat and would therefore results in a lower Signal to Noise ratio (SNR). Low SNR images produce grainy images. A way to counteract this effect can be to increase the slice thickness, increasing the number of spins and therefore the quantity of signal coming from each isochromat. In general, the user should decide whether to prioritize a fine spatial resolution (but with poor SNR), or a high SNR with low resolution. More details will be given about the SNR in Section 2.8.5.

2.6 Imaging sequence

To fill the k-space progressively, a MR imaging sequence consists in the sequential repetition of many pulse sequences, each pulse sequence usually filling one line of the k-space. A particular type of sequence might be preferred depending on the type of tissues/organs or functionality to image. For instance, spin echo

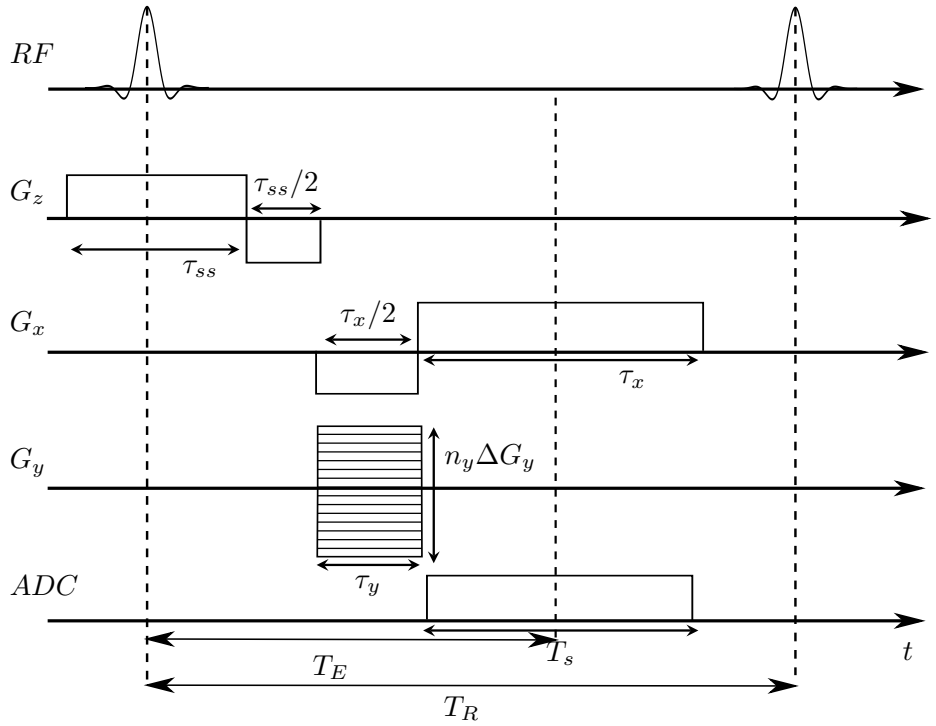

Figure 2.10: Example of a typical GRE pulse sequence. In Cartesian filling strategy, a full k-space line is filled during the time interval T_s by the ADC (Analog to Digital Converter), where data are collected by the receiver coil. The amplitude of the phase encoding gradient G_y is modified for each consecutive pulse sequence to fill a new k-space line. Note that a prephasing gradient is applied along the readout (x) direction to accelerate the FID decay signal. Dephased spins are then rephased by applying a gradient of opposite polarity, while signal is detected.

sequences are characterized by the presence of a 180° refocussing RF pulse, and will be preferred to measure the T_2 with accuracy. On the contrary, gradient echo sequences (GRE) are usually characterized by a lower flip angle and a unique RF pulse per pulse sequence, such that it results in a fast MR acquisition. A typical GRE pulse sequence is presented in Figure 2.10. Note that several groups of pulse sequences can be distinguished (spin echo, gradient echo, inversion recovery, ...) depending on the properties of the tissues to image. So far, a large variety of imaging protocols have already been developed in order to mitigate the imaging artefacts while reducing the time duration of a scan. A detailed overview of the existing sequences and their main features is provided in Bernstein et al. [12].

2.7 3D imaging

Similarly as for 2D imaging, the signal coming from the spins in the third dimension could be encoded. This could be achieved either with 2D multi-slice or 3D sequences. In 2D multi-slice imaging, a series of consecutive slices are sequentially excited by varying the RF pulse to increment the position of the excited slice, while keeping constant slice-selection gradients. On the contrary, in 3D imaging, the RF excitation bandwidth is adjusted to cover the entire thickness of the volume (called a slab), and phase-encoding gradients are adjusted to encode the signal according to this direction.

2.8 Phase-contrast MRI

So far, static spins were implicitly considered. Assessing the blood flows is of interest for the reasons detailed in the previous chapter. However, the classical imaging techniques are not suited to measure the displacement of the moving spins contained in the blood flows.To this end, two distinct MR techniques exist: the MR Angiography (MRA) and the Phase-Contrast MRI (PC-MRI). MRA is usually dedicated for the measurement of the blood vessel lumen while PC-MRI is used to quantify the blood velocity inside the vessels. PC-MRI is based on the principle that in the presence of moving spins, the phase of the spatially encoded signal could be expressed as a function of the velocity of these spins. The phase accumulated between the end of the RF excitation ($t = 0$, by convention) and echo time (TE) where the signal is collected is expressed as:

$$\phi(\mathbf{r}, TE) - \phi(\mathbf{r}, 0) = -\int_0^{TE} \omega(\mathbf{r}, t')dt' = -\gamma \int_0^{TE} \mathbf{r}(t) \cdot \mathbf{G}(t')dt' \tag{2.47}$$

Note that since the signal is demodulated with respect to the Larmor frequency induced by the static magnetic field, the contribution of γB_0 cancels out. Note also that local field phase that arise due to magnetic fields inhomogeneities are for now neglected and will be discussed later. A second-order Taylor expansion of the spin location $\mathbf{r}(t)$ at the vicinity of t_0 gives:

$$\mathbf{r}(t) = \mathbf{r}(t_0) + (t - t_0) \left.\frac{\partial \mathbf{r}}{\partial t}\right|_{t_0} + \mathcal{O}((t - t_0)^2) \tag{2.48}$$

Introducing this decomposition of $\mathbf{r}$ in the expression of the phase accumulated at echo time TE gives:

$$\phi(\mathbf{r}, TE) = \phi_0 - \gamma \mathbf{r}_0 \cdot \underbrace{\int_0^{TE} \mathbf{G}(t')dt'}_{M_0} - \gamma \mathbf{u}_0 \cdot \underbrace{\int_0^{TE} t' \mathbf{G}(t')dt'}_{M_1} \tag{2.49}$$

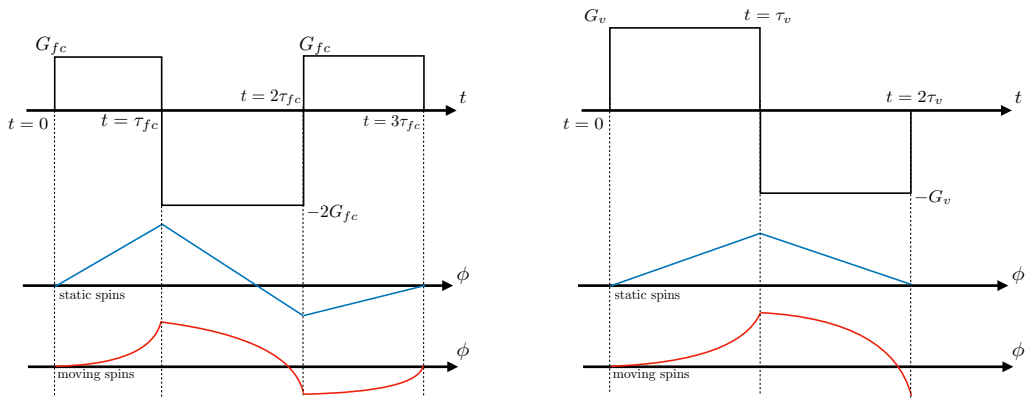

Figure 2.11: Illustration of the effects of applying either flow compensating (left) or bipolar encoding velocity gradients (right) on the phase of the magnetization vector. The static spins (blue) result in a zero accumulated phase at the end of the application, while the moving spins (red) result in a non-zero phase, such that $M_1(2\tau_v) = -\gamma \int_0^{2\tau_v} tG(t)dt = \gamma\tau_v^2 G_v$ for bipolar gradients while $M_1(3\tau_{fc}) = 0$ for flow compensating gradients applied.

where $\mathbf{u}_0 = \frac{\partial \mathbf{r}}{\partial t}\Big|_{t=0}$ and $\phi_0 = \phi(\mathbf{r}, 0) = \phi(\mathbf{r}, \tau_{\text{rf}})$ is an additional background phase. To simplify the notation, M_0, M_1 are introduced as the zero and first order moments of $\mathbf{G}(t)$. Note that $\mathbf{r}(t)$ is here approximated at the second order, i.e with a constant velocity, but a more complete description could be obtained using a third-order Taylor expansion, considering the acceleration of the spin. Bipolar velocity encoding gradients are used to encode the velocity according to the three spatial directions. A bipolar gradient is a succession of a negative and positive lobes of the same amplitude. They are particularly useful in phase-contrast MRI since a bipolar gradient results in a zero phase for static spins ($M_0 = 0$) while $M_1 \neq 0$ for the moving spins, as illustrated in Fig. 2.11. Nevertheless, background phase effects remains after bipolar gradients application. To remove the contribution of ϕ_0, two consecutive measurements of first moments M_1^1 and M_1^2 are necessary, with bipolar gradients of opposite polarities. Considering the x-component of the velocity, the difference of the resulting phases $\Delta\phi$ leads to:

$$\Delta\phi(\mathbf{r}, TE) = \phi^2(\mathbf{r}, TE) - \phi^1(\mathbf{r}, TE) = \gamma u M_{1,x}^2 - \gamma u M_{1,x}^1 \tag{2.50}$$

and finally, the expression the velocity can be obtained as:

$$u = \frac{\Delta\phi(\mathbf{r}, TE)}{\gamma \Delta M_{1,x}} \tag{2.51}$$

Note that three velocity encoding gradients along (x,y,z) are required to encode all spatial directions. Therefore, at least 4 measurements are required (1 reference and 3 direction encodings pulse sequences), given that the same flow compensating

gradient (resulting in both $M_0 = 0$ and $M_1 = 0$) is used as a common reference measurement. Several variant of velocity encoding strategies exist, as described by Pelc et al. (1991) [124]. An important feature to consider in PC-MRI is that the phase only varies between $\phi \in [-\pi, \pi]$. Therefore, an encoding velocity must be set by the user in such a way that it is representative of the maximum velocity of the flow in this encoding direction. The maximum velocity chosen $(u_{enc}, v_{enc}, w_{enc})$ is then defined as the velocity producing a phase shift of π, and could be expressed along the x-axis as:

$$u_{enc} = \frac{\pi}{\gamma \Delta M_{1,x}} \tag{2.52}$$

If at some points the velocity of the flow is higher than the encoding velocity, aliasing (or phase wrapping) will occur. Multiple methods to correct the phase wrapping exist [139], but are not covered in this thesis. From the previous expression, one can rewrite the 3 velocity components as:

$$\begin{aligned} u &= \frac{u_{enc}}{\pi} \Delta\phi_x \\ v &= \frac{v_{enc}}{\pi} \Delta\phi_y \\ w &= \frac{w_{enc}}{\pi} \Delta\phi_z \end{aligned} \tag{2.53}$$

2.8.1 PC-MRI sequences

The first 3D cine PC-MRI sequence with 3 directional velocity encodings was developed in Markl et al., (2003) [100] and referred to as 4D Flow MRI. A PC-MRI sequence is based on gradient echo sequence already presented in Figure 2.10, where flow compensating and velocity encoding gradients are added. Nowadays, one of the main drawback of the PC-MRI sequences is the time of acquisition T_{acq} needed to acquire the full 3D velocity field, that reads:

$$T_{acq} = 4 N_y N_z T_R \tag{2.54}$$

where N_x, N_y, N_z is the k-space matrix size, T_R is the repetition time (i.e: the time between to consecutive pulse sequences). On top of that, as cardiovascular flow are pulsatile flow, the cardiac cycle should be split into N_p time-frames (or phases) of duration Δt. As the time duration of one cardiac cycle $T_c = N_p \Delta t$ is not sufficient to acquire all the data, the k-space is filled progressively during several cycles, each phase data being acquired in a synchronised way from one cycle to another. This synchronization is usually performed using the electrocardiogram (ECG) signal and is called ECG-gating. Therefore, in pulsatile flows with ECG-gating, the acquisition time is extended to:

$$T_{acq} = \frac{N_y N_z N_p}{N_{seg}} \Delta t \tag{2.55}$$

where N_{seg} is the number of k-space lines that can be filled during each time frame of duration Δt. In other words, it can be defined as: $N_{seg} = \left\lfloor \frac{\Delta t}{4T_R} \right\rfloor$, where the $4T_R$ corresponds to the time needed to acquiring 1 reference measurement (ϕ_0) and 3 velocity encoded measurements (ϕ_x, ϕ_y, ϕ_z).

Typically, to measure the 3D velocity field in the aorta (pulsatile flow), a repetition time $T_R = 5 - 10ms$, and a number of subsets filled in one time frame of $N_{seg} = 2$ would result in a temporal resolution of $\Delta t = 40 - 80ms$. Moreover, a spatial resolution of $2 \times 2 \times 2\ mm^3$, approximately corresponding to a matrix size $N_x = 240$, $N_y = 240$, $N_z = 20$, would result in an acquisition time of about $30 - 40\ min$.

2.8.2 Spoiling of the residual magnetization

While the assumption that the transverse magnetization is completely refocussed at the end of a pulse sequence (i.e $TR > T_2$) is valid for certain types of sequences with long TR, it is generally false for PC-MRI sequences due to very small repetition times (few milliseconds). A non-negligible residual transverse magnetization should remain between two consecutive pulse sequences, therefore transmitting a non equilibrium magnetization vector as initial condition of the next pulse sequence. For this reason, RF- or gradient- spoilers are usually added to PC-MRI sequences. Spoiling is a method used to destroy the transverse magnetization that may persist from one pulse sequence to another. It is realized either through application of a gradient or a varying phase RF impulsion. Usually the RF-spoiling is preferred since it does not generate gradients-induced artefacts and is constant in space. RF-spoiling consists in applying a varying phase offset to each successive RF pulse. For more details about the design of a RF-spoiler, the reader can refer to Bernstein et al. [12].

2.8.3 Pre-saturation of the longitudinal magnetization

Given a spin system at initial equilibrium state such that $\mathbf{M}(t = 0) = (0, 0, M_0)^T$, if we apply a RF pulse with flip angle α and duration τ_{rf} to this system, the longitudinal and transverse components of the magnetization vector would take the following form:

$$\begin{aligned} M_z(0^+) &= M_0 \cos(\alpha) \\ M_{xy}(0^+) &= M_0 \sin(\alpha) \end{aligned} \tag{2.56}$$

where the notation $^+$ refers to the end and $^-$ to the beginning of the RF pulse. Then, if one applies another RF pulse after a time T_R that is not sufficient to fully relax the longitudinal magnetization ($M_z(T_R^-) \neq M_0$) whereas the transverse magnetization is spoiled (i.e $M_{xy}(T_R^-) = 0$), then $M_z(T_R^+)$ is modified by the

second RF and therefore different from $M_z(0^+)$. After a sufficient number of RF pulses n applied consecutively interleaved by T_R, the longitudinal magnetization should reach a steady-state value (M_z^{ss}) such as:

$$M_z(nT_R^-) = M_z^{ss} \tag{2.57}$$

Therefore, spoiled GRE sequences usually start with a repetition of RF pulses so that the longitudinal magnetization can reach this steady state. Note that the number of repetitions needed to reach a steady state value is proportional to the flip angle and T_R. One can derive from Eq.(2.20) the analytical expression of M_z after n repetitions as:

$$M_z(nT_R^-) = M_0(1 - e^{-T_R/T_1}) + M_z((n-1)T_R^-)\cos(\alpha)e^{-T_R/T_1} \tag{2.58}$$

Now considering that a steady state value is reached after m repetitions means that $M_z(mT_R^-) = M_z((m-1)T_R^-) = M_z^{ss}$, and therefore the expression of M_z^{ss} reads:

$$M_z^{ss} = \frac{M_0(1 - e^{-T_R/T_1})}{(1 - \cos(\alpha))e^{-T_R/T_1}} \tag{2.59}$$

The longitudinal magnetization at $t = nT_R^-$ can also be expressed from the first repetition, and reads:

$$M_z(nT_R^-) = M_0(1 - E_1)\sum_{i=0}^{n-1}(\cos(\alpha)E_1)^i + M_0(\cos(\alpha)E_1)^n \tag{2.60}$$

where $E_1 = e^{-T_R/T_1}$. Using that,

$$\sum_{k=0}^{n} a^k = \frac{1 - a^{n+1}}{1 - a} \tag{2.61}$$

the previous expression simplifies to:

$$M_z(nT_R^-) = \frac{M_0(1 - E_1)}{1 - \cos(\alpha)E_1}(1 - (\cos(\alpha)E_1)^n) + M_0(\cos(\alpha)E_1)^n \tag{2.62}$$

Introducing the expression of M_z^{ss} gives rise to the following expression:

$$M_z(nT_R^-) = (M_0 - M_z^{ss})(\cos(\alpha)e^{-T_R/T_1})^n + M_z^{ss} \tag{2.63}$$

The evolution of M_z under consecutive RF pulses for different T_R and α is shown in Figure 2.12. For the cases considered, increasing the flip angle leads to a reduce number of repetitions needed. However, to minimize the acquisition time, the best compromise seems to be the case where $T_R = 20\ ms$ and $\alpha = 30°$.

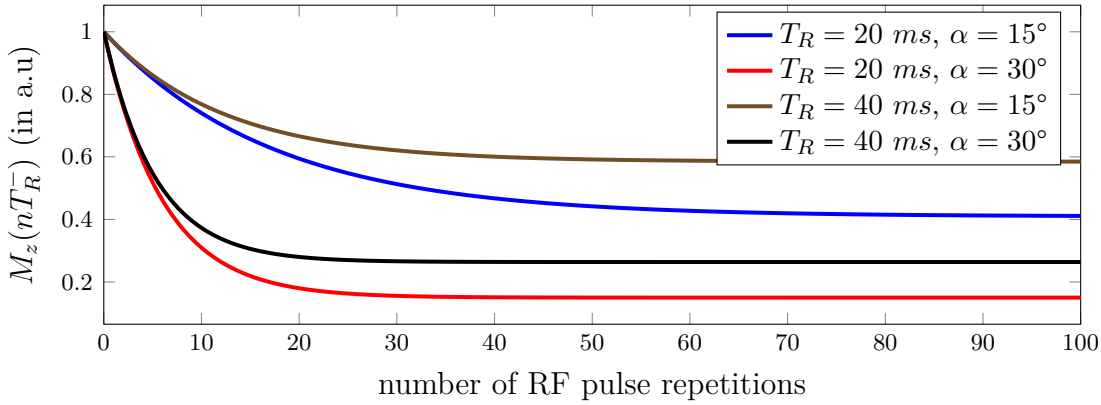

Figure 2.12: Evolution of the longitudinal magnetization at T_R^- for n consecutive RF pulses with $M_0 = 1$ and $T_1 = 0.85$ (blood).

2.8.4 Small tip-angle approximation

If one neglects the relaxation effects, the transverse component of the Bloch equations can be expressed as:

$$\frac{dM_{xy}}{dt} = \gamma M_y B_z - \gamma M_z B_y + i(\gamma M_z B_x - \gamma M_x B_z) \tag{2.64}$$

Considering that the RF pulse only shifts the longitudinal magnetization by a small angle (small tip-angle approximation), meaning that $M_z(t) \approx M_0 = constant$, the following simplification applies:

$$\frac{dM_{xy}}{dt} = \gamma \left(iM_0 \left(B_x + iB_y \right) - iB_z \left(M_x + iM_y \right) \right) \tag{2.65}$$

Therefore, by decomposing B_1 such that $B_1 = B_{1,x} + iB_{1,y}$, and $B_z = \mathbf{G} \cdot \mathbf{r}$, it appears that:

$$\frac{dM_{xy}}{dt} = i\gamma M_0 B_1(t) - i\gamma \mathbf{G}(t) \cdot \mathbf{r} M_{xy}(t) \tag{2.66}$$

Solving this equation leads to the following expression:

$$M_{xy}(t) = i\gamma M_0 e^{-i\gamma \int_0^T \mathbf{G}\cdot\mathbf{r}dt} \int_0^T B_1(t) e^{i\gamma \int_0^T \mathbf{G}\cdot\mathbf{r}dt} dt \tag{2.67}$$

Using the k-space notation $\mathbf{k}(t) = \gamma \int_0^T \mathbf{G}(t)dt$,

$$M_{xy}(t) = i\gamma M_0 e^{-i\mathbf{k}(t)\cdot\mathbf{r}} \int_0^T B_1(t) e^{i\mathbf{k}(t)\cdot\mathbf{r}} dt \tag{2.68}$$

This analytical description of the transverse magnetization during a RF excitation is especially well-suited to PC-MRI sequences, as the flip angle is generally included between 5°and 30°.

2.8.5 Signal and noise

Noise is always present in MRI and can be a non-negligible source of errors. It generally originates from the electromagnetic interaction within the MRI scan room (receiver coils), or can be due to patient body electronic charges. As demonstrated in [65], its relationship with the signal magnitude is given by the Signal-to-Noise Ratio, which is proportional to the voxel size, and the square root the acquisition time as:

$$SNR_{mag} \propto \Delta x \sqrt{T_{acq}} \tag{2.69}$$

As already discussed, decreasing the voxel size increases the noise. Similarly, if one considers a PC-MRI sequence with a squared matrix size, the SNR takes the following form:

$$SNR_{mag} \propto \sqrt{\frac{\Delta x FOV_x T_c}{N_{seg}}}$$

The noise also impacts the phase of the MR signal. Low signal intensities can result in a prominent bias due to the acquisition noise. As expressed in [124] a measure of the velocity SNR (SNR_u) is:

$$SNR_u = \frac{\pi}{\sqrt{2}} \frac{u}{u_{enc}} SNR_{mag} \tag{2.70}$$

Several previous works focused on proposing analytical expressions of the noise. Among them, Edelstein et al. [49] showed that pure noise in magnitude image can be expressed as a Rayleigh distribution. Later, Bernstein et al. [11] proposed a more general Rician distribution of the noise in magnitude data, related to the SNR. Finally, Gudbjartsson expanded the analytical expression of the noise to phase contrast images [63].

2.9 Limitations and PC-MRI artifacts

In the previous section, idealized magnetic fields were considered, with no inhomogeneities or image artifacts. In practice, however, artifacts are almost systematically present in MRI, and induced by many different factors (motions, tissues, hardware, signal-processing, etc.). As the aim of this thesis is not to provide the reader with a complete overview of the existing artifacts, we will focus exclusively on the most common artifacts that appear in flow MRI.

2.9.1 Motion-related artifacts

In-vivo motions

Motions are inevitable in-vivo. These motions generally produce ghosting and blurring on the images. These motions can be random, as patient motion during

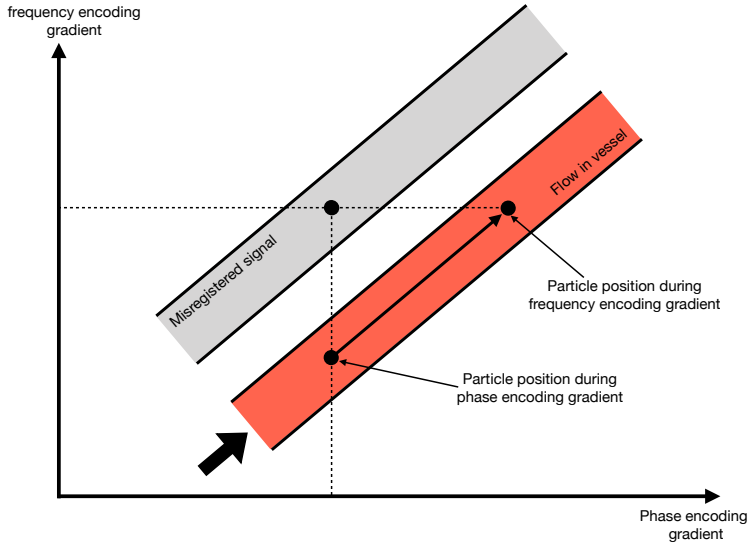

Figure 2.13: Illustration of the flow misregistration artifact. The flow particle is first phase-encoded at a given position while when the frequency encoding occurs, the particle has changed position. For this reason, the particle appears misregistered.

an exam, or cyclic, as the cardiac and respiratory motions. In flow MRI of pulsatile flows, cardiac gating is usually necessary to locate and store the measured data at the correct phase within the cardiac cycle. Moreover, cardiovascular imaging usually require to compensate for the respiratory motions. During free-breathing measurements (as for 4D Flow MRI), it is common to add a navigator gating that record the diaphragm position at the end of each cardiac cycle. If the current diaphragm position lies into a predefined acceptance interval, then the data is accepted; otherwise, the data is rejected [101].

Flow misregistration

Flow-induced artifacts could also be prominent in flow MRI. As illustrated in Figure 2.13, a flow misregistration artifact occurs whenever the moving spins have changed position between the frequency and phase-encoding gradients times. The resulting encoded position of the phase is then shifted by the distance travelled by this parcel during a $\Delta t = t_{phase} - t_{freq}$ where t_{freq} is the time at the frequency encoding gradient. This artifact is most prominent for in-plane flows. See [146] for more detailed discussions about the misregistration artifacts in phase-contrast MRI.

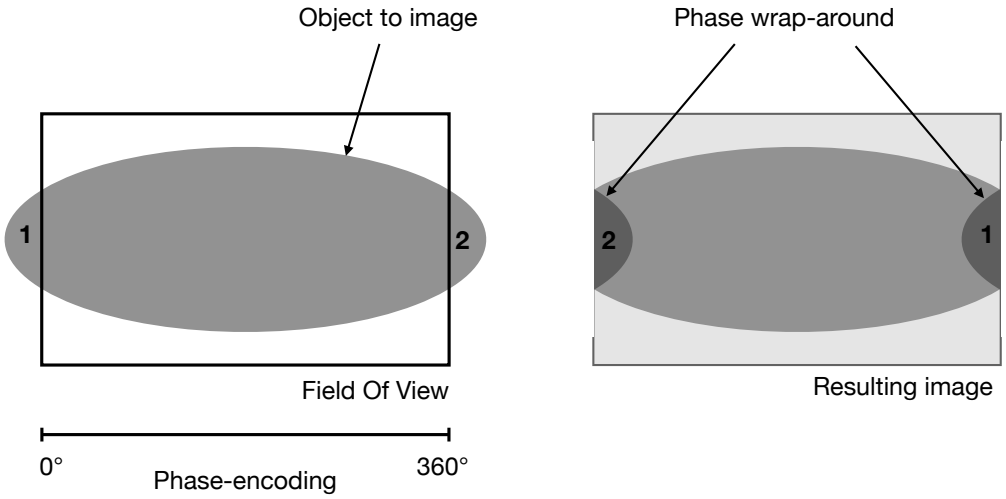

Figure 2.14: Illustration of the phase wrap-around artifact. The object segments that lay out of the FOV are subjected to phase-wrapping (i.e: the part labelled 1. is encoded with phases that range between $[330, 360]$ while the part 2. is encoded with phases that range between $[0, 30]$.

Inflow effects

Successive RF-excitations associated with small TR are responsible for a progressive saturation of the longitudinal magnetization (see Section 2.8.3 of the tissues, reducing at the same time the amplitude of the magnetization vector. However, as the blood flowing in the vessels is continuously replaced by non-saturated blood, it results in higher magnitude of the magnetization vector and therefore in higher amplitude of the signal on the image. This phenomenon constitutes the basis of time-of-flight angiography techniques.

2.9.2 Technique-related artifacts

Phase wrap-around

A wrap-around artifact is a result of an FOV smaller than the size of the object to image. In practice, it manifests as a fold-over of the object at the boundary where the object is larger than the FOV (see Figure 2.14). It results from a violation of the Nyquist theorem, which states that the sampling rate must be twice the maximal frequency that occurs in the image. It is generally avoided by phase-oversampling (i.e: assigning a larger matrix size to a phase cycle).

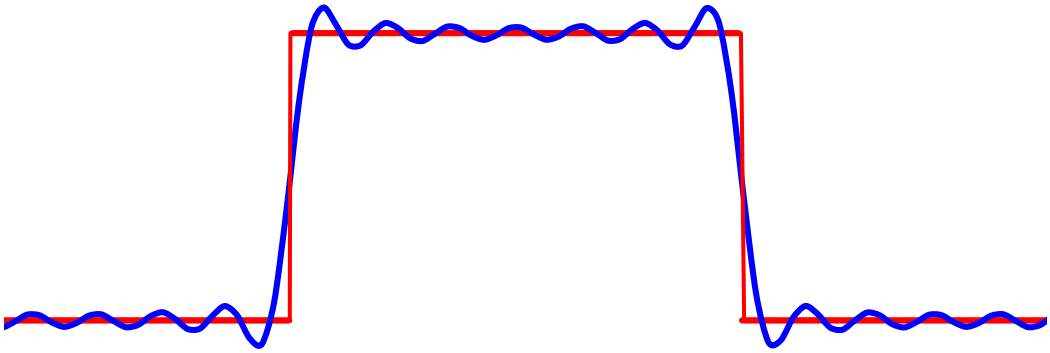

Figure 2.15: Illustration of the Gibbs artifact. The red square wave is described as a Fourier series with the first 7 harmonics only.

Gibbs artifact

The Gibbs artifact or truncation artifact occurs as a consequence of the Fourier transform. In theory, an MR signal is represented by an infinite number of harmonics, while in practice a finite number of harmonics depending on the sampling is used. Therefore, the signal is trucated. A concrete example of the Gibbs artifact is illustrated in Figure 2.15 where the finite-number of Fourier harmonics used to describe the square waveform generates oscillations (ringing).

2.9.3 Tissues-related artifacts

Partial volume effects

Partial volume effects appear when a voxel lies at the interface of two tissues with different resonance properties. For example, a voxel at the interface blood-wall would raise a signal averaged from the contributions of blood spins and artery walls spins.

Chemical shift

Some variations of the resonance frequencies may occur depending on the chemical environment around the protons (i.e: the molecules it belongs to). A local induced magnetic field opposed to the external magnetic field is created due to the shielding effect produced by the proton's molecular environment. The chemical shift corresponds to this small variation of resonance frequency induced by the shielding effect.

Magnetic susceptibility

The magnetic susceptibility is intrinsic to each material properties and corresponds to its ability to either disperse the surrounding magnetic field (diamagnetic) or to concentrate it (paramagnetic, ferromagnetic). Magnetic field distortions then appear due to the magnetic field susceptibility differences at the interface between two tissues. This artifact is present essentially around metal implants and air-tissue interfaces. Shorter TE and increased gradient strength allow to alleviate this artifact.

2.9.4 Hardware-related artifacts

Eddy-currents artifacts

Due to the rapid switches on and off of the gradient fields, time-varying magnetic fluxes induce deviations of the gradient waveform profile, and therefore perturbs the spatial encoding. Active shielding of the gradient coils can be a way to reduce the eddy-currents effects [22]. Otherwise, their effects can be partially removed by post-processing the images. This will be discussed in a later Section 4.4.2.

Static field inhomogeneities

Imperfections in the homogeneity of the static field are natural, and can be additionally caused by the object to image. Shimming (passive or active) of the machinery consists in adding supplementary coils or ferromagnetic elements that help recovering the magnetic field homogeneities. The inhomogeneities caused by the object to image can be corrected by post-processing the images [135].

Gradient field non linearities

One of the artifact that produces the most significant distortions is due to the spatial non-linearities of the gradient fields along the three axes. While usually linear gradients field are assumed along the three axes $\omega(\mathbf{r}) = \omega_0 + \gamma \mathbf{G} \cdot \mathbf{r}$, one can show that in practice this linearity is not compatible with Maxwell's equations [22]. These effects can be corrected either by using predefined displacement tables, or measuring the distortions for a reference object.

Chapter 3

Numerical framework

Chapter contents

This chapter develops the numerical methods implemented in the YALES2BIO[1] solver [106]. The YALES2BIO solver is an in-house numerical software designed to perform numerical simulations of blood flows in complex geometries. The YALES2BIO solver uses the finite-volume method, high-order non-dissipative numerical schemes and massively parallel capabilities inherited from the YALES2 solver to solve the full Navier-Stokes equations (NSE) on unstructured meshes [117]. Developed and maintained at CORIA[2], the YALES2 solver is principally designed for the research in turbulent flows. In this chapter, the numerical methods to simulate the fluid dynamics are expanded, and four numerical test cases are presented. The developments related to the numerical simulation of 4D Flow MRI acquisition process are detailed in Chapter 6.

[1] https://imag.umontpellier.fr/~yales2bio/
[2] https://www.coria-cfd.fr/index.php/YALES2/

3.1 The YALES2BIO solver

Blood is an incompressible fluid characterized by complex rheological properties an Non-Newtonian behaviour. However, at the macroscopic scale, blood flows experiencing high shear rates in large vessels are often modelled as a Newtonian fluid [123]. To this respect, the motion of a Newtonian incompressible fluid on which is exerted a volume force of density f can be described by the well-known Navier-Stokes equations (NSE), that reads:

$$\begin{cases} \dfrac{\partial \mathbf{u}}{\partial t} + \nabla \cdot (\mathbf{uu}) = -\dfrac{1}{\rho}\nabla p + \nu \nabla^2 \mathbf{u} + \dfrac{1}{\rho}\mathbf{f} \\ \nabla . \mathbf{u} = 0 \end{cases} \tag{3.1}$$

The first equation expresses the conservation of momentum of the system, while the second imposes the mass conservation. Although no generally valid analytical solution was found yet, several numerical methods have been developed that allows to approximate the solution. To numerically solve the NSE, the fluid domain of interest is partitioned with polyhedral mesh elements (generally hexahedral or tetrahedral in 3D). Among the large variety of methods that allow to discretize and solve the NSE on a numerical mesh, the finite-volume method was implemented in the YALES2BIO solver. It is beyond the scope of this thesis to develop the other methods.

3.1.1 The finite volume method

In the finite volume method, the discretization procedure is based on the integral of the conservation equations over polyhedral control volumes (CV). A CV could either be centred on the node or the element of the mesh. In YALES2BIO, node-centred CV are utilized, as illustrated in Figure 3.1. Finite volumes approach is often adopted in the field of computational fluid dynamics since the integral formulation of the discretized surface forces naturally conserves the momentum.

Integrating the momentum equation (Eq. 3.1) over a control volume Ω leads to:

$$\int_{\Omega_i} \frac{\partial \mathbf{u}}{\partial t} dV = \int_{\Omega_i} \nabla \cdot \left(-\mathbf{uu} - \frac{1}{\rho} p \mathbb{I} + \nu \nabla \mathbf{u} \right) dV + \int_{\Omega_i} \frac{1}{\rho} \mathbf{f} dV \tag{3.2}$$

Using the Gauss theorem $\int_{\Omega_i} \nabla \cdot \phi dV = \oint_{\partial \Omega_i} \phi \cdot d\mathbf{S}$ to transform the volume integrals to surface integrals :

$$\begin{aligned} \int_{\Omega_i} \frac{\partial \mathbf{u}}{\partial t} dV &= \oint_{\partial \Omega_i} \left(-\mathbf{uu} - \frac{1}{\rho} p \mathbb{I} + \nu \nabla \mathbf{u} \right) \cdot d\mathbf{S} + \int_{\Omega} \frac{1}{\rho} \mathbf{f} dV \\ &= \sum_{j=1}^{Nf_i} \int_{S_{ij}} \left(-\mathbf{uu} - \frac{1}{\rho} p \mathbb{I} + \nu \nabla \mathbf{u} \right) \cdot d\mathbf{S} + \int_{\Omega_i} \frac{1}{\rho} \mathbf{f} dV \end{aligned} \tag{3.3}$$

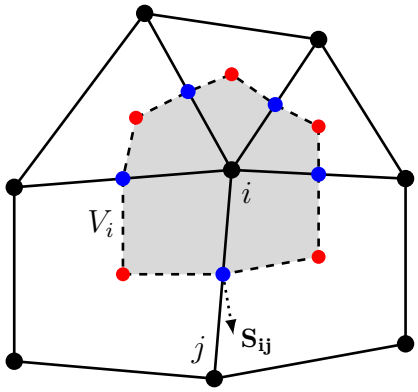

Figure 3.1: Control volume V_i created around the node i of an unstructured hybrid mesh constructed by linking the centroids of the neighboring elements (red dots) and the centres of the edges adjacent to the node i (blue dots).

where each control volume is bounded by Nf_i pair face normals $\mathbf{S}_{ij} = \mathbf{n}_{ij} S_{ij}$ where S_{ij} is the pair face, as illustrated in 2D in Fig. 3.1.

3.1.2 Spatial discretization

From Eq. 3.3, the body force and unsteady terms need to be integrated over the control volume. The average of a variable ϕ over a control volume is defined as:

$$\overline{\phi}_{\Omega_i} = \frac{1}{V_i} \int_{\Omega_i} \phi dV \tag{3.4}$$

A Taylor expansion in the vicinity of the CV node i leads to:

$$\phi = \phi_i + \left.\frac{\partial \phi}{\partial x_k}\right|_i \left(x^k - x_i^k\right) + \frac{1}{2}(x^k - x_i^k)(x^l - x_i^l) \left.\frac{\partial^2 \phi}{\partial x^k \partial x^l}\right|_i + \mathcal{O}\left(||x^k - x_i^k||^3\right) \tag{3.5}$$

If the CV centre of mass $\overline{\mathbf{x}}_{\Omega_i} = \frac{1}{V_i} \int_{\Omega_i} \mathbf{x} dV$ is located at the node position i, then

$$\overline{\phi}_{\Omega_i} = \frac{1}{V_i} \int_{\Omega_i} \phi dV \approx \phi_i \tag{3.6}$$

is second-order accurate on regular grids. Nevertheless, as the CV barycentre and the node do not necessarily have the same position, Eq. 3.6 generally reduces to first-order accuracy.

Similarly, the surface integral in Eq. 3.3 must be discretized. The average of the variable ϕ over the pair surface S_{ij} is given by:

$$\overline{\phi}_{S_{ij}} = \frac{1}{S_{ij}} \int_{S_{ij}} \phi d\mathbf{S} \tag{3.7}$$

If this CV pair centre $\mathbf{x}_{ij}$ is located at the barycentre of surface S_{ij}, the approximation

$$\int_{S_{ij}} \phi d\mathbf{S} \approx \phi_{ij} \mathbf{S}_{ij}$$

becomes second-order accurate. Adding that,

$$\phi_{ij} \approx \frac{\phi_i + \phi_j}{2}$$

This approximation is always second-order accurate since, by definition, each pair centre ij is located at the midpoint between i and j.

Discretization of the derivative operators

The gradient, divergence and Laplacian operator can be discretized from the previous discretization of the CV surface integrals. The second-order discretization stencil for the gradient reads:

$$\mathcal{G}(\phi)|_i = \frac{1}{V_i} \sum_{j=1}^{Nf_i} \frac{\phi_i + \phi_j}{2} \mathbf{S}_{ij} \tag{3.8}$$

From a similar observation, the second-order discretization for the divergence operator can be obtained such as:

$$\mathcal{D}(\mathbf{u})|_i = \frac{1}{V_i} \sum_{j=1}^{Nf_i} \frac{\mathbf{u}_i + \mathbf{u}_j}{2} \cdot \mathbf{S}_{ij} \tag{3.9}$$

The most straightforward way to discretize the Laplacian operator is to apply successively the gradient and divergence operator. Nevertheless, this leads to non-compact stencil, which might involve non-physical solutions of the Poisson equation as it misrepresents some frequencies of the variable due to the even spatial sampling of the discretization: this phenomenon is often called the checkerboard problem. Moreover, this stencil is not straightforward to implement according to the data structure which only allows to reach the first neighbours of a node. An alternative scheme can be derived in order to get a compact stencil, where the Laplacian operator of a scalar variable ϕ is expressed as:

$$\mathcal{L}(\phi)|_i = \sum_{j=1}^{Nf_i} \nabla\phi|_{ij} \cdot \mathbf{S}_{ij} \tag{3.10}$$

By expansion in Taylor series of ϕ_i and ϕ_j, the following approximation arises:

$$\begin{aligned} \phi_i &= \phi_{ij} + \nabla\phi|_{ij} \cdot (\mathbf{x}_i - \mathbf{x}_{ij}) + \mathcal{O}(\Delta x^2) \\ \phi_j &= \phi_{ij} + \nabla\phi|_{ij} \cdot (\mathbf{x}_j - \mathbf{x}_{ij}) + \mathcal{O}(\Delta x^2) \end{aligned} \tag{3.11}$$

Then, it comes that:

$$\nabla\phi|_{ij} = (\phi_j - \phi_i) \frac{(\mathbf{x}_j - \mathbf{x}_i)^T}{\|(\mathbf{x}_j - \mathbf{x}_i)\|^2} \tag{3.12}$$

and finally second-order discretization for the Laplacian operator is obtained:

$$\mathcal{L}(\phi)|_i = \sum_{j=1}^{Nf_i} (\phi_i - \phi_j) \frac{(\mathbf{x}_j - \mathbf{x}_i)^T}{\|(\mathbf{x}_j - \mathbf{x}_i)\|^2} \cdot \mathbf{S}_{ij} \tag{3.13}$$

If the CV face normal $\mathbf{S}_{ij}$ is parallel to the pair edge, one can decompose the dot product in Eq. 3.13 and the Laplacian operator becomes:

$$\mathcal{L}(\phi)|_i = \sum_{j=1}^{Nf_i} \frac{(\phi_i - \phi_j)}{\|(\mathbf{x}_j - \mathbf{x}_i)\|} \|\mathbf{S}_{ij}\| \tag{3.14}$$

However, it is usually not the case in practice for general unstructured grids and each component of the gradient should be assessed. Given the Laplacian operator discretized from the previous expression, it is therefore important to generate meshes with a cell skewness as low as possible to minimize the associated approximation errors.

Note that all these second-order discretization procedures are fully described in the PhD. thesis of S. Vantieghem [159].

High-order discretization

High order schemes are generally preferred for resolving the small scale turbulence of the flow in LES and DNS frameworks as it reduces the numerical diffusion and dispersion. The spatial discretization scheme implemented in the YALES2BIO solver provides a 4th-order accurate approximation of the finite-volume integration on regular grids. It mainly consists of an operation that allows to transfer the variable averaged over the CV $\overline{\phi}_{\Omega_i}$ towards the CV node ϕ_i. This procedure is refereed to as a deconvolution of the finite-volume integration, and detailed explanations can be found in [81]. A Taylor expansion of ϕ at the vicinity of node i inserted into Eq. 3.6 can be seen as an averaging operator applied to the nodal value ϕ_i. An inversion of this operator allows to express ϕ_i as a function of $\overline{\phi}_{\Omega_i}$ [145]. After some simplifications, the resulting deconvolution reads:

$$\phi_i = \overline{\phi}_{\Omega_i} - \overline{\delta x}_i^k \frac{\partial \overline{\phi}_{\Omega_i}}{\partial x^k} - \left(\frac{1}{2} \overline{\overline{\delta^2 x}}_i^{kl} - \overline{\delta x}_i^k \overline{\delta x}_i^l \right) \frac{\partial^2 \overline{\phi}_{\Omega_i}}{\partial x^k \partial x^l} + \mathcal{O}(\delta x^3) \tag{3.15}$$

where

$$\overline{\delta x}_i^k = \frac{1}{V_i} \int_{\Omega_i} \left(x^k - x_i^k \right) dV$$

and

$$\overline{\overline{\delta^2 x}}_i^{kl} = \frac{1}{V_i} \int_{\Omega_i} \left(x^k - x_i^k \right) \left(x^l - x_i^l \right) dV$$

Now if one writes the previous approximation at the CV barycentre $\phi_{\bar{i}} = \phi(\overline{\mathbf{x}}_{\Omega_i})$:

$$\phi_{\bar{i}} = \overline{\phi}_{\Omega_i} - \frac{1}{2} \overline{\overline{\delta^2 x}}_{\bar{i}}^{kl} \frac{\partial^2 \overline{\phi}_{\Omega_i}}{\partial x^k \partial x^l} + \mathcal{O}(\delta x^3) \tag{3.16}$$

since $\overline{\delta x}_{\bar{i}}^{k} = 0$.

The surface integrals in Eq. 3.3 can be discretized from a similar observation. The value of ϕ at barycentre of the surface S_{ij} can be defined as:

$$\overline{\phi}_{S_{ij}} \mathbf{S}_{ij} = \int_{S_{ij}} \phi d\mathbf{S}$$

A Taylor expansion of ϕ in the vicinity of the control volume pair centre ij leads to:

$$\phi = \phi_{ij} + \left.\frac{\partial \phi}{\partial x^k}\right|_{ij} \delta x_{ij}^{k} + \frac{1}{2} \delta x_{ij}^{kl} \left.\frac{\partial \phi}{\partial x^k \partial x^l}\right|_{ij} + \mathcal{O}\left(\delta x^3\right) \tag{3.17}$$

Now, we can decompose the value at the pair centre as:

$$\phi_{ij} = \frac{\phi_{ij/\Omega_i} + \phi_{ij/\Omega_j}}{2}$$

where ϕ_{ij/Ω_i} is the contribution of CV i to the pair centre ij. Another Taylor expansion of ϕ_{ij/Ω_i} in the vicinity of the barycentre $\bar{i}$ leads to:

$$\phi_{ij/\Omega_i} = \phi_{\bar{i}} + \delta x_{\bar{i},ij}^{k} \frac{\partial \phi_{\bar{i}}}{\partial x^k} + \frac{1}{2} \delta^2 x_{\bar{i},ij}^{kl} \frac{\partial^2 \phi_{\bar{i}}}{\partial x^k \partial x^l} + \mathcal{O}(\delta x^3)$$

The barycentric value $\phi_{\bar{i}}$ can be replaced by the expression found in Eq. 3.16, and after some simplifications (see [81] for details), ϕ_{ij} reads:

$$\begin{aligned} \phi_{ij} = & \left(\frac{\overline{\phi}_{\Omega_i} + \overline{\phi}_{\Omega_j}}{2} \right) + \frac{1}{2} \left(\overline{\delta x_i}^{k} + \overline{\delta x_j}^{k} \right) \frac{\partial}{\partial x^k} \left(\frac{\overline{\phi}_{\Omega_i} + \overline{\phi}_{\Omega_j}}{2} \right) + \\ & \frac{1}{2} \left(\frac{\delta x_{\bar{i},ij}^{k} \delta x_{\bar{j},ij}^{l} + \delta x_i^k \delta x_j^l}{2} - \frac{\overline{\delta^2 x_{\bar{i}}}^{kl} + \overline{\delta^2 x_{\bar{j}}}^{kl}}{2} \right) \frac{\partial}{\partial x^k \partial x^l} \left(\frac{\overline{\phi}_{\Omega_i} + \overline{\phi}_{\Omega_j}}{2} \right) + \mathcal{O}(\delta x^3) \end{aligned} \tag{3.18}$$

where $\delta x_{\bar{i},ij}^{k} = x_{\bar{i}}^{k} - x_{ij}^{k}$ and $\delta x_{\bar{i},ij}^{kl} = (\delta x_{\bar{i}}^{k} - \delta x_{ij}^{k})(\delta x_{\bar{i}}^{l} - \delta x_{ij}^{l})$. Finally, introducing this expression in Eq. 3.17 and integrating over the surface S_{ij} leads to an expression of $\overline{\phi}_{S_{ij}}$. This deconvolution procedure raises the approximation to fourth-order for regular grids, and to third-order for isotropic unstructured meshes.

3.1.3 Time advancement

Resolving numerically the incompressible version of the Navier-Stokes equations is usually more challenging than for compressible flows as there is no state equation that pilots the evolution of the pressure. For this reason, the time advancement scheme implemented in YALES2BIO is based on a fractional step method, initially developed in Chorin (1968) [34], and later modified by Kim and Moin, (1985) [78]. This splitting algorithm is based on the Helmholtz-Hodge decomposition which

states that any sufficiently smooth vector field $\mathbf{u}$ defined in a domain Ω could be uniquely decomposed as irrotational ($\nabla\times = 0$) and solenoidal ($\nabla\cdot = 0$) parts, such as:

$$\begin{aligned} \mathbf{u} &= \mathbf{u}^{sol} + \mathbf{u}^{irr} \quad \text{on } \Omega \\ \mathbf{u}^{sol} \cdot \mathbf{n} &= 0 \text{ on } \partial\Omega \end{aligned} \tag{3.19}$$

where $\mathbf{n}$ is the outward normal vector on the $\partial\Omega$ boundary. As the irrotational part verifies $\nabla \times \mathbf{u}^{irr} = 0$, it derives from a potential and can be written as $\mathbf{u}^{irr} = \nabla\phi$. Then, taking the divergence of the previous Eq. 3.19 gives rise to a Poisson equation:

$$\nabla \cdot \mathbf{u} = \nabla^2\phi \tag{3.20}$$

since $\nabla \cdot \mathbf{u}^{sol} = 0$. Then, by solving this equation, the divergence-free velocity field can be recovered:

$$\mathbf{u}^{sol} = \mathbf{u} - \nabla\phi \tag{3.21}$$

This is equivalent to defining an orthogonal projector $\mathbb{P}$ that maps $\mathbf{u}$ into its divergence-free part $\mathbf{u}^{sol}$ such that $\mathbb{P}\mathbf{u} = \mathbf{u}^{sol}$. Of course, this projector verifies:

$$\mathbb{P}\nabla\phi = 0$$

and

$$\mathbb{P}\mathbf{u}^{sol} = \mathbf{u}^{sol}$$

In the Navier-Stokes equations, the pressure plays the role of the operator that projects the velocity field into a divergence-free vector field. In practice, the algorithm developed by Chorin is split in two steps: first an intermediate velocity is predicted from the momentum equations expressed with no pressure contribution. Then, a pressure Poisson equation is raised to correct the intermediate velocity field and ensure the divergence-free of the velocity. An illustration of this algorithm is presented where the explicit Euler scheme is considered for the time integration. Note that the velocity is expressed at time steps $n, n+1$ while the pressure is solved at shifted time steps $n-1/2, n+1/2$. A first prediction of the intermediate velocity $\mathbf{u}^*$ is obtained by integrating the momentum equations with no pressure term:

$$\frac{\mathbf{u}^* - \mathbf{u}^n}{\Delta t} = -\left(\mathbf{u}^n \cdot \nabla\right)\mathbf{u}^n + \nu\nabla^2\mathbf{u}^n + \frac{1}{\rho}\mathbf{f}^n \tag{3.22}$$

the velocity is then corrected by integrating the new pressure gradient:

$$\frac{\mathbf{u}^{n+1} - \mathbf{u}^*}{\Delta t} = -\frac{1}{\rho}\nabla p^{n+1/2} \tag{3.23}$$

Then to determine the pressure $p^{n+1/2}$, we take the divergence of the previous equation which raises the following Poisson equation for the pressure:

$$\frac{1}{\rho}\nabla^2 p^{n+1/2} = \frac{\nabla \cdot \mathbf{u}^*}{\Delta t} \tag{3.24}$$

since $\nabla \cdot \mathbf{u}^{n+1} = 0$. Later, Kim and Moin [78] highlighted that the boundary condition prescribed for the intermediate velocity u^* is inconsistent and could lead to erroneous results. They proposed a modified version of the splitting algorithm. At first, we predict an intermediate velocity $\hat{\mathbf{u}}$ including the pressure gradient at $n - 1/2$:

$$\frac{\hat{\mathbf{u}} - \mathbf{u}^n}{\Delta t} = -\left(\mathbf{u}^n \cdot \nabla\right)\mathbf{u}^n - \frac{1}{\rho}\nabla p^{n-1/2} + \nu\nabla^2\mathbf{u}^n + \frac{1}{\rho}\mathbf{f}^n \tag{3.25}$$

with boundary condition $\hat{\mathbf{u}} = \mathbf{u}^{n+1}$ on $\partial\Omega$. The pressure contribution is then removed:

$$\mathbf{u}^* = \hat{\mathbf{u}} + \Delta t\frac{1}{\rho}\nabla p^{n-1/2} \tag{3.26}$$

and the pressure is updated by taking the divergence of Eq. 3.23:

$$\nabla^2 p^{n+1/2} = \frac{\nabla \cdot \mathbf{u}^*}{\Delta t} \tag{3.27}$$

with classical homogeneous Neumann boundary conditions:

$$\frac{\partial p^{n+1/2}}{\partial \mathbf{n}} = 0 \text{ on } \partial\Omega \tag{3.28}$$

Then finally the velocity is corrected with the new pressure gradient:

$$\mathbf{u}^{n+1} = \mathbf{u}^* - \Delta t\frac{1}{\rho}\nabla p^{n+1/2} \tag{3.29}$$

In this formulation, $\mathbf{u}^*$ at boundaries is second-order accurate (while $\hat{\mathbf{u}}$ is first order accurate). This last version of the algorithm is implemented in YALES2BIO.

3.1.4 Temporal discretization

The temporal discretization of the intermediate velocity $\mathbf{u}$ is then performed using a 4th-order Runge-Kutta scheme in time (RK4). Note that other time schemes are available in YALES2BIO, such as the TFV4A scheme [81], but are not presented here. Rewritting Eq. 3.1.3 as:

$$\frac{\hat{\mathbf{u}} - \mathbf{u}^n}{\Delta t} = \mathbf{rhs}\left(\mathbf{u}^n, p^{n-1/2}\right), \tag{3.30}$$

the velocity $\hat{\mathbf{u}}$ is advanced such as:

$$\begin{cases} \mathbf{u}^{(1)} = \mathbf{u}^n + \dfrac{1}{4}\Delta t\mathbf{rhs}\left(\mathbf{u}^n, p^{n-1/2}\right), \\ \mathbf{u}^{(2)} = \mathbf{u}^n + \dfrac{1}{3}\Delta t\mathbf{rhs}\left(\mathbf{u}^{(1)}, p^{n-1/2}\right), \\ \mathbf{u}^{(3)} = \mathbf{u}^n + \dfrac{1}{2}\Delta t\mathbf{rhs}\left(\mathbf{u}^{(2)}, p^{n-1/2}\right), \\ \mathbf{u}^* = \mathbf{u}^n + \Delta t\mathbf{rhs}\left(\mathbf{u}^{(3)}, p^{n-1/2}\right). \end{cases} \tag{3.31}$$

Note that in practice, a low-storage version of this RK4 scheme is implemented [161] for improved computational efficiency.

3.1.5 Resolution of the Poisson equation for the pressure

To determine the pressure that enforces the velocity to meet the divergence-free condition, an elliptic Poisson equation (Eq. 3.27) has to be solved. From the discretization of the Laplacian operator presented in Eq. 3.13, this equation could be written as a linear system $\mathbf{Ap} = \mathbf{b}$. As iterative methods are well-suited for solving large linear systems, a Deflated Preconditioned Conjugate Gradient (DPCG) algorithm was implemented in the YALES2BIO solver. More details about this algorithm can be found in [97].

3.1.6 Turbulence modelling

As explained in the Section 1.5.1, several reasons motivated the use of LES rather than RANS modelling strategy to account for the turbulence effects in the YALES2BIO solver. In LES strategy, the largest turbulent scales are explicitly resolved as a solution of the low-pass filtered Navier-Stokes equations while the subgrid scales are modelled. In RANS approaches, all the scales are averaged and the entire turbulence spectrum is modelled. According to Kolomogorov's theory [80], the statistics of the smallest structures are universal and only depend on the rate of kinetic energy dissipation and the viscosity of the fluid. On the contrary, large scales fluctuations are geometry-dependant and their shape is less generic. As it generally harbours many large scale fluctuations induced by the complex geometries of in the cardiovascular system [32], LES strategy seems then more adapted to solve this type of flows.

Formally, the basis of LES consists in filtering a field of interest Φ with a convolution filter (F) (low-pass filter) defined as:

$$\overline{\Phi}(\mathbf{x}) = \int_{\Omega} \Phi(\mathbf{x}')F(\mathbf{x} - \mathbf{x}')d\mathbf{x}' \tag{3.32}$$

where Ω is the flow domain considered, and F satisfies a normal distribution $\int F(x-x')dx' = 1$. Note that for simplicity, a spatially varying field was considered, but the filter could be similarly defined along the temporal direction for time varying variables. Using the previous definition, the variable Φ can be split into a resolved $\overline{\Phi}$ and Φ' fluctuating (unresolved) part as:

$$\Phi(\mathbf{x}) = \overline{\Phi}(\mathbf{x}) + \Phi'(\mathbf{x}) \tag{3.33}$$

An important difference with Reynold's averaging (used in RANS strategy) is that the filtered fluctuations are generally not null (e.g $\overline{\Phi'}(\mathbf{x}) \neq 0$). Usually, the convolution filters take the form of cut-off, box, or Gaussian function. We can apply a LES filter the incompressible NSE using Einstein notation:

$$\begin{cases} \frac{\partial \overline{u}_i}{\partial x_i} = 0 \\ \frac{\partial \overline{u}_i}{\partial t} + \frac{\partial \overline{u_i u_j}}{\partial x_j} = -\frac{1}{\rho}\frac{\partial \overline{p}}{\partial x_i} + \nu \frac{\partial^2 \overline{u_i}}{\partial x_j \partial x_j} + f_i \end{cases} \tag{3.34}$$

The filtered advection term can be split up according to Leonard's decomposition [89]:

$$\overline{u_i u_j} = \overline{(\overline{u}_i + u'_i)(\overline{u}_j + u'_j)} = \overline{\overline{u}_i\,\overline{u}_j} + \underbrace{\overline{\overline{u}_i u'_j} + \overline{u'_i \overline{u}_j}}_{C_{ij}} + \underbrace{\overline{u'_i u'_j}}_{R_{ij}} \tag{3.35}$$

where C_{ij} (cross-scale tensor) represents the interactions between large and small scales and R_{ij} (Reynolds subgrid tensor) the interactions between the subgrid scales. The following decomposition was additionally proposed [89]:

$$\overline{\overline{u}_i\,\overline{u}_j} = \underbrace{(\overline{\overline{u}_i\,\overline{u}_j} - \overline{u}_i\overline{u}_j)}_{L_{ij}} + \overline{u}_i\overline{u}_j \tag{3.36}$$

where L_{ij} is the Leonard tensor that represents the interactions among large scales. Finally, the NSE can be written as:

$$\begin{cases} \frac{\partial \overline{u}_i}{\partial x_i} = 0 \\ \frac{\partial \overline{u}_i}{\partial t} + \frac{\partial \overline{u}_i \overline{u}_j}{\partial x_j} = -\frac{1}{\rho}\frac{\partial \overline{p}}{\partial x_i} + \nu \frac{\partial^2 \overline{u_i}}{\partial x_j \partial x_j} - \frac{\partial \tau_{ij}^{SGS}}{\partial x_j} + f_i \end{cases} \tag{3.37}$$

where $\tau_{ij}^{SGS} = L_{ij} + C_{ij} + R_{ij} = \overline{u_i u_j} - \overline{u}_i\overline{u}_j$ is the sub grid scale tensor (SGS) stress tensor that arises from the non linear convective term in the NSE. Since it describes the effect of unresolved scales, this tensor is unknown and should be modelled. Eddy-viscosity-based models use the following Boussineq assumption to close the equations:

$$\tau_{ij}^{SGS} = -2\nu_{SGS}\overline{S}_{ij} \tag{3.38}$$

where $\overline{S}_{ij} = \frac{1}{2}(\frac{\partial \overline{u}_i}{\partial x_j} + \frac{\partial \overline{u}_j}{\partial x_i})$ the rate of strain tensor of the resolved scales, and ν_{SGS} the sugrid scale viscosity to be modelled. Many subgrid scale models have been proposed, where most of them taking the following form:

$$\nu_{sgs} = (C_m \Delta)^2 \mathcal{D}_m(\mathbf{u}) \tag{3.39}$$

where C is the model constant, Δ is the subgrid characterstic length scale (usually taken as the mesh size), and $\mathcal{D}_m$ the differential operator of the model acting on the resolved scales. Among the most common models, one could cite the Smagorinsky model where $\mathcal{D}_s = \sqrt{2\overline{S}_{ij}\overline{S}_{ij}}$ and $C_s = 0.18$. Since this model is known for being very dissipative near walls, improvements were proposed, that lead to models such as dynamic Smagorinsky [91], WALE [118], or σ-models [119]. The σ-model ($C_\sigma = 1.35$ and $\mathcal{D}_\sigma = \frac{\sigma_3(\sigma_1-\sigma_2)(\sigma_2-\sigma_3)}{\sigma_1^2}$ with $\sigma_3, \sigma_3, \sigma_3$ the singular values of the velocity gradient tensor) was used in all the simulations, as it has revealed better agreement than well-known dynamic Smagorinsky model as compared to experimental data in a configuration relevant to cardiovascular flows (unsteady jet with a rigid wall [154]). Moreover, this model results in a null SGS viscosity in a number of canonical flows, where the structure of the velocity gradient tensor indicates laminar flow features. This is particularly suited for transitional flows [30].

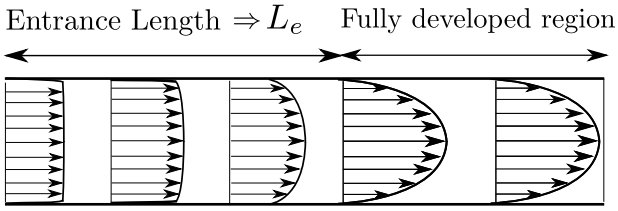

$$\left.\frac{\partial u_z}{\partial z}\right|_{z=L_e} = 0$$

Figure 3.2: Establishment of a fully developed velocity profile

3.2 Numerical test cases

Validation test cases are important to optimize the calculation parameters in the configuration of interest (optimal mesh size, numerical scheme, turbulent model, stability conditions) but also to ensure there is no parametrization errors in the computations. To test the validity of the CFD solution in the entire domain, the complex features encountered in the phantom were treated separately through validation test cases.

First, the development length of a pulsatile flow in a straight pipe was established and compared with the analytical Womersley velocity profile. As will be mentioned in Section 4.3, pilot simulations were performed to predict the development length upstream the flow phantom inlet necessary to guarantee a fully developed unidirectional inflow profile and well-controlled conditions.

A second test case is then presented where the behaviour of a pulsatile flow in a pipe bend is numerically predicted and compared with experimental results from the literature. In all the validation test cases presented, mesh convergence analyses were performed but are not expanded here.

3.2.1 Entrance flow

Development length (or entrance length) is defined as the axial distance needed to the boundary layers to reach and merge at the centre of the pipe. In other words, a flow whose velocity profile no longer varies with axial position is defined as fully developed, as illustrated in the Figure 3.2. The definition adopted in practice is the distance from the inlet where the centreline velocity has reached 99% of its asymptotic value. Several publications have already proven that the entrance length is longer at the centreline than at all other radial positions in a pipe [25, 43]. The entire velocity profile is then fully developed when the centreline velocity has reached an asymptotic value. Note that to define fully developed turbulent flows, time-averaged velocity are usually considered instead.

Steady flow

Under the assumptions of steady, laminar, incompressible flow in a straight pipe of circular cross-section and driven by a steady axial pressure gradient, the condition of fully developed flow can be verified by the well-known Hagen-Poiseuille velocity profile, expressed as:

$$u_z(r,\theta,z) = u_z(r) = 2u_{mean}\left(1-\left(\frac{r}{a}\right)^2\right)$$

where r is the radial coordinate, a is the radius of the pipe, and u_{mean} the mean velocity over the cross section considered. This profile applies at low enough Reynolds number only. Transitional and fully turbulent flows appear to have much larger wall shear stress and thinner boundary layer than the laminar case, implying flatter velocity profiles. Turbulent velocity profiles are often represented by logarithmic or power laws, from semi-empirical derivations, such as:

$$\frac{u}{u_{max}} = \left(1-\frac{r}{a}\right)^{1/n}$$

Over the past century, entrance length in straight pipes has been widely investigated by analytical and numerical methods mainly, as reviewed by Durst et al. [43]. Experimental measurements have also been published by Nikuradse [120].

By considering an order of magnitude of velocity convection term in the flow direction and diffusion term in the radial direction, Durst et al. [43] suggested a semi-analytical expression of the development length as a function of Reynolds such as : $\frac{L}{D} = C_0 Re + C_1$. Then, they validated this expression using a finite volume numerical approach for laminar pipe and channel flows. Finally, a more extensive non-linear correlation was proposed, such as: $\frac{L}{D} = \left[(C_0)^{1.6} + (C_1 Re)^{1.6}\right]^{1/1.6}$ where $C_0 = 0.619$ and $C_1 = 0.0567$ for pipe flows in the range $0 < Re < 2000$.

He et al. [68] published spectral finite element simulations of the flow with Reynolds varying in the range $40 < Re < 1400$. For $Re = 1000$, the development of centreline velocity along the axial length demonstrates very good agreement with the experimental data published by Nikuradse [120].

In this test case the flow through a straight pipe is predicted by simulation with the YALES2BIO solver for Reynolds number ranging in $Re \in [0, 2000]$. The resulting development lengths are compared with the development length proposed by Durst et al [43], the experimental measurements of Nikuradse [120], as well as the numerical simulations proposed by He et al [69].

Numerical set up

As physiological Reynolds numbers generally range between laminar and transitional regime, computations were performed in the range $10 < Re < 2300$. An incompressible Newtonian flow with kinematic viscosity $\nu = 4.02 \times 10^{-6} m^2/s$ was modelled within a 3 m length pipe of radius $a = 13$ mm meshed with 8 million tetrahedra. To reduce the influence of the velocity profile on the development length, we prescribed to each computation a flat inlet velocity profile on which was added up to 1% of white random noise.

The numerical establishment of a fully developed velocity profile was compared with the theoretical Poiseuille profile at $Re = 60$ and the results are shown on Figure 3.3a. The evolution of the development length with the Reynolds number is presented on Figure 3.3b.

Results

The fully developed velocity profile shown in Figure 3.3a are, as expected, in excellent agreement with the theoretical Poiseuille flow profile. Note that an overshoot appears on the developing velocity profiles (at $z/L_e = 0.042$), which is not predicted by classical first order boundary layer theory since the main assumption of this theory is to consider that $\delta << L$, where δ is the boundary layer thickness and L is the axial length scale. Near the trailing edge of the wall (inlet), this assumption is not valid. As shown on Figure 3.3b, the present results are in good agreement with Durst et al [43] and in excellent agreement with He et al. [68]. Practically speaking, a pipe length of 1.75 m would be necessary to ensure a fully developed flow with a 100 mL/s continuous flow rate.

Pulsatile flow

While steady flow validation is always informative, pulsatile flows are studied in the framework of this thesis. A pulsatile flow is defined as a steady flow on which is added an oscillatory component, such as: $u_{pulsatile}(t) = u_{st} + u_{osc}(t)$. Pulsatile flows have been widely studied since 1950 to understand the motion of blood flows through arteries. One of the first analytical work was proposed by Womersley in 1954. To characterize the effect of pulsation-induced inertia over viscous forces, he introduced the Wormersley number, a dimensionless number derived from a linearisation of the incompressible Navier-Stokes equations, and formulated as:

$$\alpha = a\sqrt{\frac{\omega}{\nu}} \tag{3.40}$$

where a, ω, and ν are the radius of the pipe, the angular frequency of the oscillations, and the kinematic viscosity of the fluid respectively. This number

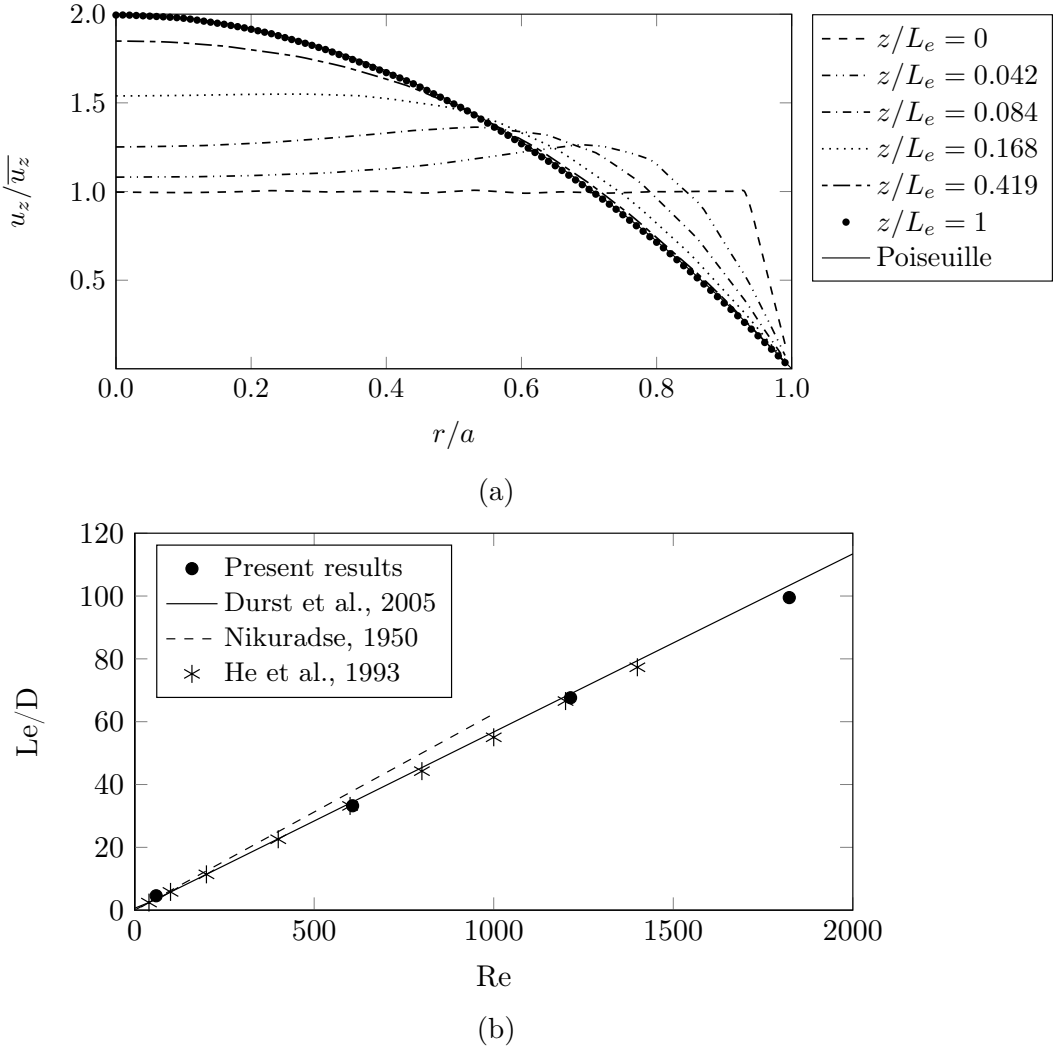

Figure 3.3: (a). Normalized velocity profile development with axial location at $Re = 60$. (b). Evolution of the entrance length as Re increases for laminar pipe flows.

evaluates the ratio between transient inertial forces and viscous forces. He also proposed an analytical formulation for the velocity profile of a fully developed flow in a rigid circular cross-section pipe, driven by a pulsatile pressure gradient. This velocity profile is obtained by solving of the incompressible Navier-Stokes equations projected on the axial direction in cylindrical coordinates, such as:

$$\frac{\partial u_z}{\partial t} + u_r\frac{\partial u_r}{\partial r} + \frac{u_\theta}{r}\frac{\partial u_z}{\partial \theta} + u_z\frac{\partial u_z}{\partial z} = -\frac{1}{\rho}\frac{\partial p}{\partial z} + \nu\left(\frac{\partial^2 u_z}{\partial r^2} + \frac{1}{r^2}\frac{\partial^2 u_z}{\partial \theta^2} + \frac{\partial^2 u_z}{\partial z^2} + \frac{1}{r}\frac{\partial u_z}{\partial r}\right) \tag{3.41}$$

where a fully developed ($\frac{\partial u_z}{\partial z} = 0$) axisymmetric ($\frac{\partial}{\partial \theta} = 0$) flow is considered with an uni-axial velocity component $u_r = u_\theta = 0$ due to the symmetry of the pipe.

Eq. 3.41 then simplifies:

$$\frac{\partial u_z}{\partial t} = -\frac{1}{\rho}\frac{\partial p}{\partial z} + \nu\left(\frac{\partial^2 u_z}{\partial r^2} + \frac{1}{r}\frac{\partial u_z}{\partial r}\right) \tag{3.42}$$

Then, in the context of pulsatile flows, Womersley used a decomposition in Fourier series to represent a purely oscillatory pressure gradient as a periodic function of the time, such as:

$$\frac{\partial p}{\partial z}(t) = -\operatorname{Re}\left[\sum_{n=0}^{N} \left.\frac{\partial p}{\partial z}\right|_n\right]$$

where $Re[.]$ stands for the real part of a complex-valued quantity. Therefore, for each harmonic n, one can write each component of the pressure gradient as a complex exponential such as:

$$\left.\frac{\partial p}{\partial z}\right|_n = c_n e^{jn\omega t}$$

Note that if the pressure gradient is a real-valued function, it may be written as:

$$\frac{\partial p}{\partial z}(t) = a_0 + \sum_{n=1}^{N} a_n \cos(n\omega t) + b_n \sin(n\omega t)$$

with $\omega = \frac{2\pi}{T}$ the angular frequency of the periodic pulse. $c_n = a_n + jb_n$ are the complex Fourier coefficients of the n^{th} harmonic. Then, Eq. 7.7 becomes for each harmonic n:

$$\frac{\partial^2 u_n}{\partial r^2} + \frac{1}{r}\frac{\partial u_n}{\partial r} - \frac{1}{\nu}\frac{\partial u_n}{\partial t} = \frac{1}{\rho\nu} c_n e^{jn\omega t} \tag{3.43}$$

Here the use of the subscript n indicates that the equation is solved for one component, summing over the entire harmonics, and taking the real part of the result.

Then, one possible solution of Eq. 3.43 may be written as:

$$u_n = f_n(r) e^{jn\omega t}$$

which leads to the following equation:

$$\frac{d^2 f_n}{dr^2} + \frac{1}{r}\frac{df_n}{dr} - \frac{jn\omega}{\nu} f_n(r) = -\frac{c_n}{\rho\nu} \tag{3.44}$$

Equation 3.44 is a general form of the zero-order Bessel differential equation. The solution reads:

$$f_n(r) = \frac{jc_n}{\rho\omega_n n}\left(1 - \frac{J_0(j^{3/2}\alpha_n \frac{r}{a})}{J_0(j^{3/2}\alpha_n)}\right) \tag{3.45}$$

Taking the pressure gradient as a the real part of $c_n e^{jn\omega t}$ allows to express the n^{th} component of the velocity as a time dependent function. Then, adding the steady component u_0 to the temporal solution leads to the entire velocity profile:

$$u_z(r,t) = u_0(r) + \sum_{n=1}^{N} \mathrm{Re}\left[u_n(r,\omega)\right]$$

$$u_z(r,t) = u_0(r) + \sum_{n=1}^{N} \mathrm{Re}\left[\frac{jc_n}{\rho\omega_n n}\left(1 - \frac{J_0(j^{3/2}\alpha_n\frac{r}{a})}{J_0(j^{3/2}\alpha_n)}\right)e^{jn\omega t}\right] \tag{3.46}$$

with $u_0(r) = c_0 8\mu\left(1 - \left(\frac{r}{a}\right)^2\right)$

From the previous Eq. 7.5, the pressure gradient is required to deduce the velocity profile at a position where the flow is fully developed. Nevertheless, when performing numerical simulations, it is more common to impose velocity or flow rate as inlet boundary conditions rather than a pressure gradient. Consequently, a modification of Womersley's analysis has been proposed to obtain the velocity profile as a function of the flow rate in a straight pipe [69], by decomposing the oscillatory flow rate component as a Fourier series: $q_n(t) = \mathrm{Re}\left[\hat{q_n}(\omega)e^{jn\omega t}\right]$, which allows to deduce from Eq. 3.45:

$$q_n(\omega) = 2\pi\int_0^a u_n(r,\omega)rdr = \pi a^2\frac{jc_n}{\rho\omega_n n}\left(1 - \frac{2}{j^{3/2}\alpha_n}\frac{J_1(j^{3/2}\alpha_n)}{J_0(j^{3/2}\alpha_n)}\right)e^{jn\omega t} \tag{3.47}$$

$$\hat{q}_n(\omega) = \pi a^2\frac{jc_n}{\rho\omega_n n}\left(1 - \frac{2}{j^{3/2}\alpha_n}\frac{J_1(j^{3/2}\alpha_n)}{J_0(j^{3/2}\alpha_n)}\right) \tag{3.48}$$

with the similar relation as Eq. 7.5:

$$q(t) = q_0 + \sum_{n=1}^{N} \mathrm{Re}\left[q_n(\omega)\right]$$

where $q_0 = c_0\frac{\pi a^4}{8\mu}$

Combining Eq. 3.48 and Eq. 3.45 results in:

$$f_n(r) = \frac{\hat{q}_n(\omega)}{\pi a^2}\frac{J_0(j^{3/2}\alpha_n) - J_0(j^{3/2}\alpha_n\frac{r}{a})}{J_0(j^{3/2}\alpha_n) - \frac{2}{j^{3/2}\alpha_n}J_1(j^{3/2}\alpha_n)}$$

Finally, taking the real part of the Fourier series decomposition, summing over all the harmonics, and adding the steady state Poiseuille velocity leads to:

$$u_z(r,t) = u_0(r) + \sum_{n=1}^{N} \mathrm{Re}\left[\frac{\hat{q}_n(\omega)}{\pi a^2}\frac{J_0(j^{3/2}\alpha_n) - J_0(j^{3/2}\alpha_n\frac{r}{a})}{J_0(j^{3/2}\alpha_n) - \frac{2}{j^{3/2}\alpha_n}J_1(j^{3/2}\alpha_n)}e^{jn\omega t}\right] \tag{3.49}$$

where $u_0(r) = \frac{64\mu^2 q_0}{\pi a^4}\left(1 - \left(\frac{r}{a}\right)^2\right)$. Note that the z-axis dependence out in the axial velocity was omitted since the flow is fully developed $z >> L_e$. For entrance pulsatile flows, we define the development length after He et al., [68] as:

$$\frac{u_z(0,\infty,t) - u_z(0,L_e,t)}{\frac{1}{T}\int_0^T u_z(0,\infty,t)dt} = 0.01 \tag{3.50}$$

To evaluate the ability of the flow solver to predict the entrance length correctly, numerical simulations were then performed in the same pipe configuration as in the previous case for steady flow considering a pulsatile flow rate such that $q(t) = 1 + \sin(\theta)$, where $\theta = \omega t = 2\pi t/T$ and $Re_{st} = \frac{\overline{u}D}{\nu} = 200$ the time-averaged Reynolds number. The fully developed velocity profile was compared to the Womersley profile given in Eq. 3.49. Then, the maximum entrance length defined as $\max(L_e/D)$ was compared to the results obtained by He et al., [68] for Womersley numbers ranging from 1 to 12.5.

Results

Figure 3.4a reveals excellent agreement between the numerical and analytical velocity profile at $\theta = 90°$ and $\theta = 270°$. Figure 3.4b also shows a good agreement with the results obtained by He et al. [68]. The maximum entrance length could be decomposed into three main parts: it slowly decreases for $\alpha < 3$, then suddenly drops between $\alpha \in [3, 6]$, and stabilizes to an asymptotic value for $\alpha > 6$. This asymptotic value is close to the steady entrance length at the same Reynolds number ($Re = 200$) found in the previous section (see Fig. 3.3b). The limit where $\alpha \to 0$ also tend towards the steady entrance length found for the peak Reynolds number $Re = 400$.

As mention beforehand, this validation test case was also used to build a criterion to adjust the length of the experimental test rig. The simulations, extrapolated to match the pulsatile flow regime of the experiment ($\alpha = 15$ and $Re_{st} = 1000$), finally predict a development length around $L_e/D = 50$. Therefore, a pipe of 1.3 m length was installed upstream the flow phantom to ensure a fully developed flow profile (cf Section 4.2.2).

3.2.2 Flow in a pipe bend

A quick review of the literature clearly shows that flows in curved pipes have been subject to numerous research works for the past century, with a particular interest to understanding the flow behaviour in human arterial network. The analytical velocity profile solution for a steady fully developed Newtonian flow in a pipe with circular cross section and small curvature was proposed by Dean in an early study [39]. He first highlighted the presence of secondary flows appearing as a pair of

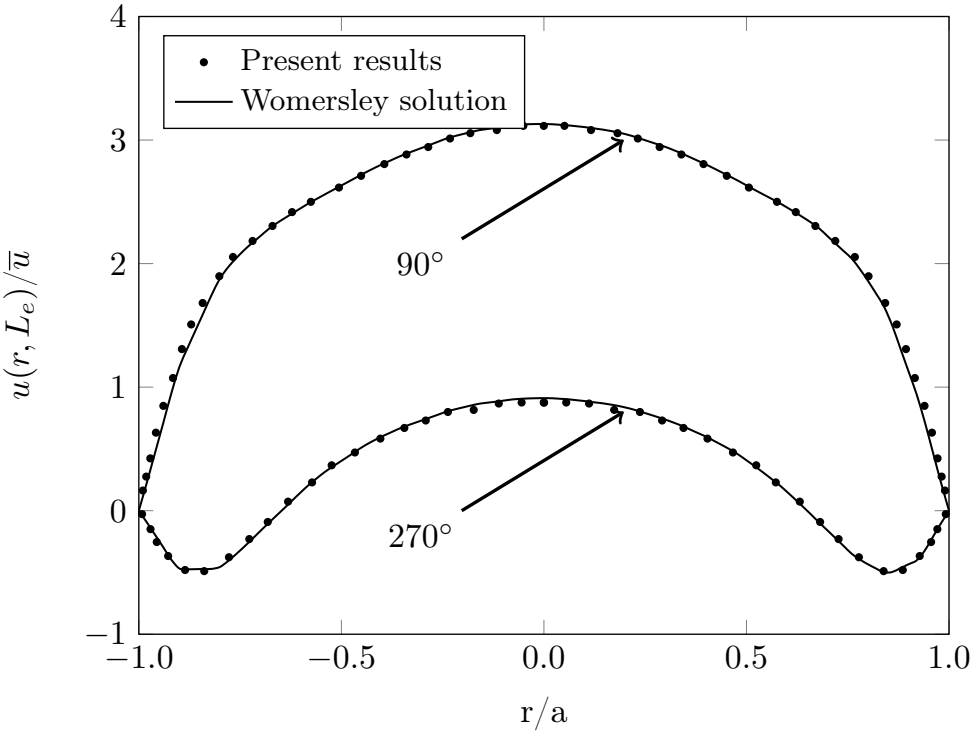

(a)

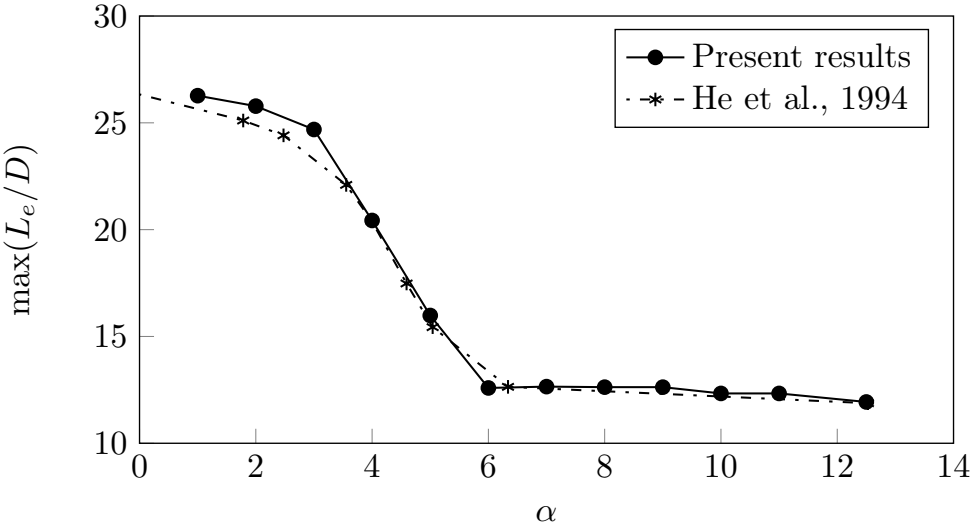

(b)

Figure 3.4: (a). Comparison of the velocity profile obtained numerically with the analytical Womersley solution at different phases ($\theta = 90°$ and $\theta = 270°$), far downstream in the pipe where the flow is fully developed at $Re_{st} = 200$ and $\alpha = 12.5$. The velocity is normalized by the time-averaged value of the inlet velocity $\overline{u}$. (b). Normalized maximum entrance length at $Re_{st} = 200$ and $\alpha \in [1, 12.5]$ obtained numerically and compared with the results obtained by He et al.[68].

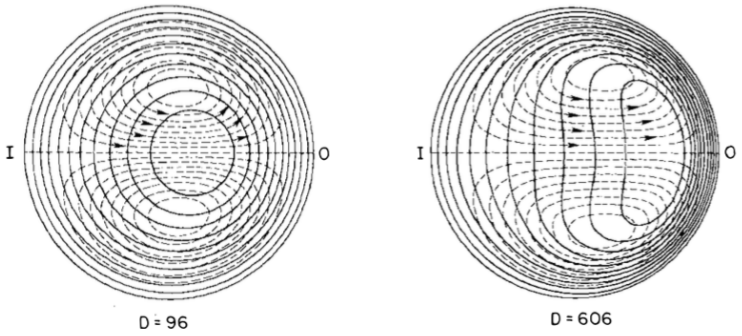

Figure 3.5: (—) Axial velocity contour and (- - -) secondary streamlines in a pipe bend as provided in [105].

counter-rotating vortices (call Dean vortices) and induced by the centrifugal forces sweeping the flow towards the outer wall. An illustration of these vortices is given in Fig 3.5. He also introduced the Dean number [40], a dimensionless number that assesses the effect of the inertial forces in comparison with the viscous forces, and giving emergence of this secondary flow. Many variants of the original definitions have been proposed in the literature but the definition adopted in Berger et al. [10] is probably the most intuitive:

$$D = \sqrt{\frac{a}{R_c}} Re \tag{3.51}$$

where a is the radius of the pipe and R_c the radius of curvature (also denoted $\delta = \frac{a}{R_c}$), and Re the Reynolds number based on the mean axial velocity. Later, Lyne established theoretical solutions of unsteady flow velocity profiles for small Dean number and large Womersley values. He showed that secondary structures are composed with two extra pairs of vortices now called the Lyne vortices [95], rotating in opposite direction as compared to Dean vortices.

Steady flow

In this section, a steady flow through an infinite pipe bend was simulated at varied Dean numbers. Note that to simulate an infinite pipe bend and avoid dealing with entry flow, a small numerical domain was designed (see Figure 3.6, and periodic boundary conditions were prescribed at the inlet and outlet of the flow domain. Nevertheless, imposing periodic boundary condition numerically results in a null pressure gradient, thus leading to a stagnant flow. To bypass this issue, a source term has been introduced to artificially act as a pressure gradient driving the flow. The following source term was imposed:

$$S_\phi = \frac{4\nu^2 D}{a^3\sqrt{\delta}} \frac{R_c}{R} \tag{3.52}$$

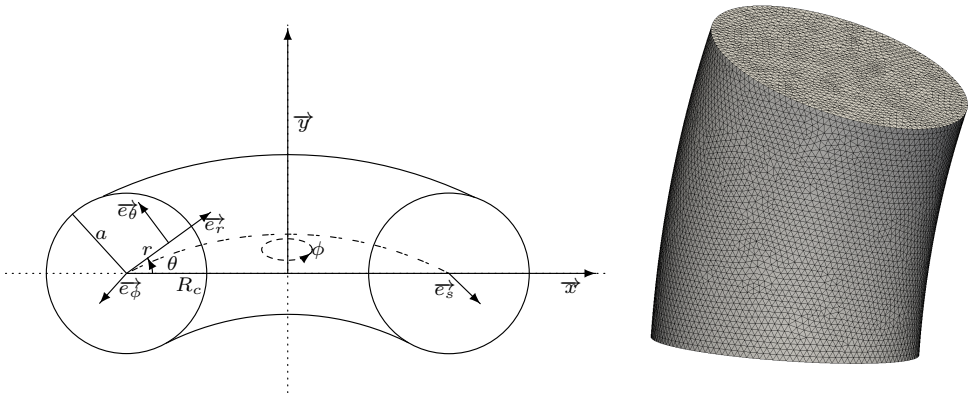

Figure 3.6: (**Left**) Cylindrical coordinates system defined to describe the source term in the simulation of a steady flow in a pipe bend. (**Right**) Numerical mesh associated with periodic boundary conditions. The mesh contains 700 000 tetrahedrons.

The derivation of this source term could be found in Appendix 7.4. By implementing the above source term along the centreline of the curved duct, it is possible to perform a periodic simulation of flow in a curved pipe directly piloted by the Dean number.

Siggers and Waters [137] performed simulations with a pseudospectral code, whose algorithms are usually very accurate. The resulting axial velocity profiles are compared to their simulation results at Dean number $D = (1.77, 17.7, 441)$.

Results

The axial velocity countours obtained by simulation are compared to [137] in Figure 3.7. Results are very accurate in term of axial velocity profiles for both of them, and trends are the same for the axial vorticity contours. As D increases, the velocity profile moves toward the outer bend of the wall, driven by the inertial forces. The latter trend has been previously verified by [105].

Pulsatile flow

The effect of the pulsation on the flow in a curved channel was investigated. To this respect, a validation test case was developed, where the flow through a 90 °circular cross-section pipe bend was predicted with the YALES2BIO solver and compared to a previous work proposed Timite et al. [153]. An incompressible Newtonian flow was modelled in a curved pipe with a $a = 2\ mm$ radius and a $R_c = 220\ mm$ radius of curvature. The flow was driven by a pulsatile flowrate

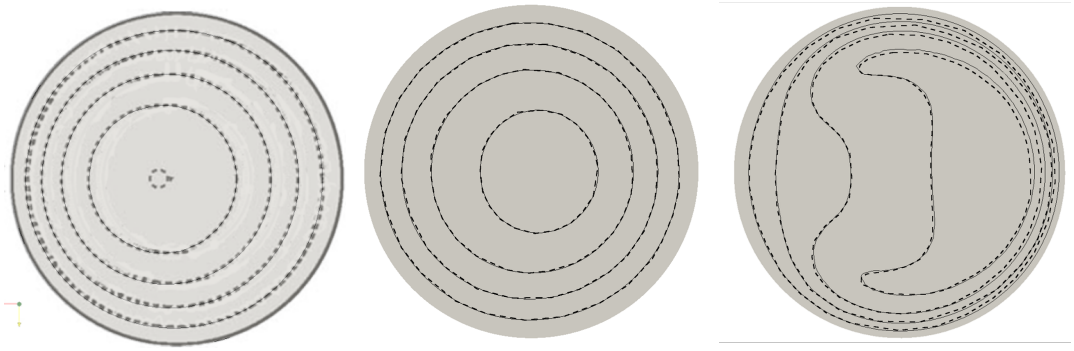

Figure 3.7: Contour of the axial velocity profiles. **left** $\delta = 0.3$, $D = 1.77$, **middle** $\delta = 0.3$, $D = 17.7$, **right** $\delta = 0.3$, $D = 441$. (—) Reference simulations from Siggers and Waters [137], (- - -) present numerical results.

such that:

$$Q(t) = Q_0(1 + \beta \sin \omega t) \tag{3.53}$$

where Q is the flowrate, $\beta = \frac{Q_{max}}{Q_0}$, Q_{max} the peak oscillatory flowrate, Q_0 the mean (steady) flowrate and ω the angular frequency. The steady Reynolds is defined as $Re_{st} = \frac{2Q_0}{\nu \pi a}$.

Results

The axial velocity profiles in the middle of the bend resulting from the numerical simulations are compared to the experimental results obtained with Laser Doppler Velocimetry by Timite et al [153] in Fig. 3.8 for various phases and Womersley numbers ($\alpha = 12.14$ and $\alpha = 17.17$). Results show an overall good agreement for each case. At $\omega t = 90°$ on Fig. 3.8a), the peak axial velocity is located near the inner wall, as observed in Yearwood and Chandran (1982) [167]. However, during the deceleration phase, when inertial forces are dominant, the peak velocity shifts towards the outer wall. When increasing the Womersley number, the peak velocity gets closer to the wall. At $\omega t = 270°$, a reverse flow occurs at the inner wall of the tube and maximum velocity is located at the outer side, due to the stopping effect (deceleration phase), described by Weinbaum and Parker (1975) [160]. Similarly, the peak reverse flow value seems closer to the wall for higher Womersley number. The dominance of the inertial effects as compared to viscous effects can explain the reduction of the viscous layer as the Womersley increases. The axial velocity along the y-axis (Fig. 3.8b and Fig. 3.8d) is symmetrical and a valley is observed as well as the peak velocity close to the wall. The valley is observed due to the centrifugal forces increasing the tangential velocity component close to the external wall. The fluid particles initially at the centre then move towards the external wall and a secondary flow is produced, with the formation of

Dean vortices as mentioned above (see Fig. 3.5). The peak velocity near the walls represents the centre of these vortices.

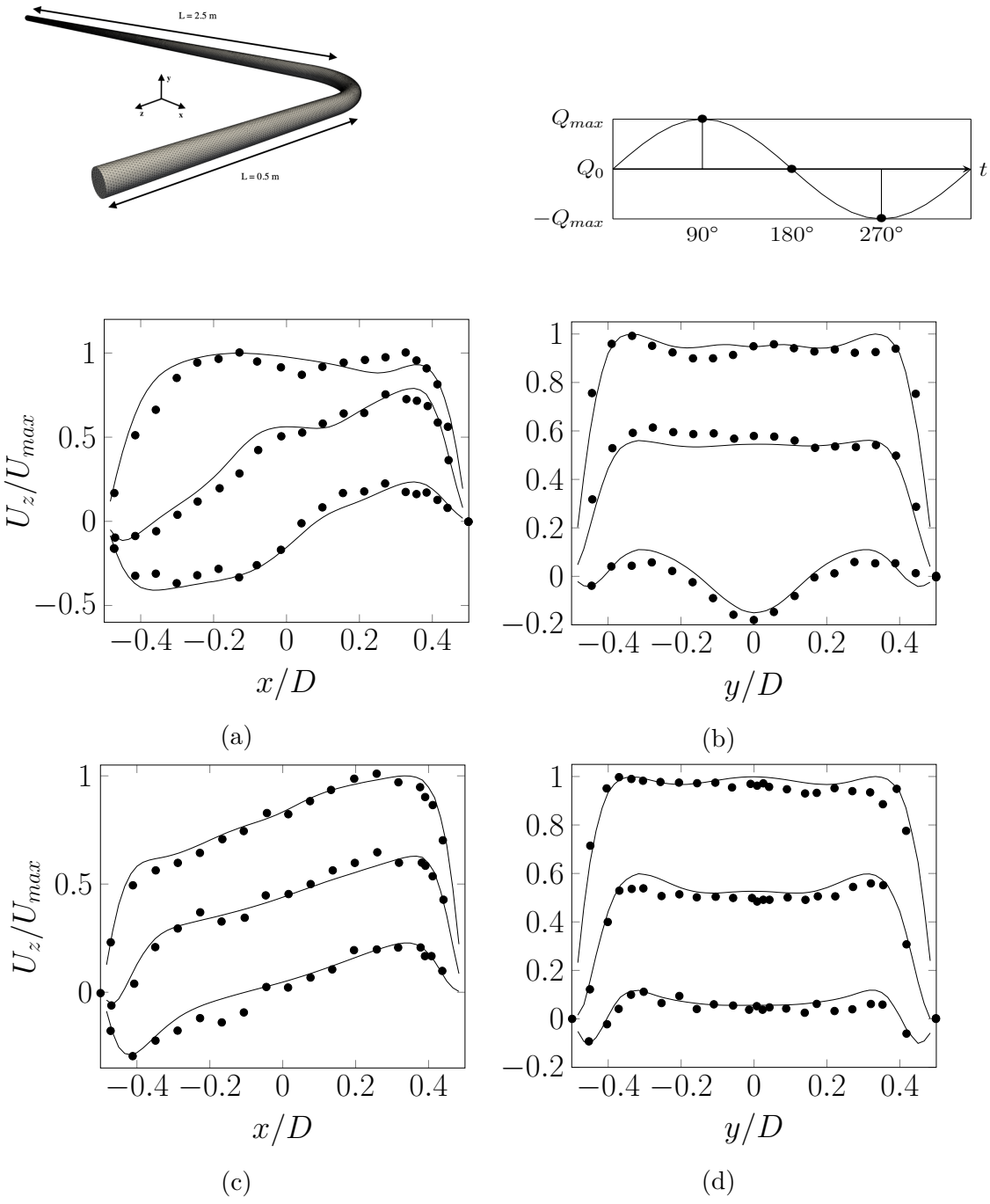

Figure 3.8: Normalized axial velocity profiles in the middle of the bend (45 °) at phases $\omega t = 90,\ 180,\ 270°$ for upper, middle and lower curves respectively. The experimental results (•) are obtained with Laser Doppler Velocimetry [153] while computations (——) are performed with the YALES2BIO solver. (a) and (b) show a case where $Re_{st} = 600$ the steady component Reynolds number, $\alpha = 12.14$, and $\beta = 1$. (c) and (d) show a case where $Re_{st} = 600$, $\alpha = 17.17$ and $\beta = 1$.

Chapter 4

CFD-based methodology to assess PC-MRI

Chapter contents

4.1 Introduction

As detailed in the first chapter, one of the main objectives of this thesis is to develop a standardized procedure for comparing PC-MRI and CFD under complex flow conditions representative of the cardiovascular system. To establish this procedure, a preliminary step is to mitigate the sources of discrepancies coming from each technique in order to focus on the errors relevant to the comparison itself. For this purpose, we designed a fully controllable, reproducible and MRI compatible experiment delivering a flow of a blood-mimicking fluid within a phantom which gathers topological complexities typical of that observed in-vivo. We have full control of the geometry of the non deformable flow domain and fluid rheology, thus removing classical sources of uncertainties that could be found in-vivo: segmentation errors, wall motion, blood properties. In addition, although branching is present within the considered flow domain, there is only one outlet boundary so that a simple zero pressure condition can be safely prescribed without determining the flow split in the branches. The corresponding flow is predicted by means of a high resolution LES solver, and compared with velocity fields acquired using conventional 4D PC-MRI scans at various spatial resolutions. A quantitative analysis of the differences is then performed to highlight the potential discrepancies induced by a straightforward comparison. Finally, several post-processing steps are encompassed and a generic comparison protocol is proposed to systematically correct these sources of discrepancies.

4.2 Design of a well-controlled experiment

4.2.1 Flow phantom

The flow phantom was constructed to generate a complex and realistic flow, such as that observed in the cardiovascular system. The aim was not to reproduce a patient-specific geometry, but to gather several geometrical features yielding complex flow patterns analogous to in-vivo flow patterns, while keeping a relatively compact and well-controlled flow phantom. A pipe bend with 26 mm of inner diameter was designed with a 50 mm radius of curvature to mimic aortic arch blood flows. A bifurcation was set in analogy with collateral arteries. Daughter vessel sizes were designed to replicate typical flow split that can be found in-vivo

between supraceliac and infrarenal arteries [151]. Finally, a protuberance was attached at the intersection between the collateral and main branch, to mimic blood flows patterns in aortic aneurysms. Figure 4.1 shows the final design of this MRI flow phantom. The flow in such a geometry is expected to feature complex flow structures such as flow recirculation in the aneurysm, regurgitation in the bifurcation, or a mixing layer produced by the jet at the junction of the collateral branch with the main branch.

Stereo-lithography based 3D printing technique was used to make a first version of the flow phantom from a photopolymer resin (FormLabs Inc, Somerville, USA). Stereo-lithography has the advantage to produce complex models with excellent surface conditions, with a geometric tolerance down to 25 µm. Nevertheless, a major constraint of this technique is its limitation in terms of printable volume, which imposes to print the phantom in 4 separated parts and assemble it afterwards. Even with a slide link limiting to one translation its degrees of freedom, the collateral was braced between its two junctions, and finally broke after a few months. A second flow phantom was therefore designed as a single component made of Nylon PA 12 with a 60 µm geometric tolerance (Sculpteo, Villejuif, France). The surface state of slightly quality than for the resin but the structure was less brittle and therefore more adapted for transport. Four holes were drilled in the structured and drain systems were attached for possibly inserting pressure transducers, and to evacuate the residual air blocked in the flow phantom when filling the circuit. Owing this high fidelity, we could compute the flow directly from the computer aided design (CAD) model with no surface approximations associated with a segmented geometry. Finally, as detailed in Section 4.4.2, static tissues are necessary to post-correct for the eddy currents effects on the phase images. For this reason, and to increase the quantity of signal emitted within the acquired field of view, the phantom was fully immersed in a silicon bath (see Figure 4.2b). Additionally, the silicon bath protects the flow phantom from collisions.

4.2.2 Experimental test bench

A schematic diagram of the experimental setup is shown in Figure 4.3. A blood-mimicking fluid (Newtonian fluid) with a kinematic viscosity of $\nu = 4.02 \times 10^{-6}\ m^2/s$ and a fluid density of $\rho = 1020\ kg/m^3$ was supplied to the circuit. To avoid undesired artifacts and for MR safety reasons, all the circuit components, apart from the pump, were MR compatible. Inside the scanner room, the pump was positioned outside the 5 Gauss Line (perimeter around the scan where the static magnetic field is higher than 5 Gauss) also for MR safety considerations. A reservoir was added to empty and purge the system. Flexible tubing at the inlet and outlet of the pump were necessary to easily change its position while keeping

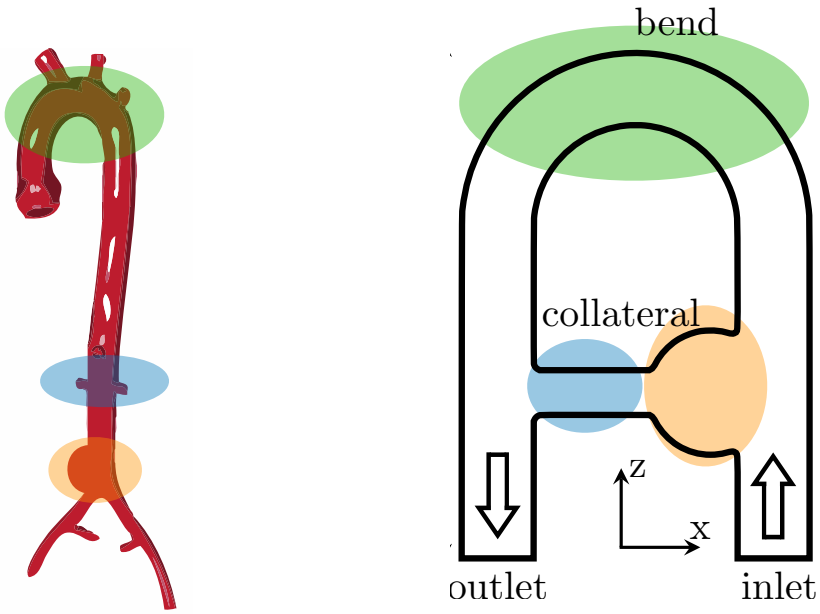

Figure 4.1: Analogy with cardiovascular system

static the remaining part of the circuit. Nevertheless, the in-line arrangement of tubes and devices coming up with specific features (such as diameter, surface state, compliance, etc.) between the pump and the phantom's inlet surface certainly results in non-negligible flow perturbations. To reduce the swirling motion of the entering fluid and avoid complex profile at the inlet of the flow phantom, a flow straightener was set upstream of a long straight (26 mm inner diameter) rigid plastic pipe. The development length necessary for the pulsatile flow profile to be fully developed downstream the flow straightener was estimated using the CFD simulations presented in Section 3.2.1. This pilot simulation constitutes an important consideration in the design of the test rig to reduce and optimize any cumbersome or unnecessary part. The flow phantom was then connected downstream with plug-in connectors between junctions to split the circuit and facilitate the transport. The experiment was carried out using a computer controlled pump (CardioFlow 5000 MR, Shelley Medical Imaging Technologies, London, Ontario, Canada) providing user-defined pulsatile flow waveforms such that $q(t) = q_0\,(1 + \sin(2\pi t/Tp))$ where $q_0 = 100\ mL/s$ is the mean flow rate delivered by the pump and T_p is the duration of one cycle.

A preliminary calibration of the programmable pump was performed to control the inflow waveform precision and reproducibility over time during a scan. The calibration was performed by measuring the time t_{fill} needed by the pump to fill a 3000 mL water tank with a programmed sine inlet waveform. The mean error was defined as: $\epsilon_{pump} = |\frac{t_{prog} - t_{fill}}{t_{fill}}|$ where t_{prog} is the time that should be required to fill the tank according to the programmed flowrate waveform. Results

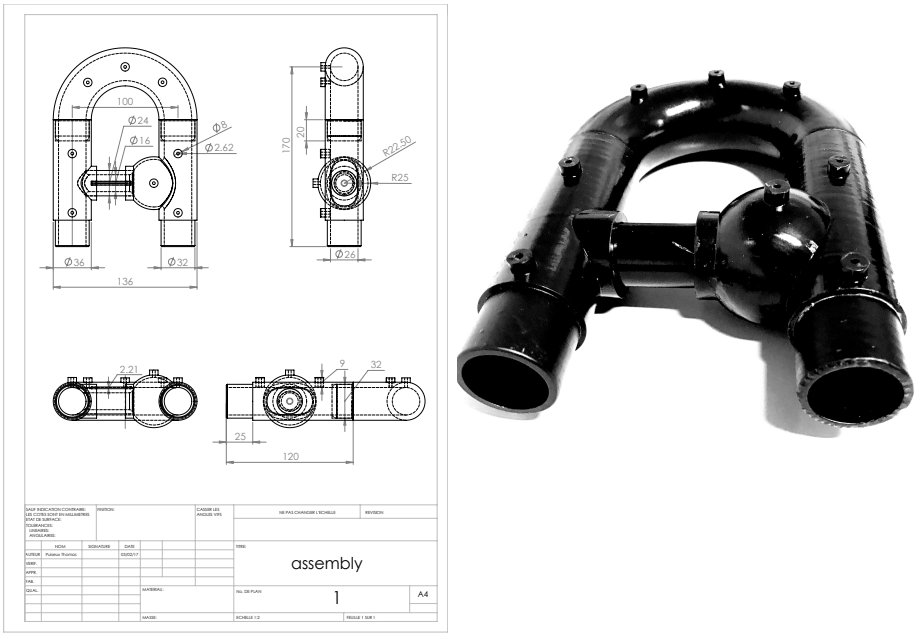

(a)

(b)

Figure 4.2: a). (left) Engineering drawing and (right) the first version of the flow phantom, made with photopolymer resin. b). (left) Second version of the phantom, made with Nylon, and (right) immersed within the silicon bath .

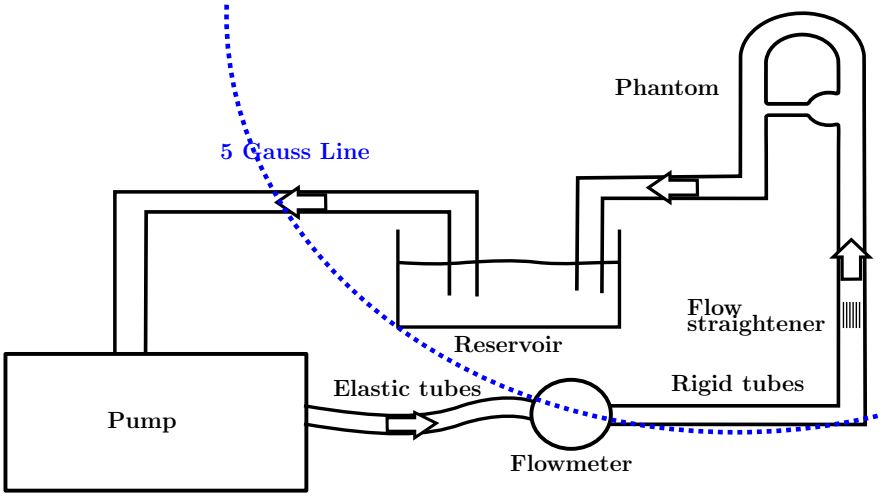

Figure 4.3: Schematic diagram of the experimental setup.

Table 4.1: Pump and flow meter calibration results. Fourteen cases are considered, varying the inflow rate waveform parameters (time period, peak and mean flow rates) programmed in the pump.

N	Period (ms)	Q_{max} (mL/s)	Q_{mean} (mL/s)	Re_{max}	ϵ_{pump} (%)	$\epsilon_{flowmeter}$ (%)
1	1200	200	60.867	2980	42.98	10.40
2	1200	200	60.867	2980	46.45	5.80
3	1200	200	60.867	2980	35.12	13.65
4	1200	250	60.867	2980	18.39	3.30
5	1200	250	60.867	2980	12.81	10.33
6	1000	200	79.57	4900	12.96	3.13
7	1000	160	79.57	3900	49.49	2.20
8	920	160	79.57	3900	53.76	0.77
9	800	160	79.57	3900	56.20	0.57
10	700	160	79.57	3900	56.36	6.67
11	600	160	79.57	3900	62.48	0.83
12	1120	160	79.57	3900	31.66	8.20
13	1200	160	79.57	3900	44.42	1.97
14	2000	160	79.57	3900	28.59	6.13

of the calibration process are presented on Table 4.1. As we found a mean error of $\epsilon_{pump} = 41.47 \pm 17\%$, we then decided not rely on the pump to ensure the inflow waveform precision and reproducibility. Instead, the pulsatile flow rate delivered by the pump was measured by means of an ultrasonic flowmeter (UF25B100 Cynergy3 components Ltd, Wimborne, Dorset, UK) placed upstream of the flow straightener. As expected, a considerably better agreement was found with the flow meter ($5.28 \pm 4\%$ average error).

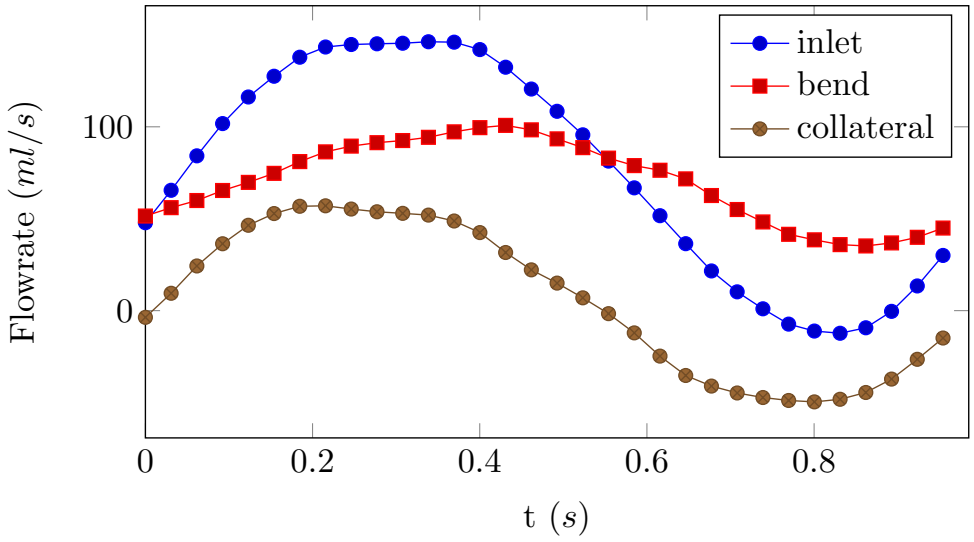

Figure 4.4: Flow split repartition over a cycle.

4.3 PC-MRI measurements

All PC-MRI scans were performed on a 1.5T scanner (Siemens Magnetom Avanto, Siemens Medical Systems, Erlangen, Germany) at Rangueil University Hospital (Rangueil, Toulouse, France).

4.3.1 2D measurements

To ensure that the CFD simulations reflect the experimental conditions as accurately as possible, it is important to prescribe high resolution velocity profiles as inflow conditions. In this sense, to guarantee that the flow is accurately measured at inlet boundary location, several retrospectively gated time-resolved 2D PC-MRI measurements were acquired at high resolution in the transverse plane and compared to the reference flow meter measurements. To increase the signal-to-noise ratio, the pixel size was set to 0.78125 x 0.78125 mm^2 and the slice thickness to 6 mm. Good agreement was found between the flowmeter and the 2D PC-MRI measurements; the mean relative error over one cycle was $\bar{\varepsilon}_{2D} = 0.32\%$. It was also verified that the flow straightener disrupts any vortex coming from upstream: the in-plane velocity component measured was less than $0.05w$, where $\mathbf{u} = (u, v, w)$ and w is the through-plane velocity component. Figure 4.4 shows the flow rate repartition measured with 2D CINE PC-MRI during a cycle.

4.3.2 Near-wall masking

The 2D cine PC-MRI inlet velocity measurements were masked to correct the velocity offsets due to the partial volume effects and random noise caused by the plastic phantom walls as well as the air surrounding the phantom (first version). The mask was applied so that the near-wall velocity is supposed linearly evolve with the radial direction, assuming a zero velocity at the boundary walls. In practice, the masked through-plane velocity component w at position $r \in [R_{lim}, R]$ (where R is the radius of the circular cross-sectional inlet surface and $R_{lim} = 0.9R$ an arbitrarily defined inner radius) equals to:

$$w(r) = \frac{w(R_{lim})}{R - R_{lim}} (R - r) \tag{4.1}$$

As compared to the reference flow meter measurements, this near-wall mask revealed a noticeable improvement of the flow waveform, with a mean relative error reduced from 0.32% to 0.15%. A second 2D PC-MRI scan was acquired with the same input parameters to ensure the reproducibility of the measurements.

4.3.3 4D measurements

Then, three successive prospectively gated 4D flow MRI measurements were then acquired with an isotropic voxel size of 2 mm, 3.1 mm and 3.4 mm. The flow phantom was scanned in coronal orientation with the following settings: encoding velocity VENC = 0.5 m/s in all three velocity encoding directions ; TE = 3.43-3.5 ms; temporal resolution = 49-52 ms; flip angle = 15 °. All scans were acquired without parallel imaging acceleration so that every line of the k-space was filled and for an improved SNR. Also to maximize the SNR, the encoding velocity was set according to a numerical estimation of the maximum velocity in the flow domain and a particular attention was paid to avoiding phase aliasing.

4.3.4 Consistency and reproducibility

As shown in Figure 4.5 and Table 4.2, an overall good agreement was found between the inlet flow rate reconstructed from 4D Flow MRI measurements and the 2D CINE PC-MRI measurements. As expected, the error generally increases with the voxel size. Also, mainly at peak systole, the best improvements between raw and masked data are obtained for the largest voxel size, since partial volume effects are more important.

Table 4.2: Comparison of the raw and masked inlet flow rates measurement errors between 4D Flow MRI and 2D cine PC-MRI. The error is here defined as: $\epsilon = |\frac{1}{N_p}\sum_{i=1}^{N_p}\frac{q_i^{4D}-q_i^{2D}}{q_i^{2D}}|$ where q is the flow rate and N_p the number of cardiac phases. Note that the inlet near-wall mask was applied to both the 4D and 2D MRI.

Error (%) (raw/masked)	inlet		collateral	
	2D (1)	2D (2)	2D (1)	2D (2)
4D Flow MRI (2 mm)	5.15/4.74	3.37/3.42	12.93/11.10	3.80/1.21
4D Flow MRI (3.1 mm)	7.37/5.50	5.56/4.18	19.08/13.79	9.46/3.66
4D Flow MRI (3.4 mm)	10.53/8.08	8.67/6.72	15.03/11.76	5.73/1.81

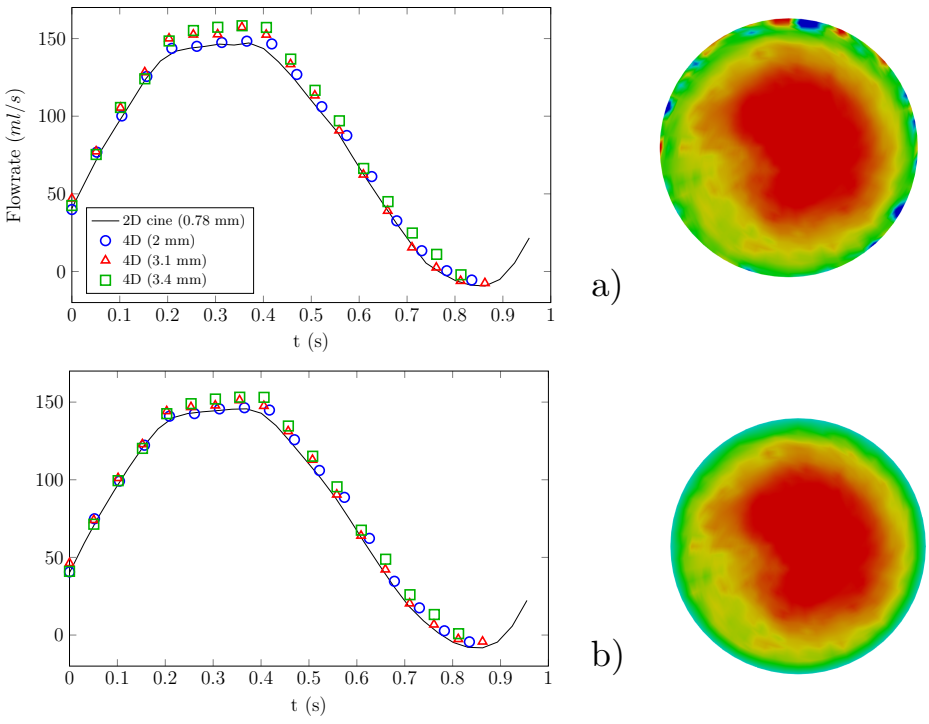

Figure 4.5: **Left** Inlet flow waveforms over one cycle measured at different isotropic voxel sizes **(a)** without and **(b)** with near-wall velocity masking. **Right (a)** Raw and **(b)** masked velocity field measured from 2D PC-MRI scan during systole.

4.4 MRI dataset processing

The MRI post-processing steps required to correct for velocity artifacts, as well as to prepare the MR data for comparison with CFD, are described in this section.

The first step consists in applying an affine transform matrix to the raw DICOM (expressed in the image coordinate system) to express them into the unique "world" coordinate system. The data are reordered and a velocity mapping is then computed from the phase images, and the resulting dataset is written as a structured grid in the VTK format (Visualisation ToolKit, Kitware, Inc, Clifton Park, NY). These steps are performed using an in-house Matlab program (The MathWorks, Natick, USA) developed and kindly provided by Dr. Anou Sewonu. All the following processings steps were implemented through VTK-based Python programs.

4.4.1 Noise masking

As detailed in the previous Section 2.8.5, the noise affects the quality of the magnitude image but also the phase image.

Low intensity signal denoising

When the SNR_{mag} is low, as it is the case for low signal intensities regions where tissues contain few protons such as in air or plastic, the velocity images contain randomly distributed phases. In the vicinity of a wall, this noise can strongly affect the quantification of certain hemodynamics biomarkers such as wall shear stress by introducing a random phase deviation to the integrated signal in the voxels crossing the walls. A straightforward way to mask this noise is to compute the pixel-wise maximum value of image magnitude over all the cardiac phases. As the magnitude signal emitted by the air and plastic wall of the phatom is low, a binary mask can easily be generated and noisy regions excluded. Another way to remove the noise consists in thresh-holding the time-course standard deviation of the velocity field voxel-by-voxel [18]. Since velocity noise results in higher temporal variation as compared to the static tissues and blood flow, it can be separated and removed. A measure of the time-course pixel velocity corresponding to blood, noise, and static tissues is presented in Figure 4.6. A mix of these two approaches can easily be implemented and most probably provide better noise masking (see Fig. 4.7).

Divergence-free denoising

An additional reduction of the residual noise is possible by introduction of physical knowledge in the processing of MRI dataset. According to the conservation of

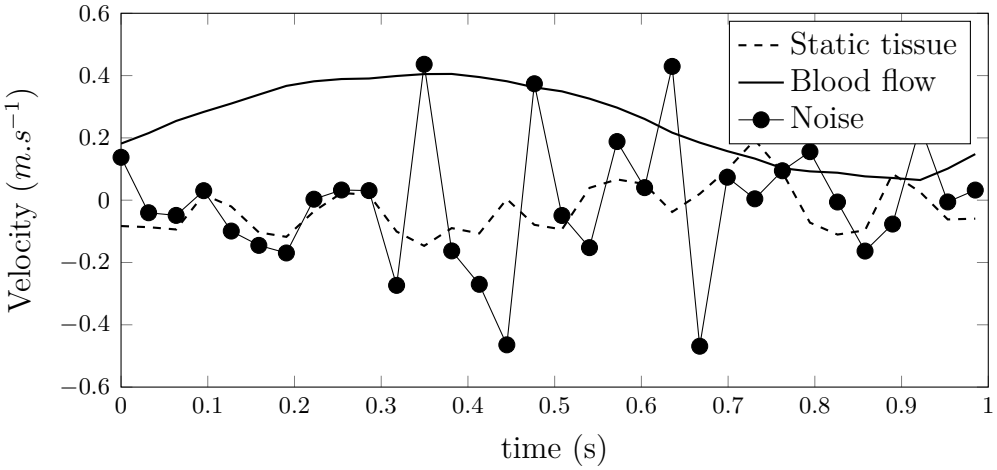

Figure 4.6: A typical temporal evolution of the velocity, for blood flow, static tissue and noise. The static tissues here corresponds to the silicon while the noise corresponds to the air surrounding the phantom. The higher variability of the noise velocity results in a larger standard deviation compared to blood flows or static tissues.

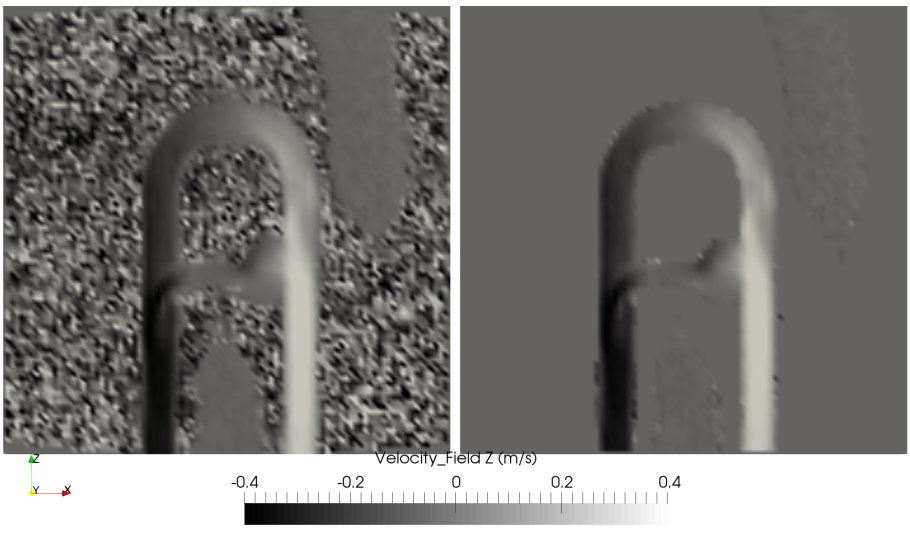

Figure 4.7: (left) Raw measurement velocity field (right) masked velocity field with both magnitude and time-course standard deviation technique.

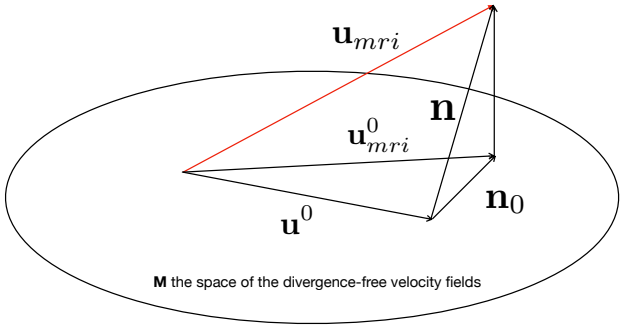

Figure 4.8: Schematic representation of the divergence-free velocity field space (**M**), adapted from [140]. u^0 is the exact velocity field while u^0_{mri} is the projection of the MRI velocity onto **M** which still contains the divergence-free part of the noise.

the mass, and as blood is incompressible, the continuity equation imposes the divergence of the velocity field to be zero. A way to enforce the velocity field to meet the divergence-free condition can be achieved by defining a projection operator $\mathbb{P}$ that orthogonally projects the velocity field onto the space of divergence-free fields (see the previous Section 3.1.3). An illustration of the projection is presented in Figure 4.8. To this end, the classical approach already detailed in Section 3.1.3 is to decompose the MRI velocity field $\mathbf{u}_{mri}$ as the sum of an irrotational and solenoidal parts, such as:

$$\begin{aligned} \mathbf{u}_{mri} &= \mathbf{u}^0_{mri} + \nabla q \text{ on } \Omega \\ \mathbf{u}^0_{mri} \cdot \mathbf{n} &= 0 \text{ on } \partial\Omega \end{aligned} \tag{4.2}$$

where $\nabla \cdot \mathbf{u}^0_{mri} = 0$, Ω is the flow region delimited with $\partial\Omega$ boundary. In other terms, the projector $\mathbb{P}$ could be expressed as:

$$\mathbb{P}\mathbf{u}_{mri} = \mathbf{u}_{mri} - \nabla q = \mathbf{u}^0_{mri} \tag{4.3}$$

where $\mathbb{P}\mathbf{u}^0_{mri} = \mathbf{u}^0_{mri}$ and $\mathbb{P}\nabla q = 0$. Then, taking the divergence of the previous equation raises the Poisson equation to solve, where q is the solution of the following Neumann problem:

$$\begin{aligned} \nabla^2 q &= \nabla \cdot \mathbf{u}_{mri} \text{ on } \Omega \\ \frac{\partial q}{\partial \mathbf{n}} &= \mathbf{u}_{mri} \cdot \mathbf{n} \text{ on } \partial\Omega \end{aligned} \tag{4.4}$$

where $\mathbf{n}$ is the outward normal to the boundary and the classical no-slip boundary condition $u^0_{mri} \cdot \mathbf{n} = 0$ is assumed at walls. It can be shown that this equation admits an unique solution up to an additional constant [33].

Song et al., (1993) [140] first applied this physical principle to regularize MRI velocity field. They posed the problem in a different way, and used Lagrange multipliers method to demonstrate the existence of the previous projector $\mathbb{P}$.

Note that even if $\mathbf{u}_{mri}$ is divergence free, the projection does not eliminate all the noise but only the part which is not divergence free. As illustrated in Figure 4.8, one can decompose the velocity field as follows:

$$\mathbf{u}_{mri} = \mathbf{u}^0 + \mathbf{n} \tag{4.5}$$

where $\mathbf{u}^0$ is the exact velocity field (exempted of noise), $\mathbf{n} = \mathbf{n}^0 + \mathbf{n}^\perp$ with $\mathbf{n}_0 \in M$ the divergence-free noise, and $\mathbf{n}^\perp$ the noise which is orthogonal to this direction. The projection of the velocity can also be written as function of the exact velocity field (see Fig. 4.8:

$$\mathbf{u}^0_{mri} = \mathbf{u}^0 + \mathbf{n}^0 \tag{4.6}$$

A straightforward way to numerically solve the Neumann problem given in Eq. 4.4 is to adopt a finite difference discretization of the equation with discretization nodes located at voxel centres in the imaging matrix (viewed as a regular Cartesian grid). Although the Poisson equation can easily be discretized on rectangular flow domains, the fluid regions found in the cardiovascular system are most of the time irregular. In this case, defining the normal vector along the walls is more challenging [140]; instead the fluid domain outline is generally segmented and a proper boundary conditions are deduced from the "smooth" walls topology.

In the scope of this thesis, the a priori knowledge of the flow phantom morphology (provided by the 3D CAD model) was used for spatial interpolating the MRI dataset on the phantom's volume mesh. Note that a prior registration of the MRI images with this morphology is necessary ; this processing step is detailed in Section 4.4.3. The Neumann problem was then discretized on the defined nodes and the Biconjugate Gradient Stabilized algorithm implemented in the YALES2BIO solver was used to solve the resulting linear system. Results of the divergence-free processing are shown in Figure 4.9. Qualitatively it clearly shows a diminution of the blurring. Quantitatively, the resulting error map shows an error up to 10% of the VENC in the collateral branch.

Note that other methods exist to constraint the velocity field as the decomposition into radial basis functions [23]. It was however not implemented in this thesis.

4.4.2 Eddy currents correction

Eddy currents are currents induced within the conducting parts of the scanner by the time-varying magnetic fields emitted by the gradient coils. Their effects are

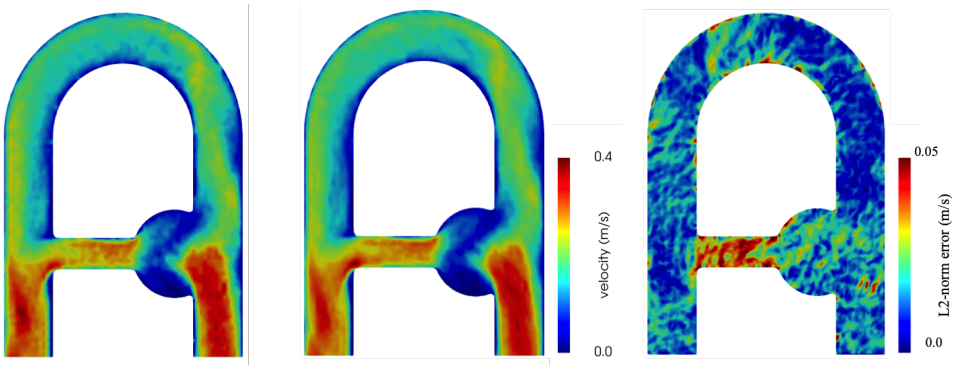

Figure 4.9: Magnitude velocity field at $t/T_p = 0.2\ s$.(left) raw MRI $||\mathbf{u}_{mri}||$, (middle) divergence-free velocity $||\mathbf{u}^0_{mri}||$, (right) L2-norm error defined as: $E_{L2}(\mathbf{x}_i, t^n) = ||\mathbf{u}_{mri}(\mathbf{x}_i, t^n) - \mathbf{u}^0_{mri}(\mathbf{x}_i, t^n)||$

proportional to the gradient slew rate and described by the Faraday's law. They particularly affect the phase image accuracy by creating a non-linear phase offset (even though often assumed linear near the isocentre) [28]. An algorithm based on a method developed in Lorenz et al., (2014) [92] was implemented to correct for their effects on the velocity field in 4D flow images. The main steps are as follows:

1. Given that a prior mask of the noise was performed (see Section 4.4.1), static regions are extracted in the full 3D volume by thresholding the signal magnitude to remove blood flow regions.

2. Slice-wise 2D least-square fit (linear, quadratic, polynomial) of the remaining static velocity map is performed and propagated on the entire image as a global indicator of velocity offset.

3. Each resulting offset velocity fit is subtracted to the original velocity image to correct for eddy current effects

4. The procedure is repeated for each phase in the cycle and for each velocity component.

This approach was implemented and tested for several types of surface fit orders and the results are provided in Figure 4.10. Among all, the second-order fit shows high spatial variations and indeed seems to be very sensitive to the location of the static tissues in the images. For this reason, and as also concluded in Lorenz et al. [92], the first-order fit outperformed the second-order fit at $1.5T$ and should be selected.

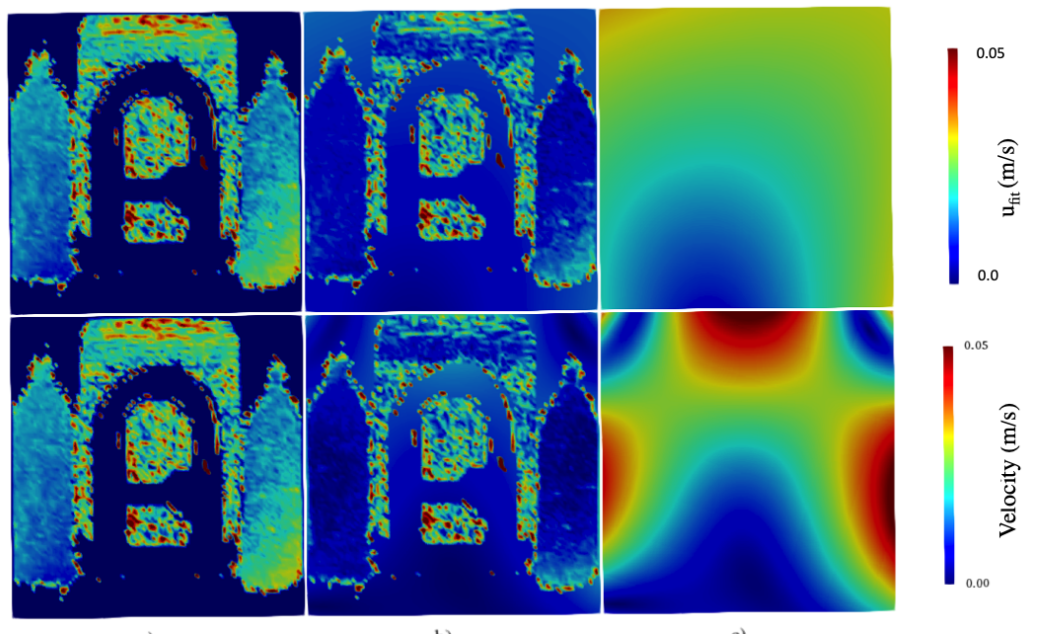

Figure 4.10: Eddy current correction at the middle of the flow phantom. (a).Static region velocity field, (b). velocity field corrected from eddy currents (c). (top) Linear surface fit correction where $u_{fit}(x, y) = ax + by + c$, (bottom) second-order fit where $u_{fit}(x, y) = ax^2 + by^2 + cxy + dx + ey + f$. Note that bottles of water were added to generate additional static regions.

4.4.3 Image registration

As described previously, a main advantage of using 3D printing technique to make the phantom is that the surface approximations caused by the MR image segmentation process are removed. Nevertheless, this method is not completely free of errors since it require to spatially register the real MR images onto the CAD surface model. This process could induce additional errors according to the registration accuracy. An important step in order to minimize this error is to correctly choose the registration algorithm. Image registration algorithms are generally formulated as optimization problems where the aim is to find the geometric transformation matrix M that minimizes the difference between a given metric calculated from the two datasets.

Let us consider that the "reference" dataset (CFD) is fixed in space while the "moving" dataset (MRI) is displaced to match the reference dataset, as illustrated in Figure 4.11. Registering the MRI dataset towards the CFD mesh seems to be a natural choice since the flow phantom position and orientation are specific to each MRI experiment while kept fixed at each CFD simulation. Intensity-based registration algorithms assign metrics to compare intensity patterns between the two dataset and iteratively optimize the orientation of the moving dataset,

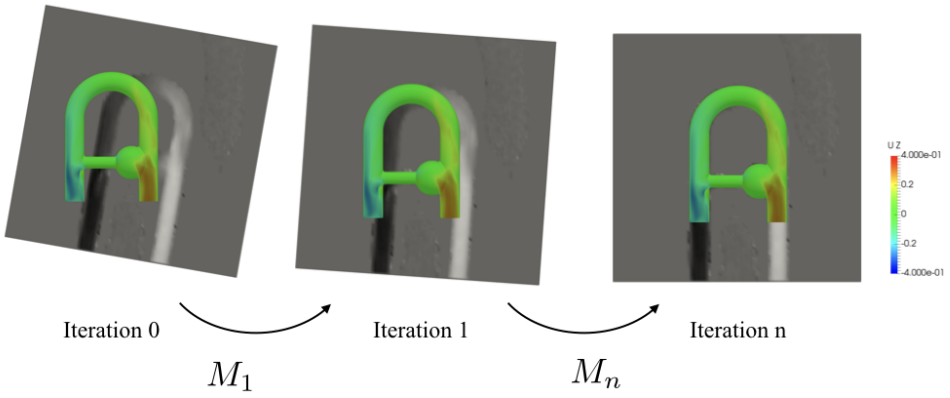

Figure 4.11: Schematic representation of the CFD-MRI registration process.

while feature-based methods find correspondence between features such as points, contours, surfaces, etc. Note also that only linear (rigid) transformations (3 translations and 3 rotations) were authorized since MRI images were rescaled to real world value beforehand (see Section 4.3).

Supposing that $r_i(\mathbf{q})$ is the residual function describing the difference between the moving $f_i(\mathbf{q})$ and reference data g_i at node i, $\mathbf{q} = (q_1, q_2, q_3, q_4, q_5, q_6)$ is the vector containing the 6 transformation parameters (3 rotations + 3 translations). Then the transformation matrix $\boldsymbol{M} = \boldsymbol{TR}$ can be defined as:

$$\begin{aligned} \boldsymbol{T} &= \begin{bmatrix} 1 & 0 & 0 & q_1 \\ 0 & 1 & 0 & q_2 \\ 0 & 0 & 1 & q_3 \\ 0 & 0 & 0 & 1 \end{bmatrix}, \boldsymbol{R_x} = \begin{bmatrix} 1 & 0 & 0 & 0 \\ 0 & \cos(q_4) & \sin(q_4) & 0 \\ 0 & -\sin(q_4) & \cos(q_4) & 0 \\ 0 & 0 & 0 & 1 \end{bmatrix}, \\ \boldsymbol{R_y} &= \begin{bmatrix} \cos(q_5) & 0 & \sin(q_5) & 0 \\ 0 & 1 & 0 & 0 \\ -\sin(q_5) & 0 & \cos(q_5) & 0 \\ 0 & 0 & 0 & 1 \end{bmatrix}, \boldsymbol{R_z} = \begin{bmatrix} \cos(q_6) & \sin(q_6) & 0 & 0 \\ -\sin(q_6) & \cos(q_6) & 0 & 0 \\ 0 & 0 & 1 & 0 \\ 0 & 0 & 0 & 1 \end{bmatrix} \end{aligned} \tag{4.7}$$

where $\mathbf{R} = \mathbf{R_x R_y R_z}$. A commonly adopted cost function is the sum of squared differences, defined as follows:

$$S(\mathbf{q}) = \sum_{i}^{N_{nodes}} r_i^2(\mathbf{q}) \tag{4.8}$$

where $r_i(\mathbf{q}) = f(\mathbf{q}) - g_i$, and N_{nodes} is the number of comparison nodes of the dataset. A straightforward way to minimize the cost function consists in computing either the gradient or the Hessian of the cost function with respect to each of the parameters, to find the steepest descent direction. For the (normalized) descent gradient algorithm, the updated value of the transformation parameters $\mathbf{q}$ at each

iteration is given by:

$$\mathbf{q}^{n+1} = \mathbf{q}^n - \alpha \frac{\nabla_{\mathbf{q}} S(\mathbf{q}^n)}{\|\nabla_{\mathbf{q}} S(\mathbf{q}^n)\|} \tag{4.9}$$

where α is the descent rate arbitrarily set between $\alpha \in [10^{-2}; 10^{-3}]$. The descent gradient algorithm is generally robust but slow to converge. The descent step size α could help increasing the convergence rate but should be kept small to ensure numerical stability. Another way to improve the convergence rate is to compute the Gauss-Newton algorithm defined as:

$$\mathbf{q}^{n+1} = \mathbf{q}^n - \alpha \frac{\boldsymbol{H}_{\boldsymbol{GN}}^{-\mathbf{1}} \nabla_{\mathbf{q}} S(\mathbf{q}^n)}{\|\boldsymbol{H}_{\boldsymbol{GN}}^{-\mathbf{1}} \nabla_{\mathbf{q}} S(\mathbf{q}^n)\|} \tag{4.10}$$

If we define the Jacobian of the residual as the following matrix:

$$(J(\mathbf{q}))_{ij} = \frac{\partial r_i(\mathbf{q})}{\partial q_j} = \frac{\partial f_i(\mathbf{q})}{\partial q_j} \tag{4.11}$$

Then, the gradient of the cost function can be written as:

$$\nabla_{q_j} S(\mathbf{q}) = \frac{\partial S}{\partial q_j} = \sum_{i=1}^{N_{nodes}} r_i(\mathbf{q}) \frac{\partial r_i(\mathbf{q})}{\partial q_j} \tag{4.12}$$

and therefore,

$$\nabla_{\mathbf{q}} S(\mathbf{q}) = J(\mathbf{q})^T \mathbf{r}(\mathbf{q}) \tag{4.13}$$

From Equation 7.1, the Gauss-Newton algorithm takes the following form:

$$\mathbf{q}^{n+1} = \mathbf{q}^n - \alpha (\boldsymbol{J}^T \boldsymbol{J})^{-1} \boldsymbol{J}^T \mathbf{r}(\mathbf{q^n}) \tag{4.14}$$

where $\mathbf{H}_{GN} = \mathbf{J}^T \mathbf{J}$

The main drawback of the Gauss-Newton algorithm resides in the fact that the Hessian matrix can become singular if any column of the Jacobian matrix linearly depend to another.

To minimize the chance of failure of the iteration, a term is added such that $\boldsymbol{H}_{\boldsymbol{LM}} = \lambda diag(H_{GN}) + \boldsymbol{H}_{GN}$; this leads to the Levenberg-Marquardt algorithm. The main advantage of this method is that for low λ, the algorithm converges as fast as Gauss-Newton steps while for high λ, more robust steep descent steps are utilized. In practice no explicit line search is needed for this algorithm. Moreover, the λ coefficient is updated at each iteration such as: if $S(q^{n+1}) < S(q^n)$, $\lambda = 10^{-1}\lambda_{old}$, else: $\lambda = 10\lambda_{old}$.

Intensity-based metrics For automatic registration of medical images, intensity-based approaches are usually accurate, even though less robust notably because of the presence of noise and bias between the datasets [3]. The magnitude velocity

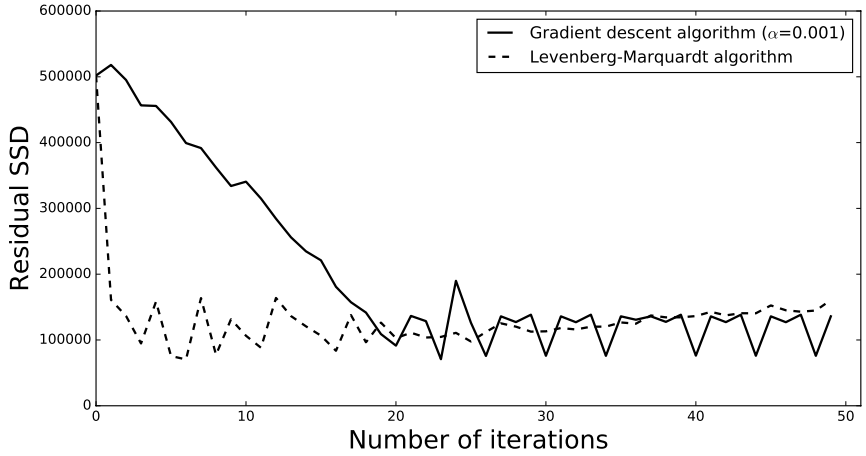

Figure 4.12: Comparison between gradient descent and Levenberg-Marquardt algorithms for registration of two MR images. The Levenberg-Marquardt algorithm generally outerperforms the classical gradient descent in terms of convergence rate due to the second-order derivative of the Hessian. Nevertheless, the gradient descent is generally more robust and stable.

field was used as the registration metric, assuming that both CFD and MRI velocity patterns are sufficiently similar to converge towards an accurate transformation. At the beginning of each iteration, the MRI velocity field was linearly interpolated into the CFD mesh to compute the residual based on similar comparison points. Several tests were computed using the velocity field as registration metrics, varying the step size as well as the initial guess; all these tests generally resulted in non robust results and large errors in the transformation matrix. To illustrate this, one of the computations is presented in Figure 4.12 and reveals, as expected, a faster convergence of the Levenberg-Marquardt algorithm as compared to the descent gradient algorithm. Nevertheless, both algorithms show quite unstable convergence results (with high residual level). This behaviour seems mainly due to the sensitivity of the algorithms to the noise in the velocity images. The relative differences between the two velocity fields can also be responsible for this instabilities.

To conclude, using an intensity-based metric seems generally inadequate to comparing two dataset coming from different imaging modalities.

Feature-based metrics Due to the unsatisfactory results obtained using the magnitude velocity field as metric, an iterative closest point algorithm was tested. In the Iterative Closest Point algorithm, the residual quadratic metric is based on the distance from each of the source point $\mathbf{p}_i$ (MRI) to a reference point $\mathbf{x}_i$ (CFD). As this algorithm compares only surfaces, a preliminary rough segmentation of

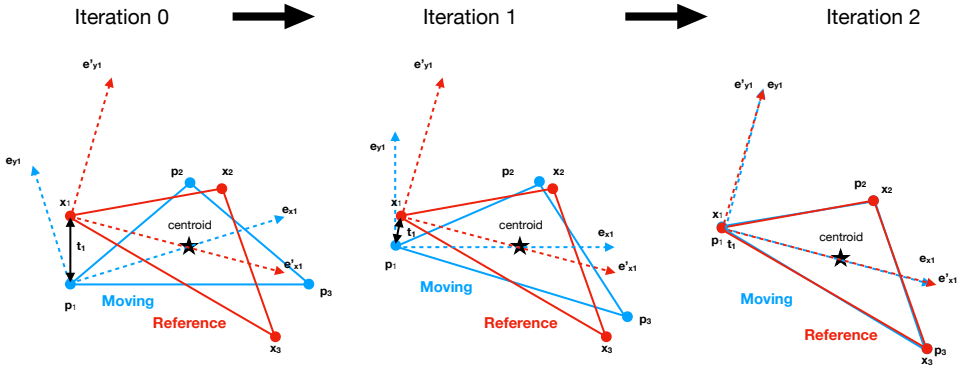

Figure 4.13: Illustration of the Iterative closest Point algorithm procedure. Note that a prior step (not represented here) necessary to form the triad is to juxtapose the centroids of the moving and reference surfaces. Then, an orthonormal triad is formed from each point $\mathbf{p}_i$ of the moving surface, centroid, and the closest point on the reference surface $\mathbf{x}_i$. Another triad is computed by taking the reference surface point as origin instead. A transformation (rotations and translations) matrix is deduced for each couple of points.

the MRI dataset was computed to extract the surface of the flow phantom. This segmentation was computed by thresholding the image magnitude. Given an initial guess of the rigid body transformation (as aligned centroids), the nearest neighbour of each point in the source dataset is calculated. Then, a reference orthonormal triad is constructed from the three reference points (centroid, $\mathbf{p}_i$ and $\mathbf{x}_i$), and the same is done for the source points. A transformation matrix (rotation and translation) is then deduced from the rotations and translations between the two constructed triads. This process is repeated for each points lying on the surfaces. Weights are attributed to pairs of points in order to reject outliers and to better match the final transform (bigger weights to points with small distances from each other). By combination of each point's transformation matrix, a sum of squared distances $S(R,t) = \sum_{i=1}^{N_p} \|\mathbf{x}_i - \mathbf{R}\mathbf{p}_i - \mathbf{t}\|_2^2$ is deduced, where $\boldsymbol{R}$ and $\mathbf{t}$ are the rotation matrix and translation vector describing the transformations between the corresponding points $\mathbf{x}_i$, $\mathbf{p}_i$ of the source and moving models respectively. The optimal transformation matrix is finally iteratively obtained. An illustration of the ICP process is presented in Figure 4.13. More detailed explanations of the method are provided in [71].

The algorithm was tested with the phantom datasets and results are shown in Figure 4.14. In this case, the algorithm converges with order $q = 2.3$ to a mean distance between the two surface below 10^{-6} m. This algorithm was tested in multiple configurations, for multiple MRI datasets, and found to be quite robust as long as the initial rotation does not exceed about $90°$ along each spatial direction.

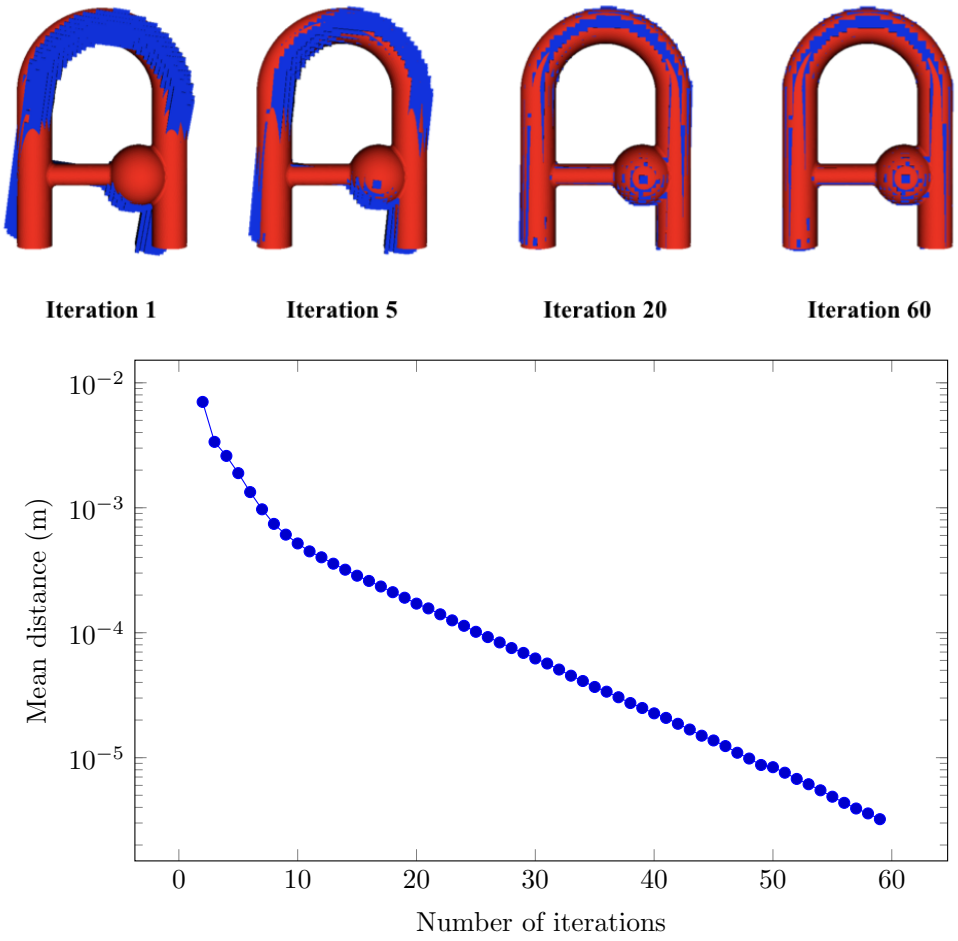

Figure 4.14: Convergence of the ICP algorithm as function of the mean distance between the two surfaces.

4.5 Simulations of the experimental configuration

In this section, the simulation of the flow within the phantom is presented. The simulation set up is detailed, the resulting simulations are shown, and the post-processing steps of the results explained. The sensitivity of the resulting simulations to several parameters is investigated and in order to ensure that the simulation is well-converged.

4.5.1 Simulation setup

The blood-mimicking fluid is modelled as an incompressible Newtonian fluid of kinematic viscosity $\nu = 4.02 \times 10^{-6}\ m^2/s$. A centred fourth-order numerical scheme with an explicit fourth-order Runge-Kutta time advancement scheme was

used to solve the Navier-Stokes equations. The time step was computed in order to ensure that the Courant–Friedrichs–Lewy (CFL) number remains equal to 0.9 for numerical stability. The pressure advancement and divergence-free condition were met thanks to the fractional step algorithm [78] (see Section 3.1.3). A Deflated Preconditioned Conjugate Gradient algorithm was used to solve the associated Poisson equation [97]. The Sigma eddy-viscosity-based LES model [119] was used to account for turbulence effects (see Section 3.1.6). A convective outlet boundary condition was imposed such that:

$$\frac{\partial \mathbf{u}}{\partial t} + U^{conv}\frac{\partial \mathbf{u}}{\partial \mathbf{n}} = 0 \tag{4.15}$$

where $\mathbf{n}$ is the outward normal to the outlet surface, and U^{conv} the convective velocity adjusted in such a way that it meets the global mass conservation of the entire flow domain. All the walls were assumed rigid, consistently with the material selected for manufacturing the phantom, and no-slip boundary condition was prescribed.

The peak systolic Reynolds number is $Re = \frac{2u_{bulk}a}{\nu} = 1830$ where a is the radius of the principal duct and u_{bulk} the averaged inlet velocity. Likewise, the Womersley number characterizing the pulsatility of the flow is $\alpha = R\sqrt{\frac{\omega}{\nu}} = 16.4$, where $\omega = \frac{2\pi}{T}$.

Spatial interpolation of the MRI inflow signal

A pixel-based inflow velocity was derived from 2D cine PC-MRI measurements acquired at the inlet surface of the flow domain (see Section 4.3) and imposed as inlet boundary condition of the simulations. First, the transformation matrix found from the 4D Flow MRI registration was applied to register the 2D PC-MRI measurements to the numerical mesh. This was possible as the two measurements were performed sequentially, with no changes of the phantom's position. Then, a 2D spatial interpolation of the measured 2D PC-MRI velocity field was performed on the corresponding inlet surface of the CFD domain, for each of the $N_p = 32$ frames in the cycle independently. A simple and fast way to interpolate the MRI velocity on the inlet surface nodes is to use a finite element formulation. Each MRI pixel is subdivided into two equivalent triangles and a linear shape function is defined for each triangle. This shape function takes the following form:

$$f_{ij} = \alpha x_i + \beta y_j + \gamma \tag{4.16}$$

where $x_i = x_0 + i\Delta x$ and $y_j = y_0 + j\Delta y$ with x_0, y_0 the coordinates of the lower left pixel. Given the values at the three vertices of the triangle $(f_{i,j}, f_{i,j+1}, f_{i+1,j+1})$,

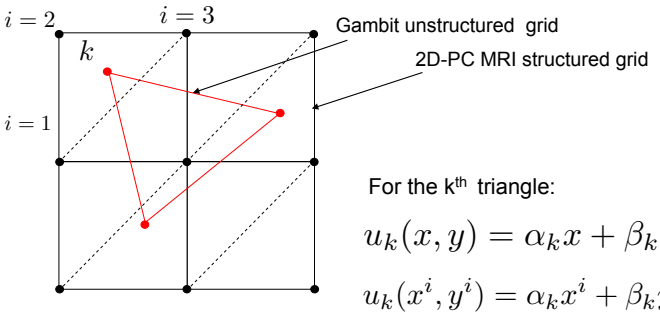

Figure 4.15: Schematic illustration of the pixel-based inlet velocity interpolation procedure.

the coefficients are determined as:

$$\begin{aligned} \alpha &= \frac{f_{i+1,j+1} - f_{i,j+1}}{\Delta x} \\ \beta &= \frac{f_{i,j+1} - f_{i,j}}{\Delta y} \\ \gamma &= f_{ij} - \alpha i \Delta x - \beta j \Delta y \end{aligned} \tag{4.17}$$

The velocity at position x, y can then be estimated from the previous shape function. This approach has the advantage to require low computational effort and to be robust since the values at the interface of each triangle are continuous. An illustration of the interpolation method is presented in Figure 4.15.

Temporal interpolation of the MRI inflow signal

The discrete temporal evolution of the spatially-interpolated signal was then converted into a time-continuous signal by node-wise trigonometric interpolation. A list of $N_k = \lfloor \frac{N_p}{2} \rfloor + 1$ non-redundant complex Fourier coefficients $\hat{\mathbf{u}}_{i,k}$ can be extracted from the interpolated velocities at each $N_p = 32$ phases and for each inlet surface node i, as follows:

$$\hat{\mathbf{u}}_{i,k} = \sum_{n=0}^{N_p - 1} \mathbf{u}_{i,n} e^{-2\pi j k n / N_p} \tag{4.18}$$

where $k \in [0, N_k - 1]$, and $j^2 = -1$. The corresponding continuous input velocity signal can then be retrieved by injecting back the Fourier harmonics coefficients $\hat{\mathbf{u}}_{i,k}$ in a Fourier series expansion of the signal again computed for each node of the inlet surface, such as:

$$\mathbf{u}_i(t) = \sum_{k=0}^{N_k - 1} \hat{\mathbf{u}}_{i,k} e^{2\pi j k t / T} \tag{4.19}$$

where $\mathbf{u}_i(t)$ is the continuous velocity vector function at inlet node i and time t, and T is the period of a cycle. Trigonometric interpolation is well adapted in this

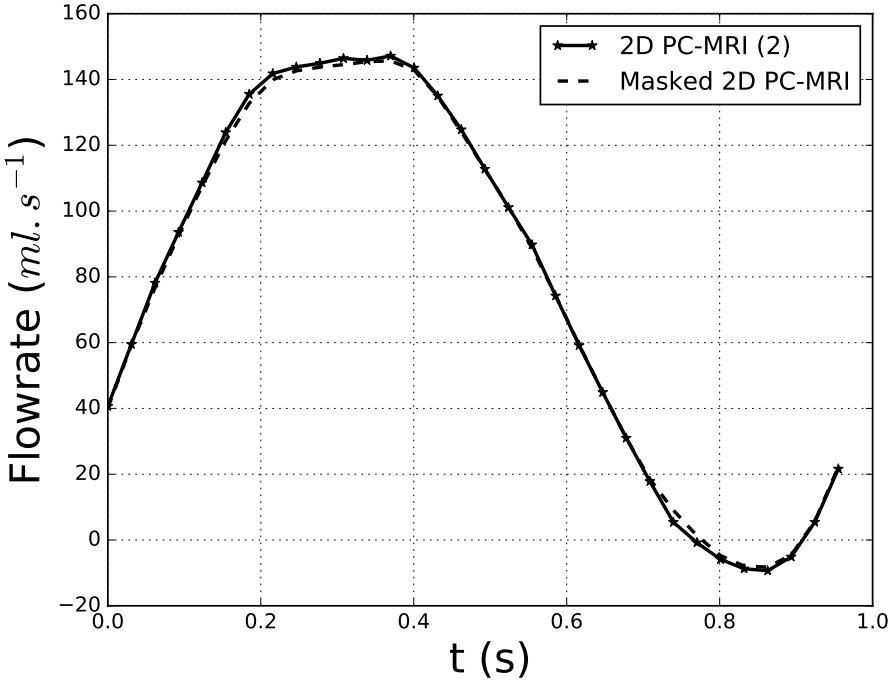

Figure 4.16: Inlet flow waveform prescribed as inlet boundary condition of the simulations. Comparison with the flow rate before spatio-temporal interpolation of the 2D PC-MRI measurement.

case since the signal emitted by the pump is periodic. Moreover, there is no need to compute an interpolation at each iteration since the N_k Fourier coefficients are stored at the initialization of the calculation and injected along the simulation in the analytical expression of the periodic signal, with no control points. This is also valuable since in practice, the time steps are generally not constants.

The effect of interpolation on the resulting inlet flow rate waveform is expected to be negligible, as shown in Fig. 4.16.

4.5.2 Phase-averaging

During a conventional PC-MRI scan, the k-space is progressively filled over hundreds of cycles and pulse sequences are often repeated to increase contrast. For this reason, confronting MRI measurements with instantaneous CFD velocity fields might not be relevant. Moreover, cycle-to-cycle fluctuations may appear for such high Reynolds number unsteady flows [32]. Hence, a proper way to analyse the computed flow is to phase-average the flow velocity over a sufficiently representative amount of cycles [32]. The phase averaged velocity $\overline{\mathbf{u}}(\mathbf{x}, t)$ at spatial

coordinates $\mathbf{x} = (x, y, z)$ and at time t is defined as:

$$\overline{\mathbf{u}}(\mathbf{x}, t) = \frac{1}{N} \sum_{k=0}^{N-1} \mathbf{u}(\mathbf{x}, t + kT) \tag{4.20}$$

where $\mathbf{u}(\mathbf{x}, t)$ refers to instantaneous velocity vector and N the total number of cycles of period T. The phase root-mean square velocity is therefore defined as:

$$\mathbf{u}_{rms}(\mathbf{x}, t) = \sqrt{\overline{\mathbf{u}^2(\mathbf{x}, t)} - \overline{\mathbf{u}(\mathbf{x}, t)}^2} \tag{4.21}$$

4.5.3 Down sampling

Two classical methods may be adopted for comparing CFD to MRI velocity fields on identical grids: the MRI velocity fields can be interpolated on the high resolution CFD grid (termed as HR-CFD), or HR-CFD velocities at nodes localized within a given MRI voxel might be averaged to obtain the corresponding down sampled CFD field, noted low resolution CFD (LR-CFD) [35]. The down sampling process was achieved by linear interpolation of the CFD data on an MRI sub grid where each MRI voxel contained 216 isotropic sub voxels. The resulting down sampled field at each MRI voxel was then calculated as an average of the 216 sub sampled fields. The down sampling process is illustrated in Figure 4.17.

4.5.4 Data convergence

Mesh sensitivity analysis

A mesh sensitivity analysis was performed to ensure the spatial convergence of the computations. Results are reported in Table 4.3. The magnitude of the phase-averaged velocity in the aneurysmal sac results in a numerical uncertainty of 1.88% for the fine mesh, with an apparent spatial order of convergence $p = 2.0$ (see Sigüenza et al. [138] for details). Therefore, the fine mesh ($h = 0.7\ mm$) was considered fine enough for the velocity field to be spatially converged and independent of the spatial resolution.

Phase-averaging sensitivity analysis

A phase-averaging sensitivity analysis was performed to estimate the number of cycles necessary for the phase-averaged velocity field to converge. Beforehand, the first 10 cycles were removed to cancel the effect of the arbitrary initial condition (zero velocity condition). The results presented in Figure 4.18 show that the main components of the velocity (u and w) are well-converged after few cycles (about 5 cycles) while the transverse component of the velocity (v) requires more (about 30 cycles). Since the transverse velocity correlation is expected

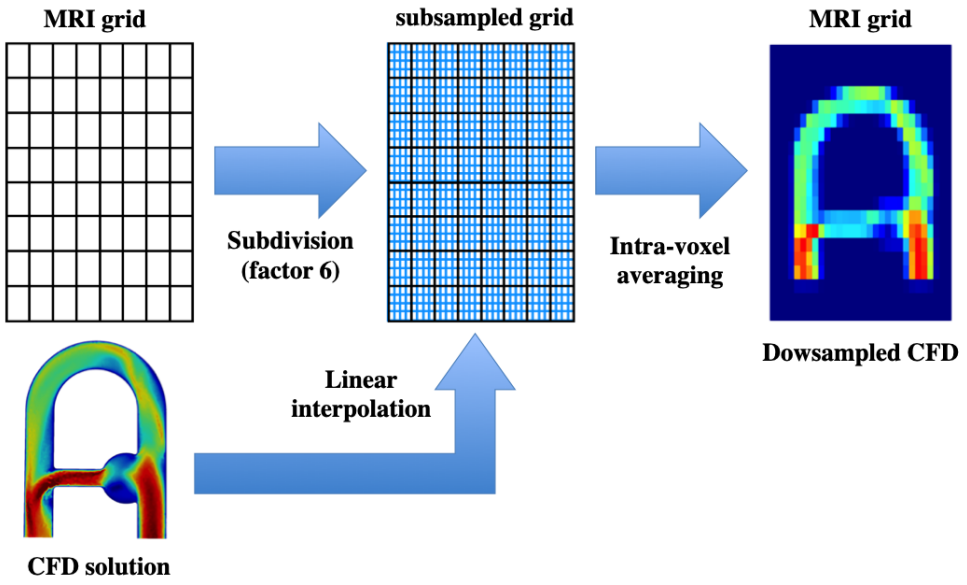

Figure 4.17: Illustration of the down sampling of a CFD velocity field. The MRI grid is first subsampled with 6 voxels in each direction (216 sub-voxels per voxel). The CFD solution is linearly interpolated on the sub sampled grid, and the sub sampled grid is down sampled back to the MRI grid by averaging the velocity over the 216 subvoxels included in each voxel.

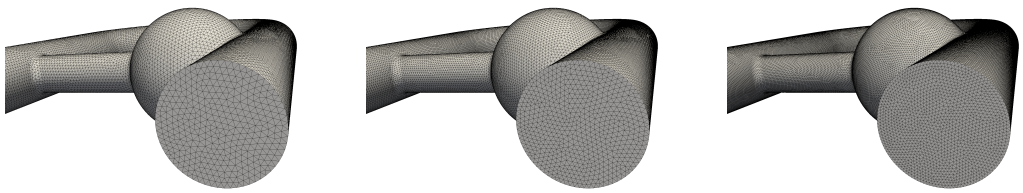

Grid	h (mm)	Cells $\times 10^3$
Coarse	1.3	622
Medium	1.0	1 284
Fine	0.7	3 812

Table 4.3: Properties of meshes used for the sensitivity analysis, as reported in Celik et al. [1]. h corresponds to the representative cell size. The corresponding (left) coarse, (middle) medium and (right) fine meshes are represented above.

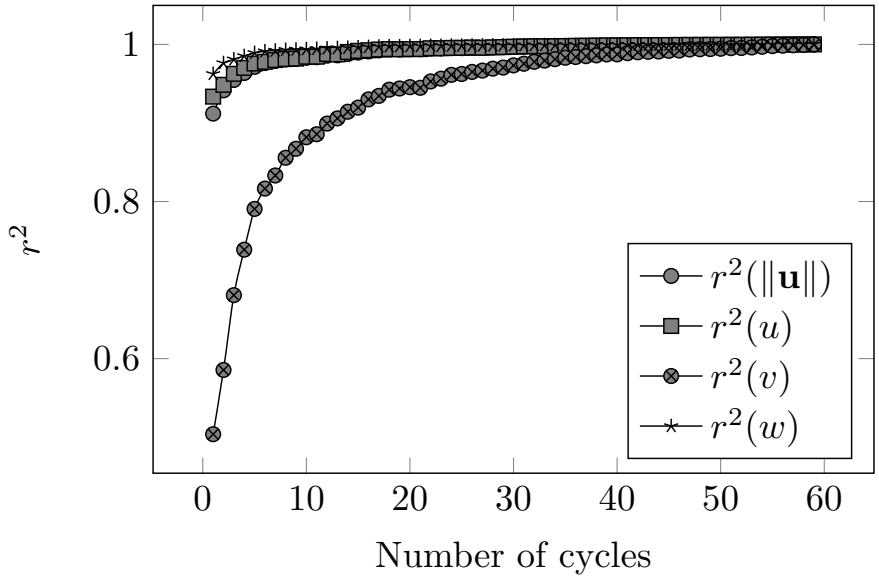

Figure 4.18: Evolution of the Pearson's correlations (r^2) between phase-averaged CFD velocity computed over different numbers of cycles and the 60-cycle phase-averaged CFD velocity. The correlations are performed on each node of the domain.

to be zero by symmetry, it is mostly representative of the velocity fluctuations induced by turbulence, thus justifying the slower convergence rate observed in Figure 4.18. Among the 60 simulated cycles, velocity field was phase-averaged over 30 cycles which was deemed sufficient for v to reach a reasonable asymptotic value. The reproducibility of the phase-averaging process was tested by extracting and independently phase-averaging two subsequent sets of 30 cycles from the 60 cycles simulated. High correlation levels were found ($r^2(u) = 0.995$, $r^2(v) = 0.930$, $r^2(w) = 0.999$ and $r^2(\|\mathbf{u}\|) = 0.997$ where r is the Pearson's correlation coefficient introduced in Sec. 4.6.1), showing that the outcome of the phase-averaging process does not depend on the set of cycles selected.

Whereas phase-averaging over 30 cycles seems enough for the global correlation to converge, a more 'local' sensitivity analysis was performed to ensure the convergence at key sites within the phantom. Three probes were then seeded in the aneurysm, collateral and bend. The magnitude of the velocity field at these locations were recorded at each peak systolic phase during 50 cycles and the cumulative average of the field was computed to track the evolution of the convergence. Results are shown in Figure 4.19. As expected, the highest velocity fluctuations occur in the aneurysm. Moreover, eliminating the first ten cycles to evacuate the initial condition seems sufficient at the sight of the initial velocities. It seems however difficult to discern any cyclic repetition of reproducible patterns.

Therefore, all the velocity fields were phase averaged over 30 cycles and the first

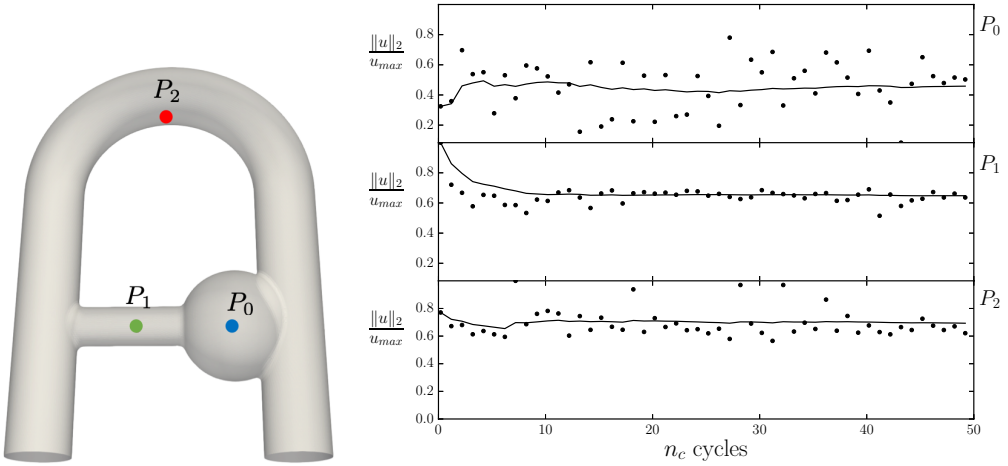

Figure 4.19: **Left** Locations of the probes in the flow phantom. **Right** (black dots) Dimensionless magnitude of the instantaneous velocity at peak systole for the three probes, (solid lines) cumulative average associated. The instantaneous velocity magnitude used to compute the cumulative average at i-th cycle are marked with black dots.

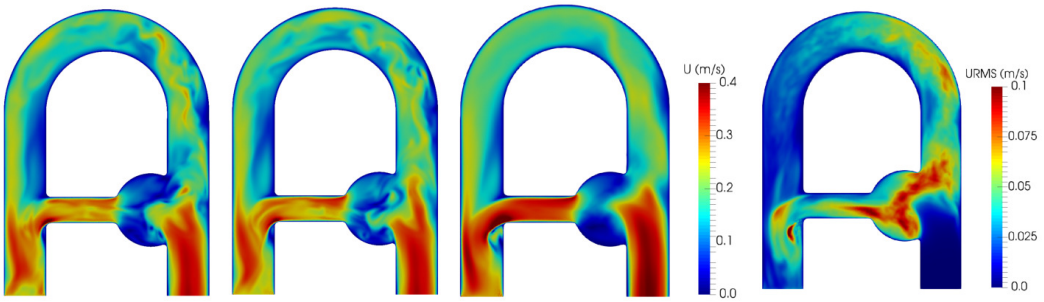

(a) Cycle 20 (b) Cycle 30 (c) Phase averaged (d) Fluctuations

Figure 4.20: Magnitude of the velocity fields in the flow phantom at peak systole for cycle 20 (a), cycle 30 (b), phase-averaged (c). The velocity fluctuations (d) are expressed through $\mathbf{u}_{rms}$. Important cycle-to-cycle fluctuations between the instantaneous fields indicate non reproducible disturbed zones, where turbulence is more likely to appear, while the phase averaged field encompasses dominant flow patterns.

ten cycles were removed. The resulting velocity fluctuations were calculated as the root-mean-square velocity and are presented at peak systole in Figure 4.20. This figure well-illustrates the large velocity variations from one cycle to another, and therefore emphasizes the importance of phase-averaging the velocity to compare with MRI.

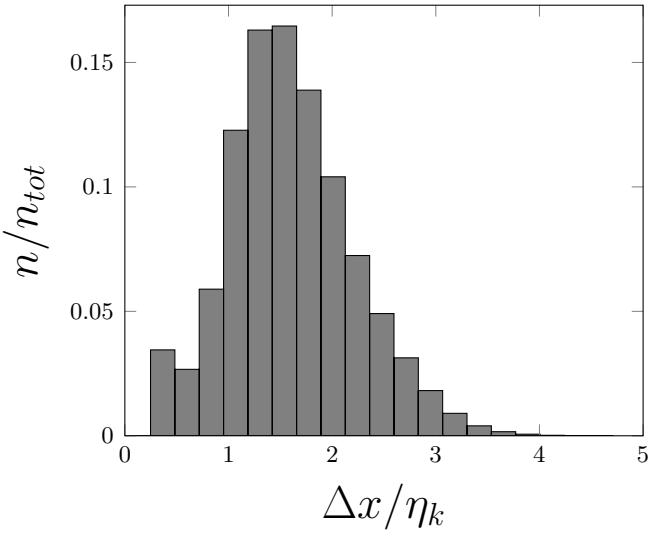

Figure 4.21: Probability density function of the ratio local mesh size over the Kolmogorov length scale where n_{tot} is the total number of mesh nodes.

Indicators of the LES resolution

As detailed in Section 3.1.6, the σ-model was used in the simulations. To assess the turbulence resolution in the simulation, it is necessary to estimate the size of the smallest turbulent structures. According to Kolmogorov's theory, the smallest turbulent length scale (η_k) is universal and reads:

$$\eta_k \equiv \left(\frac{(\nu + \nu_{sgs})^3}{\epsilon} \right)^{1/4} \tag{4.22}$$

where

$$\epsilon = 2(\nu + \nu_{sgs}) S'_{ij} S'_{ij}$$

$$S'_{ij} = \frac{1}{2}\left(\frac{\partial u'_i}{\partial x_j} + \frac{\partial u'_j}{\partial x_i}\right)$$

where ϵ is the dissipation rate and S'_{ij} the symmetric part of the fluctuating strain rate tensor. Under the hypothesis of homogeneous isotropic turbulence, the smallest length scale measured in the simulations equals 1.56×10^{-4} m , while the average scale is about 1.05×10^{-3} m. To this respect, a mesh resolving the entire turbulence spectrum (DNS) would require more than 68 million cells. As specified in Moin and Malesh [112], an acceptable level of spatial resolution for DNS should verify $\Delta x \approx 2\eta_k$, where Δx is the characteristic mesh size. As shown in Figure 4.21, about 30% of the elements in the present simulation are above this limit.

A general measure of the turbulence resolution in LES was proposed by Pope [127]. It considers that for a LES to be well-resolved, at least 80% of the turbulent

kinetic energy should be solved. Formally, this can be written as:

$$M(\mathbf{x},t) = \frac{k_{sgs}(\mathbf{x},t)}{k_{tot}(\mathbf{x},t)} < 0.2 \tag{4.23}$$

where $k_{tot}(\mathbf{x},t) = k_{sgs}(\mathbf{x},t) + k_{res}(\mathbf{x},t)$ is the total turbulent kinetic energy, a sum of k_{sgs} the turbulent kinetic energy of the unresolved scales and k_{res} the turbulent kinetic energy of the resolved eddies. k_{res} is defined as:

$$k_{res}(\mathbf{x},t) = \frac{1}{2}\mathbf{u}_i' \cdot \mathbf{u}_i' \tag{4.24}$$

As the he subgrid scale kinetic energy is not explicitly calculated in this LES, k_{sgs} should be estimated. The following estimate was proposed by Yoshizawa and Horitu [169]:

$$k_{sgs}(\mathbf{x},t) = \frac{\nu_{sgs}^2}{(C\Delta)^2} \tag{4.25}$$

where $C \approx 0.1$.

Another formulation derived by Pope [127] estimates the Pope criterion as:

$$\frac{k_{sgs}}{k_{tot}} \approx \frac{3C}{2}\left(\frac{\Delta}{\pi L}\right)^{2/3} \tag{4.26}$$

where L is the characteristic length of the largest structures ($L \equiv \left(\frac{k_{tot}^{3/2}}{\epsilon}\right)$), $C = 1.5$. As shown in Figure 4.22, about 5% of the nodes show turbulence resolution superior to 20%. As expected, the highest ratio of unresolved turbulent kinetic energy arise at phase 5 (peak sytole), when the Reynolds number reaches its maximum. These unresolved scales are mainly located at the inlet and outlet of the collateral branch, where high fluctuating velocity gradients are induced by the geometric singularities and the jet.

Another simulation was performed with a finer mesh (27 million instead of 3.8 millions cells) for which the Pope criterion was satisfied ($M < 0.2$ for all the nodes). The turbulent viscosity ratio $\frac{\nu_{sgs}}{\nu}$ associated with the two meshes are shown in Figure 4.23. For the reference mesh (3.8 million elements), the level of SGS viscosity ratio observed is generally quite low (less than 20%) and viscosity is added mainly in the aneurysm, and in the jet outflows the collateral branch. For the refined simulation, almost no viscosity is added. The phase-averaged velocity relative error between the two simulations equals 0.8% of the maximum velocity. Given the small gain associated with this mesh refinement, we considered the reference simulation with the 3.8 million element mesh as sufficiently well resolved to estimate the velocity with accuracy.

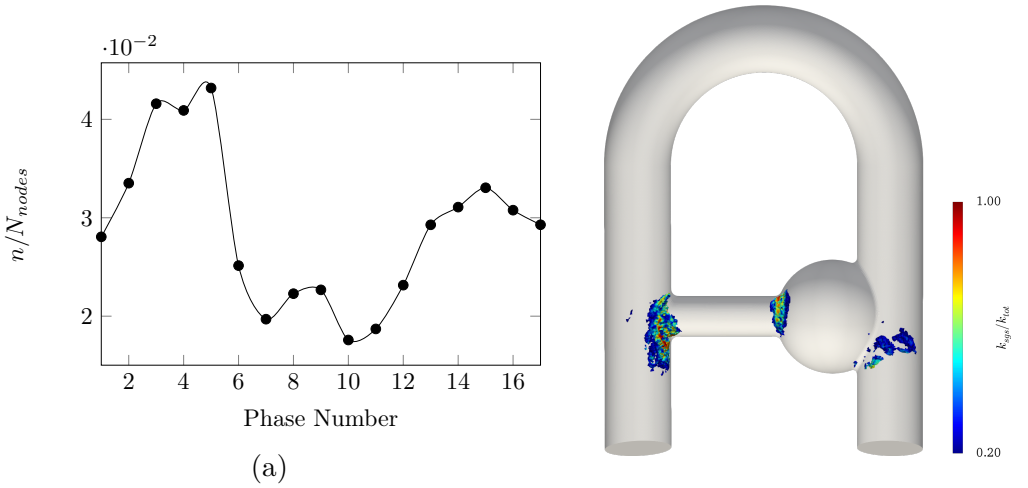

(a) (b)

Figure 4.22: a). Temporal evolution along a cycle of the node fraction verifying $M > 0.2$. b) Volume rendering of the sites where $M > 0.2$ at phase 5.

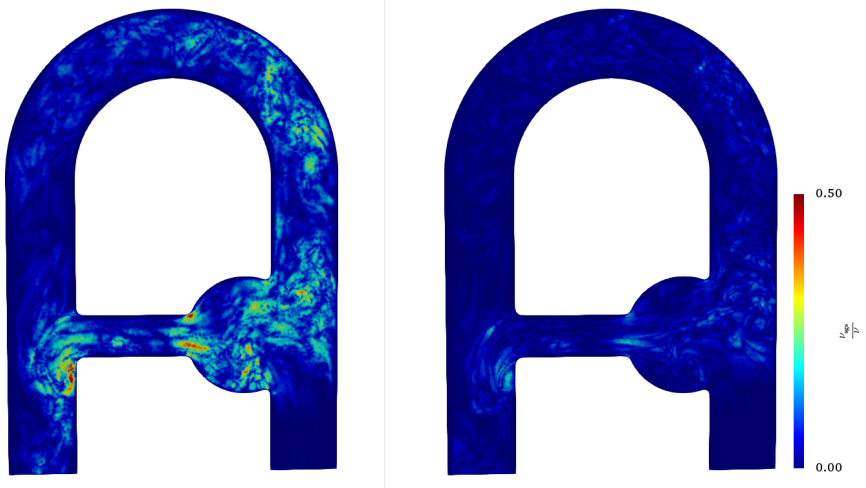

Figure 4.23: Eddy viscosity ratio at peak systole ($t/T_p = 0.25$) interpolated on the xz-middle plane of the phantom. Comparison between **left** the reference mesh (3.8 million elements) and **right** 27 million element mesh.

4.5.5 Results of the simulations

Figure 4.24 shows the 3D magnitude vorticity field computed from the phase-averaged velocity field at different instants in the cycle. At $t/T_p = 0.04$, initially regurgitant flow in the collateral vessel is convected by the entering flow, and starts changing direction. At $t/T_p = 0.2$, the flow structure entering the main branch induces a counter-clockwise rotating motion of the fluid particles located in the aneurysm. At $t/T_p = 0.36$ (end of the peak systole), the inflow acceleration stops, and the flow trajectory in the main branch near the inlet surface is deviated by the rotating motion in the collateral branch. This creates a detached flow structure that persists during the next phases in the main branch upstream of the bend. Also, a jet with small rotating structures is formed at the junction between the collateral outlet and the main branch. At phase $t/T_p = 0.52$, the jet extends and a mixing layer appears due to the differential velocity directions between the collateral and main branch flows. A focus on the jet flow streamlines at the collateral outlet elbow is presented in Figure 4.26. As the jet flows out the collateral branch towards a cross directional flow that comes from an upper location in the main branch, this latter deflects its trajectory and circumvent the collateral jet. As a consequence, the separated principal flow reattaches in the stagnation zone right under the jet, symmetrically on both sides of the pipe. Additionally, counter-rotating vortices are created due to the stagnation zone produced by the local momentum increase of the jet. The-jet-in-cross flow is typical of the patterns observed in Mendez et Nicoud [107].

Note also the existence of a detached structure in the pipe bend, due to the centrifugal forces pushing the flow towards the outer wall and inducing counter-rotating vortices located near the inner wall. These vortices are expected and are described in Section 3.2.2. A closer look of these vortices (and the cycle-to-cycle variations associated) is provided in Figure 4.25. As expected, a stagnation zone close to the concave wall is observed and Dean vortices are formed near the inner wall. At $t/T_p = 0.73$ and $t/T_p = 0.9$, only the flow in the collateral branch regurgitates due to the negative inlet flowrate. The flow in the bend does not change significantly its direction, since the total pressure loss necessary to move this fluid column would be higher than in the collateral branch.

Figure 4.27 shows maps of the phase-averaged velocity vectors in the middle plane of the aneurysm. The vectors are scaled by the magnitude of the phase-averaged velocity at each time. At $t/T_p = 0.2$, the entering flow structure in the main branch detaches and starts expanding in the aneurysm. The z-component of the velocity structure confers its counter-clockwise rotative motion to the flow in the aneurysm. A high pressure gradient appears at the entrance of the collateral due to the increase of the flow rate (mass conservation), and is amplified by the sudden cross-sectional narrowing until the peak systole (at $t/T_p = 0.36$). At

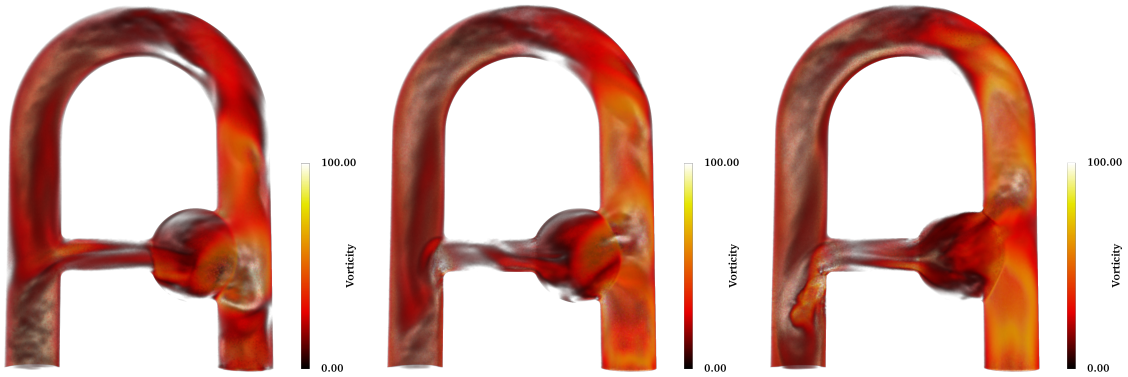

(a) $t/Tp = 0.04$ (b) $t/Tp = 0.2$ (c) $t/Tp = 0.36$

(d) $t/Tp = 0.52$ (e) $t/Tp = 0.73$ (f) $t/Tp = 0.89$

Figure 4.24: Dimensionless volumetric maps of vorticity magnitude of the phase-averaged velocity fields at different phases of the simulation.

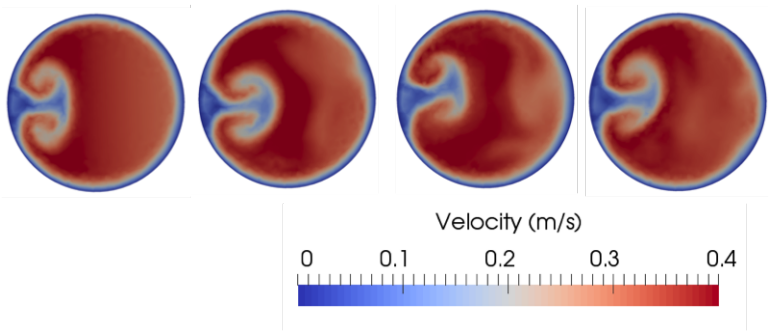

Figure 4.25: Axial velocity field in the pipe section at the middle of the bend at 4 consecutive cycles. Given that $R_c = 50\ cm$, $r = 26\ mm$ and $Re_{mean} = 1000$, a flow with a Dean number $D = 613$ is expected.

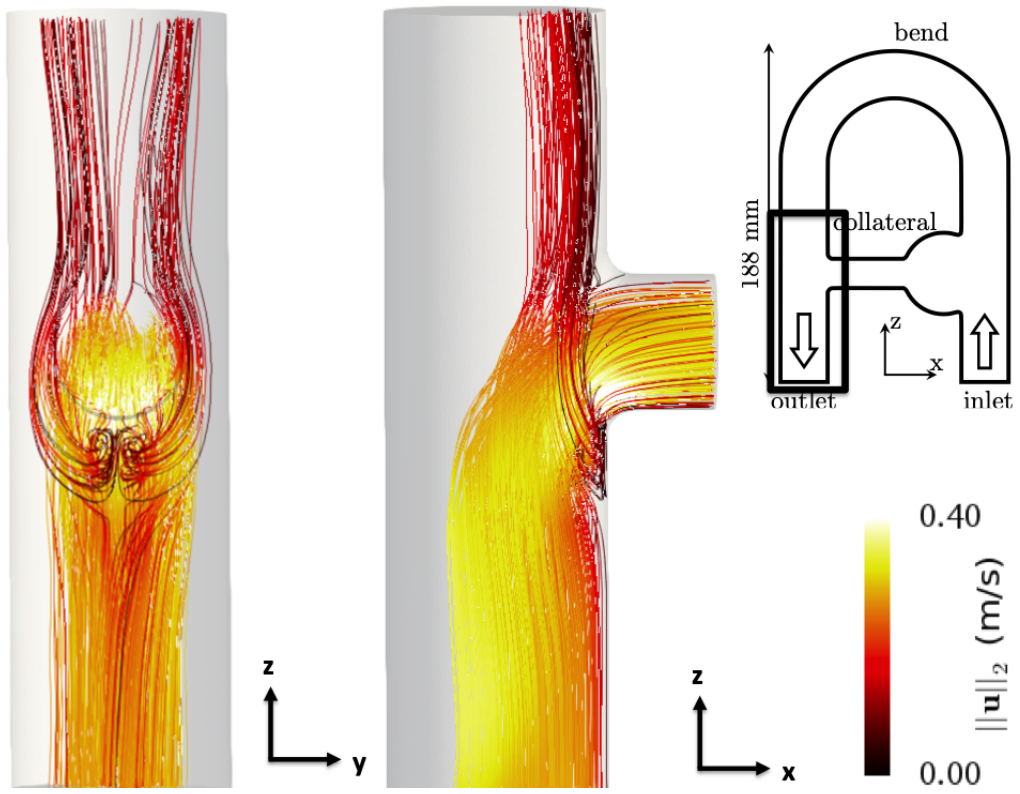

Figure 4.26: 3D phase-averaged velocity streamlines (magnitude) at the junction between collateral outlet and main branch. **Top** YZ-plane view and **bottom** XY-plane view.

$t/T_p = 0.52$ when the inflow starts decelerating, the flow impacts the aneurysm neck (upper zone). This impingement zone is characteristic of about 20% of the aneurysms, and the velocity structure associated could be classified into type 1 patterns as proposed by Cebral et al. [27]. At $t/T_p = 0.73$, when the inlet flowrate is close to zero, the collateral flow regurgitates into the lower part of the aneurysm (close to the inlet), which was a stagnation zone at peak systole. As the collateral flow regurgitation intensifies, a jet is convected towards the centre of the aneurysm and two distinct stagnation zones appear. The flow pattern is now typical of the separation zones raised in structures of type 3 [27]. This configuration therefore seems to adequately reproduce the large variety of flow structures generally observed in aneurysms. Another primordial feature of this configuration which was not treated here is the pressure distribution into the two branches: it will be discussed in the next chapter.

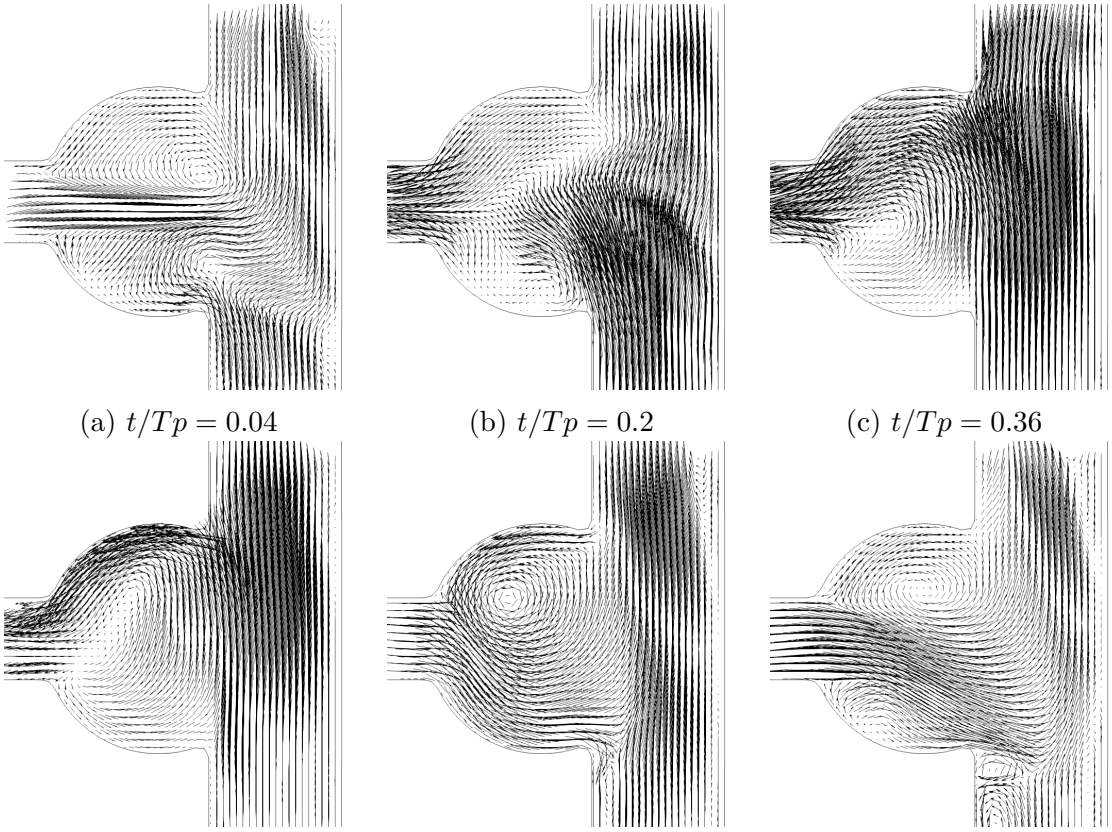

(a) $t/Tp = 0.04$ (b) $t/Tp = 0.2$ (c) $t/Tp = 0.36$

(d) $t/Tp = 0.52$ (e) $t/Tp = 0.73$ (f) $t/Tp = 0.89$

Figure 4.27: Phase-averaged velocity vectors in the middle plane of the aneurysm at different instants in the cycle.

4.6 Baseline comparison: proof of concept of the methodology

In this section, we compare the CFD velocity field with the 2 mm isotropic spatial resolution 4D PC-MRI measurements described in the previous Section 4.3. A quantitative analysis of the differences is performed with different levels of post-processing of the two modalities to investigate the discrepancies induced by a straightforward comparison. A generic comparison protocol is then proposed to systematically correct for these sources of discrepancies.

4.6.1 Pearson's correlation

The Pearson's product moment correlation is often used as a metric to compare two independent modalities. It indicates the affine relation that exists between a variable x and a variable y. It is defined as the ratio of their covariance σ_{xy} by

the product of their standard deviations $\sigma_x \sigma_y$, as:

$$r = \frac{\sigma_{xy}}{\sigma_x \sigma_y} \tag{4.27}$$

where $\sigma_x = \sqrt{\frac{1}{N}\sum_{i=1}^{N}(x_i - \overline{x})^2}$ and $\sigma_{xy} = \frac{1}{N}\sum_{i=1}^{N}(x_i - \overline{x}) \cdot (y_i - \overline{y})$ are the standard deviation of x and covariance of (x, y) respectively. The resulting r ranges in $[-1, 1]$. While it does not indicate the sign of the linearity, it is more common to see r^2 rather than r as it ranges in $[0, 1]$. Two variables with $r^2 = 0$ are uncorrelated while a perfectly linear relation would result in $r^2 = 1$. Given that u_1 and u_2 are the MRI and CFD velocity components, one can reformulate the Pearson's correlation as:

$$r = \frac{\overline{(u_1 - \overline{u_1})(u_2 - \overline{u_2})}}{\sqrt{\overline{(u_1 - \overline{u_2})^2}}\sqrt{\overline{(u_2 - \overline{u_2})^2}}} \tag{4.28}$$

By decomposing of the velocity in a mean and fluctuating part ($u = \overline{u} + u'$), it follows that:

$$r = \frac{\overline{u_1' u_2'}}{\sqrt{\overline{u_1'^2}}\sqrt{\overline{u_1'^2}}} \tag{4.29}$$

where $\overline{u'} = 0$. Written in this form, it represents the covariance normalized by the rms values of u_1 and u_2. It is important to differentiate the spatial deviations associated the average velocity over the entire domain at a given phase, and the temporal fluctuations from the phase-averaged velocity at a given node, as illustrated previously in Figure 4.20.

4.6.2 Qualitative comparison

In Figure 4.28 the HR-CFD phase averaged velocity field is first qualitatively compared with MRI velocity data with corrected phase offsets (i.e: noise masking and eddy currents) in the in-plane direction (foot-head and right-left) at several phases during the cycle. Magnitude velocity maps reveal excellent agreements and show highly similar velocity patterns even in complex flow regions, such as in the aneurysm. For instance, both MRI and CFD capture the small separation region in the main branch at early systole (Figure 4.28a), as well as the recirculation in the aneurysm or the back flow in the bifurcation at late diastole (Figure 4.28c).

Through-plane (antero-posterior) velocity comparison shows larger visual discrepancies (Figure 4.28g-i). This was expected given the low signal amplitudes ($v \in [-5, 5]$ cm/s) with respect to the VENC (50 cm/s).

In addition, the length of the jet issued from the collateral segment appears smaller in the MRI at peak systole. In this region, the MRI does not seem to capture the mixing layer as well as CFD does. A misregistration artifact due to the

unavoidable time delays that exist between different velocity encoding directions (see Section 2.9.1) could be responsible for these distortions, as described in Steinman et al. [146]. In practice, for the 2 mm voxel-size acquisition, a time delay of 12.5 ms was measured between u and w. This corresponds to the time needed for a flow structure in the jet issued by the collateral to travel through approximately 2 voxels at 0.3 m/s. Note that the diameter of the collateral branch contains 8 voxels.

The corresponding velocity error were computed at each node and for each velocity component independently as $\epsilon_i = \sqrt{(u_{CFD,i} - u_{MRI,i})^2}$, where u_i represents the i-th velocity component. The resulting errors maps are presented in Figure 4.29. One can observe in Figure 4.29d) that a large right-left velocity u error pattern is located between the aneurysm and collateral branch inlet at early systole. A closer look onto the root-mean-square velocity map at this particular phase reveals that it coincides with the site of highest cycle-to-cycle fluctuations. Moreover, as shown in Figure 4.29b), the highest velocity error levels are located in the recirculation region under the collateral branch outlet elbow and at peak systole (see Figure 4.26. This region corresponds to the site of highest convective acceleration where small rotating structures are formed (see Figure 4.26). An explanation is that eddies smaller than the voxel size should produce intravoxel phase dispersion due to the vector summation of the spins different velocity vector directions within a voxel [12]. On the contrary, a better agreement is found in the regions where velocity gradients are small. Down sampling the CFD to PC-MRI spatial resolution should reduce the errors associated as it mimics the intravoxel spin velocity averaging process inherent to PC-MRI.

Time evolution and flow profiles comparison

Figure 4.30 compares the temporal evolution of flow rate and peak velocity in the collateral segment measured by MRI with HR-CFD predictions. Excellent agreement is found for both the flow rate and the peak velocity evolution between CFD, 2D PC-MRI and 4D Flow MRI.

4.6.3 Quantitative comparison

A statistical analysis of the velocity differences observed between the low resolution CFD (LR-CFD) and 4D Flow MRI at peak systole is presented in Figure 4.31. An excellent correlation was found for the main velocity component along z-axis. As observed qualitatively in the previous section, the in-plane velocity components (u and w) yield better correlations than the through-plane component (v).

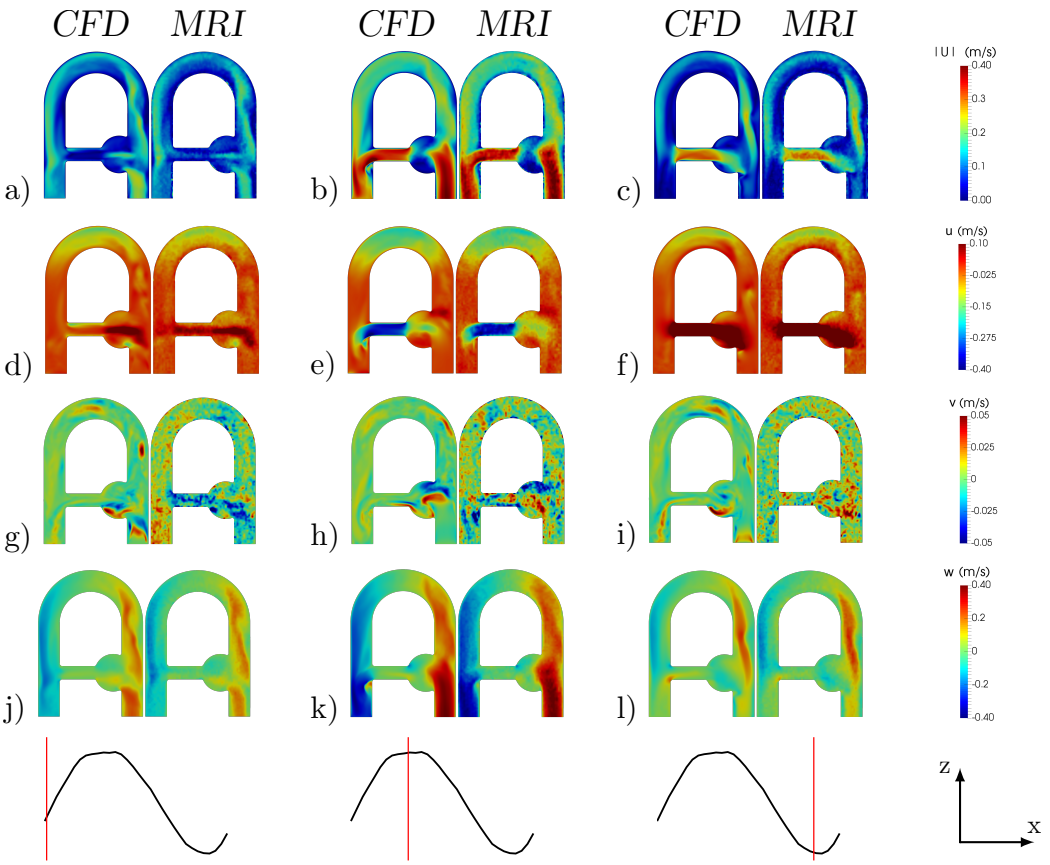

Figure 4.28: Comparison in the coronal plane of HR-CFD velocity fields with MRI measurements at 2 mm resolution at different instants of the cycle. First row represents the velocity magnitude, while second, third and last rows depict right-left (u), up-down (v) and foot-head (w) velocity components respectively. The corresponding instant of the inlet flow rate evolution is represented below as title of indication (see Fig. 4.16).

Influence of the processing on the correlation

To better understand the impact and influence of each processing step on the final comparison, statistical analyses were performed for various processing levels as defined in Table 4.4. Note that only the velocity magnitude correlation results are reported, as a global indicator of the three velocity components.

The first striking result is the low correlation between raw MRI data and the instantaneous high-resolution CFD results (case 1). Note that the 63% correlation was obtained by imposing the measured velocity profile at the inlet of the computational domain as obtained by 2D cine PC-MRI. However, an approach often adopted in the literature consists in applying an idealized velocity profile (flat or parabolic) with the same integral as the actual measured profile. This approach was tested and resulted in even worse correlations, with only $r^2 = 0.58$.

Results in Table 4.4 also show that main correlation improvements are obtained either by down sampling the phase-averaged CFD field or by correcting for the phase offset artifacts (i.e: noise masking and eddy currents). Note that the low correlation between raw MRI and the LR-CFD is mainly due to the impact of the noise surrounding the flow phantom in the MRI measurements and affecting the points located on the wall surface. In LR-CFD, about 35% of the points are located on the surface (only 13% in HR-CFD). The noise is then masked between case 3 and 6, producing a significant improvement of the correlations. Finally, the range of variations of the correlation coefficient over the last row of Table 4.4 (0.89-0.97) shows the importance of degrading the CFD prediction to match the MRI spatial resolution and temporal sampling. The gain obtained by degrading the CFD data is not negligible, yet smaller, compared to the improvement generated by processing, denoising and correcting the raw MRI data (which improves the correlation from 63 % to 89 %, see first column of Table 4.4).

$r^2_{\|\mathbf{u}\|}$	inst HR-CFD	HR-CFD	LR-CFD
Raw MRI	0.63 (1)	0.67 (2)	0.21 (3)
Phase offset corr.	0.81 (4)	0.85 (5)	0.85 (6)
$\mathbf{u}_{wall} = 0$	0.89 (7)	0.92 (8)	0.96 (9)
$\nabla \cdot \mathbf{u} = 0$	0.89 (10)	0.93 (11)	0.97 (12)

Table 4.4: Evolution of Pearson's product moment correlation ($r^2_{\|\mathbf{u}\|}$) for the velocity magnitude at peak systole, as a function of the level of post-processing. "inst HR-CFD" stands for the instantaneous high resolution CFD velocity field of the 30th computed cycle. "HR-CFD" corresponds to the phase-averaged CFD field and "LR-CFD" to the phase-averaged velocity down sampled to the MRI spatial resolution. "Phase offset corr." corresponds to the raw MRI dataset corrected from eddy currents and noise artifacts. "$\mathbf{u}_{wall} = 0$" refers to the corrected MRI dataset where a no-slip boundary condition is applied at walls and "$\nabla \cdot \mathbf{u} = 0$" refers to the resulting MRI velocity field modified to meet the divergence-free condition. Each comparison case is denoted with a superscript number between brackets to ease the discussion. Note that the qualitative comparison shown in Fig. 4.28 represents the case (5).

4.7 Influence of the spatial resolution

Figure 4.32 compares the temporal evolution of the flow rate and peak velocity in the collateral segment at different spatial resolutions. Regardless of the spatial resolution, the MRI measurements seem to well-predict the flow rates. Being an integrated quantity, the flow split is not sensitive to local errors such as the near-wall noise. Results show that enforcing a zero velocity at boundary walls

seems adapted for computing the velocity gradient and that the latter is also very sensitive to the spatial resolution. The peak axial velocity in the collateral also agree very well for all the spatial resolutions although at $t = 0$ only the 3.1 mm measurement matches with the CFD results for unexplained reasons.

The situation is not as favourable when considering velocity profiles in the middle of the bend, as shown in Figure 4.33. Results indicate that PC-MRI velocity tends to underestimate the HR-CFD profile mainly where high velocity gradients occur. On the contrary, a better agreement is found in the regions where velocity gradients are small. Note that the MRI dataset without near-wall velocity masking was willingly presented here to highlight the significant discrepancies raised close to the walls due to partial volume effects. As an illustration, the mean relative error spans from $\varepsilon = 17.3\%$ without to $\varepsilon = 14.4\%$ with near-wall velocity masking.

4.8 Conclusion

In this chapter, we developed a CFD-based procedure for assessing the quality of 4D Flow MRI measurements. A proof-of-concept workflow for mutual validation of MRI and CFD under well controlled and idealized conditions was first established. The results obtained for the idealized flow clearly highlight that some discrepancies remain even after errors associated with boundary conditions, numerics, or turbulence modelling are minimized in the CFD part. Indeed, we noted that a straightforward comparison of the two modalities only produces a very poor agreement ($r^2_{|\mathbf{u}\|} = 0.63$). Some post-processing corrections were thus proposed, that drastically increased the velocity correlations ($r^2_{|\mathbf{u}\|} = 0.97$). To this respect, post-processing of PC-MRI dataset such as correcting phase-offset errors and near-wall velocity masking produces a more realistic output and better matches with the CFD outcome. Moreover, forcing the flow to meet the incompressibility constraint and imposing a zero velocity at the boundary walls is an efficient way of correcting the non-physical noise present in the measurement. As for imaging data post-processing, some CFD downgrading are required to match the MRI spatio-temporal resolution, and therefore improve the correlation. Phase-averaging of velocity fields produces a mean representation of the flow which is suitable to match the MRI data acquisition process. Down sampling CFD velocity fields allows to mimic the acquisition of PC-MRI signal, and leads to a consistent comparison.

These results prove that in a well-controlled environment with suitable prior processing, both MRI measurements and CFD predictions bring trustworthy and equivalent global flow quantities. Moreover, this validation work is essential to consider the CFD solution as a reference flow for evaluating the accuracy which

can be expected in clinical routine, when using time-restrained low-resolution MRI protocols to assess an hemodynamic outcome. Indeed, this framework might further be used to estimate the level of confidence that the MRI signal can guarantee as a function of the MRI input settings. For instance, if the MRI signal agrees locally well with HR-CFD, one could assume that some flow-sensitive hemodynamic variables such as WSS might be reasonable estimated. On the contrary, a MRI signal providing only global flow information might be reliable in terms of flow split but not for direct estimation of local and sensitive quantities like the WSS.

Nevertheless, several discrepancies were not corrected, and some limitations remain. Poor correlations due to a low Velocity-to-Noise ratio (VNR) in the y-component of the velocity v were noticed. This may be bypassed by using multiple VENC based on several flow acquisitions with phase wraps correction using phase unwrapping [88]. Moreover, MRI temporal delays between different velocity encoding direction systematically raise misregistration artifacts. Reducing the echo time decreases this delay and thus could mitigate the velocity error associated. Another possibility is to use non interleaved velocity encoding sequences [66]. As well, acceleration-induced artifacts induced by the neglecting of second and higher order motions in the signal phase expression most probably impacts the flow at sites where accelerated flows occur. Moreover, tripolar acceleration-encoding gradient sequences could be used to measure the acceleration field and therefore reduce this offset [15]. This however leads to highly prohibitive acquisition times. Post-processing corrections are also possible to correct the velocity errors raised [152]. It was also observed that the largest velocity differences are mainly located where CFD yields fluctuating velocities. As already discussed, this could be explained by the signal loss due to intravoxel dephasing. In order to quantify these remaining divergences, one could estimate the amount of PC-MRI subvoxel velocity fluctuations by deriving the intravoxel velocity standard deviation from two signal measurements with different first moment gradients [45]. Additionally, partial k-space filling or parallel imaging such as GRAPPA or SENSE technologies should reduce the acquisition time, while decreasing the SNR. To improve the agreement, one could also take part of the phase images noise into account by considering the theoretical Rician distribution of the noise in the CFD velocity field [63].

As the present analysis was limited to in-vitro idealized flow conditions, several in-vivo features were not discussed and would certainly produce very different outcomes. For example, considering non-rigid walls would either require a dynamic assessment of the wall position during the cardiac cycle or an a priori knowledge of the mechanical properties of the walls to account for the fluid-structure interaction in the simulations. The velocity patterns should be significantly affected and

the velocity errors would certainly increase. Although the blood-mimicking fluid used in the experiment is Newtonian, modelling blood rheology under in vivo conditions is still very challenging.

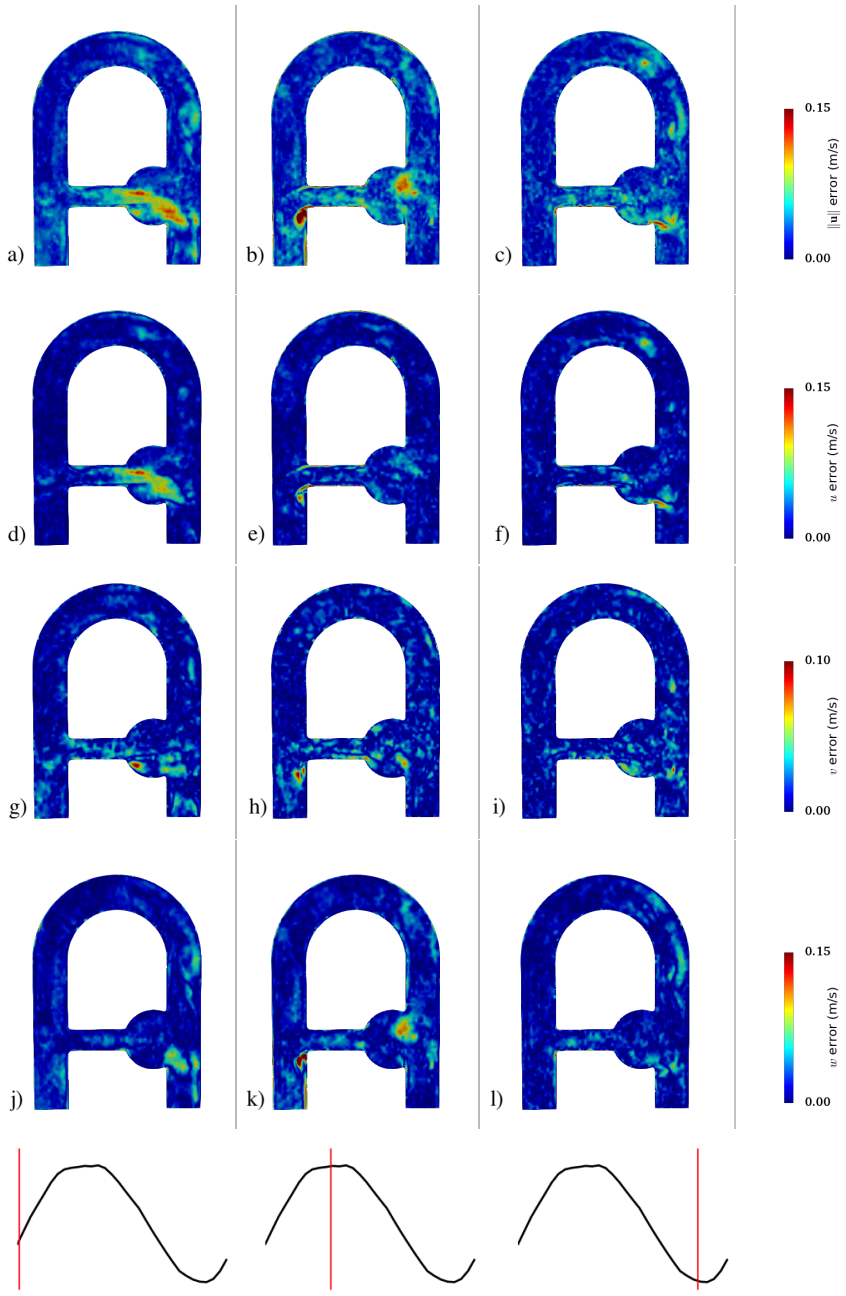

Figure 4.29: Comparison of the velocity errors corresponding to the comparisons shown in Fig. 4.28. The error of the i-th velocity component is calculated as: $\epsilon_i = \sqrt{(u_{CFD,i} - u_{MRI,i})^2}$. First row represents the velocity magnitude, while second, third and last rows depict right-left (u), up-down (v) and foot-head (w) velocity components respectively.

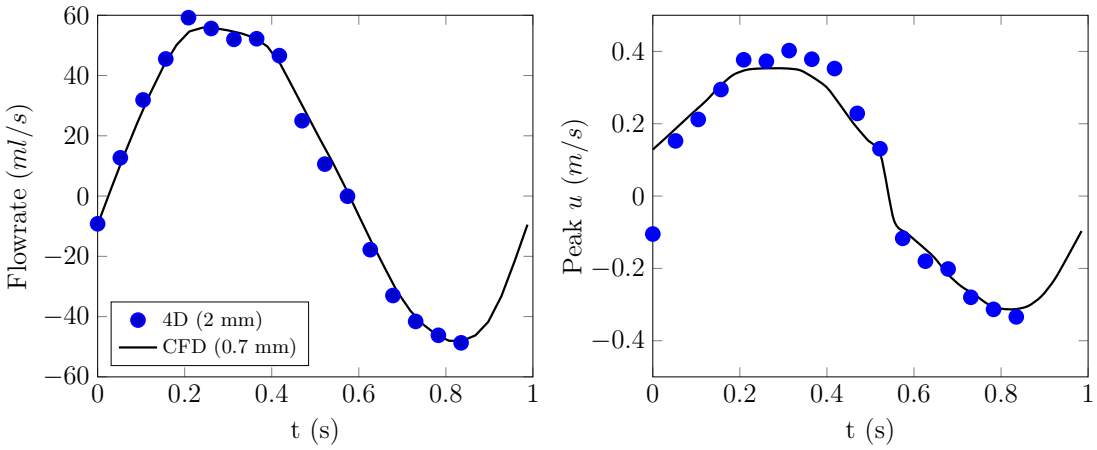

Figure 4.30: **left** Flowrate and **right** peak axial velocity evolution over one cycle in the collateral branch.

Velocity	u	v	w	$\|\mathbf{u}\|$
Mean differences (cm/s)	-0.09	-0.08	0.27	-0.39
Standard deviation (cm/s)	2.07	1.99	2.48	2.54
r^2 coefficient	0.93	0.29	**0.98**	0.95
Slope	0.97	0.73	1.02	1.01
Intercept ($\times 10^{-3}$)	-0.25	0.76	-2.76	2.30

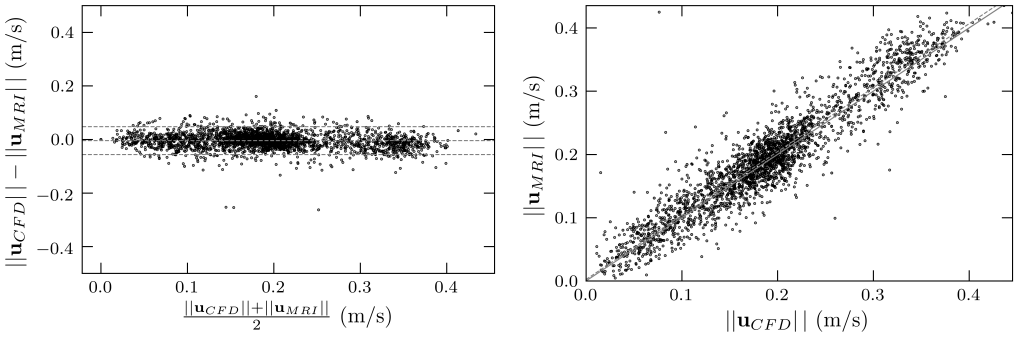

Figure 4.31: **Top** Pearson's product moment correlation analysis for each velocity component on the entire domain at peak systole between LR-CFD and PC-MRI measurements. **Bottom** Corresponding Bland-Altman and linear regression charts of the magnitude of the velocity. Note that for clarity, only 1 over 10 data point randomly selected were plotted. Middle grey line on the Bland-Altman chart stands for mean difference $\overline{\|\mathbf{u}_{CFD}\| - \|\mathbf{u}_{MRI}\|}$, surrounded by its 95% confidence interval grey lines ($\pm 2\sigma$ where σ is the standard deviation). The resulting linear regression is shown in the bottom right figure with a grey dashed line, while the solid line denotes the ideal regression line.

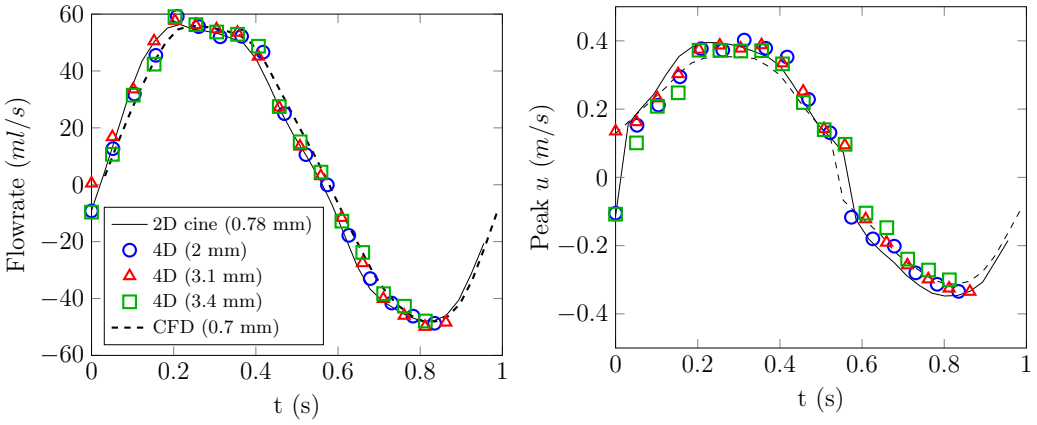

Figure 4.32: **left** Flowrate and **right** peak axial velocity evolution over one cycle in the collateral branch at different spatial resolutions.

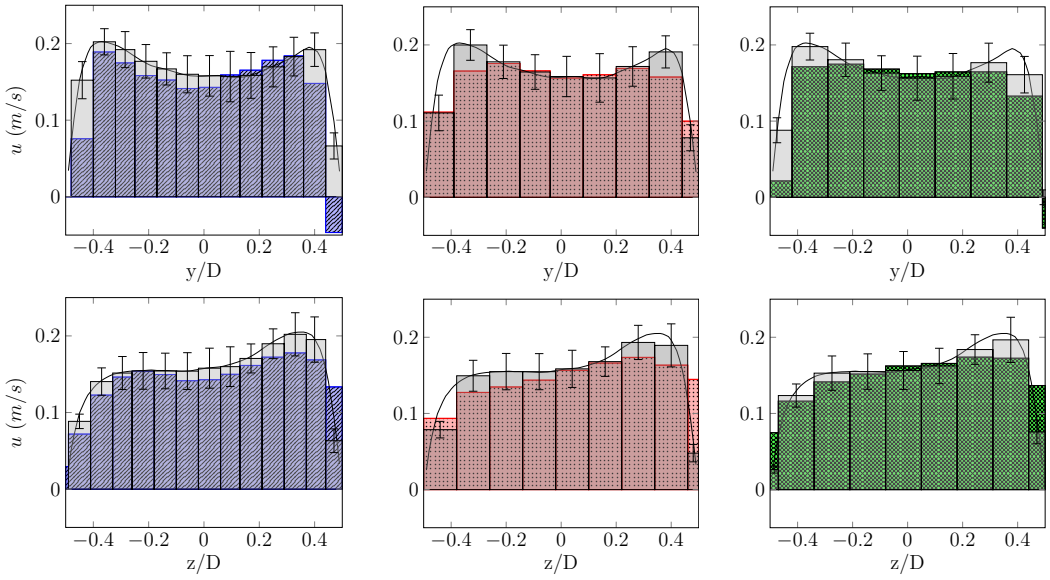

Figure 4.33: Axial velocity profiles in the middle of the bend of the flow phantom. along y (up-down) and z (foot-head) axis. The solid lines and the grey filled bar chart correspond to the HR-CFD and LR-CFD, respectively. The coloured filled chart bars in 1st, 2nd and 3rd columns represent the 2 mm, 3.1 mm and 3.4 mm voxel size 4D Flow MRI acquisitions respectively. Error bars correspond to $u \pm u_{rms}$

Chapter 5

PC-MRI based evaluation of velocity-derived quantities

Chapter contents

5.1 Introduction

The aim of this chapter is to evaluate the accuracy which can be reached when reconstructing derived quantities from PC-MRI velocity measurements. As mentioned in the introduction chapter, the wall shear stress (WSS) and relative pressure field are two pertinent biomarkers to explain the pathogenesis and to

diagnose CVD. For this reason, several algorithms were developed to reconstruct these biomarkers from MR velocity measurements. However, these algorithms differ by nature, and generally raise contradictory results and varied robustness to the input MRI dataset. In this chapter, by first ensuring the correct convergence of the pressure and WSS fields, we reuse the CFD solution developed in the previous chapter for the comparing and validating the existing reconstruction approaches found in the literature. This chapter illustrates an alternative way to use such a reference framework as a benchmark to evaluate and compare the accuracy of different reconstruction approaches.

5.2 Wall shear stress reconstruction methods from PC-MRI

5.2.1 Introduction

The wall shear stress (WSS) is a flow quantity that is often regarded as biomarker of CVD such as aortic diseases, aneurysm, congenital heart diseases, or valve regurgitation. In particular, WSS plays an important role in aneursym initiation, growth and rupture, since changes in WSS influence endothelial cell function and thus, promote vascular remodelling and vessel dilatation [110].

However, reconstructing WSS from MRI measurements is challenging, especially in cardiovascular regimes where high near-wall velocity gradients occur. Moreover, the accuracy which can be expected when reconstructing WSS from MRI dataset highly depends on both wall delineation and spatial resolution [128, 158].

A straightforward approach to reconstruct the WSS field from MRI consists in a finite difference discretization of the gradient field at boundary walls from the velocity measured at MRI voxels [115]. In the case of complex geometries with tortuous boundary walls as found in the arterial circuit, finite-difference methods are less adapted since the definition of the wall normal vectors requires simplifications that could introduce important errors [140]. Instead, the vessel wall topology is generally segmented, discretized with triangular elements, and the velocity gradient computed at boundary walls is associated to the face inward normals. In practice, existing methods to estimate wall positioning and inward normal orientation often imply uncertainties that could cause large WSS errors [128, 158]. To minimize the segmentation errors and to get a smooth and continuous description of vessel walls, Stalder et al. [144] proposed to fit the vessel walls with cubic B-splines. In the case of low spatial resolution, the results showed a high WSS underestimation and errors up to 50% were reported. Potters et al. [128] calculated the WSS vector field from the full velocity gradient matrix generated

using smooth weighted splines to fit the MRI velocities at voxels close to the boundary walls. They found that at least 3 voxels across the vessel diameter and a wall inward normal distance as long as 50% of the vessel are recommended to reach a 5% accuracy of the WSS reconstruction. Still, according to the authors, the algorithm tends to overestimate the WSS for in-vivo datasets mainly because the velocity field does not undergo any spatial filtering. Sotelo et al. [142] also reconstructed the WSS using a decomposition in finite-element shape functions of the velocities measured inside the lumen. They highlighted the importance of incorporating both the in-plane and longitudinal velocity gradients into the WSS computation, instead of only the 2D planar projection, as classically done [126, 144, 158]. Nevertheless, the authors reported some inconsistent patterns associated with the piece-wise linear interpolations.

The large number of different approaches proposed in the literature to estimate the WSS from MRI suggests the importance of a gold standard WSS solution to assess the accuracy and robustness of the proposed methods under realistic complex flow conditions (cf. conditions other than the simple analytic Womersley or Poiseuille flow solutions as used so far). For this reason, several studies use numerical simulations as a validation tool to evaluate the robustness and accuracy of the WSS reconstruction from MRI dataset [19, 125, 142, 158]. Petersson et al. [125] performed PC-MRI simulations of flow data to evaluate and compare the accuracy of different WSS reconstruction approaches. They found considerable errors depending on VENC, velocity and spatial resolution, irrespective of the method used. Cibis et al. [35] compared the WSS reconstruction from CFD and 3D PC-MRI in carotid arteries and found that $\mathrm{WSS_{MRI}}$ always underestimates $\mathrm{WSS_{CFD}}$, but also noticed a clear improvement of the correlations when the CFD is down sampled to MRI resolution. Boussel et al. [19] also computed the flow with CFD simulations of in-vitro intracranial aneurysms and found generally poor WSS correlations although correlations were good in terms of velocity fields. Sotelo et al., [142] reported errors up to 20% between their 3D WSS reconstruction method and the CFD in a funnelled-tube model.

In all these studies, the ability of the CFD simulation to provide a reliable estimate of the velocity gradients at the vicinity of the boundary walls has however not been questioned and convergence analysis of the hemodynamics parameters derived by CFD is often disregarded [19, 35, 158]. On the contrary, Les et al. [90] performed patient-specific CFD simulations of aortic aneurysms at several mesh resolutions, and found that the mean WSS does not properly converge with mesh refinement.

Given the large variety of WSS errors and the contradictory results found in the literature from the different approaches cited above, it seems important in a first instance to guarantee the value of $\mathrm{WSS_{CFD}}$, the wall shear stress extracted

from CFD results, and particularly its convergence with mesh resolution. It will then make sense to use the CFD field as a reference to evaluate the MRI-based WSS reconstruction approaches, where appropriate.

The objective of this section is to reuse the previous reference CFD simulation to evaluate several WSS reconstruction approaches from MRI. A preliminary mesh sensitivity analysis is first performed to study the $\mathrm{WSS_{CFD}}$ field convergence. In order to assess the sensitivity of the reconstruction to the input parameters, the $\mathrm{WSS_{MRI}}$ is then reconstructed from the experimental MR velocity data obtained in Sec. 4.3, and using the same gradient discretization method as in the CFD simulations. The impact of the gradient discretization order as well as the interpolation mesh on the resulting $\mathrm{WSS_{MRI}}$ are then assessed by comparison with $\mathrm{WSS_{CFD}}$. To highlight the influence of the reconstruction algorithm on the resulting WSS field, two approaches introduced above, which conceptually differ from the one proposed (Potters et al., [128], and Sotelo et al., [143]) are tested and compared with the $\mathrm{WSS_{CFD}}$ and $\mathrm{WSS_{MRI}}$ using the same experimental MRI dataset. To separate the impact of the input velocity from the numerical treatments inherent to the presented algorithm, the $\mathrm{WSS_{CFD}}$ is down sampled and the gain on the correlation with $\mathrm{WSS_{MRI}}$ is analyzed.

As already mentioned, a major advantage of this idealized setup is that the wall position is known a priori up to a registration uncertainty errors. For this reason, the influence of the segmentation on the WSS reconstruction is not investigated in this thesis.

5.2.2 WSS computation from CFD

The viscous stress tensor of a Newtonian fluid can be written using the Einstein notation as:

$$\tau_{ij} = 2\mu S_{ij} - \frac{2}{3}\mu S_{kk}\delta_{ij} \tag{5.1}$$

where δ_{ij} is the Kronecker symbol and $S_{ij} = \frac{1}{2}\left(\frac{\partial u_i}{\partial x_j} + \frac{\partial u_j}{\partial x_i}\right)$ the strain rate tensor and μ the dynamic viscosity. Under the hypothesis of incompressible fluid, the second term cancels since $S_{kk} = \nabla \cdot \mathbf{u} = 0$, and the viscous stress tensor written in matrix form reduces to:

$$\tau = \mu \begin{pmatrix} 2\frac{\partial u}{\partial x} & \frac{\partial u}{\partial y} + \frac{\partial v}{\partial x} & \frac{\partial u}{\partial z} + \frac{\partial w}{\partial x} \\ \frac{\partial v}{\partial x} + \frac{\partial u}{\partial y} & 2\frac{\partial v}{\partial y} & \frac{\partial v}{\partial z} + \frac{\partial w}{\partial y} \\ \frac{\partial w}{\partial x} + \frac{\partial u}{\partial z} & \frac{\partial w}{\partial y} + \frac{\partial v}{\partial z} & 2\frac{\partial w}{\partial z} \end{pmatrix} \tag{5.2}$$

Then, the wall shear stress is defined as the normal vector component of the viscous stress tensor at a boundary wall:

$$\mathbf{WSS} = \tau \cdot \mathbf{n} \tag{5.3}$$

where $\mathbf{n}$ is the inward normal to the boundary wall.

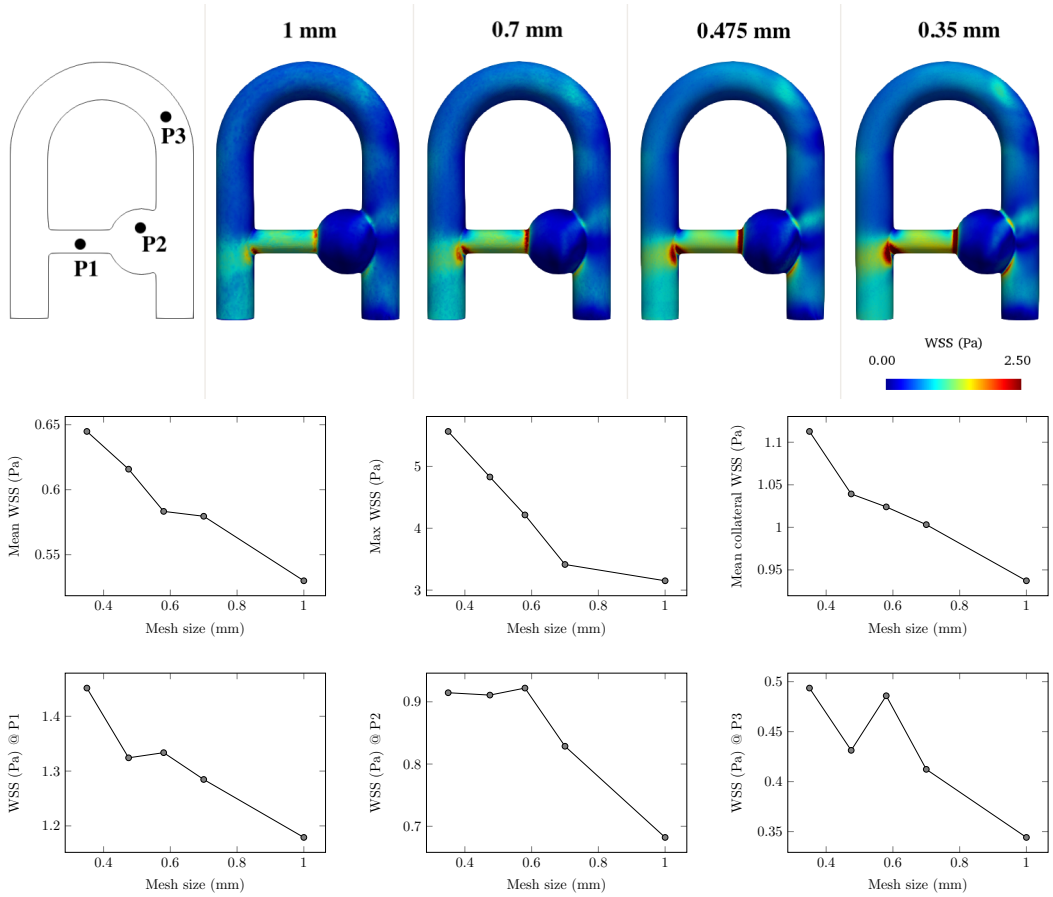

Figure 5.1: Results of the $\mathrm{WSS}_{\mathrm{CFD}}$ mesh convergence analysis at peak systole ($t/T_p = 0.2$). **First row**: **left** Location of the probes within the phantom, and resulting $\mathrm{WSS}_{\mathrm{CFD}}$ maps at different spatial resolutions. **Second row**: **left** WSS averaged over the whole domain, **middle** maximum WSS and **right** WSS averaged over the collateral branch only. **Last row**: WSS values at **left** probe $P1$, **middle** probe $P2$, **right** probe $P3$.

Mesh sensitivity analysis

To ensure the convergence of reference $\mathrm{WSS}_{\mathrm{CFD}}$ field, a preliminary mesh sensitivity analysis is performed using the phase-averaged velocity field as input for the gradient calculation. Five meshes are considered with varied characteristic mesh sizes, as follows: M1: $\Delta x = 1$ mm (1.3 million cells), M2: $\Delta x = 0.7$ mm (3.8 million cells), M3: $\Delta x = 0.58$ mm (8.3 million cells), M4: $\Delta x = 0.475$ mm (15.4 million cells), and M5: $\Delta x = 0.35$ mm (27.4 million cells).

Results are presented in Figure 5.1. Visually, the highest $\mathrm{WSS}_{\mathrm{CFD}}$ magnitude levels are located at both the collateral inlet contraction and outlet expansion. The first hotspot at the collateral inlet occurs as a consequence of the high singular pressure drops due to abrupt cross-sectional changes. At the collateral outlet

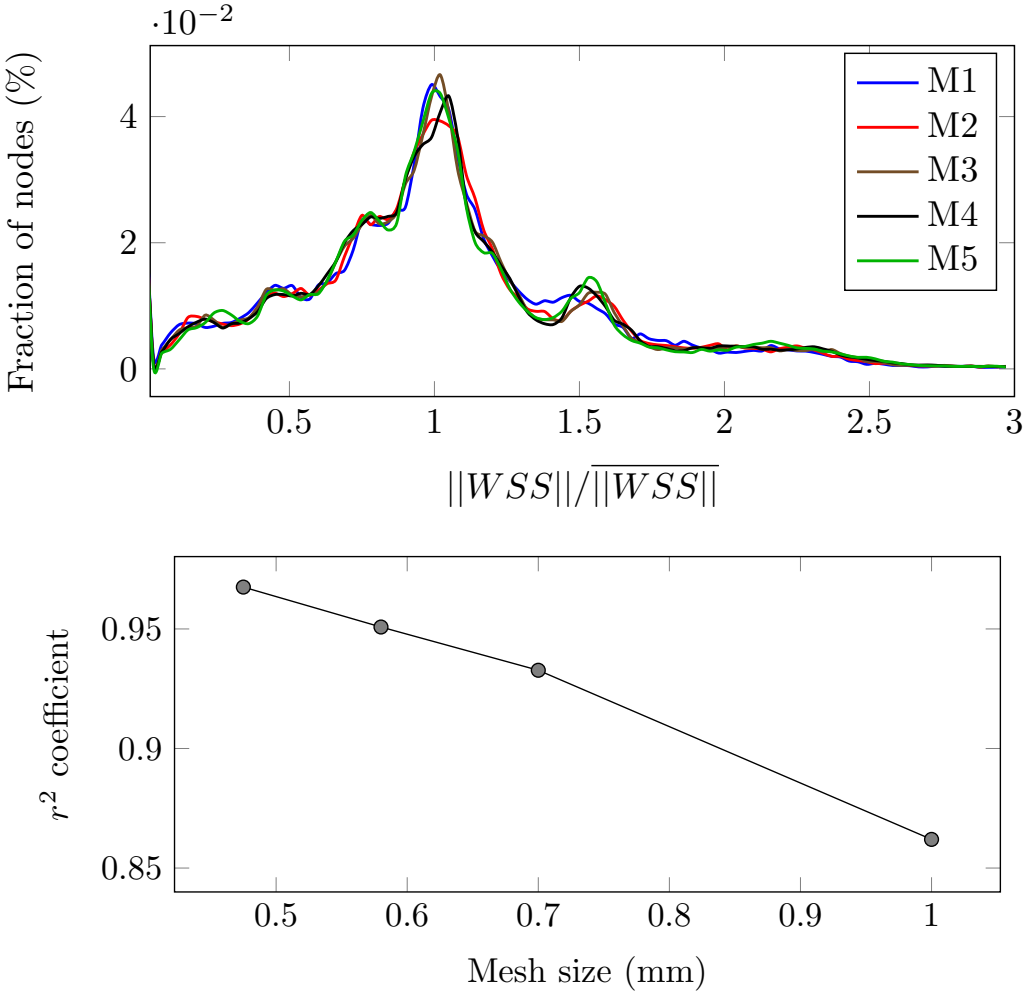

Figure 5.2: **Top**: Dimensionless WSS magnitude distribution histogram for meshes from M1 to M5. **Bottom**: Pearson's correlation coefficient for the WSS magnitude with M5 as reference.

elbow, the high momentum of the jet forms a stagnation zone and therefore an increase of the pressure gradient. As a consequence, the deflected principal flow structure reattaches in the stagnation zone right under the jet, symmetrically on both sides of the pipe, with the formation of counter-rotating vortex due to the radial pressure gradient. This phenomenon induces a local increase of the velocity gradients at the boundary walls, distributed symmetrically on the pipe surface on both sides of the jet.

The first striking result in Figure 5.1 is that despite the high resolution meshes used for the simulation (up to 27 million elements), the mesh independence of the WSS seems clearly not reached. On the contrary, one can see significant changes between the maximum WSS magnitude as the mesh size decreases (380%

relative error between M1 and M5). The mean WSS magnitude also increases at a relatively smaller rate, as observed with the 20% relative error between M1 and M5. This non convergence behaviour was already found in Les et al. [90], although the inverse trends were found (decrease of the WSS as the mesh size decreases).

Nevertheless, from a qualitative observation of the WSS maps, the WSS patterns seem similarly located irrespective of the mesh resolution. This observation is supported by the dimensionless WSS distribution histogram shown in Figure 5.2. The high similarity also suggests that a proportionality relationship exist between each mesh. The dimensionless WSS seems therefore to provide a correct convergence. As an indicator of the linearity, the Pearson correlation coefficient is additionally shown in Figure 5.2. The high correlation reported ($r^2 = 0.98$) as well as the very small increase of the correlation with mesh refinement (especially for M2,M3 and M4) confirms this behaviour.

The insufficient resolution in the near-wall regions constitutes the most obvious explanation of the lack of convergence observed. A rapid estimation of the boundary layer thickness using the Womersley solution results in $\delta = \frac{R}{\alpha} = 0.8\ mm$ (where α is the Womersley number and R the characteristic length scale). This corresponds to a boundary layer discretized with only two cells in the radial direction for the finer mesh M5, which seems unsufficient to resolve the complex pulsatile velocity profile. It is important to notice that isotropic tetrahedral meshes with low cell skewness are preferred for minimizing the errors associated with the discretization of the Laplacian operator [159]. Therefore, we did not perform any local mesh refinement. Assuming that about 8 cells in the boundary layer thickness is a good compromise for an accurate estimation of the velocity in the viscous layer, a computational mesh of more than 1.3 billion isotropic cells would be required, inducing highly prohibitive calculation cost.

The dimensionless wall distance y^+ is a commonly used metric to assess the near-wall mesh resolution. It is defined as $y^+ = \frac{\sqrt{WSS/\rho}\Delta n}{\nu}$ where Δn here is the distance of the first mesh node in the direction normal to the wall. A maximum $y^+ = 6.7$ and a mean $y^+ = 0.14$ was found at the collateral outlet elbow. As observed by Gross-Hardt et al. [62], a $y^+ < 0.2$ was necessary to correctly resolve the WSS in the presence of such sharp angles.

It seems important to note that to each mesh resolution is associated a unique discretization of the phantom's surface topology. The variations of surface mesh generally come with modifications of the surface normal vector orientation and WSS changes could be raised from these topological changes. One may suggest that these changes are responsible for the non-convergence behaviour of the WSS with mesh refinements. For this reason, to remove the errors associated with the topology variation, additional numerical meshes were generated by fixing an initial

topology of the surface mesh. From the initial mesh, a refinement was performed by dividing each tetrahedron in 8 sub-tetrahedra so that the boundary faces lay on the same plane, and therefore the normal vector is kept constant. A second similar refinement step was performed on the mesh and WSS were compared. However, the results were roughly similar as what is observed in Fig. 5.1.

In the following sections, M3 is considered as a reference WSS solution intended for qualitative assessment only; given the lack of convergence, it seems unwise to consider as a reference field the absolute value of $\mathrm{WSS}_{\mathrm{CFD}}$.

5.2.3 WSS reconstruction from MRI

Proposed approach

Even though the second term in Eq. 5.1 is generally removed because of the assumed incompressibility of the flow, the MRI velocity contains experimental noise which is not divergence-free; the pertinence of assuming the flow incompressibility for the computation of WSS from raw MRI remains therefore questionable. To remove any doubt, the MRI velocity field was systematically projected onto the space of divergence-free fields.

PC-MRI velocity fields corrected from phase-offsets artifacts as described in the previous chapter were used to compute $\mathrm{WSS}_{\mathrm{MRI}}$. As the true position of the boundary walls is known, the MRI velocity field was interpolated on an unstructured phantom mesh M2 with second order Shepard's interpolation method (Inverse distance weighting). The ideal mesh resolution for the interpolation will be discussed in more details in the next section. At the boundary walls, a zero velocity is prescribed to respect the no-slip boundary condition. The velocity gradient at wall is then computed from the interpolated MRI velocity field. As already mentioned above, the high-order spatial discretization of the gradient operator implemented in the YALES2BIO solver and described in Sec. 3.1.2 is used to compute the WSS from 4D PC-MRI velocity measurements. In practice, the gradient operator is discretized at the nodes as the average gradient over the control volume. Note that the volume integral can be rewritten as the sum of the velocity fluxes over all the faces of the control volume. It is important to note that is approach is quite straightforward and does not intend to provide the best representation of the WSS, but only to highlight the influence of different numerical treatments and evaluate the sensitivity to the input MR velocity field of the WSS reconstruction.

Potters' approach

In the approach developed in Potters et al [128], the WSS is computed at the wall points defined from a triangular surface mesh segmentation of the vessel.

The boundary surface of the phantom's mesh M2 was provided as the input segmentation to the algorithm. A zero velocity was prescribed at these wall points. A local coordinate system was then defined where one direction is oriented along the inward normal of the boundary. According to the authors recommendations, three points along the normal are defined between the wall and the middle of the vessel. The MR velocities are then projected with natural neighbour interpolation method on these points. Finally, a smoothing spline (piecewise polynomial functions) is defined through these points and the velocity derivatives are computed from the analytical expression of the spline.

Sotelo's approach

The second algorithm tested was proposed by Sotelo et al., [142]. In this approach, the 3D WSS is computed using a finite-element interpolation scheme with piecewise linear shape functions to interpolate the the WSS on the nodes of the mesh. The phantom tetrahedral mesh $M2$ was provided as input of the algorithm. A smoothing distribution filter is needed due to the poor convergence of the algorithm. This algorithm is part of an entire 4D Flow MRI post-processing Matlab tool kindly provided by the author.

5.2.4 Sensitivity to the numerical parameters

The sensitivity of the proposed reconstruction algorithm to the resolution of the interpolation mesh as well as the influence of the gradient discretization order are presented.

Influence of the interpolation mesh

The impact of the interpolation mesh necessary for the computation of $\mathrm{WSS_{MRI}}$ is analysed and compared with the $\mathrm{WSS_{CFD}}$ computed from $\Delta x_{m3} = 0.475$ mm. A mesh size ratio is here defined as $MSR = \frac{\Delta x_{interp}}{\Delta x_{mri}}$ where Δx_{interp} is the tetrahedral interpolation grid characteristic mesh size and Δx_{mri} the MRI voxel size ($\Delta x_{mri} = 2\ mm$ used for the convergence study).

As shown in Figure 5.3, $\mathrm{WSS_{MRI}}$ levels seem more uniformly distributed along the collateral branch and the stress concentrations observed at the collateral inlet/outlet are more diffuse as compared to $\mathrm{WSS_{CFD}}$. A mean error was calculated as: $ME = \frac{\left| \frac{1}{m} \sum_{i=1}^{m} ||\mathbf{WSS}_{MRI}(\mathbf{x}_i)|| - \frac{1}{n} \sum_{j=1}^{n} ||\mathbf{WSS}_{CFD}(\mathbf{x}_j)|| \right|}{\frac{1}{n} \sum_{j=1}^{n} ||\mathbf{WSS}_{CFD}(\mathbf{x}_j)||}$ where m, n are the number of surface nodes of MRI and CFD respectively. Figure 5.3 also reports mean $\mathrm{WSS_{MRI}}$ differences up to 58% between $MSR = 1$ and $MSR = 1/4$. As compared to $\mathrm{WSS_{CFD}}$, the lowest error is raised at $MSR = 1/3$ (5.3%) which seems to be an optimal value also from visual observation of the WSS levels. These trends can

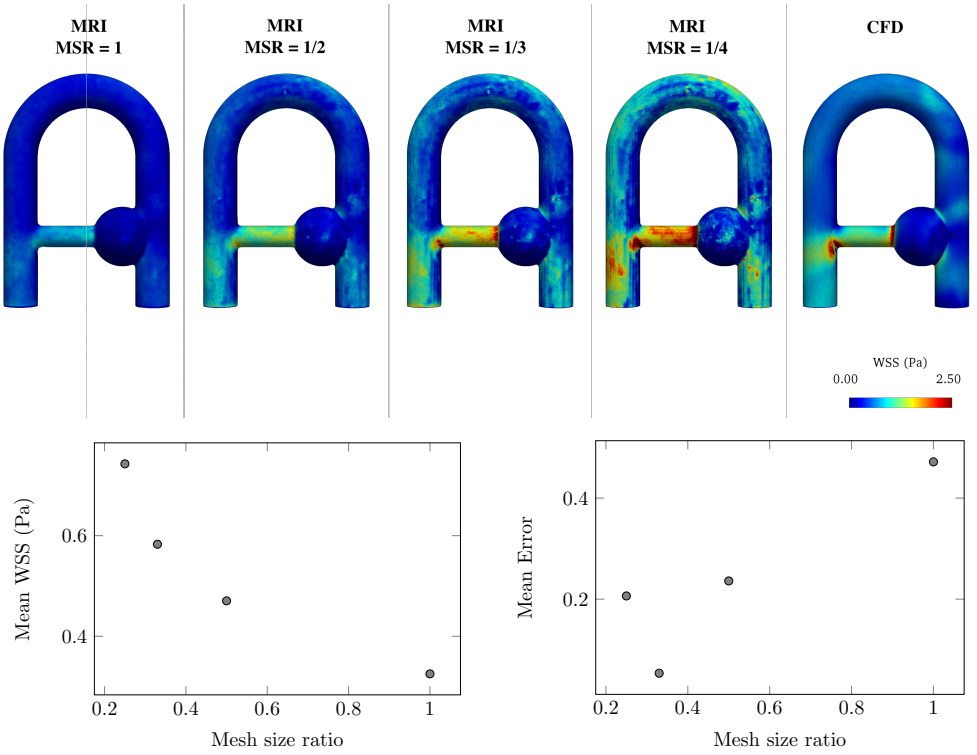

Figure 5.3: Sensitivity of the MR velocity field to the interpolation tetrahedral mesh with size ratio comprised between $MSR = 1$ and $MSR = 1/4$. **Top** Magnitude of the WSS maps for different MSR at $t/T_p = 0.2$. **Bottom** Corresponding mean WSS value and mean WSS error.

partially be explained as a result of the second order inverse distance weighting interpolation used to interpolate the MRI velocity field, which tends to amplify the velocity gradient as the mesh size decreases. Note that in Sotelo et al. [142], the MRI velocity field was interpolated on a tetrahedral mesh with $MSR = 1/4$. which should induce from the present results a non negligible WSS overestimation, although they used a different WSS computation methodology and a cubic velocity interpolation. It is also important to note that the low-dissipative high-order numerical schemes used in the present computations generally add very few numerical diffusion, which makes the velocity gradients very sensitive to the mesh quality.

Influence of the gradient discretization order

The impact on both the $\mathrm{WSS}_{\mathrm{MRI}}$ and $\mathrm{WSS}_{\mathrm{CFD}}$ of the spatial discretization order of the gradient operator is investigated in this section. An illustration of the discretization procedures at second and fourth orders are provided in Section 3.1.2 and detailed in the PhD thesis of M. Kraushaar [81].

Table 5.1: Magnitude of the WSS vector at peak systole ($t/T_p = 0.2$) computed with second and fourth-order gradient discretization. The mean, standard deviation and maximum WSS over the entire wall surface of the phantom's mesh M2 are reported.

	CFD (2nd)	CFD (4th)	MRI (2nd)	MRI (4th)
Mean WSS (Pa)	0.54	0.58	0.59	0.58
Std WSS (Pa)	0.30	0.33	0.35	0.35
Max WSS (Pa)	3.0	3.5	2.59	2.65

Table 5.2: WSS correlations with $\mathrm{WSS}_{\mathrm{CFD}}$ at peak systole, for the entire boundary surface of the phantom. The WSS correlations are calculated for each vector component separately.

	Potters et al.	Sotelo et al.	Present method
$r^2_{WSS_x}$	0.78	0.77	0.82
$r^2_{WSS_y}$	0.19	0.38	0.37
$r^2_{WSS_z}$	0.90	0.84	0.88
$r^2_{\|\|\mathbf{WSS}\|\|}$	0.57	0.51	0.60

Results are presented in Table 5.1. It can be observed that the higher order systematically results in higher maximum WSS, as it is more sensitive to the high near-wall velocity frequency variations. Moreover, a higher order implies higher variations of maximum $\mathrm{WSS}_{\mathrm{CFD}}$ as compared to $\mathrm{WSS}_{\mathrm{MRI}}$. Generally speaking, these low variations observed suggest that the $\mathrm{WSS}_{\mathrm{MRI}}$ is much less sensitive to the order of accuracy of the gradient discretization than to the choice of the interpolation mesh or to the MRI spatial resolution.

5.2.5 Comparison of the approaches

Comparison with HR-CFD

The presented WSS reconstruction algorithm (see Sec. 5.2.3) is compared with two conceptually different algorithms proposed in the literature, where the experimental MR velocity measurements presented in Section 4.3 are used as input of the reconstruction algorithms. Figure 5.4 shows the WSS computed from the three presented approaches, as compared to the $\mathrm{WSS}_{\mathrm{CFD}}$. Statistical analyses are illustrated through Blandt-Altman plots and Table 5.2 reports the corresponding correlations.

In the present method, the high WSS sites near the boundary outlet and along the collateral seems globally in agreement with CFD; nevertheless, a large overestimation of the WSS in the collateral branch can be observed. As the same gradient discretization method is used, the observed small spots of high WSS

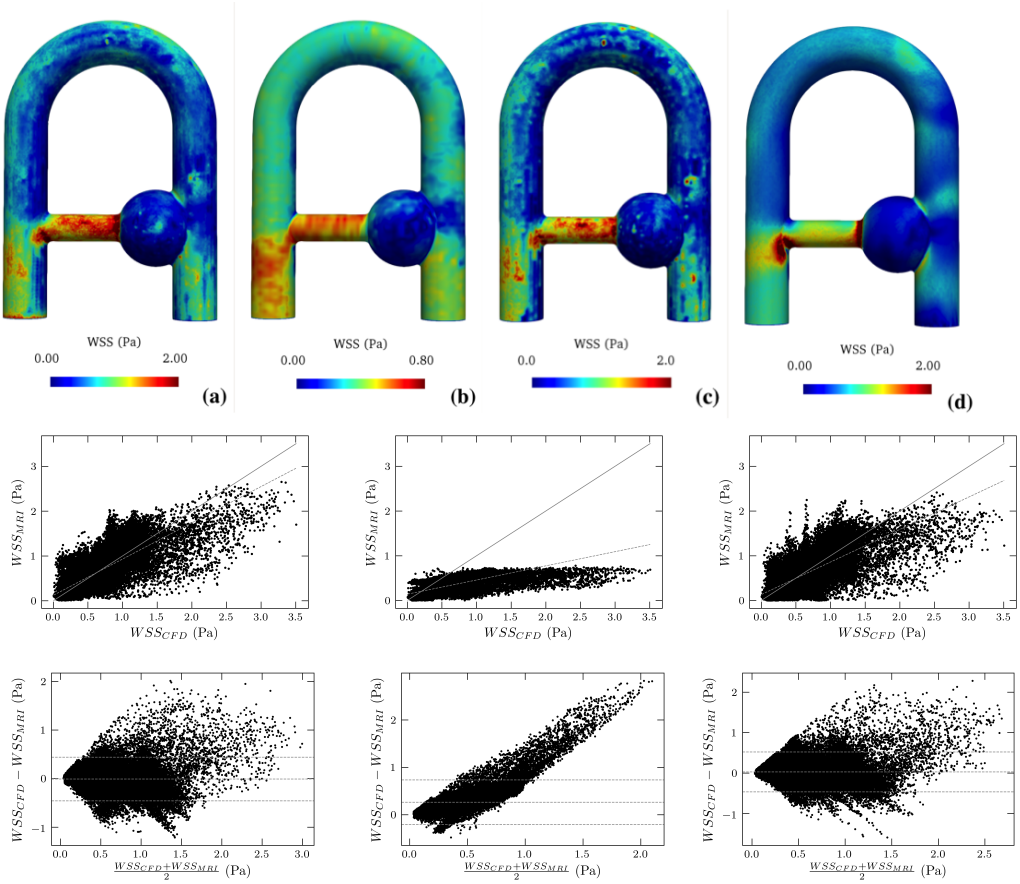

Figure 5.4: WSS maps at peak systole $t/T_p = 0.25$ reconstructed from different algorithms. **Top** (a) Presented method, (b) Potters et al, (c) Sotelo et al, (d) CFD. Different color scales are associated with each dataset for visual clarity. **Bottom** WSS magnitude linear regression and Bland-Altman plots computed from the **left** current numerical method, **middle** Potters et al. and **right** Sotelo et al., and compared with CFD.

variations along the entire surface can be attributed to the high sensitivity of the method to the input velocity. As shown in Table 5.2, it results in very low WSS magnitude correlations $r^2_{||\mathbf{WSS}||} = 0.60$ as compared to the corresponding velocity correlations $r^2_{||\mathbf{u}||} = 0.93$. This larger discrepancy can be explained by both the loss of information associated with the down sampling process and by the sensitivity of the WSS computation to the residual noise in the near-wall voxels. As well, the WSS correlations for the x and z-axis outperforms the y-direction. This was expected since the corresponding x and z velocity correlations are more favourable. Finally, a WSS underestimation can be noticed, especially where high WSS levels occur.

The WSS reconstructed from the algorithm proposed by Potters et al. shows a large underestimation of the $\mathrm{WSS_{CFD}}$ and $\mathrm{WSS_{MRI}}$ as illustrated by the linear

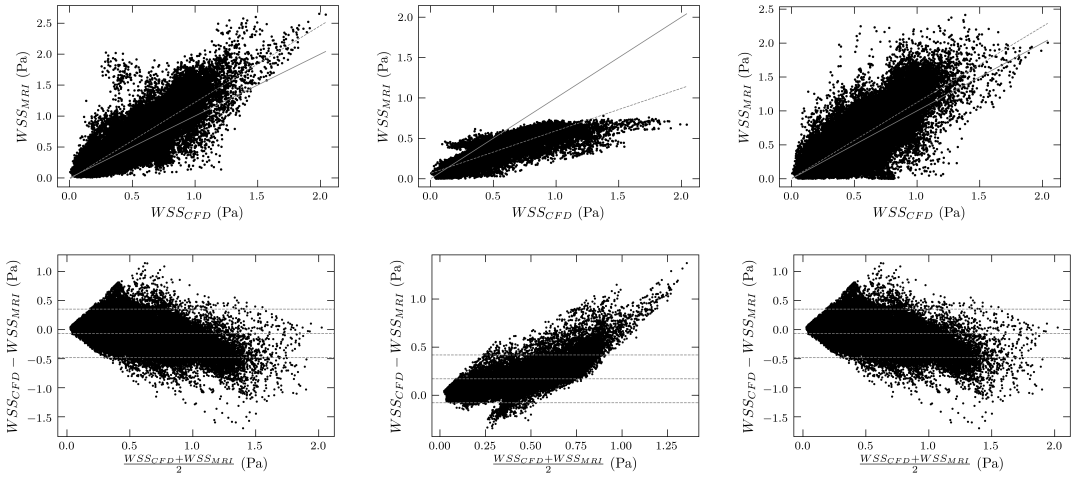

Figure 5.5: WSS maps at peak systole $t/T_p = 0.25$ reconstructed from different algorithms. **Top** (a) Presented method, (b) Potters et al, (c) Sotelo et al, (d) LR-CFD. Different color scales are associated with each dataset for visual clarity. **Bottom** WSS magnitude linear regression and Bland-Altman plots computed from the **left** current numerical method, **middle** Potters et al. and **right** Sotelo et al., and compared with LR-CFD.

regression and Bland-Altman plots. However, in terms of WSS repartition, roughly similar trends are observed, with an increase of the shear in the collateral as well as near the outlet in the main branch. The generally diffuse WSS repartition could be explained due to the large distance along the inward normal vector used to compute the b-spline; this tends to lower the near-wall gradient by averaging the high frequency variations of the near-wall velocity as compared to the low variations of the velocity at proximity to the centerline. This method seems by nature less sensitive to the noise present at the vicinity of the walls. Although it largely underestimates the $\mathrm{WSS_{CFD}}$, a linear relationship exists and the resulting correlation is very close to the proposed method $r^2_{||\mathbf{WSS}||} = 0.57$.

Finally, as shown in Fig. 5.4b), the WSS map obtained from the algorithm proposed by Sotelo et al. report very similar patterns as compared to the proposed approach ($\mathrm{WSS_{MRI}}$). This was also expected as the two reconstructions methods are inherently close from each other (smoothed finite-element vs. finite volume). However, small spots of higher WSS are observed as compared to the present method. This can be explained as in finite-element method the WSS is interpolated at nodes while in finite-volume formalism the nodal value corresponds to an average over the control volume, which by definition systematically lower the local maxima.

Table 5.3: WSS correlations with $\mathrm{WSS_{LR}}$ at peak systole, for the entire boundary surface of the phantom. The WSS correlations are calculated for each vector component separately.

	Potters et al.	Sotelo et al.	Present method
$r^2_{WSS_x}$	0.90	0.81	0.88
$r^2_{WSS_y}$	0.27	0.34	0.34
$r^2_{WSS_z}$	0.96	0.87	0.90
$r^2_{\|\|\mathbf{WSS}\|\|}$	0.79	0.60	0.69

Comparison with LR-CFD

To estimate the sensitivity of the presented reconstruction algorithm to the input velocity, the CFD field was down sampled to the MRI spatial resolution ($\mathrm{WSS_{LR}}$). Figure 5.5 shows the WSS computed from the three presented approaches, as compared to the $\mathrm{WSS_{LR}}$. Statistical analyses are illustrated through Blandt-Altman plots and Table 5.3 reports the corresponding correlations. As expected,$\mathrm{WSS_{MRI}}$ better matches the LR-CFD ($r^2_{||\mathbf{WSS}||} = 0.69$) than the HR-CFD ($r^2_{||\mathbf{WSS}||} = 0.6$). As WSS sensitivity to spatial resolution and wall position induces high relative discrepancies, down sampling and applying a no-slip boundary condition improve the agreement. Nevertheless, as shown from the Bland-Altman and linear regression analysis in Figure 5.5 a small overestimation of $\mathrm{WSS_{MRI}}$ is observed as compared to $\mathrm{WSS_{LR}}$, especially in the collateral branch. To highlight the impact of the down-sampling on the correlation and hide the influence of the velocity field, $\mathrm{WSS_{LR}}$ and $\mathrm{WSS_{HR}}$ were compared and resulted in $r^2_{||\mathbf{WSS}||} = 0.86$. The analysis thus shows that intravoxel averaging significantly degrades the accuracy of the gradient computation and is partly responsible for the poor WSS correlations observed between HR-CFD and MRI in Table 5.3. This was expected since the voxel averaging performed through the MRI acquisition smoothens the (strong) velocity gradients present in the wall region. Note also that downsampling has higher influence on the WSS than on the velocity. The striking result is the large correlation improvement that results from the algorithm proposed by Potters et al. (+22%). In Figure 5.5, the Bland-Altman and linear regression plots show that a strong linear relationship exists between the two values, while a proportional underestimation error propagates as the WSS magnitude increases (linear regression slope=0.52). This result can be explained by the low sensitivity to near-wall noise of the algorithm proposed by Potters as compared to the Sotelo's and presented algorithms.

This result suggests that the reconstruction algorithm is mostly responsible for the low correlation observed and that the differences observed between MRI and CFD velocity fields has low influence on the WSS reconstruction.

5.2.6 Conclusion

In this section, the high-order finite-volume methods implemented in the YALES2BIO solver were used to assess different WSS reconstruction approaches. We performed a mesh sensitivity analysis of the $\mathrm{WSS_{CFD}}$ field but found no proper convergence, even for highly refined mesh (27 millions cells). The convergence was unreachable especially where highly sharp angles occurs. To this respect, it seems unwise to consider as a reference field the absolute value of $\mathrm{WSS_{CFD}}$. Nevertheless, the WSS histogram showed that the $\mathrm{WSS_{CFD}}$ spatial distribution was correctly predicted, irrespective of the mesh resolution; in this sense, we infer that one can still reasonably use $\mathrm{WSS_{CFD}}$ as a reference field to evaluate the ability of an algorithm to predict the WSS distribution.

It was also observed that systematic errors are raised as a consequence of the MR velocity field interpolation onto a tetrahedral phantom mesh. These errors were found to highly change depending on the interpolation phantom mesh size and an optimum was found at mesh size ratio $MSR = 1/3$. The low-dissipative high-order numerical method used for the gradient discretization generally adds very few numerical diffusion, which makes the resulting velocity gradients very sensitive to the mesh quality. However, decreasing the gradient discretization order did not significantly affect the resulting WSS. It should be noted that this result is most probably case-sensitive and extensive analyses should be carried on to generally understand the behaviour of these errors. Furthermore, the influence of the velocity interpolation method was not investigated but most probably has a large influence in the WSS reconstruction. Others interpolation methods should be tested, such as spline interpolation, kriging. As it provides an estimation of the intravoxel velocity distribution, Fourier-velocity encoding MRI that could be used to improve the near-wall velocity profile [125].

Two WSS reconstruction algorithms found in the literature (Potters et al., Sotelo et al.,) were then tested on real 4D Flow MRI measurements (see Section 4.3) and compared with the presented approach as well as the WSS computed from the high resolution CFD field. Both algorithms underestimated $\mathrm{WSS_{CFD}}$ at sharp angles locations. However, the distributions and WSS levels found with the Sotelo methodology were in good agreement with the presented approach, as expected given the similarities of the two reconstruction approaches. The WSS reconstruction proposed by Potters generally presented diffuse WSS, while the present results and Sotelo's contained noise and reveal small spots of high WSS variations. A possible explanation for the diffuse patterns is that the MR velocity was fitted along a normal wall distance equal to half the vessel diameter (as recommended by the author). In our configuration, increasing the normal wall distance would come down to decreasing the MSR and result in a global overestimation of the WSS field.However, the pertinence of increasing the wall

normal distance (or reducing the MSR) is questionable in terms of consistence of the field calculated; the larger the boundary wall normal distance used to discretize the gradient, the falser is the approximation of the velocity normal derivative at wall. On the other side, a less sensitive field could be obtained since the increase of the discretization distance acts as a smoothing filter and limits the impact the outliers values due to partial volumes and noise effects.

While low correlations were found between the proposed approaches and $\mathrm{WSS}_{\mathrm{CFD}}$, downsampling the CFD field to the MRI resolution resulted in a non negligible improvement for all the approaches. The comparisons between HR-CFD and LR-CFD revealed that solely the differences of spatial resolutions are responsible for about 15% of the total discrepancies observed on the reconstructed WSS. Moreover, while the approach proposed by Potters et al. leaded to WSS underestimates with factor three errors as compared to the other approaches, a stronger WSS correlation was observed. If one considers the LR-CFD as a free of noise MRI WSS field, then this large correlation improvement confirms the low sensitivity to noise of the approach proposed by Potters et al. In this sense, the Pearson's correlation turns out to be a suited metric to evaluate the relative WSS distribution, as it evaluates the linearity between two methods, with no reflect on the absolute WSS levels.

Finally, even if a slight underestimation at higher WSS values was observed, low WSS levels generally agreed quite well with the $\mathrm{WSS}_{\mathrm{CFD}}$. Because low WSS are associated with aneurysm growth [20] and atherosclerotic plaques [90], the WSS could reasonably be quantified in these regions [125]. Nevertheless, the results found in section 5.2.2 suggest that there is no guarantee that the flow is well predicted even in regions of low WSS. Looking at the WSS distribution or evaluating metrics such as OSI could therefore bring more precise and reliable information.

The presented work intents to show how sensitive the WSS computation is. From the CFD point of view, particular attention should be paid to systematic convergences analysis in order to estimate the degree of reliability of the field. A local mesh refinement is essential to ensure that the boundary layer is sufficiently resolved and this is even more true for highly pulsatile regimes. This can be performed by a field-guided mesh adaptation strategy such as presented in [38]. From a MRI point of view, given the large variety obtained from three different algorithms, it seems therefore difficult to draw any generalized conclusions on how reliable and accurate it could be.

5.3 Relative pressure field reconstruction from PC-MRI

5.3.1 Introduction

The relative pressure drop is a common biomarker used clinically to detect and characterize the severity of cardiovascular disorders such as aortic valve stenosis, aneurysm, aortic coarctation, or pulmonary hypertension [5, 7, 36]. For example, the transstenotic pressure drop is a commonly adopted marker to assess the severity of stenosis or aortic coarctation in clinical practice. The transvalvular pressure drop is also used as a criterion to assess the myocardial load, and determine whether or not a surgical treatment should be planned. Moreover, as it drives the dilatation of the vessels, it also plays a key role in aneurysm initiation and rupture.

Nowadays, pressure catheterization is still considered as the clinical gold standard to obtain a measure of the relative pressure in-vivo. However limited by the risks due to its invasiveness, this procedure is only used to treat severe or urgent cases. Alternative approaches have been developed to estimate the relative pressure non-invasively. Among them, the most common approach consists in measuring the peak velocity in a region of interest using Doppler echocardiography to deduce the peak pressure from the simplified steady Bernoulli relation. By neglecting the pressure losses due to fluid friction irreversibilities, this method has shown to significantly overestimate the true pressure gradient [26]. These strong assumptions have led to extended versions of the Bernoulli relation that account for the pressure recovery [57]. Morevoer, the pressure estimate in the simplified Bernoulli relation is based on the peak velocity measurement and assumes steady flow condition. For this reason, the accuracy of the pressure estimates can be improved by working with the Generalized Bernoulli relation that includes the unsteady contributions of the velocity [50].

Recently, Donati et al., (2015) [42] proposed a method to evaluate the pressure drop between two surfaces from integration of the work-energy equation over a region of interest. More complete than Bernoulli since it does account for the viscous and unsteadiness effects, this method is also fast to compute. However, it indicates the pressure drop between two surfaces which could be insufficient if the local repartition is needed. Also, the in-vivo applicability can be problematic if dealing with regurgitant flows since the pressure admits a discontinuity when the flow rate tends towards zero. A modification of this algorithm based on the Virtual work-energy equation was more recently proposed to correct for this divergent behaviour [102].

A local repartition of the pressure can also be obtained by solving the pressure

Poisson equation (PPE) (derived from the NSE) from the velocity field measured with PC-MRI. This approach was first developed by Yang et al. [166], but earlier work applied to the estimation of the relative pressure from Computed Tomography (CT) cardiac images was covered by Song et al. [141]. Although providing the local pressure distribution (up to an additive constant), this method is usually associated with higher computational costs than the other approaches and its use is therefore limited to research purposes. Moreover, the pressure drop estimates highly depend on the accuracy of the PC-MR velocity measurements, and therefore on the MR acquisition itself. In this sense, the questioning of the pressure reconstruction sensitivity to the input velocity field remains unclear.

It is moreover important to notice that each of the contributors to the pressure could be associated with a specific function of the cardiovascular circuit affecting the blood flow dynamics. For example, the transient term represents the acceleration imposed by the cardiac pump to the blood into the cardiovascular system. The convective term expresses the impact on the flow of the vessel geometry variations, while the viscous terms correspond to the loss due to wall friction. In this sense, another interest of the PPE is that it allows to decouple each of the contributors to the pressure drop; this could help tracing cardiovascular dysfunctions and understanding the dominant pressure behaviour. Lamata et al. [86] solved the full PPE in aortic flows configuration and found that the transient term plays the key role in the resulting pressure gradient.

In this section, we reuse the developed CFD-based methodology to assess the relative pressure field computed from different Bernoulli-based methods derived from 4D flow MRI velocity measurements. We aim at finding the best accuracy which can be expected when reconstructing the pressure field from MRI measurements. The accuracy of the pressure computation methods are evaluated thanks to the high resolution CFD solution, where a prior mesh sensitivity analysis is undertaken to study the convergence of the pressure field. The influence of the transient contribution term in the NSE on the resulting pressure drop is compared to the convective and viscous contributions. Finally, we use this pressure contribution splitting to assess the steady and unsteady Bernoulli formulations.

As this work was not fully completed within the allocated time, several methodologies for computing the relative pressure based on solving the PPE using 4D Flow MRI velocity measurements are presented and compared in Appendix 7.4.

5.3.2 Pressure computation from CFD

As for the velocity field, the relative pressure field was phase-averaged over 30 cycles. Figure 5.6 illustrates the impact of phase-averaging on the pressure field. The highest levels of pressure fluctuations are located in the aneurysm and do

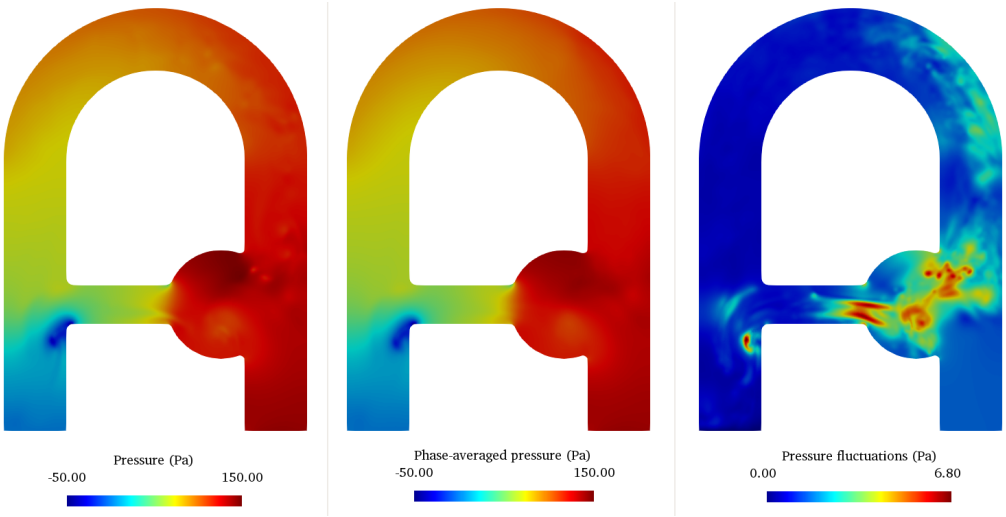

Figure 5.6: Pressure distribution in the middle XZ-plane of the phantom at $t/T_p = 0.44$ **left** instantaneous pressure, **middle** phase-averaged pressure and **right** pressure fluctuations (RMS).

not exceed 5% of the maximum relative pressure. CFD pressure fluctuations are therefore much lower than the corresponding velocity fluctuations.

A mesh sensitivity analysis of the phase-averaged relative pressure field was then performed and is presented in Figure 5.7. Qualitatively, the pressure patterns look very similar irrespective of the mesh and no significant differences can be distinguished. The mean and maximum pressure over the entire domain are tightly close to one another and M2 ($\Delta x = 0.7\ mm$) results in errors of 0.6% and 0.7% respectively as compared to M5 ($\Delta x = 0.35\ mm$). In the collateral branch, similar behaviour is observed but with slightly higher errors with 2.5% and 2.4%. As it seems to provide a reasonably converged phase-averaged pressured field, we consider mesh M2 for the following pressure comparisons.

5.3.3 Pressure reconstruction from MRI

Bernoulli principle

The kinetic energy conservation for an inviscid incompressible fluid with volume external forces deriving from a potential ($\mathbf{f} = -\frac{\partial F}{\partial \mathbf{x}}$) reads:

$$\rho \mathbf{u} \cdot \frac{\partial \mathbf{u}}{\partial t} + \nabla \cdot \left(\frac{\rho}{2} (\mathbf{u} \cdot \mathbf{u}) \mathbf{u} \right) = -\rho \mathbf{u} \cdot \nabla F - \nabla \cdot (p \mathbf{u}) \tag{5.4}$$

Recalling that $\nabla \cdot (A\mathbf{B}) = A \nabla \cdot \mathbf{B} + \mathbf{B} \cdot \nabla A$, it comes that:

$$-\rho \mathbf{u} \cdot \frac{\partial \mathbf{u}}{\partial t} = \mathbf{u} \cdot \nabla \left(\rho \frac{\mathbf{u} \cdot \mathbf{u}}{2} + \rho F + p \right) \tag{5.5}$$

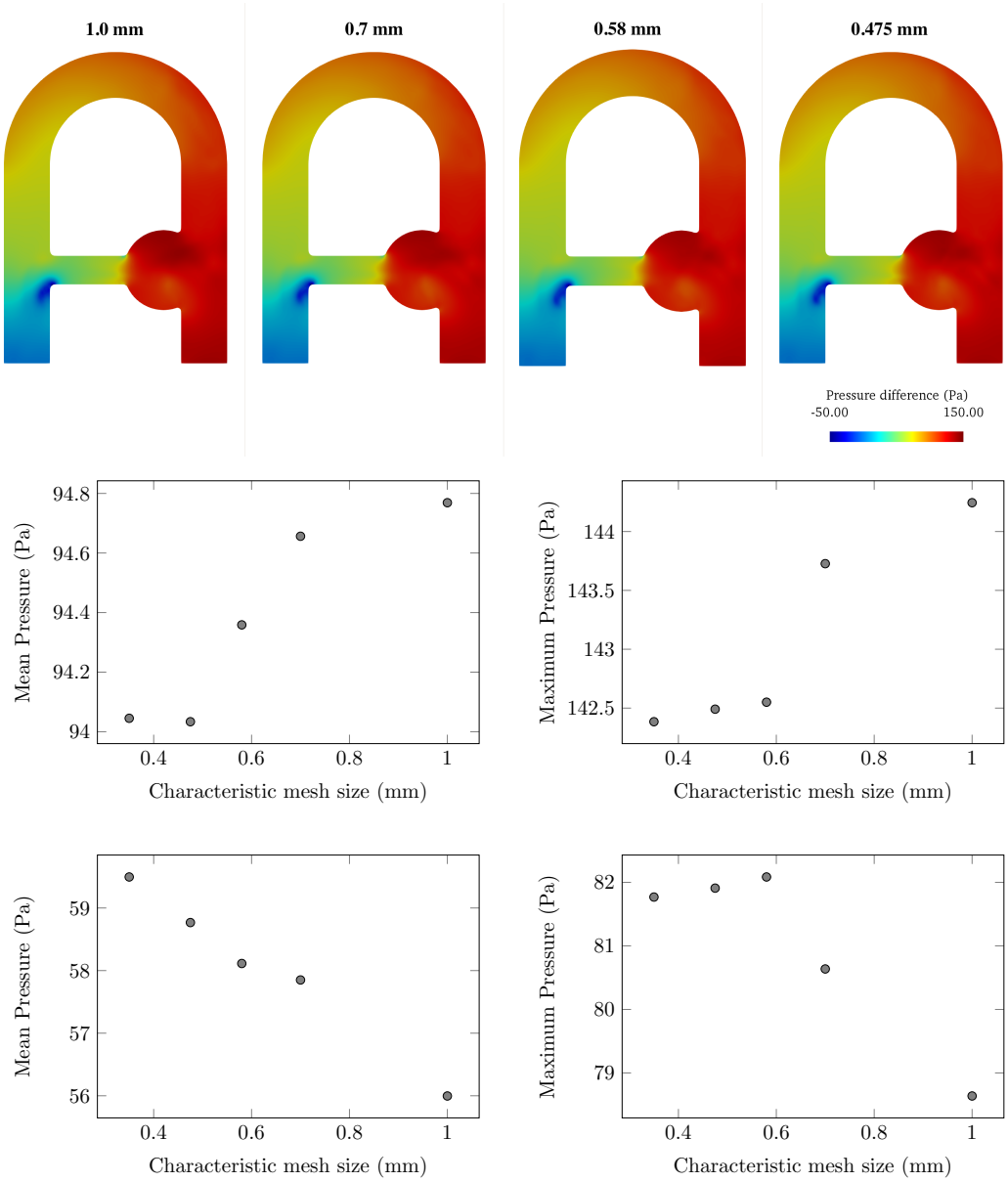

Figure 5.7: Mesh convergence of the CFD pressure field for meshes M1 to M5 at peak systole. **First row**: Pressure difference maps in the middle slice of the flow phantom at peak systole ($t/T_p = 0.25$). **Second row**: **left** Mean and **right** maximum pressure field over the entire domain. **Last row**: **left** Mean and **right** maximum pressure field over the collateral branch.

If steady flow is considered, the weak formulation of the Bernoulli principle is raised:

$$\rho\frac{\mathbf{u}\cdot\mathbf{u}}{2}+\rho F+p=cste=\mathcal{H} \tag{5.6}$$

This relation is valid along all the isovalues of $\mathcal{H}$, which are equivalent to the velocity streamlines as $\mathbf{u}\cdot\nabla\mathcal{H}=0$.

Simplified Bernoulli

From this formulation, a common simplification in clinical practice consists in measuring the peak velocity from PC-MRI to deduce the peak pressure from a simplified Bernoulli relation:

$$\Delta P=K\left(\mathbf{u}\cdot\mathbf{n}\right)^2 \tag{5.7}$$

where $\mathbf{u}\cdot\mathbf{n}$ is the velocity normal to the centreline of the vessel, and K the loss coefficient which is taken as 4.0 mmHg.s^2/m^2 as recommended in Baumgartner et al. (2009) [7]. It will be denoted as Simplified Bernoulli (SB) formulation in the next paragraphs. The strong assumptions behind in the simplified Bernoulli relation (steady, inviscid, incompressible fluid) have led to several extended versions of the Bernoulli relation that account for the viscous dissipation as a function of the geometry of the vessel.

Unsteady Bernoulli

A more general (strong) formulation of the Bernoulli principle valid for time-varying flows (denoted UB for Unsteady Bernoulli) can also be derived. Under the assumption of irrotational flow, one can write the velocity as $\mathbf{u}=\nabla\phi$, and the previous Eq. 5.5 simplifies:

$$\rho\frac{\partial\phi}{\partial t}+\rho\frac{\mathbf{u}\cdot\mathbf{u}}{2}+\rho F+p=cste=\mathcal{H} \tag{5.8}$$

This relation is called the strong formulation of the Bernoulli principle since it is true regardless of the streamline. It is common to find another formulation of the unsteady Bernoulli principle, obtained by integration of the Euler equation along a streamline between points A and B:

$$\rho\int_A^B\frac{\partial\mathbf{u}}{\partial t}\cdot\mathbf{ds}+\rho\frac{\mathbf{u}_B\cdot\mathbf{u}_B}{2}+\rho F_B+p_B=\rho\frac{\mathbf{u}_A\cdot\mathbf{u}_A}{2}+\rho F_A+p_A \tag{5.9}$$

where the flow path is defined by the curvilinear coordinates s. This equation stands valid while the flow streamlines do not change with time. In this sense, a simplification adopted to compute pressure from the unsteady Bernoulli formulation is that the streamline considered follows the centreline of the vessel.

The simplicity of the Bernoulli-based pressure estimation approaches makes them generally valuable for fast evaluation of pressure drops. Nevertheless, as viscous effects are not accounted for, this can raise pressure estimation errors.

Pressure Poisson equation

On the other side, a more local (spatio-temporal) relative pressure distribution has been made accessible by the apparition of 4D Flow MRI. The methods that fully benefit from the use of local spatio-temporal velocity distribution are based on the full Pressure Poisson equation (PPE). Recalling the incompressible NSE:

$$\nabla p = \underbrace{-\rho \frac{\partial \mathbf{u}}{\partial t}}_{\text{transient}} \underbrace{- \rho \mathbf{u} \cdot \nabla \mathbf{u}}_{\text{convective}} + \underbrace{\mu \Delta \mathbf{u}}_{\text{viscous}} \tag{5.10}$$

A straightforward way to get the pressure could be by direct integration of the pressure gradient (Eq. 5.10) to recover the pressure up to an additive constant. However, for noisy input velocity data, this integration step depends upon the path chosen, which is not appropriate [46]. Instead, by taking the divergence of Eq. 5.10, a PPE arises:

$$\nabla^2 p = \nabla \cdot \left(\mu \Delta \mathbf{u} - \rho \left(\frac{\partial \mathbf{u}}{\partial t} + \mathbf{u} \cdot \nabla \mathbf{u} \right) \right) \tag{5.11}$$

where $\mathbf{u}$ is the velocity, μ the dynamic viscosity, p the pressure, and ρ the density of the fluid. If $\nabla \cdot \mathbf{u} = 0$, the previous equation can be simplified:

$$\nabla^2 p = -\nabla \cdot (\rho \mathbf{u} \cdot \nabla \mathbf{u}) \tag{5.12}$$

The relative pressure can be recovered by solving this equation. Note that this equation stands only if the velocity field verifies $\nabla \cdot \mathbf{u} = 0$, which is generally false for raw MRI measurements.

Dynamic forcing

If the pressure is computed for each MRI image independently, the transient contribution ($\frac{\partial \mathbf{u}}{\partial t}$) of the pressure gradient reduces to zero and a steady pressure is calculated.

A dynamic forcing term can also be added to ensure the flow continuity between two MRI phases and to account for inertial effects. In practice, we constraint the inflow velocity at each inlet boundary surface node i and at time n such that :

$$u_i^{n+1} = \alpha^n u_i^n \tag{5.13}$$

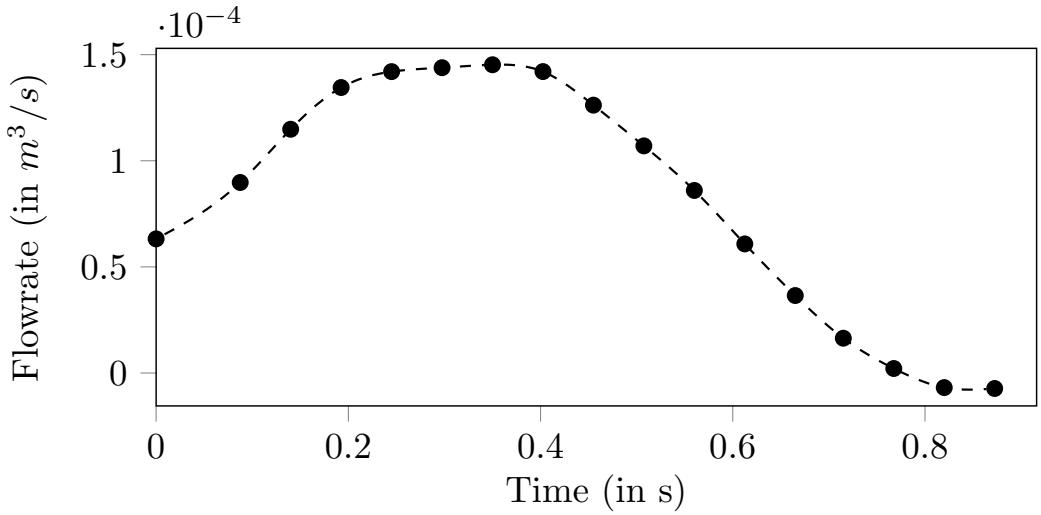

Figure 5.8: Temporal evolution of the inlet flow rate. • MRI measurements and - - spline cubic interpolation.

where α^n is the forcing coefficient that guarantee a continuous flow rate variations between two iterations, such as:

$$\alpha^n = \frac{q^{n+1}}{q^n} \tag{5.14}$$

where q^n the inlet volume flow rate at current phase t^n in the cycle. q^{n+1} is estimated by interpolating the measured inlet flow rates between two subsequent 4D Flow MRI images q^m and q^{m+1} (where m is the MRI phase number). A piecewise cubic spline interpolation was then performed at each iteration to re-evaluate q^{n+1} as well as the forcing coefficient. This allows a smooth variation of the transient term (first order derivative), as well as a continuous second-order derivative. The resulting spline cubic interpolation of the inlet flow rate is presented on figure 5.8.

This forcing term allows to account for the inertial contribution in the Unsteady Bernoulli principle.

5.3.4 Comparison with Bernoulli-based approaches

In Figure 5.9, the pressure drops computed from the simplified Bernoulli (SB) and unsteady Bernoulli (UB) approaches are compared to the reference CFD. As the UB pressure drop depends on the integration path, both collateral and bend centrelines were considered. The CFD (steady) corresponds to the CFD pressure field with only the viscous and convective contributions kept and the transient term suppressed ($\frac{\partial \mathbf{u}}{\partial \mathbf{t}} = \mathbf{0}$). Similarly, CFD (transient) corresponds to a CFD

where the viscous and convective terms are set to zero and only the transient contribution is kept.

The first interesting result is that the steady CFD and full CFD provide totally inverse pressure drop trends. The steady CFD pressure drop evolution follows the flow rate evolution, while the full CFD agrees with the flow rate time derivative (i.e: transient term). This can be verified looking at the full CFD pressure evolution, where a plateau arises at peak systole and a zero-crossing happens when the flow rate starts decreasing.

As it does not include the transient pressure contribution, the SB approach provides a pressure drop which is largely not representative of the full CFD pressure evolution. Nevertheless, as it roughly follows the steady CFD pressure drop, it might be well suited for estimating pressure drop for steady flows.

The UB approach underestimates the full CFD pressure drop, irrespective of the path used; this could be due to the inviscid flow assumption of the Bernoulli principle that tends to reduce the overall pressure due to the lack of diffusion term. Note that the main pressure drop differences between the two paths closely follow the flow split temporal distribution illustrated in Figure 4.4. At the beginning of the cycle, the higher flow rate time-derivative observed in the collateral branch corresponds to a higher pressure drop, while from peak systolic to diastolic phase, higher flow rate acceleration occur in the bend that results in a pressure drop overestimation.

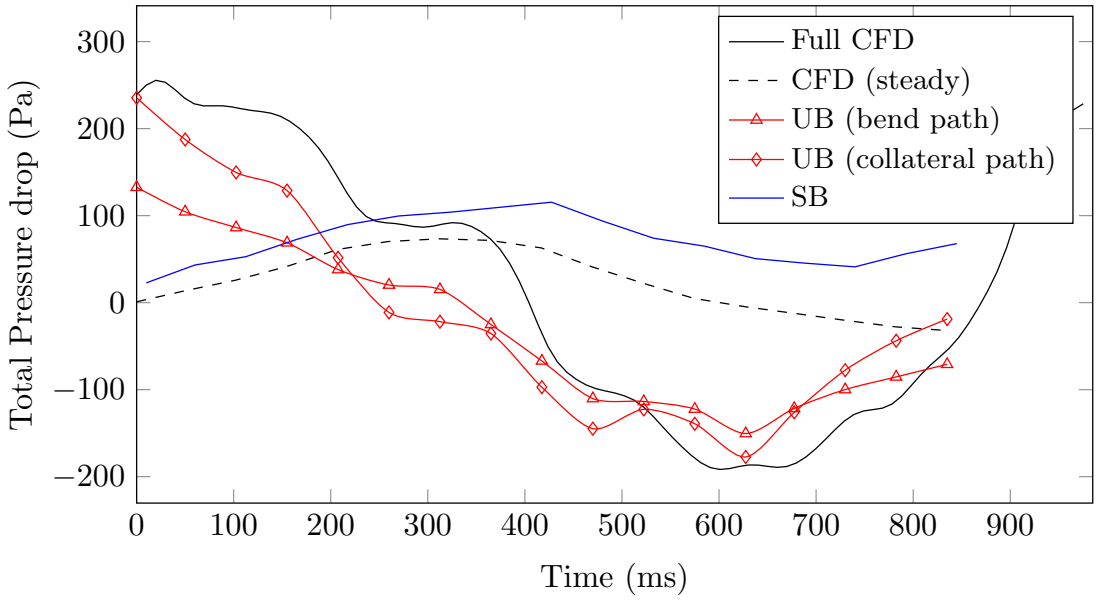

Figure 5.9: Total pressure drop evolution in a cycle. Simplified Bernoulli (SB) corresponds to the pressure drop given in Equation 5.7 while Unsteady Bernoulli (UB) is the solution of Equation 5.9. CFD (steady) corresponds to a CFD solution where no dynamic forcing is applied.

5.3.5 Conclusion

The total pressure drop evolution in the cycle was compared for the different pressure reconstruction methods. Additionally, several PPE-based methods are presented and compared in Appendix 7.4.

Regarding the Bernoulli-based methods, as expected the simplified Bernoulli equation brings very few information about the pressure drops at highly pulsatile regime. It should however be better suited to the estimation of the pressure drop where the viscous and convective contributions dominate as for example in smallest cerebral arteries. On the contrary, the unsteady Bernoulli relation exhibits global good trends with small variations depending on the path followed (either the main segment or the collateral segment). This result shows that the pressure in this configuration is fully piloted by the transient contribution and that viscous and convective terms only play a minor role. This emphasizes the importance of systematically including the transient contribution ($\frac{\partial \mathbf{u}}{\partial t}$) in the pressure computation. This can easily be achieved with an adapted numerical post-processing of the MRI measurements.

In this sense, under cardiovascular regime (where the transient term dominates), a fast and reliable pressure drop can be estimated from the unsteady Beenoulli principle computed with only a 2D CINE PC-MRI acquisition at the inlet surface and the morphology of the vessel. While it provides a reasonable estimate as compared to the computational effort required, solving the full PPE from 4D Flow MRI measurements should be more adapted where a local estimate of the relative pressure is needed.

Chapter 6

Simulation of 4D Flow MRI

Chapter contents

6.1 Introduction

The principal concern of the previous chapters was to evaluate the discrepancies that arise either from direct MR velocity measurement or when reconstructing an hemodynamics field, as compared to a pre-established ground truth CFD flow

field. The errors relative to the comparison with the CFD were alleviated, so that one can reasonably assume that the remaining divergences are principally due to the MRI acquisition process. While some hypothetical culprits were inferred, the origins of the discrepancies were not formally identified so far. Indeed, the complex physical principles governing the MR signal acquisition process, the signal processing steps required to reconstruct an MR image, as well as the large variety of user-dependent acquisition parameters, are as many potential sources of errors that make it generally difficult to localize with precision the sources an error in a particular measurement..

6.1.1 The simulation of the MRI acquisition process

The numerical simulation of the MRI acquisition process could be an efficient way to decompose these modalities and to understand the mechanism that lead to the measurement errors: it has already proven its usefulness to describe and correct some sources of imaging artifacts [122], as well as to optimize MRI pulse sequences [4] for morphological MRI. The well-known MR fingerprinting technique [96] is a good illustration of a possible use of MRI simulation to generate a dictionary containing a representative variety of tissue MR signatures.

As already detailed in Chapter 2, the main core of the acquisition process is based on the phenomenon of Nuclear Magnetic Resonance (NMR), described at the macroscopic scale by the Bloch equations [17]:

$$\frac{d\mathbf{M}(t)}{dt} = \gamma \mathbf{M}(t) \times \mathbf{B}(t) + \frac{M_0 - M_z(t)}{T_1}\hat{e}_z - \frac{M_x(t)}{T_2}\hat{e}_x - \frac{M_y(t)}{T_2}\hat{e}_y \tag{6.1}$$

where γ is the gyromagnetic ratio, $\mathbf{B}$ is the external magnetic field experienced by the nuclei, $\mathbf{M} = (M_x, M_y, M_z)$ is the nuclear magnetization vector, T_1 and T_2 are the relaxation times of the magnetization and M_0 is the steady state magnetization.

6.1.2 The simulation of Bloch equations for flowing spins

Although many simulation frameworks have already been developed for static tissues imaging [8, 16, 148, 164], modelling the flow MRI is still a challenging issue. This is mainly due to the necessity to account for the dynamics of the spins, which results in a considerable increase of the computational load. In its classical formulation (see Equation 6.1), the Bloch equations are ordinary differential equations (ODE) expressed with a Lagrangian formalism. Nevertheless, when moving spins are considered, the input velocity field required to simulate the dynamics of the spins is usually predicted by Computational Fluid Dynamics (CFD) on a fixed numerical mesh.

Eulerian approach

A classical approach often adopted in the literature is then to consider the Eulerian formulation of the Bloch equation [67, 75, 93]. In this case, the CFD velocity is used to transport the magnetization vector and a non linear convection term is explicitly added to the time rate of change of the magnetization vector ($\mathbf{M}$), which becomes:

$$\frac{d\mathbf{M}}{dt}(\mathbf{r},t) = \frac{\partial \mathbf{M}(t)}{\partial t} + (\mathbf{u}(\mathbf{r},t)\cdot\nabla)\mathbf{M}(t) \tag{6.2}$$

The Eulerian approach has a relatively low computationaly cost since both the flow and Bloch equations can be solved on the same fixed mesh and no velocity interpolation is needed. Nevertheless, the Eulerian equations becomes a partial derivative equations and does not admit a generally valid analytical solution. Moreover, it encompasses some modelling assumptions as the necessity to prescribe boundary conditions for the magnetization vector, and some transformations of the mesh are needed to correct for the spatial misregistration effects [75, 93], although another method uses local magnetization transformations to account for the flow-related effects [76]. Finally, this approach is less adapted to complex flow configuration, where the time scale of the velocity variations is small as compared to the time scale of the MR sequence [93].

Lagrangian approach

An alternative approach consists in modelling the spins with Lagrangian particles, using the CFD velocity to update each particle position. The Bloch equations can then be solved independently for each particle, with no spin-spin interaction [54, 103, 126]. Therefore, the computational load can easily be partitioned on multiple cores to accelerate the calculations. Nevertheless, a sufficient number of particles is necessary to accurately approximate the MR signal. As found in [136], at least 3 particles/direction/voxel are necessary to reduce the MR signal error to 1.5%: this may require high computational resources depending on the image spatial resolution. Homogeneous particle repartition within the domain is also needed to avoid zones with spurious MR signals [54]. In the usual procedure [54, 76, 79, 103, 126, 146, 164], a prior CFD simulation is performed to store all the particle positions during the entire simulation; this approach can be suited for steady flows but seems irrelevant for pulsatile flows simulations where very large physical time (and thus particle position) are generally simulated. To illustrate this, particle tracking along the simulation of a 4D Flow MRI scan of physical duration $T_{acq} = 6\ min$, with a constant time step $\Delta t_{CFD} = 10^{-3}\ s$, injecting 3 particles per direction per voxel would require to store about 60 TB of memory for an acquisition matrix of size $(160, 160, 20)$. The huge file size and the repeated accesses to this file, on top with the temporal interpolation needed to update the

particle position at different time point of interests during the MRI simulation would most probably lead to highly prohibitive computational costs. To address this problem, the CFD simulations can be performed "on the fly", i.e. performed simultaneously to update the particle positions at each iteration, with no particles path tracking required.

With the gain of computational power due to the recent improvements of hardware and software capabilities, well resolved computations are now achievable at reasonable costs: to that extent, Lagrangian computations then become feasible and adapted to simulate complex flow MRI measurements [93]. Moreover, the widespread interests expressed since the development of time-resolved 3D PC-MRI have involved many new developments to mitigate some artifacts (cardiac and respiratory motion [99]) and to reduce overall scan duration with compressed sensing [94] or parallel imaging [41]. However, to the author's knowledge, no simulation framework of time-resolved 3D PC-MRI sequences has ever been proposed yet, as summarized in the literature review presented on Table 6.1.

Table 6.1: Review of the published works in flow MRI simulations.

Publication	**Configuration**	**Formulation**	**Sequence**
Steinman et al., 1997 [146]	steady 3D idealised bifurcation	Lagrangian	2D/3D PC
Jou et Saloner, 1998 [75]	pulsatile 2D carotid bifurcation	Eulerian	2D GE VC/VU
Lorthois et al., 2005 [93]	steady 2D carotid bifurcation	Eulerian	2D GE VC/VU
Marshall, 2010 [103]	steady 3D carotid bifurcation	Lagrangian	3D PC
Petersson et al., 2010 [126]	steady 3D stenosis	Lagrangian	3D PC
Jurczuk et al., 2013 [76]	steady 3D straight/U-bend tubes	Eulerian	2D/3D GE
Xanthis et al., 2014 [165]	steady 3D cylinder	Lagrangian	2D PC
Klepaczko et al., 2014 [79]	steady 3D stenosed/U-bend tubes	Lagrangian	3D GE VC
Fortin et al., 2018 [54]	steady 3D cerebral artery	Lagrangian	3D PC

GE : gradient echo; VC: velocity compensated; VU: velocity uncompensated; PC: phase contrast.

The objective of this chapter is then to present a workflow for simulating realistic RF-spoiled time-resolved 3D PC-MRI acquisitions. To this aim, the numerical procedure for simulating the Bloch equations as well as the coupling with CFD are introduced. To reduce the computational cost associated with the simulations, a semi-analytical solution of the Bloch equations was implemented.

A series of validation test cases are then presented, where each independent block of the solver is validated in an incremental fashion. First, the resolution of Bloch equation for spins flowing along a 1-D line is compared with the literature [67, 171]. Then, the full velocity reconstruction pipeline (i.e. k-space filling, Fourier transform and velocity calculation) is tested through a Poiseuille flow configuration, where the reconstructed velocity is compared to the analytical Poiseuille flow profile imposed to the particles. The CFD coupling is also validated through the full simulation of a 4D Flow MRI sequence of the phantom experiment. The sensitivity of the solution to the temporal discretization and spin density is then analysed, and the parallel scalability of the code is presented. The influence of the spatial resolution on the resulting reconstructed velocity field is evaluated. Realistic 4D Flow MRI measurements are finally compared to the corresponding coupled CFD-MRI simulations. One of the interests of developing such a simulation framework is also briefly illustrated through the simulation of a common ghosting artifact.

6.2 Methods

6.2.1 4D Flow MRI simulation procedure

The CFD setup was already detailed in Section 4.5 and is not re-expanded. The entire CFD-MRI simulation procedure is illustrated in Figure 6.1. A pseudo-code of the procedure is provided in Algorithm 1.

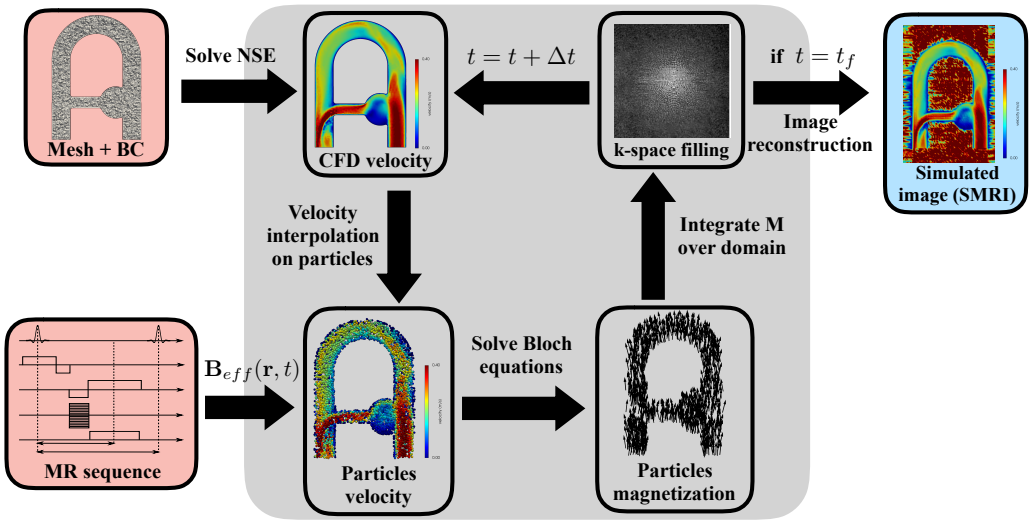

Figure 6.1: Main steps of the CFD-MRI simulation procedure. BC: Boundary conditions. The grey block corresponds to the simulation framework kernel, while the red/blue blocks are inputs/outputs to the simulation.

Algorithm 1: Pseudo-code of the coupled CFD-MRI simulation procedure.

Input :

$B_1(t), G_x(t), G_y(t), G_z(t), time, readout \longleftarrow$ InputSequence()

$T_1, T_2, \mathbf{M}(t=0), \mathbf{M}_{inj}(t) \longleftarrow$ ParticlesData()

```
1
2  Initialize Data:
3  x^p ⟵ FillWithParticles()
4  for p = 1 : n_pt do
5  |   M^p = M_z^ss
6  |   u^p = u_0
7  end
8  B_1(t), G_x(t), G_y(t), G_z(t), time, readout ⟵ ReadInputSequence(InputSequence)
9
10 Temporal Loop:
11 while not done do
12 |   t^m = t^n
13 |   Δt_cfd ⟵ CalcCFLTimeStep(CFL)
14 |   t^n = t^n + Δt_cfd
15 |   for i = 1 : n_nodes do
16 |   |   U^i ⟵SolveNavierStokes(U^i, Δt_cfd)
17 |   end
18 |   if spoiling==True then
19 |   |   DeactivateAllParticles(n_pt)
20 |   |   n_pt ⟵ FillWithParticles()
21 |   end
22 |   while t^m < t^n + Δt_cfd do
23 |   |   for p = 1 : n_pt do
24 |   |   |   B_eff^p ⟵CalcBeff(B_1(t^m), G_x(t^m), G_y(t^m), G_z(t^m))
25 |   |   |   Δt_mri^p ⟵ CalcMRTimeStep(B_eff^p)
26 |   |   |   t^m = t^m + Δt_mri^p
27 |   |   |   u^p ⟵ InterpolateVelocityOnParticle(U)
28 |   |   |   x^p ⟵AdvanceParticlePosition(x^p)
29 |   |   |   M^p ⟵SolveBloch(B_eff^p, Δt_mri^p)
30 |   |   end
31 |   |   if readout==True then
32 |   |   |   S(t^n) ⟵ CalcMRSignal(M^p)
33 |   |   end
34 |   end
35 end
36
```

Output : $S(t)$

Injection of particles

To model the spins, a homogeneous spatial distribution of N_p Lagrangian particles is injected within the fluid domain at the initialization of the computation. $N_{p,el}$ particles are injected inside each element of the Eulerian grid following a uniformly random distribution [133]. This randomization avoids spurious rephasing artifacts induced by regularly-spaced spins [150]. An injection magnetization $\mathbf{M}(t=0) = \mathbf{M_{inj}} = (0, 0, M_{inj})$ is prescribed as initial condition of each particle injected. The longitudinal magnetization is set to its steady state value $M_{inj} = M_z^{ss}$ so that no presaturation of the magnetization is required (see Section 2.8.3). To each particle p injected inside an element of volume V_{el} is associated an isochromat volume of weight $w^p = \frac{V_{el}}{N_{p,el}}$ to the magnetization vector. To each particle are also affected some magnetic properties (T_1, T_2, M_0).

Fluid-particle velocity interpolation

To advance the position of the particles, a fluid iteration is first performed (i.e. solve the NSE on the fixed numerical mesh) such that the Eulerian velocity field is advanced at time $t + \Delta t_{CFD}$. For numerical stability purposes, the CFD time step Δt_{CFD} was computed such that the CFL number remains equal to 0.9. In practice, it means that the distance travelled by a fluid particle during an iteration can not travel more than 90% of the smallest mesh element size. The velocity is interpolated from the CFD velocity field onto the particles with an inverse distance weighting interpolation. The particle position is then advanced using the interpolated velocity, as followed:

$$\mathbf{x}^p(t + \Delta t) = \mathbf{x}^p(t) + \int_t^{t+\Delta t} \mathbf{u}(\mathbf{x}^p) dt \tag{6.3}$$

where Δt is a numerical time step. This numerical time step is associated to the particle advancement which depends on the discretization of the Bloch equations. It can therefore differ from Δt_{CFD}. The integration is performed with a third-order Runge-Kutta method (RK3).

Simulation of the RF-spoiling

As found in [54], a realistic simulation of an RF-spoiling event that raise an error under 3% should require 1000 isochromats/voxel to avoid constructive vector summation resulting in spurious signal due to the discrete spatial distribution of particles. This however would lead to a dramatic increase of the computational costs. To circumvent this problem, the RF-spoiling was modelled by nulling the transverse magnetization of each particles. In practice at each spoiling event, all the particles within the domain are suppressed, and N_p particles are reinjected at

the same location as initially, with the magnetization vector reset to its initial value $\mathbf{M_{inj}} = (0, 0, M_z^{ss})$. Although the longitudinal magnetization is not affected by the spoiling, M_z converges by definition towards the same value M_z^{ss} after each repetition time as it is systematically reset to $M_{inj} = M_z^{ss}$. The re-injection of particles at the same initial location is a key step of the methodology that allows to keep the particles distribution homogeneous, and to avoid zones of spurious signal due to either a lack of particles in regions of high velocities, or the accumulation of slow velocity particles near the boundaries. Under certain circumstances that will be discussed later, it also allows to partition the simulation into independent sub-computations with respect to time.

Effective magnetic field

Between each fluid iteration, the Bloch equations are solved in the frame of reference that rotates clockwise around the z-axis at Larmor frequency $\omega = \omega_0 = \gamma B_0$, by convention. It is recalled that Bloch equations in Eq. 6.1 expressed in the rotating frame allow to cancel the static magnetic field contribution, such that it can be expressed as a function of the effective magnetic field $\mathbf{B_{eff}} = \mathbf{B} - \frac{\omega_0}{\gamma}\hat{e}_z$. The effective magnetic field perceived by a particle at position $\mathbf{x}^p$ and iteration t^n in this frame of reference is calculated as:

$$\mathbf{B_{eff}}(\mathbf{x}^p, t^n) = \begin{pmatrix} B_x \\ B_y \\ B_z \end{pmatrix} = \begin{pmatrix} B_1(t^n)\cos(\omega_1 t^n) \\ -B_1(t^n)\sin(\omega_1 t^n) \\ \mathbf{x}^p \cdot \mathbf{G}(t^n) + \Delta B_z(\mathbf{x}^p, t^n) \end{pmatrix} \tag{6.4}$$

where B_1 is the RF field that rotates around the z-axis at frequency ω_1 with respect to the frame of reference. $\mathbf{x} \cdot \mathbf{G}$ corresponds to the magnetic field induced by the gradient coils for spatial and velocity encoding and $\Delta B_z(\mathbf{x}^p, t^n)$ represents the deviations of the magnetic field due to off-resonance effects. The off-resonance effects mainly comprise non linear gradients, concomitant fields, eddy currents, chemical shift, $T2^*$ dephasing, and magnetic susceptibility. In the initial development phase, these effects are neglected. Note that all the sequences were generated with the JEMRIS sequence development interface [148].

Temporal discretization

A multi-criterion time-stepping approach was implemented to solve the Bloch equations while ensuring the numerical stability of the solution as well as a sufficient temporal resolution to capture the highest frequencies of the external magnetic field. The first time step criterion corresponds the CFL stability Δt_{CFD}. It imposes a regular update of the information between Eulerian (CFD) and Lagrangian (particles) variables.

Similarly, as will be detailed in the next Section 36, a numerical integration is adopted under some conditions to advance the Bloch equations. During magnetic events when the RF is off, a numerical stability criterion for the explicit Runge-Kutta scheme could be obtained from a stability analysis, which enforces the following time step constraint:

$$\Delta t_{stab} < \frac{2}{T_2 \left(\frac{1}{T_2^2} + \gamma^2 B_z^2 \right)} \tag{6.5}$$

A derivation of this result can be found in Appendix 7.4.3. To capture the stiff variations of the magnetization induced by the abrupt changes of the magnetic field source term, an additional time step is calculated as:

$$\Delta t_{rf} = \frac{b_n}{\gamma B_{eff,max}} \tag{6.6}$$

where $B_{eff,max}$ corresponds to the maximum effective magnetic field imposed in the sequence. where b_n (for Bloch Number) is a dimensionless coefficient fixed by the user. A convergence analysis of the Bloch number was performed and is presented in Section 6.3.

When the particle experiences a ramping gradient field, an additional time constraint applies:

$$\Delta t_{grad} = 0.1 \frac{G_{max}}{\left| \frac{\partial G}{\partial t} \right|} \tag{6.7}$$

where G_{max} is the maximum gradient amplitude specified in the sequence. This constraint ensures that each gradient ramps is sampled by at least ten time points. It was notably added to cover the instants with small or null $\mathbf{B_{eff}}$ and with high gradient time derivative.

A supplementary time constraint Δt_{seq} was added to ensure the adequate sampling of the RF waveform, as well as the correct spacing between readout samples.

Finally, the magnetic time step is calculated as: $\Delta t = \min\left(\Delta t_{CFD}, \Delta t_{stab}, \Delta t_{rf}, \Delta t_{grad}, \Delta t_{seq}\right)$. Note however that the resulting magnetic time constraints are generally more restrictive (three or four order of magnitude lower) than the fluid time steps. A typical time step distribution is illustrated in Fig. 6.2. To avoid somewhat redundant CFD calculations, the fluid velocity is kept constant while the sum of the magnetic time steps is below the CFD iteration length. This multi-time step integration strategy significantly reduces the overall computation time as compared to a classical uniform time stepping strategy for all the physics.

Numerical advancement of the Bloch equations

So far, two classes of approaches have been adopted in the literature to solve the Bloch equations. The first approach was initially developed in the work

Figure 6.2: Evolution of the simulation time step over an arbitrary pulse sequence (RF and gradient) as a function of the magnetic event. Between each Δt_{CFD}, the fluid velocity is kept constant. The particle velocity is updated at each iteration as a function of its updated position.

of Bittoun et al. [16]. It consists of approximating the driving magnetic field as a series of piecewise constant waveforms (rectangular pulses and gradients), and accounting for each contribution as a transformation of the magnetization vector. This approach was initially designed for static tissues simulations but later extended to the flow-related effects [76, 164]. Because of the explicit formulation of the magnetization, this method requires a relatively low computational effort. However, this approach is only valid for hard pulse and not allow to simulate both arbitrary RF-pulse shapes and gradients ramps. The term explicit here corresponds to an analytical formulation but differs from the one presented in this work.

Another approach is based on a full numerical integration, where an iterative method is used to approximate the Bloch equations, with no preliminary assumption on the magnetic field waveform [54, 93, 148]. This resolution method is relatively simple to implement and the accuracy depends on the order of truncation. However the numerical integration steps result in higher computational cost as compared with an explicit formulation. The numerical integration approach could be unnecessarily time consuming in regimes where the Bloch equations admit analytical solutions. For this reason, in this study, a semi-analytical solution was implemented. The Bloch equations are solved with full numerical integration (RK4) during the RF excitations, and analytically whenever the particles experience a relaxation or encoding gradients events. Obviously, this approach is valid only if gradient waveforms can be described analytically.

Considering $t = 0$ as the end of the RF pulse (where $B_x(t) = B_y(t) = 0 \; \forall 0 < t < t^n$), the Bloch equations can be expressed as:

$$\frac{dM_{xy}}{dt} = -(\frac{1}{T_2} + i\gamma B_z)M_{xy} \tag{6.8}$$

The previous equation admits the following solution:

$$M_{xy}(\mathbf{x}^p, t^n) = |M_{xy}(\mathbf{x}^p, 0)|e^{i\phi_0}e^{-t^n/T_2}e^{-i\gamma\phi(\mathbf{x}^p,t^n)} \tag{6.9}$$

where $\phi(\mathbf{x}^p, t^n) = \int_0^{t^n} \gamma B_z(\mathbf{x}^p, t)dt$ and ϕ_0 is the phase of the transverse magnetization at the end of the RF pulse. In the ideal case where off-resonance effects are neglected, the phase can be decomposed in the rotating frame of reference as a sum of piecewise analytical expressions, such as the phase reads:

$$\phi(\mathbf{x}^p, t^n) = \int_0^{t^n} \mathbf{x}^p(t) \cdot \mathbf{G}(t)dt = \sum_{m=0}^{n-1} \int_{t^m}^{t^{m+1}} \mathbf{x}^p(t) \cdot \mathbf{G}(t)dt \tag{6.10}$$

As piecewise constant gradients with linear ramps are assumed, one can write:

$$\mathbf{G}(t) = \mathbf{G}(t^m) + \left.\frac{\partial \mathbf{G}}{\partial t}\right|_m (t - t^m) \tag{6.11}$$

An important approximation of the phase-contrast MRI formulation is the constant velocity assumption between each relaxation. To this respect, in order to conserve the benefits of the 3rd-order accurate particle position advancement (see Eq. 6.3), the phase is advanced as:

$$\mathbf{x}^p(t) = \mathbf{x}^p(t^m) + \mathbf{u}^p_{rk}(t^m)(t - t^m) \tag{6.12}$$

where $\mathbf{u}^p_{rk} = \frac{\mathbf{x}^p(t^{m+1}) - \mathbf{x}^p(t^m)}{t^{m+1} - t^m}$ is obtained from the RK3 particle position advancement. Replacing these expressions in the previous Equation 6.10 gives rise to the following phase:

$$\phi(\mathbf{x}^p, t^n) = \sum_{m=0}^{n-1} \gamma \left(\mathbf{a}^m \Delta t^m + \mathbf{b}^m (\Delta t^m)^2 + \mathbf{c}^m (\Delta t^m)^3 \right) \tag{6.13}$$

where $\Delta t^m = t^{m+1} - t^m$, and

$$\begin{aligned} \mathbf{a}^m &= \mathbf{x}^p(t^m) \cdot \mathbf{G}(t^m) \\ \mathbf{b}^m &= \frac{1}{2}\mathbf{x}^p(t^m) \cdot \left.\frac{d\mathbf{G}}{dt}\right|_m + \mathbf{u}^p(t^m) \cdot \mathbf{G}^p(t^m) \\ \mathbf{c}^m &= \frac{1}{3}\mathbf{u}^p(t^m) \cdot \left.\frac{d\mathbf{G}}{dt}\right|_m \end{aligned} \tag{6.14}$$

This formulation could easily be implemented and is valid either when encoding gradients are on or during relaxation processes. Here the gradients waveforms are assumed linear for sake of simplicity but the same reasoning could be adopted for non linear gradients waveforms as long as it can be analytically described (such as for non-Cartesian k-space trajectories or when adding off-resonance effects). Note also that the assumed linear evolution of the spin position was not only a modelling assumption, but also constraint in the phase-velocity expression, where the high-order terms are neglected.

The phase ϕ can then be reintroduced in Eq. 6.9 so that the magnetization can be explicitly calculated.

At the end of each iteration, the particle position is updated from the velocity vector, and this procedure is repeated until the end of the pulse sequence.

Signal reception and velocity reconstruction

During the readout events, M_{xy} is integrated over the entire flow domain Ω. The complex signal is then obtained by:

$$s(t^n) = \sum_{p=1}^{N_p} C_{xy}(\mathbf{x}^p) w^p M^p_{xy}(t^n) \tag{6.15}$$

where C_{xy} is the receiver coil sensitivity profile and w^p the isochromat volume. The signal collected at instant t^n corresponds to a unique point (k_x, k_y, k_z) in the k-space. When the k-space is completely filled, a 3D Discrete Fourier Transform is applied to the complex k-space signal s to reconstruct the phase ϕ and magnitude I images in the spatial domain. Finally, the 3D velocity map along each encoding velocity direction i is obtained as:

$$u_i = \Delta\phi_i \frac{V_{enc,i}}{\pi} \tag{6.16}$$

where $\Delta\phi_i = \arg(I_0) - \arg(I_i)$ where I_0 corresponds to the reference scan image where no velocity encoding gradients are applied, and I_i to the image of the i-th velocity encoded direction.

6.2.2 Numerical efficiency of the semi-analytic formulation

To evaluate the computational efficiency of the method, the acquisition of a Poiseuille flow with a 2D PC-MRI sequence was simulated with the semi-analytic formulation and compared to the results obtained with the full numerical integration method. Results are presented in Figure 6.3. While both methods seem to linearly evolve with the number of spins/voxel, the semi-analytic method is 5 times faster for the same result: the mean residual errors were substantially the same for both formulations.

6.2.3 Scaling of the simulations

The strong scaling of the computations was evaluated to measure the parallel efficiency of the code. This allows to estimate the ideal number of cores necessary to minimize the computational cost. To compute the strong scaling, a 4D Flow MRI sequence of the phantom experiment at 3 mm^3 spatial resolution was simulated. The computational load was distributed to a varied number of cores, and the total time elapsed in the temporal loop was recorded. The strong scaling efficiency was obtained as: $speedup(n) = T_1/T_n$ where T_n corresponds to the total time needed to complete the computation with n cores. The resulting speed-up shown in Figure 6.4 reports a satisfactory scaling of the problem. This is a direct consequence of the the main parallel features (inter-process communications and double domain decomposition [117]) inherited from the optimized hybrid programming interface implemented in the YALES2BIO solver. When increasing the number of cores while keeping the problem size fixed, the speed-up stalls from the ideal scaling curve. This was expected since an ideal scaling corresponds to a computation with no time spent in inter-processor communications. However in practice, the

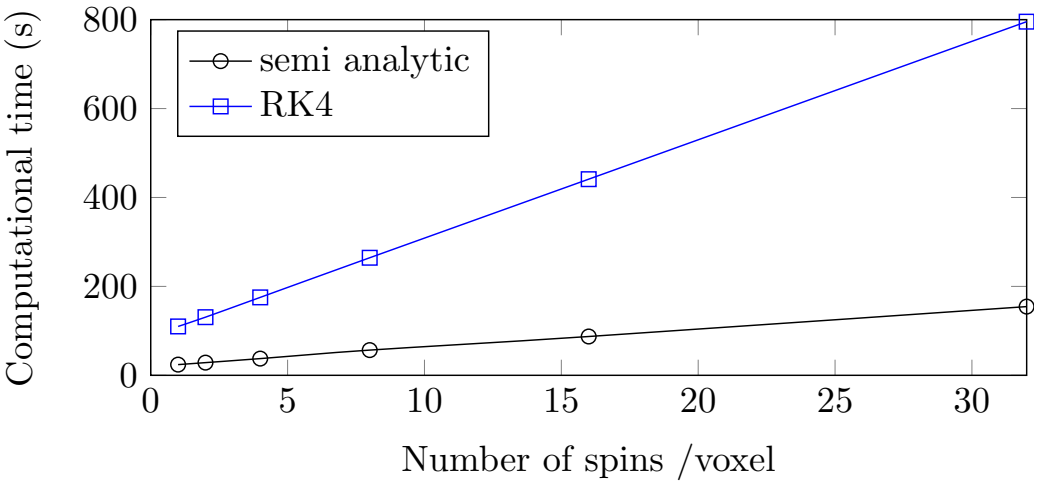

Figure 6.3: Computational time for the MRI simulation of a Poiseuille flow with a 2D PC-MRI sequence, at different spin densities with an imaging matrix of size $16 \times 16 \times 10$. The proposed semi-analytic formulation is compared to the full numerical integration method, where a fourth-order Runge-Kutta numerical scheme is adopted to discretize the Bloch equation. The computations are performed on one Dell PowerEdge C6320 node containing 28 cores Intel Xeon E5-2690 V4 2,6 GHz with 128 GB random-access memory.

time needed for inter-processor communications increases as compared to the time spent doing intra-processor operations, when the number of processors increases.

Note also that the scalability was computed for two different spin densities. The results show that a better parallel efficiency is reached when the spin density is larger and that the gap gets amplified with the number of cores. As the relative load allocated for the particles-related operations increases with increasing spin density, this behaviour well illustrates that Lagrangian computations are better suited for parallelization than the Eulerian-related operations which require processor communications.

6.2.4 Time partitioning of the computations

At each RF-spoiling, particles are removed, and reinjected with a similar initial magnetization prescribed. This complete reinitialization of the magnetization state allows a splitting of the calculation in independent partitions, where each partition simulates the filling of a specific k-space line. Given sufficient computational resources, the wall-clock time could then be significantly reduced, by a factor that equals the number of spoiling events within the sequence. Wall-clock time here means the elapsed real time required to achieve the simulations. This is thus different from the CPU-time, which should stay constant or slightly increase as multiple initialization steps are performed. Note that this partitioning was

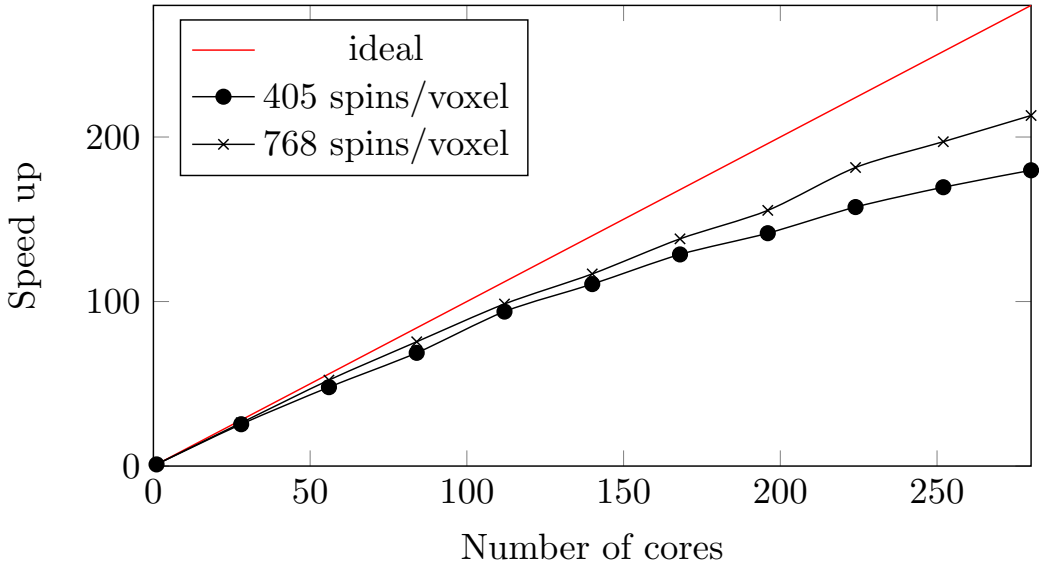

Figure 6.4: Strong scaling of the Bloch solver performed on a 4D Flow MRI sequence at $3mm^3$ spatial resolution with two different spin densities considered (405 and 768 spins/voxel).

used during the validation process for Bloch simulation of steady flows or static tissues. However, the time partitioning does not allow to capture the cycle-to-cycle velocity fluctuations since the reinitialized velocity state at spoiling event is not known a priori. Assuming negligible cycle-to-cycle fluctuations, this partitioning can be expanded to the simulations of time-resolved PC-MRI coupled with CFD by reinitializing the particle velocity state at each spoiling event with the same periodic velocity field.

6.3 Validation of the Bloch solver

6.3.1 Magnetization vector

First, the configuration proposed by Yuan et al. [171] and reproduced in [67] was tested to validate the implementation of the Bloch equation solver. The evolution of the magnetization vector produced by isochromats flowing along a 1-D segment under a simple 90° slice-selection pulse sequence (see Fig. 6.5a) was simulated and compared to the results obtained in [171]. The magnetization was recorded at the end of the rewinder gradient as marked by the arrow in Fig. 6.5a. The resulting magnetization profiles are compared for several input spins velocities (from 0 to 200 cm/s) in Figure 6.6. It results in highly similar distributions irrespective of the velocity regime. The relative error defined as $\epsilon = \| \frac{M_i - M_{i,ref}}{M_{i,ref}} \|$ where $M_{i,ref}$ is the i-th component of the magnetization found in Yuan et al., was calculated

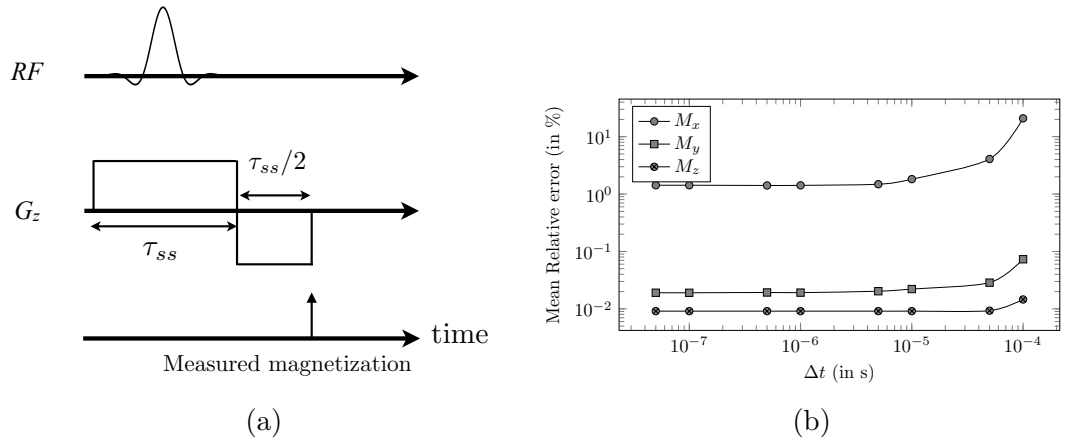

(a) (b)

Figure 6.5: (a) 90° slice selective excitation used in Yuan et al. [171]. (b) Evolution of the magnetization error with the time step, for the RK4 time integration scheme.

as a function of the time step, for the case where the velocity is zero, and is shown in Figure 6.5b. The y and z magnetization components converge towards a relative error level around $\epsilon \approx 10^{-4}$ while M_x errors are two orders of magnitude higher. This can be explained by the fact that the spins are not in phase in the x-direction, as shown by the non linear magnetization response described in the Bloch equations.

6.3.2 Full velocity reconstruction pipeline

As the previous test case validates only the magnetization, a second test case was performed to validate the full velocity reconstruction pipeline (phase and reconstruction algorithm). Moreover, it was additionally used to study the Bloch number and spin density convergence.

A Cartesian mesh of a square duct of $L = 32\ mm$ edge length was designed. At the centre, a Poiseuille velocity profile was prescribed such that:

$$\begin{aligned} w(r) &= w_{max}\left(1 - \frac{r^2}{R^2}\right) \quad \text{if } r < R \\ &= 0 \quad \text{elsewhere} \end{aligned}$$

where $R = 8\ mm$ is the radius of a cylindrical pipe and $w_{max} = 0.1\ m/s$ the maximum axial velocity. Note that a buffer zone was added upstream of the slice position in order to pre-saturate the spins near the inlet, and avoid spurious magnetization inflow effects. As it gathers both static and moving spins, this configuration allows to mimic the behaviour at the interface of a vessel. A 2D PC-MRI sequence in transversal orientation with a matrix size $N_x, N_y = (32, 32)$ and a voxel size $\Delta x = 1\ mm, \Delta y = 1\ mm, \Delta z = 10\ mm$ was simulated. 512

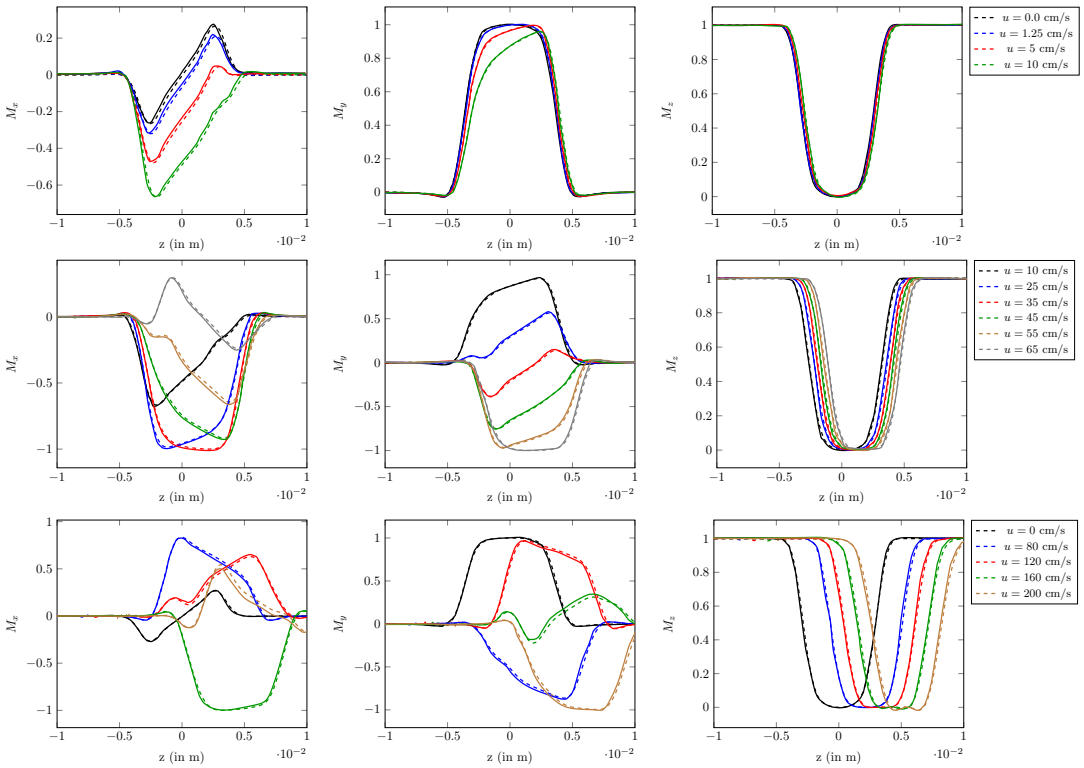

Figure 6.6: Evolution of the magnetization (M_x, M_y, M_z) along a straight line for several velocities imposed to the particles. The dashed lines correspond to the YALES2BIO simulation results, while solid lines correspond to Yuan et al. data [171].

spins/voxel were injected in the flow domain and the Bloch number was fixed to $b_n = 0.1$. The image reconstruction was performed by 2D Fourier transform of the k-space signal collected. The velocity field evaluated in the reconstructed image was compared with the analytical Poiseuille flow solution.

Results shown in Fig. 6.7b reveal an accurate reconstruction of the velocity profile, with a $RMSE = 3.6\%$ where the RMSE is the axial velocity root-mean-square error defined as: $RMSE = \sqrt{\frac{1}{N}\sum_{i=1}^{N}\left(w_{CFD}(\mathbf{x}_i, t^n) - w_{SMRI}(\mathbf{x}_i, t^n)\right)^2}$. A time convergence analysis was undertaken by varying the Bloch number (see Fig. 6.7c) and showed that $b_n = 1$ seems actually enough to converge the velocity field.

A convergence analysis of the spin density was undertaken and the results are depicted in Figure 6.7d. It reports that about 20 spins/voxels are necessary for the velocity to yield an error under 4%. This agrees with the resulting velocity error found in Xanthis et al. [165], who found 4.4% error of the maximum velocity, but for a spin density of 469 isochromats/voxel. This result agrees also with [136] where 27 spins/voxel were necessary to get a MR signal error under 1.5% as compared to an analytical signal. Note however that in this case, the

reconstructed axial velocity (and not the MR signal) is compared. Note also that the spin density necessary to get a consistant signal would be dramatically higher (around 1000 spins/voxel) if the rf-spoiling was simulated, as found in [54]. While a small number of particles is needed to get a good approximation of the signal, the error rate decreases until 20 particles/voxel where it reaches a plateau at about 3.6% error. Note that the same computation was performed without the volume weighting fraction associated with the particles, and higher errors were however produced (5% at 20 particles/voxels), suggesting that this is important to account for the isochromat volumes in the simulations. The remaining error could be a direct consequence of the finite time sampling of the RF-excitation SINC waveform. This would also explain the cut-off behaviour of the velocity error with respect to the b_n. To our understanding, the number of sampling points of the RF waveform is not user-dependent (directly fixed by the JEMRIS program). For this reason we did not undergo any in-depth researches in this direction to mitigate this error.

6.3.3 Coupling with CFD

The validity of the full coupled CFD-MRI simulation was tested through the phantom experiment presented in Chapter 4. A schematic representation of the 4D flow MRI pulse sequence (i.e. rf-spoiled gradient echo sequence with velocity encoding gradients along the three directions) is presented in Figure 6.8. The sequence parameters were prescribed to match with the experimental sequence acquired and described in Section 4.3. Indeed, the gradients slew rate was set to 200 $T/m/s$ and limited to a maximum amplitude $G_{max} = 45\ mT/m$, in accordance with the MRI device technical features. A Hanning window apodized sinc rf pulse was designed, with a flip angle $\alpha = 15°$, and an envelope expressed as follows:

$$B_1^e(t) = A\left(0.5\left(1+\cos\left(\frac{\pi t}{3\tau_{rf}}\right)\right)\mathrm{sinc}\left(\frac{\pi t}{\tau_{rf}}\right)\right) \tag{6.17}$$

where $A = 10\ \mu T$ is the peak RF amplitude occurring at $t = 0$, and τ_{rf} is half the width of the central lobe.

An isotropic $2 \times 2 \times 2\ mm^3$ voxel size was set, with a matrix size $(80, 30, 120)$. The readout bandwidth was set to $\Delta f = 0.6\ kHz/pixel$ and the k-space was entirely filled, with a Cartesian trajectory. The encoding velocity was set in the three spatial directions to $VENC = 60\ cm/s$. Each cardiac cycle was split into 17 phases, with a temporal resolution $\Delta t_p = 58\ ms$ and a repetition time $T_R = 6\ ms$, which allowed to fill two k-space lines (N_{seg}) between each T_R. As the sequence is composed by a reference and three velocity sensitive sub-sequences to encode the full 3D velocity field, each sequence was split into four sub-sequences, each treated separately to reduce the wall-clock simulation time. Therefore, $N_{seg} = \left\lfloor \frac{\Delta t}{T_R} \right\rfloor = 9$

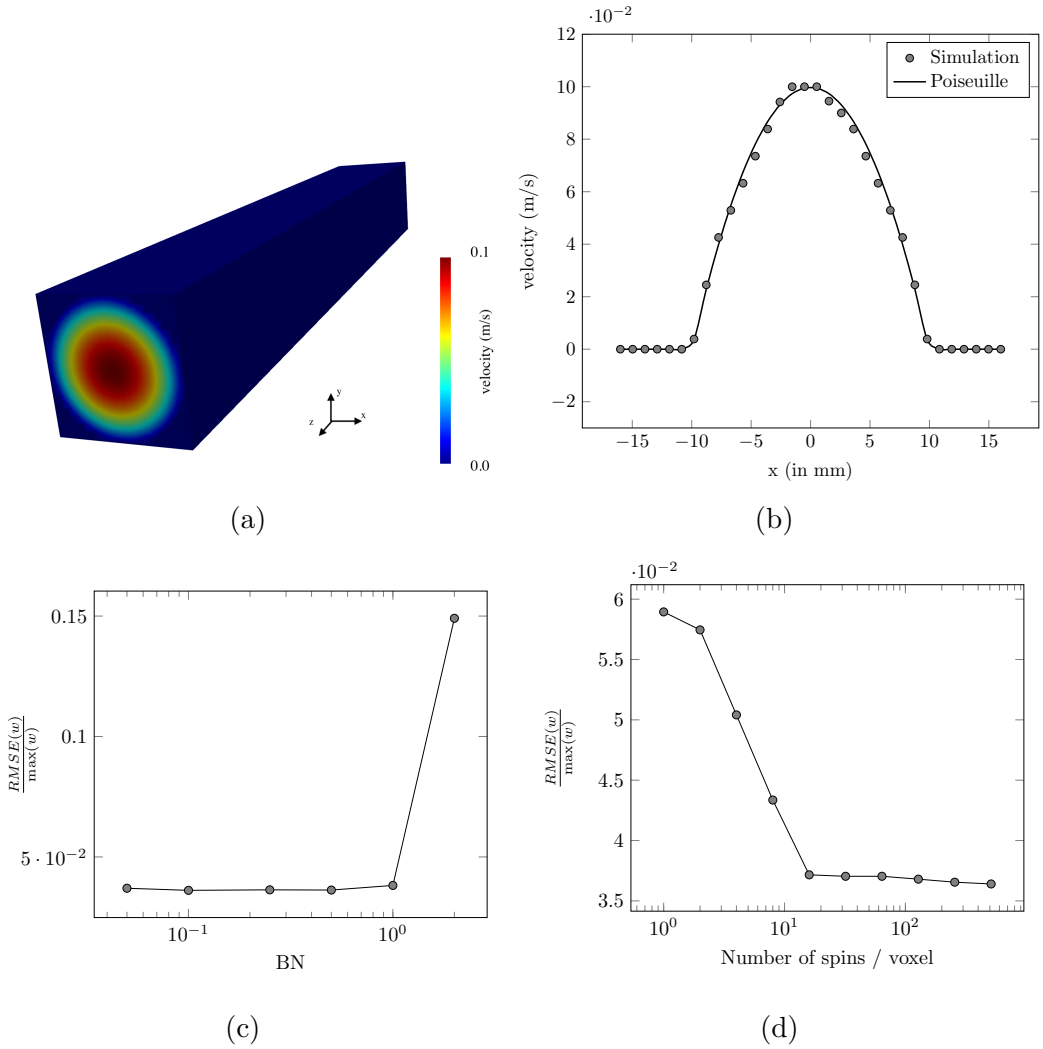

Figure 6.7: Validation of the axial velocity profile w reconstructed from a Poiseuille flow test case simulated with a 2D PC MRI sequence. **a**) Flow domain simulated. **b**) Axial velocity profile along the x-axis reconstructed by MRI; comparison between the reconstructed velocity profile and the imposed Poiseuille analytical solution. **c**). Dimensionless root-mean-square error (RMSE) evolution as a function of the Bloch number (b_n) and as a function of the **d**) spin density.

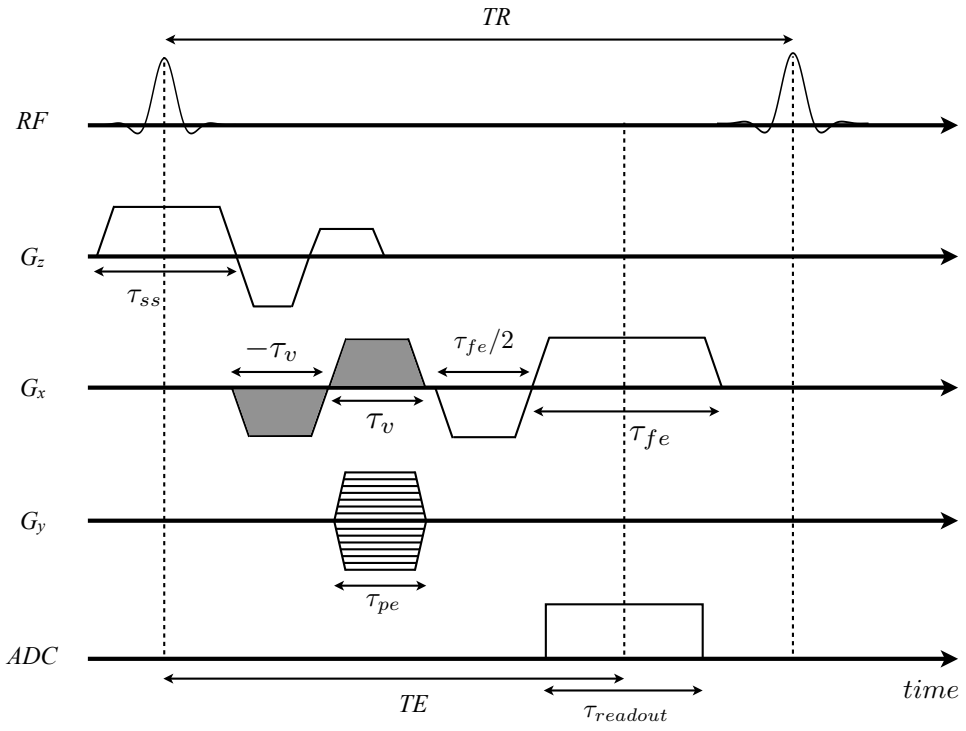

Figure 6.8: Diagram of a typical gradient echo pulse sequence with bipolar velocity encoding gradients (grey-filled) along the x-axis, frequency and phase encoding gradients along x-axis and y-axis, and slice selection gradient along z-axis. Each k-space line is filled during the readout event where the signal is measured by the rf-receiver coil. This pulse sequence is repeated changing the phase encoding gradient amplitudes (G_y) after each repetition time TR to incrementally fill the k-space lines.

subsets were filled instead of $N_{seg} = \left\lfloor \frac{\Delta t}{4T_R} \right\rfloor = 2$ normally with interleaved velocity encoding. The resulting physical time to simulate one out of 4 acquisition was then $T_{acq} = \frac{N_y N_z}{N_{seg}} T_c = \frac{120 \times 30}{9} \times 0.986 = 394.4\ s$. Note that the memory storage of such a long sequence results into huge array sizes. For this reason, the reading of the sequence was segmented so that only small arrays composed by 1000 cells or less are manipulated and stored in a data buffer. This decomposition is an efficient way to reduce the computational costs.

The semi-analytic formulation was used to solve the Bloch equations, with Bloch number set to $b_n = 1$, consistently with what was found in Section 6.3.2. To minimize the relative error while keeping a reasonable simulation time, a spin density of 48 spins/voxel was injected within the fluid domain, resulting in about 1.1 million particles injected in total. The input CFD velocity field was computed based on a numerical mesh with characteristic cell size of 2 mm.

The four 3D raw datasets were finally collected and gathered to reconstruct the full 3D velocity field. This 3D velocity field obtained from the simulated MRI image $\mathbf{u}_{SMRI}$ was compared with the input HR-CFD velocity field as well as with LR-CFD. To account for the errors due to both the magnitude and orientation of the velocity vector, the L2-norm error between the simulated velocity $\mathbf{u}_{SMRI}$ and phase-averaged CFD velocity $\mathbf{u}_{HR}$ was defined as:

$$\epsilon_{L2}(\mathbf{x}_i, t^n) = ||\mathbf{u}_{SMRI}(\mathbf{x}_i, t^n) - \mathbf{u}_{HR}(\mathbf{x}_i, t^n)||$$

.

Qualitative analysis

Figure 6.9 compares at different phases in the cycle the magnitude of the simulated MRI velocity field to the magnitude of the phase-averaged CFD velocity field. Note that for visual clarity the simulated MRI was segmented using a binary mask generated based on the magnitude of the image. A first visual comparison shows that the two fields agree well regardless of the phase, although a systematic blurring of the SMRI velocity is observed. This may be due to a Gibbs artifact induced by the finite truncation of the signal. Also, slight variations occur principally in the pipe bend, aneurysm neck and mixing layer at the collateral outlet elbow. The discrete integration of a finite sample of particles in the domain could induce intravoxel phase dispersion. Note however that this velocity discrepancies reduce after downsampling the CFD velocity field (see further).

Quantitative analysis

Figure 6.10 shows the corresponding time evolution of the Pearson's correlation coefficient computed with respect to both the high-resolution CFD phase-averaged velocity (HR-CFD) and downsampled phase-averaged velocity field (LR-CFD). As expected, the low resolution velocity better matches the simulated MRI (peak correlation $r^2 = 0.978$ and mean correlation $r^2 = 0.966$) as compared to the high resolution CFD (peak correlation $r^2 = 0.967$ and mean correlation $r^2 = 0.958$). Similarly as for the experimental MRI acquisition, the highest correlation is reached at peak systole and the distribution closely follows the flow rate evolution. Moreover, higher correlations are obtained as compared to the corresponding experimental MRI measurements (peak correlation $r^2 = 0.96$ and mean correlation $r^2 = 0.90$). Nevertheless, Bland-Altman and linear regression plots shown in Figure 6.10 reveal that some divergences still remains. One can suggest that these remaining divergence come from the MRI acquisition process itself, and take their sources in the few artifacts that were not suppressed.

The previous comparisons between CFD and experimental MRI (see Chapter 4) suggested that the errors may originate from the dependency of the correlation to

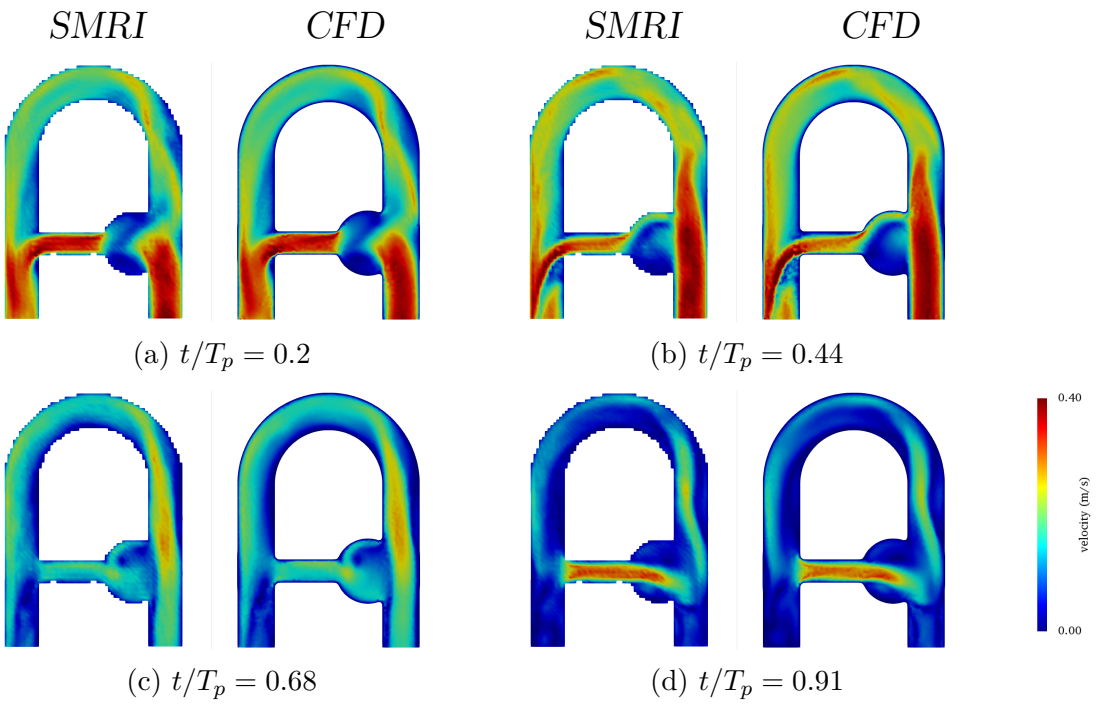

(a) $t/T_p = 0.2$ (b) $t/T_p = 0.44$

(c) $t/T_p = 0.68$ (d) $t/T_p = 0.91$

Figure 6.9: Comparison in the XZ-middle plane between $||\mathbf{u}_{SMRI}||$ and $||\mathbf{u}_{HR}||$ at four different phases during the cycle.

the velocity to noise ratio (VNR). As expressed in Sec. 2.8.5, the VNR linearly depends on the ratio $V/VENC$ where V is the flow velocity. In this sense, regions where the velocity amplitude is closer to the VENC (i.e. higher VNR) should entail better correlations with CFD. However, in the present work, the simulated MRI is by definition free of noise. Therefore, this reasoning is not valid as the correlation is independent of the VNR. Moreover, off-resonance effects were a potential culprit to the diminishing of the correlation. Once again, this MRI simulation framework was voluntarily idealised and off-resonance effects were not included.

Nevertheless, as studied in Steinman et al., [146], some remaining errors could be caused by spatial misregistrations due to the time delays between the different spatial encodings, as well as velocity displacement artifacts due to the acceleration of spins during velocity encodings. For this reason, to evaluate the impact of the spins acceleration on the MR image, the CFD phase-averaged acceleration field was computed and compared to the SMRI velocity errors. The acceleration was computed as the sum of the local ($\frac{\partial \mathbf{u}_{HR}}{\partial t}$) and convective ($(\mathbf{u} \cdot \nabla)\mathbf{u}$) contributions. Note also that $\frac{\partial \mathbf{u}_{HR}}{\partial t}$ was computed using a first-order upwind finite difference scheme.

The preferential sites of L2-norm error (computed from the LR-CFD) are qualitatively compared to the highest acceleration patterns in Figure 6.11 at

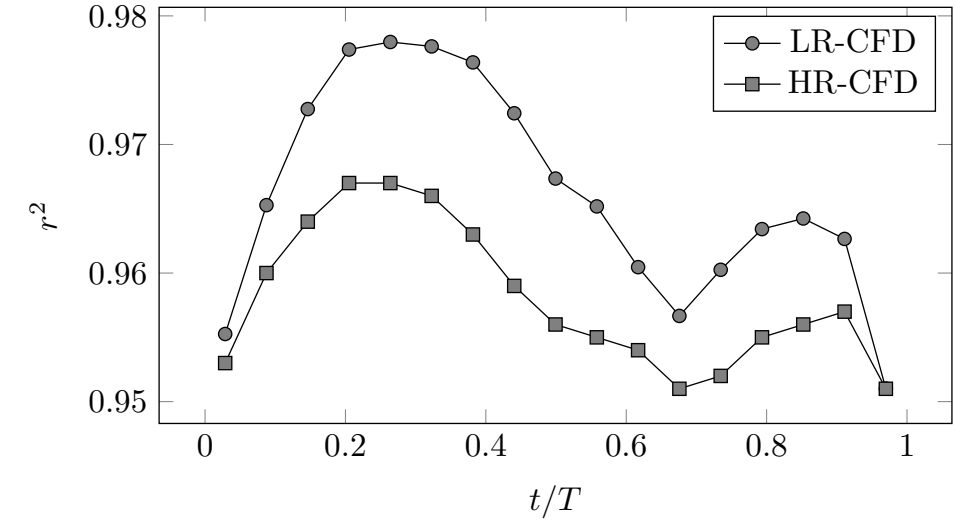

(a)

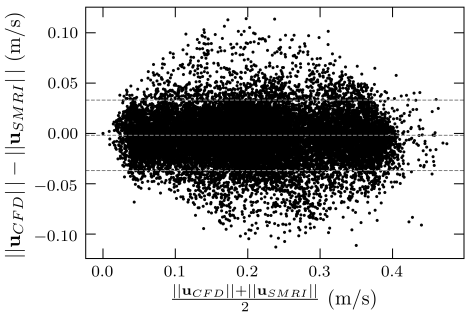

(b)

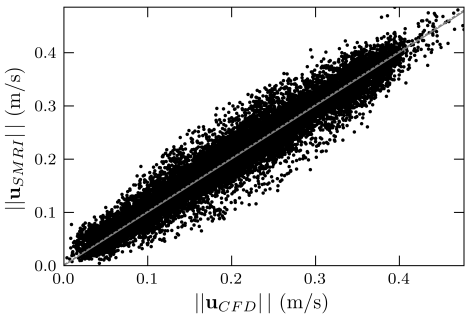

(c)

Figure 6.10: Statistical analysis of the velocity field imposed by CFD and reconstructed in-silico with MRI simulations. **a**). Evolution along a cycle of the Pearson's correlation calculated between HR-CFD and SMRI, as well as between LR-CFD and SMRI. **b**). Corresponding Bland-Altman and **c**). linear regression plots at phase $t/T_p = 0.2$ compared with LR-CFD.

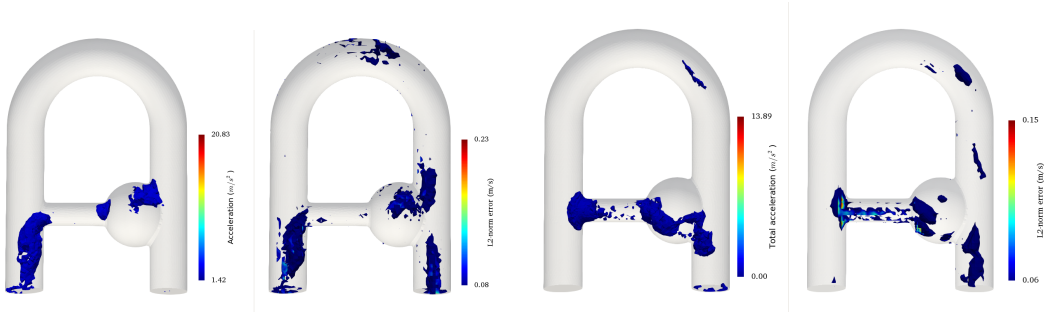

(a) $t/T_p = 0.44$ (b) $t/T_p = 0.91$

Figure 6.11: Threshold of **left** phase-averaged CFD acceleration and **right** L2-norm error of the SMRI velocity. **a**). $t/T_p = 0.44$ and **b**). $t/T_p = 0.91$.

$t/T_p = 0.44$ and $t/T_p = 0.91$. Some similar structures could be observed in the collateral jet, in the main flow detachment into the aneurysm neck, as well at the beginning of the pipe bend. The similarities suggest that some of the highest SMRI velocity errors are due to the fact that the phase equation ignores acceleration and higher order motions and assumes linear time variations of the spin position (see Eq. 2.48). Expanding the spin location up to third-order (i.e. adding the local acceleration term to the Taylor expansion of the spin position) would most probably reduce the errors. In practice, it may however largely extend the acquisition time as it might require additional segments with gradient waveforms adapted to suppress the third-order gradient moment [15]. Post-processing corrections are also a possible strategy to correct the velocity errors raised [152].

At $t/T_p = 0.44$, a substantial velocity deviation can be observed near the inlet in the main branch. This is a consequence of the sparse particle distribution in the high velocity regions, although largely alleviated by the particles reinitialization at spoiling events. To reduce this effect, a buffered zone could be added to inject particles with pre-saturated magnetization and as a function of the inflow velocity profile.

6.4 Influence of the particle density

As for the Poiseuille validation case, the influence of the number of particles per voxel was investigated in the phantom configuration. Two additional sets of simulations were performed, with 3 mm^3 and 4 mm^3 voxels. The mean L2-norm error raised at $t/T_p = 0.44$ for various spin density is plotted in Figure 6.12. The first observable trend is that the 2 mm simulation reaches a plateau at 40 spins/voxel. This trend was also found in the steady Poiseuille flow simulation, although the mean error associated was lower than in that case (about 6% of the

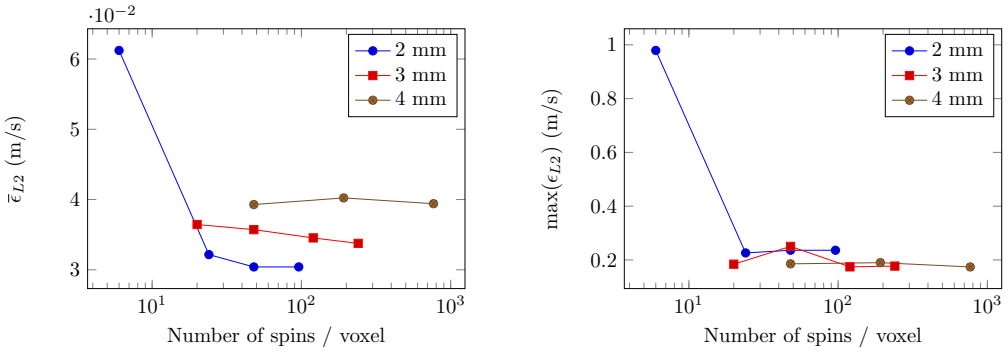

(a) (b)

Figure 6.12: Evolution of the magnitude velocity **a**) mean and **b**) maximum L2-norm error between LR-CFD and MRI simulation of the phantom with a 4D Flow sequence isotropic spatial resolution for different spin density at $t/T = 0.44$.

VENC). The higher complexity of the flow field as compared to the Poiseuille flow may explain this higher absolute error level. In the phantom case, spatial misregistration artifacts should be amplified due to the presence of an accelerated three-dimensional flow. Moreover, the complex shape of the geometry most probably induces clustering and scattering in the spin distribution that lead to spurious signal.

Similarly to the 2 mm case, the mean error associated with the 4 mm voxel size also reaches a plateau between 20 and 40 spins/voxel. For the 3 mm case, the mean error slowly decrease as the spin density increases. Similar convergence behaviour is observed for the three cases when considering the maximum error (see Fig. 6.12b), comprised between 40%-50% of the VENC. Comparing the three results, one can observe a global increase of the mean error with the spatial resolution. On the contrary, a globally slow decrease of the maximum error with increasing voxel size is reported. The straightforward explanation would be that an increase of the voxel size induces higher errors as a result of the voxel averaging process. However in this case the LR-CFD, which supposedly mimics the spatial averaging, was used to compare with SMRI. A more extensive analysis is therefore required to understand this phenomenon.

6.5 Influence of the spatial resolution

To get an in-depth understanding of the behaviour presented in the previous section, the L2-error maps in the XZ middle plane of the phantom are presented in Figure 6.13. Sites of high velocity errors at boundary walls are amplified as the voxel size increase. This effect mainly arises as a result of the SMRI processing

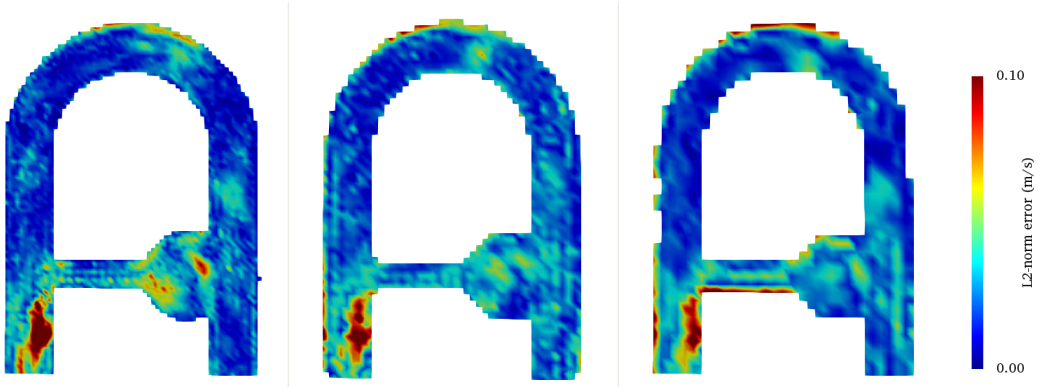

Figure 6.13: Map of the L2-norm error of the velocity at $t/T = 0.44$ between LR-CFD and SMRI at three different spatial resolutions. **Left** 2 mm^3, **middle** 3 mm^3, and **right** 4 mm^3. The error is calculated based on the LR-CFD, which is specific to each spatial resolution. In all the simulations, 50 spin/voxel are injected in the domain.

at boundary walls, where the voxel signal is partially averaged by the random phase noise induced on the outside of the phantom. Consequently, the errors are amplified at larger voxel sizes as a larger proportion of the voxel lays outside the domain. This effect is however not reproduced by the CFD down sampling, where the velocity is averaged with zero velocity contributions instead of random velocity comprised between $[-VENC, VENC]$. A simple remedy to this would be to enlarge the numerical domain by adding stationary particles around the flow phantom.

The other predominant region of large L2-norm errors seem to appear downstream of the collateral branch, in the recirculating zone located under the jet. This region harbours highly disturbed flow patterns (especially at this specific phase), where the high momentum of the collateral jet induces a recirculating flow region with adverse pressure gradient and counter rotating vortices (as illustrated in Fig. 4.26). One can infer, from the error patterns presented in Fig. 6.11, that the errors in this zone are a direct consequence of the spatial and velocity misregistration effects. The small rotating structures could be responsible for intravoxel phase dispersion. Yet, in the CFD downsampling process each voxel is divided into a fixed number of uniform subvoxels whereas in SMRI the voxel signal is averaged over a finite number of discretely distributed particles. Therefore, depending on the particle distribution, the averaging process could behave differently, especially in disturbed zones. The constant size of this error pattern with refinement of the spatial resolution consolidates this hypothesis since the spin density is kept unchanged.

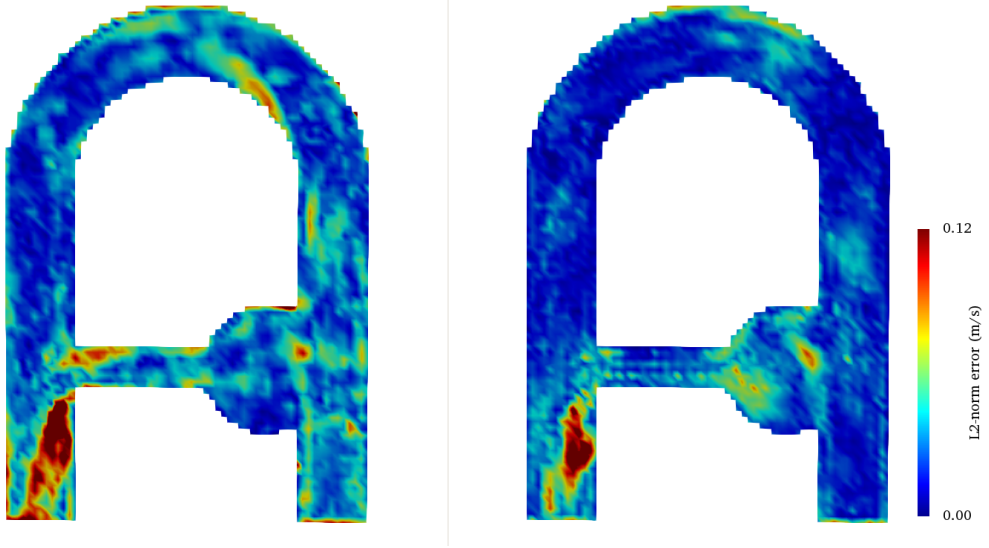

Figure 6.14: Velocity L2-norm error in the XZ-middle plane of the (**left**) experimental and (**right**) simulated MRI at peak systole $t/T_p = 0.44$. The L2-norm error is calculated based on the LR-CFD obtained from a 2 mm characteristic mesh size.

6.6 Comparisons with experimental results

The SMRI was finally compared with the experimental MRI described in the previous Section 4.3. The velocity L2-norm error maps as compared to LR-CFD are reported in Figure 6.14. A first interesting result is that the highest level error sites are similarly located under the jet, at the collateral elbow outlet. As previously suggested, they probably arise as a result of both the high convective acceleration, as well as the intravoxel dispersion. Moreover, the MRI error spreads on a larger region as compared to SMRI. As the 3 directions of the velocity are encoded simultaneously in the simulations while the velocity encoding are interleaved in the experiments, non-negligible time offsets induced could be responsible of this widespread error pattern. Moreover, it should be noted that acceleration-induced errors at a given phase could generate MRI errors in the following phases.

Generally speaking, larger errors spots are introduced in the experimental MRI. This was expected as the MRI comprises many additional sources of deviations such as magnetic field inhomogeneities, off-resonance effects and experimental noise. However, an important consideration is that the CFD mesh is coarser than the one presented in the previous chapters (2 mm vs. 0.7 mm). Even if this is sufficient to validate the simulation workflow, it does however not guarantee a well-resolved CFD flow field, as obtained in the Chapter 1. In this sense, in-depth evaluation of the mesh size influence should be considered and the comparisons with experimental MRI should be carefully looked at.

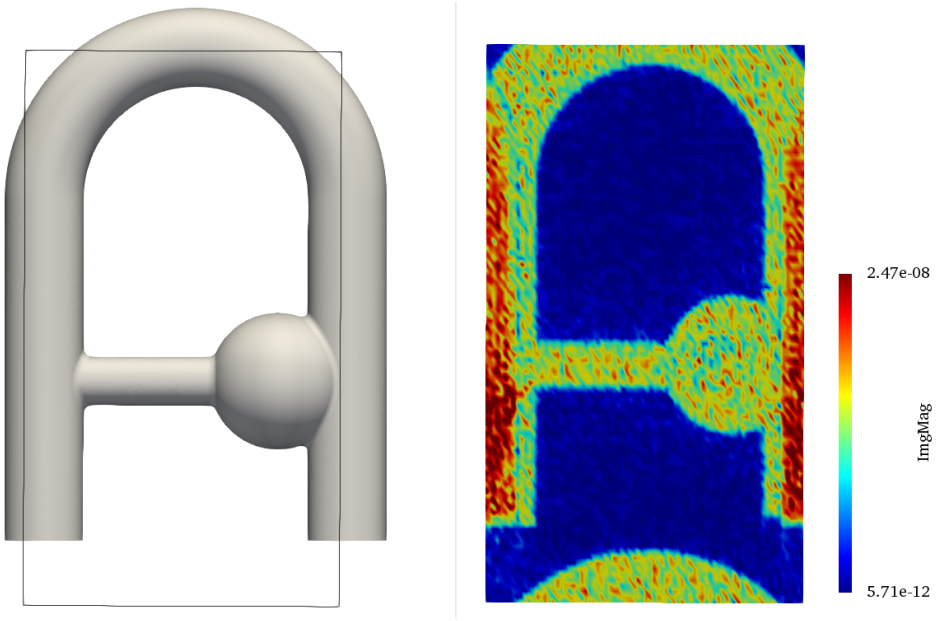

Figure 6.15: Phase wrap-around artifact resulting from the simulation of a coronal 2D PC-MRI sequence in the flow phantom. **Left** Boundaries of the flow phantom superimposed on the FOV bounds. **Right** Resulting artifact.

6.7 Simulation of displacement artifact

A simulated phase wrap-around artifact is presented in Figure 6.15. As already described in Section 2.9.2, this artifact manifests as a fold over of the object at the boundaries whenever the FOV is smaller than the size of the object. It could be easily understood that the missing top part of the phantom folds onto the bottom of the image. Similarly, the left and right sides of the phantom fold onto the right and left regions respectively. This can be observed as the signal amplitude levels are about twice higher at these locations.

6.8 Discussion

In this chapter we presented a workflow for simulating realistic time-resolved 3D PC-MRI acquisitions. To this aim we introduced a full numerical procedure with a CFD coupling "on the fly". We implemented a semi-analytic formulation of the Bloch equation to accelerate the computations. The computational gain of this formulation was evaluated, as well as the parallel efficiency of the entire program. The complete workflow was incrementally validated, and several CFD-MRI simulations of the phantom experiment were performed and compared to the input CFD velocity. The largest velocity discrepancies were reported at peak systole and were mainly located in the regions of high flow acceleration. This

is a direct limitation of the MRI acquisition process which considers a linear velocity dependence of the signal. In this sense, post-processing corrections could be applied to correct the velocity field [152].

Sensitivity of the solution to the spatial resolution temporal sampling, and spin density was analysed. As compared to the existing simulators, our method seems to provide an accurate solution with fewer particles needed. We suggest that this is a direct consequence of the particle injection strategy adopted which maintains a homogeneous particle distribution along the entire simulation. Also, the semi-analytic formulation coupled to the massively parallel capabilities of the YALES2BIO solver allows the simulation of realistic flow MRI sequences with physical times up to hundreds of seconds.

However, some numerical artifacts introduced by the modelling assumptions were not treated and require further developments. For instance, injection of pre-magnetized particles at the inlet boundary condition are necessary to avoid spurious signal resulting from sparsely distributed particles. Moreover, a relatively coarse CFD numerical mesh was used in the simulations that does not fully resolve the flow field. While it should not impact the comparison with the simulated MRI velocity, it is expected that a coarser CFD produces higher velocity deviations from the real flow field, and therefore could yield larger errors as compared to the experimental MR velocity measurements.

As a relatively coarse CFD mesh was used in the CFD-MRI simulations as compared to the one used in the Chapter 4, a less realistic flow field is expected that would certainly yield a lower correlation as compared to experimental MRI. In this sense, a similar CFD-MRI simulation should be performed with the same mesh as used in Chapter 4. Moreover, some errors are associated with the cycle-to cycle fluctuations that involve comparing a phase-averaged velocity with a MR velocity resulting from a progressive k-space filling. Simulating an unique cardiac cycle would remove the cycle-to-cycle fluctuations and thus to isolate the related errors.

The experimental MRI was finally compared to the simulated MRI. The velocity errors patterns were closely related to the simulated MRI, with a systematically higher level. Some of the errors observed are most probably associated with off-resonance effects such as gradient non-linearities, T2* relaxation effects, chemical shift, or magnetic susceptibility, which should be added to mimic more realistic MRI acquisition effects. Coil sensitivity profiles should also appear as a weighting factor of the MR signal. A more realistic representation of the magnetization dynamics can be reached by solving the Bloch-Torrey equations that accounts for the transfert of magnetization due to diffusion [155]. In practice, the attenuation of MR signal due to molecular self-diffusion can be calculated iteratively and directly added to the magnetization relaxation, as proposed by Jochmisen et al.

[74].

However, many approximations and potential discrepancies could be attributed to the differences between the simulated and experimental sequences. For example, it is important to notice that the SMRI sequence was designed as a retrospectively gated sequence while the experimental measurements presented were prospectively gated. To this respect, the readout time sampling was slightly different as compared to that of the MRI. Moreover, in the simulations, the three velocity components are encoded simultaneously, but sequentially in real MRI experiment. As a result, potential time delays between each velocity component could arise and amplify the errors. As it belongs to the manufacturers, little is known about the design of the experimental sequence. Getting an access to the source code of such sequences would certainly improve the fidelity of the simulations.

Chapter 7

Conclusion

Chapter contents

The main findings and conclusions of the accomplished work are summarized in this chapter. Future research directions as well as clinical perspectives are discussed.

7.1 CFD-based methodology to assess PC-MRI

In this chapter, a CFD-based procedure designed for quality assessment of 4D Flow MRI measurements was developed. A proof-of-concept validation of the methodology was established using idealized MRI parameters to compare with CFD flow predictions. The results obtained clearly highlighted that some discrepancies remain even after errors associated with boundary conditions, numerics, or turbulence modelling are minimized in the CFD part. Indeed, we noted that a straightforward comparison of the two modalities only produces a very poor agreement ($r^2_{|\mathbf{u}|} = 0.63$). Some post-processing corrections were thus proposed, that drastically increased the velocity correlations ($r^2_{|\mathbf{u}|} = 0.97$). These results prove that in a well-controlled environment with suitable processing, both MRI measurements and CFD predictions bring trustworthy and equivalent global flow quantities. It is important to highlight that this agreement was reachable thanks to the idealised in-vitro framework (rigid phantom, Newtonian fluid, flow rate

waveform) considered which, although not fully representative of in-vivo conditions (complex blood rheology, moving boundaries), represents several flow features relevant to the thoracic circulation (aortic arch, bifurcation, aneurysm).

7.2 Reconstruction of the hemodynamic field

In this chapter the developed framework was exploited as a benchmark database to evaluate the accuracy of different clinically relevant approaches to reconstruct the hemodynamic field from MR velocity measurements. This approach was illustrated through the evaluation of WSS and relative pressure fields.

Two different algorithms proposed in the literature [128, 143] were evaluated and compared to the WSS distribution obtained from the same numerics using the MRI velocity field as input. All the three approaches resulted in low WSS correlations ($r^2 < 0.6$) and low distribution similarities as compared to CFD field of WSS, selected as a reference although not fully converged due to the virtually unaffordable mesh refinement required to properly resolve the Womersley boundary layer. Moreover, large discrepancies were observed between the two approaches ($\epsilon = 300\%$) taken from the literature. As this result was obtained in a well-controlled environment, higher WSS errors are expected in-vivo, where complex moving vessel geometries and segmentation errors occur. It seems therefore difficult to draw any generalized conclusion given that we could not guarantee the WSS field in such an idealized in-vitro setup.

Contrary to WSS, a fast convergence of the CFD pressure field with mesh refinement was obtained. Several methodologies were then tested to reconstruct the relative pressure field from MR velocity data. The pressure field was also reconstructed using YALES2BIO numerics but with the MRI velocity field as input and a close agreement with the reference CFD pressure field ($r^2 = 0.98$) was reported. This suggests that the pressure field is not very sensitive to the small velocity variations observed. Moreover, although the steady Bernoulli formulation was found to be quite inefficient to predict the pressure drop, the unsteady Bernoulli principle provided an accurate estimate, as well as a good compromise for a rapid pressure drop estimate. This result confirms that the inertial contribution plays a key role, while the viscous terms could easily be neglected without any significant loss of information.

7.3 Simulation of phase-contrast MRI

In Chapter 6, a 4D Flow MRI simulation framework was presented, with the aim to decompose the complex MRI acquisition process in order to identify the sources of dysfunctions of an MR scan (hardware, software, protocol) that potentially

lead to velocity errors. The presented methodology benefits from a semi-analytic resolution of the Bloch equations as well as highly parallel capabilities that make affordable the simulation of 4D Flow MRI sequences. Moreover, the efficiency of the particle reinjection procedure allows a homogeneous spatial distribution, and therefore a decreased number of particles required.

The validation of the MRI simulation of the phantom experiment showed that a small velocity error (2-4%) was systematically raised, even for high spin density. The highest error levels were found to be induced at zones of disturbed flow (aneurysm, mixing layer). The analysis of the pattern error distribution suggested that acceleration-induced artifacts induced by the linear phase-velocity dependence seems partially responsible of these high error levels. Also, small structures located at the collateral elbow could be sensitive to intravoxel phase dispersion induced by high velocity gradients.

However, many approximations remained due to the differences between the simulated and experimental sequences. It is important to note that very few is known about the design of experimental sequences, as they belong to each manufacturer. Getting an access to the source code of such sequences would necessarily improve the fidelity of the simulations.

7.4 Perspectives

The work performed during this thesis was mainly devoted to the numerical developments of a rigid CFD-based reference database as well as a MRI simulation framework. Bringing this work closer to the clinical reality is now a necessity to benefit from the added value of our developments. One may apply this methodology as a quality control procedure to assess the errors induced by the time-restraint low-resolution protocols used in clinical routine. The influence of parallel acceleration, partial k-space filling strategies or on-site adaptation of protocol parameters on the resulting velocity field could then be investigated. Moreover, benchmarking of reconstruction algorithms could be systematically performed to control the quality of variable of interests such as pressure drop, WSS or turbulent features. Also, various flow regimes coexist in the arterial network that involve different hemodynamic phenomenon, depending on the geometry and mechanical characteristics of the vessel, as well as the velocity, pulsatility and blood rheology. The acquisition protocols also differ as a function of the field of view, spatial resolution, tissue type, and dynamics of the flows. For instance, MRI measurements of small size vessels are limited by technological constraints associated with MRI itself. For classical scanners capable of producing static magnetic fields between 1.5T and 3T, an increase of the spatial resolution would result in a decrease of the SNR, and therefore of the measurement accuracy [147].

To this respect, the developed methodology seems valid only to quantify the accuracy of flow measurements under cardiovascular regimes and could be adapted to cover the cerebrovascular network.

The simulation framework for MRI could be a valuable tool for sequence design and on-site protocol parameters optimization, tasks which are still most of the time performed by experimental testing. Nevertheless, more developments are still required in order to simulate realistic acquisition. Some common off-resonance effects such as gradient non-linearities, T2* relaxation induced by main magnetic field inhomogeneities, or chemical shift effects should be accounted for. As well, multi-receiver coil systems should be additionally modelled by introducing coil sensitivity profiles. The transfert of magnetization due to diffusion, neglected in this study, could also be accounted for by solving the Bloch-Torrey equations [155]. As it was initially designed for the prediction of turbulent flows, the flow solver could as well be a valuable tool to assess the MRI-based turbulence quantification techniques [45].

Finally, the developed procedure could be a valuable tool for flow MRI quality control and evaluation of post-processing associated. Although it represents a first-stage development of a larger project, we believe that numerical simulation is a promising tool for sequence prototyping, quality control purposes, and as a decision-making tool for clinical practice.

Appendix

Derivation of the pressure source term with periodic boundary condition

It has been shown from the momentum equation projected on the centreline axis $\overrightarrow{e_s}$ that velocity components are only functions of r and θ, so that the pressure gradient $\frac{\partial P}{\partial s}$ is independent of s and hence it can be written as: $P(s) = -Gs$ where G is a constant [10]. Note that this expression is applicable for $\delta \ll 1$. In other terms, it can be given as follows:

$$\frac{\partial P}{\partial s} = -\frac{1}{R_c}\frac{\partial P}{\partial \phi} = -G \tag{7.1}$$

Note that since $\nabla \times (\nabla P)) = \mathbf{0}$, for the source term to be homogeneous to a pressure gradient, it needs to verify:

$$\nabla \times \mathbf{S} = \mathbf{0} \tag{7.2}$$

To satisfy the previous Equation 7.2, the following constraint is added and S_ϕ is defined as :

$$S_\phi = \frac{G}{\rho}(\frac{R}{R_c})^n \tag{7.3}$$

Using the curl definition in the cylindrical coordinate system, this condition gives:

$$-\frac{\partial S_\phi}{\partial y} = 0 \Longleftrightarrow S_\phi = A(R, \phi)$$

$$\frac{1}{R}\frac{\partial (RS_\phi)}{\partial R} = 0 \Longleftrightarrow \frac{S_\phi}{R} = -\frac{\partial S_\phi}{\partial R}$$

These conditions conduct to $n = -1$, and Equation 7.3 simplifies in:

$$S_\phi = \frac{G}{\rho}(\frac{R_c}{R}) \tag{7.4}$$

When the duct is weakly curved (e.g: $\delta \ll 1$), one can derive a relationship between pressure gradient and velocity, assuming a Poiseuille flow with the following formulation:

$$\frac{64}{Re} = -\frac{\Delta P}{\frac{1}{2}\rho \overline{W}_0^2}\frac{2a}{L} \tag{7.5}$$

with ρ, L, ΔP respectively the fluid density, the length over which the pressure gradient is applied, and the pressure difference between the inlet and the outlet

of the almost straight pipe. Using the previous definition of the Dean number coupled with Equation 7.5 to explicit the relationship between velocity and pressure gradient, $\overline{W}_0 = -\frac{\Delta P}{L}\frac{a^2}{8\mu}$, one can express the latter as a function of the pressure gradient, as follows:

$$D = \sqrt{\delta}\frac{Ga^3}{4\rho\nu^2} \tag{7.6}$$

It is very important to note that, following the formulation adopted by Berger [10], the Dean number is valid only when the flow is fully developed and $\delta \ll 1$. For higher values of δ, the relationship between velocity and pressure gradient has to be determined a posteriori of the solution. By combining Equations 7.3 and 7.6, a simple expression of S_ϕ depending on the Dean number can easily be found, as follows:

$$S_\phi = \frac{4\nu^2 D}{a^3\sqrt{\delta}}\frac{R_c}{R} \tag{7.7}$$

By implementing the above source term along the centreline of the curved duct, it is possible to perform a periodic simulation of flow in a curved pipe at a prescribed Dean number value. Note that the Reynolds number $Re = \frac{2a\overline{W_0}}{\nu}$ is based on the mean axial velocity $\overline{W_0}$ of a straight pipe that would be driven by the same pressure gradient over a length L.

PPE-based pressure reconstruction approaches from MRI

In this section, we present and compare several methodologies for computing the relative pressure based on solving the pressure Poisson equation (Eq. 5.12) from 4D Flow MRI velocity measurements. Among the methodologies proposed, we isolate the transient from the viscous and convective pressure contribution to solve the PPE separately. We then juxtapose the full 3D PPE approach to the PPE solved from 2D planar PC-MRI inflow measurements only. We also look at the impact on the relative pressure field of the prescribed boundary condition at walls. As it was not fully achieved within the allocated time, we did not include these results to the main body of the thesis.

7.4.1 Proposed approaches

From the 3D CINE PC-MRI velocity field corrected from off-resonance effects, we first project the velocity field onto the space of divergence-free fields, as the divergence of the velocity field supposedly reduces to zero in Equation 5.12. As done in the previous Section 5.2, the resulting post-processed 3D PC-MRI velocity field is then interpolated on a tetrahedral mesh, with a mesh size ratio $MSR = 1/3$.

The relative static pressure is obtained by iteratively solving Equation 5.12 with a Deflated Preconditioned Conjugate Gradient algorithm, developed in Malandain et al. [97]. Once again, the high-order numerical methods implemented in the YALES2BIO solver are used to solve the full PPE discretized on an unstructured grid. A major interest of solving the PPE directly on the specified flow domain was highlighted by Ebbers et al. [47], who observed a non negligible improvement of the pressure estimates, especially in complex geometries, as compared to quasi-rectangular iterative approaches [46, 141], which tend to systematically underestimate the pressure field, on top of being more computationally extensive. The pressure at the outlet boundary is set to zero so that additive constant up to which the pressure is defined is set once for all. While it is still a controversial issue [131], a homogeneous Neumann boundary condition is applied to all the other boundaries of the computational domain, in accordance to what was published in [61]. If Eq. 5.12 is solved for each MRI image independently, the transient contribution ($\frac{\partial \mathbf{u}}{\partial t}$) of the pressure gradient reduces to zero and a steady pressure is calculated. This approach is referred to as *3D MRI PPE (steady)* formulation. On the contrary, the dynamic forcing term presented in Section 5.3.3 was added to ensure the flow continuity between two MRI phases and to account for inertial effects. The resulting pressure field then contains the full pressure contributions and is referred to as *3D MRI PPE* approach. At last, the *2D MRI PPE* designates

Table 7.1: Overview of the main features of the pressure computation methods considered in this section. Ω is the fluid domain delimited by boundary walls $\partial\Omega_w$ and an inlet surface $\partial\Omega_{in}$ of inward normal vector $\mathbf{n}$. Note that a time dependency was added to the velocity as we used the time-splitting algorithm presented in Section 3.1.3 to advance the velocity and incorporate the transient contribution.

Method	**Formulation**
Pressure Poisson Equation	$\nabla^2 p = -\rho \nabla \cdot (\mathbf{u} \cdot \nabla \mathbf{u})$
3D MRI PPE (steady)	$\begin{cases} \mathbf{u}(\mathbf{x}, t_0) = \mathbf{u}_{mri}(\mathbf{x}, t_0) \quad \text{on} \quad \Omega \\ \mathbf{u}(\mathbf{x}, t) = 0 \quad \text{on} \quad \partial\Omega_w \end{cases}$
3D MRI PPE	$\begin{cases} \mathbf{u}(\mathbf{x}, t_0) = \mathbf{u}_{mri}(\mathbf{x}, t_0) \quad \text{on} \quad \Omega \\ \mathbf{u}(\mathbf{x}, t) = 0 \quad \text{on} \quad \partial\Omega_w \\ \int_{\partial\Omega_{in}} \mathbf{u}(\mathbf{x}, t) \cdot \mathbf{n} dS = \int_{\partial\Omega_{in}} \mathbf{u}_{mri}(\mathbf{x}, t) \cdot \mathbf{n} dS \end{cases}$
3D MRI PPE (slip walls)	$\begin{cases} \mathbf{u}(\mathbf{x}, t_0) = \mathbf{u}_{mri}(\mathbf{x}, t_0) \quad \text{on} \quad \Omega \\ \mathbf{u}(\mathbf{x}, t) \cdot \mathbf{n} = 0 \quad \text{on} \quad \partial\Omega_w \\ \int_{\partial\Omega_{in}} \mathbf{u}(\mathbf{x}, t) \cdot \mathbf{n} dS = \int_{\partial\Omega_{in}} \mathbf{u}_{mri}(\mathbf{x}, t) \cdot \mathbf{n} dS \end{cases}$
2D MRI PPE	$\begin{cases} \mathbf{u}(\mathbf{x}, t_0) = 0 \quad \text{on} \quad \Omega \\ \mathbf{u}(\mathbf{x}, t) = 0 \quad \text{on} \quad \partial\Omega_w \\ \int_{\partial\Omega_{in}} \mathbf{u}(\mathbf{x}, t) \cdot \mathbf{n} dS = \int_{\partial\Omega_{in}} \mathbf{u}_{mri}(\mathbf{x}, t) \cdot \mathbf{n} dS \end{cases}$

a simplification of the latter in that it calculates the pressure drop when only an inflow velocity profile is prescribed, with null velocity field anywhere else in the domain. In practice, this case corresponds to measuring the inlet velocity field with 2D CINE PC-MRI, as well as the morphology of the domain. This approach is devoted to evaluate the sensitivity of the pressure to the input velocity distribution. Moreover, it is much less time-consuming than measuring the full 3D velocity field with 4D Flow MRI scan as only a 2D CINE PC-MRI scan with morphology is required. Table 7.1 summarizes the methods considered and their main features. Note that the three approaches developed here could be seen as the pressure reconstruction methods available when the input velocity datasets come from different MRI modalities: namely, *3D MRI PPE,3D MRI PPE (steady)*, and *2D MRI PPE* correspond to 4D Flow MRI, 3D PC-MRI, and 2D CINE PC-MRI respectively.

7.4.2 3D MRI PPE approach

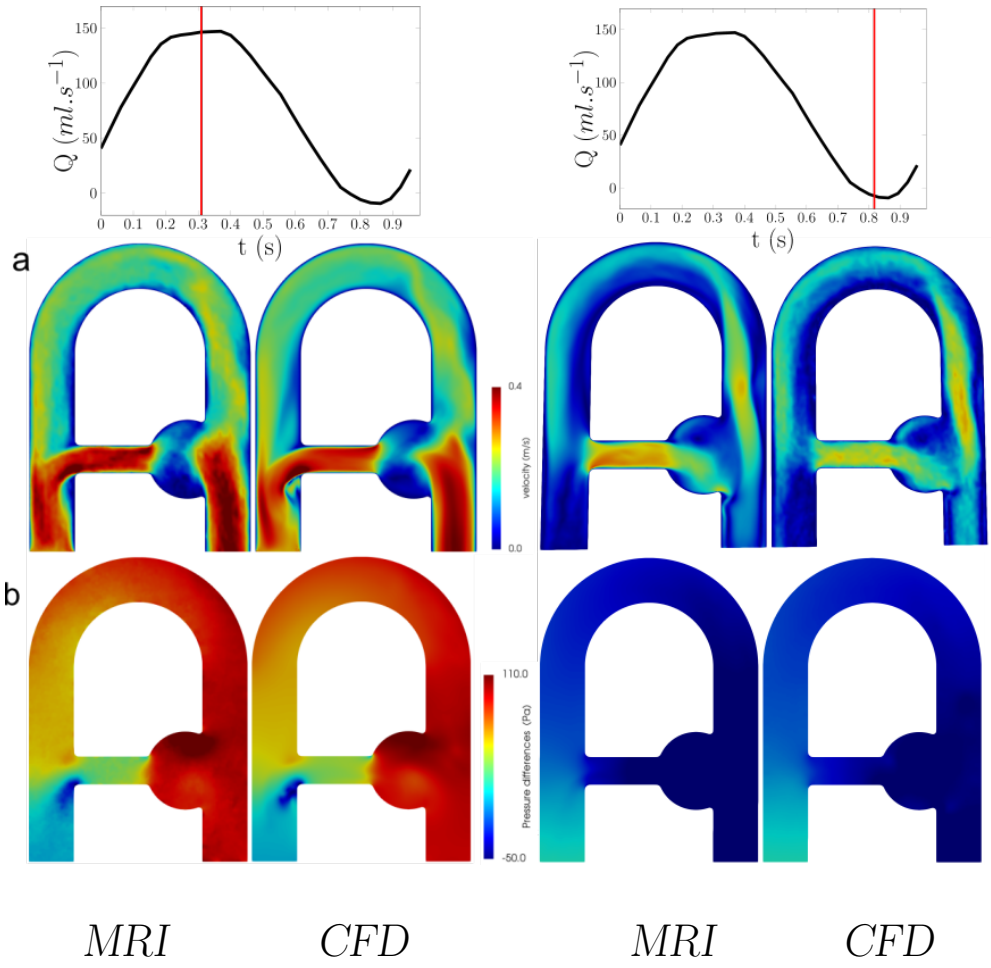

Figure 7.1: a). Velocity magnitude and b). relative pressure fields obtained from PC-MRI (2mm isotropic voxel size) and CFD at peak systole (left) and late diastole (right).

The relative pressure calculated from the full *3D MRI PPE* approach with no-slip boundary condition at walls is qualitatively compared in Figure 7.1 with the CFD phase-averaged pressure field at peak systole and late diastole. The corresponding MRI and CFD velocity fields are also shown for clarity. The MRI relative pressure field reveals very reproducible patterns at both peak systole and diastole as compared to CFD and no large visual discrepancy can be distinguished. The high pressure gradient interface at the collateral inlet seems well captured. Similarly, the pressure gradient induced at the downstream edge of the collateral branch is correctly predicted, although somewhat more diffused in the MRI field.

Quantitatively, an excellent agreement ($r^2 = 0.98$) is obtained at peak systole (see Fig. 7.2). Note however a sudden decrease of the correlation at phases when the flow rate time derivative gets close to zero, right after the peak systole and at

late diastole. These phases correspond to instants in the cycle when the transient effects are dominated by the viscous and convective effects. The Bland-Altman and regression plot in Figure 7.2 also show a net overestimation of the pressure computed from MRI at nodes that encompass the highest pressure levels. A closer look on the pressure maps reveals that these nodes correspond to the boundary walls, where the Neumann pressure boundary condition is prescribed.

To release the friction at walls responsible for the pressure overestimation, the same *3D MRI PPE* approach was solved but prescribing slip walls boundary condition instead. A general improvement of the correlations is observed, as shown in Figure 7.2. Although still present and located about one phase earlier in the cycle, the correlation collapse is alleviated. Note also that the large MRI pressure overestimation at boundary walls vanishes, as seen in the linear regression plots. On the contrary, a global underestimation of pressure by MRI is observed as a constant bias in the no-slip wall linear regression plot. This may be explained by the lower viscous resistance at boundary walls, implying a lower viscous and convective pressure contributions. Moreover, as highlighted in Ebbers et al. [46], the low MRI spatial resolution tends to underestimate the gradient and Laplacian operators necessary to calculate the viscous $\nabla^2\mathbf{u}$ and convective effects $\mathbf{u}\cdot\nabla\mathbf{u}$.

Given the overestimation/underestimation whenever no-slip/slip walls are set respectively, one can infer that the 'true' MRI pressure could be bounded by these two cases.

7.4.3 Splitting of the pressure contributions

Figure 7.3 shows the relative inlet-outlet pressure drop computed with the presented approaches. The full PPE (*3D MRI PPE*) is compared with the PPE including viscous and convective contributions only (*3D MRI PPE (steady)*), as well as with the *2D MRI PPE* comprising the transient contribution at inlet boundary only. These approaches are compared with the reference pressure drop predicted by CFD (*full CFD*). A second reference pressure drop compatible with the *3D MRI PPE (steady)* was generated by prescribing a steady inflow profile at each phase. This approach is denoted *CFD (steady)*.

Omitting the transient effects (*3D MRI PPE steady*) leads to the inverse trends as those predicted with the full CFD. As compared to the reference steady CFD field (*CFD (steady)*) however, similar pressure drops are observed, with a slight overestimation of the MRI. This trend is supported by the linear regression result in Fig. 7.2, where the pressure obtained with no-slip boundary conditions systematically overestimates the CFD pressure. This result confirms our explanation that this is the added wall resistance due to the prescribed boundary condition (i.e. viscous/convective effects) that are responsible for this overestimation.

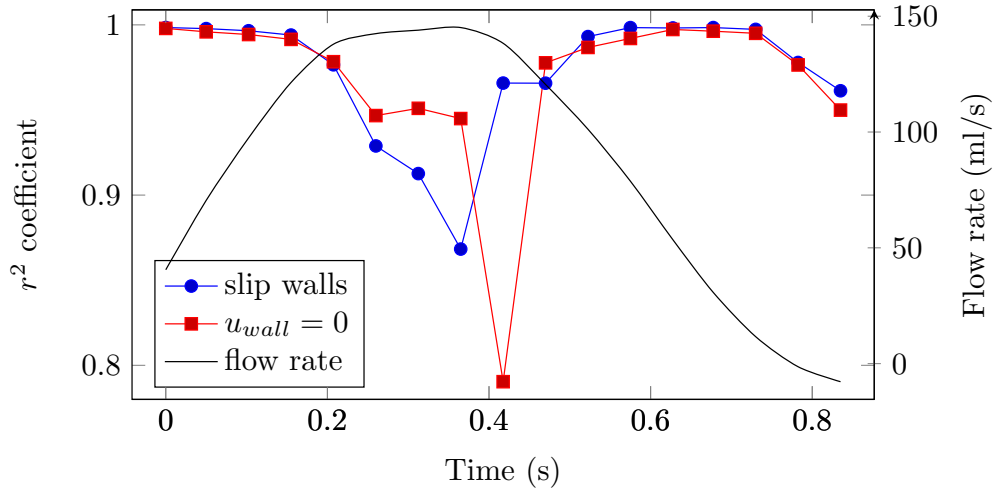

(a)

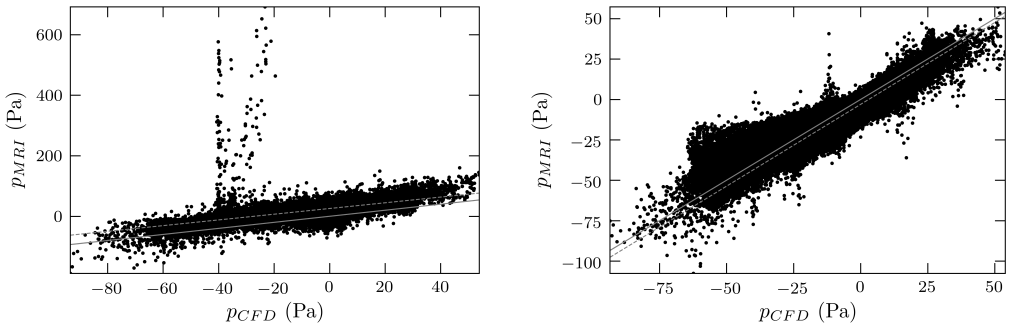

(b)

Figure 7.2: a). Correlation between the **3D MRI PPE** approach with both slip and no-slip boundary walls and compared to CFD for each phase during the cycle. The inlet flow rate is also plotted for a better comprehension. b). Linear regression plots at phase 9 (sudden decrease at $t = 0.4\ ms$) for the **left** no-slip walls and **right** slip wall case, respectively.

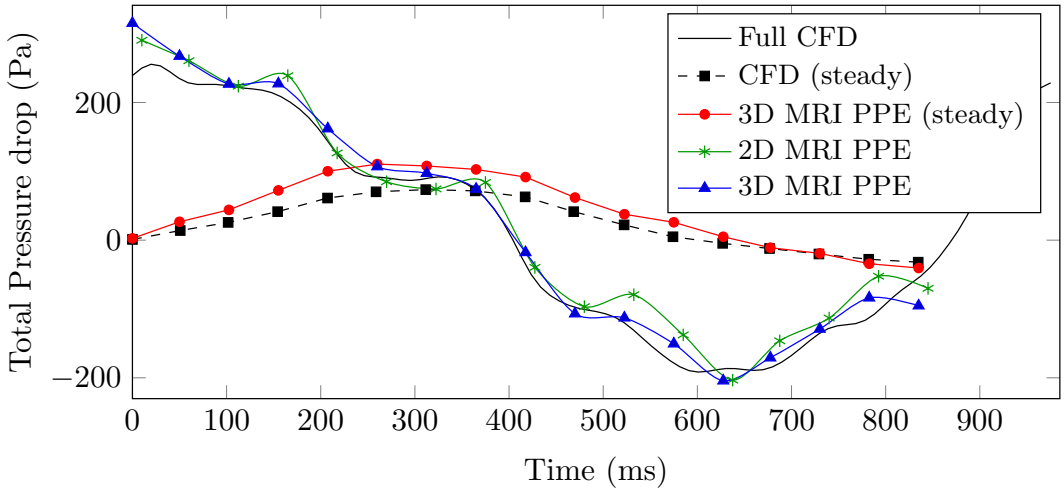

Figure 7.3: Pressure drops computed from MRI solving the 3D PPE approaches compared with CFD.

In the *2D MRI PPE* approach, the velocity is set to zero in the whole domain except at the inlet surface plane, where the time-varying velocity profile is prescribed to account for the transient contribution. The pressure drop temporal evolution reveals very similar pressure drops as compared to the full 3D MRI PPE as well as the full CFD approaches. While slightly higher oscillations are observed, this approach agrees unexpectedly well. Both the velocity magnitude and corresponding pressure maps are depicted in the middle slice of the phantom at different instants during the cycle, as shown in Figure 7.4. The high velocity magnitude differences resulting in low relative pressure discrepancies suggest that the pressure drop evolution in a rigid phantom is largely dominated by the flow rate waveform, with low dependencies on the details of the velocity profile.

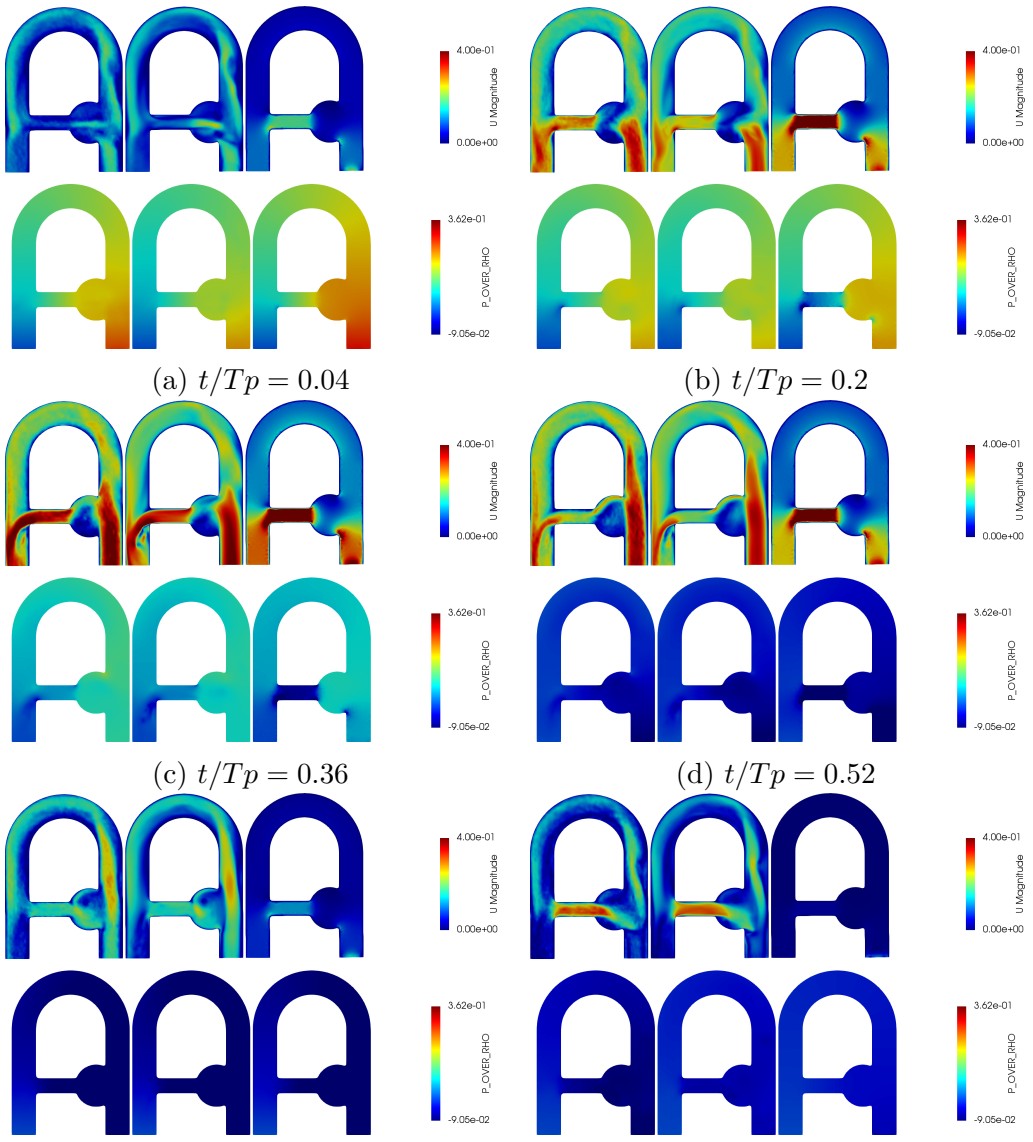

(a) $t/Tp = 0.04$ (b) $t/Tp = 0.2$

(c) $t/Tp = 0.36$ (d) $t/Tp = 0.52$

(e) $t/Tp = 0.73$ (f) $t/Tp = 0.89$

Figure 7.4: Phase-averaged velocity magnitude **top** and pressure maps **bottom** reconstructed at different instants in the cycle from **left** 3D PPE, **middle** CFD, **right** 2D PPE.

Stability criterion for explicit numerical scheme

In this section, we derive the stability criterion of the Explicit RK4 scheme presented in Section 36.

$$\mathbf{M}_i^{n+1} = \mathbf{M}_i^n + \Delta t f(\mathbf{M}_i^n, t^n) \tag{7.8}$$

where $f(\mathbf{M}_i^n, t^n)$ is the right-hand side term of Eq. (2.10). Let us analyse only one direction (called m) of the magnetization vector($\mathbf{M}$) such that one can decompose f in Taylor series around its initial value t^0 as follows:

$$f(m_i^n, t^n) = f(m_i^0, t^0) + (t^n - t^0)\frac{\partial f}{\partial t}(m_i^0, t^0) + (m_i^n - m_i^0)\frac{\partial f}{\partial m}(m_i^0, t^0) + ... \tag{7.9}$$

Then:

$$f(m_i^n, t^n) = \lambda m_i^n + \alpha_1 + \alpha_2 t^n + ... \tag{7.10}$$

where $\lambda = \frac{\partial f}{\partial m}(m^0, t^0)$,$\alpha_1, \alpha_2$ are constants. If one neglects the inhomogeneous terms in the previous expression of $f(m_i^n, t^n)$ and keep only the first term λm_i^n, it results that we can write:

$$m_i^{n+1} = m_i^n(1 + \lambda\Delta t) \tag{7.11}$$

Considering the previous equation as a geometric progression, the solution at time step n could therefore be written as:

$$m_i^n = m_i^0\,(1 + \lambda_i\Delta t)^n \tag{7.12}$$

And therefore, the scheme is stable if $|1 + \lambda\Delta t| \leq 1$. Let's consider the simple relaxation case where $\mathbf{B} = (0, 0, 0)$, then the stability constraint becomes:

$$\begin{aligned} \lambda_x &= -\frac{M'_x}{T_2} \\ \lambda_y &= -\frac{M'_y}{T_2} \\ \lambda_z &= \frac{M_0 - M_z}{T_1} \end{aligned} \tag{7.13}$$

Then, according to the 3 axes of the rotating frame of reference, the stability condition for the Euler explicit scheme imposes that:

$$\Delta t < 2\min(T1, T2) \tag{7.14}$$

From the assumption that the inhomogeneous terms are neglected in the Taylor series decomposition (see Eq. (7.10)), the time step calculated is valid for relaxation only, where RF and gradients are null. It should be noted that in practice the T_1

relaxation time is always larger than T_2, therefore, we can simplify the previous time step constraint to

$$\Delta t \leq 2T_2 \tag{7.15}$$

In the case where encoding gradients are on, but RF pulse is still off, (i.e:$\mathbf{B} = (0, 0, B_z)$), then a stability condition could be found for the transverse magnetization M_{xy}, and Equation 7.11 becomes:

$$M_{xy}^{n+1} = M_{xy}^{n} \left(1 - \Delta t \left(i\gamma B_z + \frac{1}{T_2}\right)\right) \tag{7.16}$$

Then the stability condition generalizes to:

$$\Delta t \leq \frac{2}{T_2 \left(\frac{1}{T_2^2} + \gamma^2 B_z^2\right)} \tag{7.17}$$

As expected, when $B_z = 0$ the stability constraint equals to Eq. 7.15.

Bibliography

[1] Procedure for estimation and reporting of uncertainty due to discretization in cfd applications. *Journal of Fluids Engineering*, 130(7):078001–078001–4, July 2008.

[2] Medical gallery of blausen medical 2014. *WikiJournal of Medicine*, 1(2), 2014.

[3] Robert A. McLaughlin, John Hipwell, Graeme P. Penney, Kawal Rhode, Albert Chung, and Julia Noble. Intensity-based registration versus feature-based registration for neurointerventions. 01 2001.

[4] G. Andria, F. Attivissimo, G. Cavone, and A. M. L. Lanzolla. Acquisition times in magnetic resonance imaging: Optimization in clinical use. *IEEE Transactions on Instrumentation and Measurement*, 58(9):3140–3148, Sep. 2009.

[5] A. Anjum, R. von Allmen, R. Greenhalgh, and J. T. Powell. Explaining the decrease in mortality from abdominal aortic aneurysm rupture. *British Journal of Surgery*, 99(5):637–645, 2012.

[6] Ali Bakhshinejad, Ahmadreza Baghaie, Alireza Vali, David Saloner, Vitaliy L. Rayz, and Roshan M. D'Souza. Merging computational fluid dynamics and 4d flow MRI using proper orthogonal decomposition and ridge regression. *Journal of Biomechanics*, 58:162–173, jun 2017.

[7] Helmut Baumgartner, Judy Hung, Javier Bermejo, John B. Chambers, Arturo Evangelista, Brian P. Griffin, Bernard Iung, Catherine M. Otto, Patricia A. Pellikka, and Miguel Quinones. Echocardiographic Assessment of Valve Stenosis: EAE/ASE Recommendations for Clinical Practice. *JOURNAL OF THE AMERICAN SOCIETY OF ECHOCARDIOGRAPHY*, 22(1):1–23, JAN 2009.

[8] H. Benoit-Cattin, G. Collewet, B. Belaroussi, H. Saint-Jalmes, and C. Odet. The simri project: a versatile and interactive mri simulator. *Journal of Magnetic Resonance*, 173(1):97 – 115, 2005.

[9] P. Berg, D. Stucht, G. Janiga, O. Beuing, O. Speck, and Thévenin D. Cerebral blood flow in a healthy Circle of Willis and two intracranial aneurysms:

Computational Fluid Dynamics versus four-dimensional Phase-Contrast Magnetic Resonance Imaging. *Journal of Biomechanical Engineering*, 2014.

[10] S A Berger, L Talbot, and L S Yao. Flow in curved pipes. *Annual Review of Fluid Mechanics*, 15(1):461–512, jan 1983.

[11] M. A. Bernstein, David M. Thomasson, and William H. Perman. Improved detectability in low signal-to-noise ratio magnetic resonance images by means of a phase-corrected real reconstruction. *Medical Physics*, 16(5):813–817, sep 1989.

[12] Matt A. Bernstein, Kevin F. King, and Xiaohong Joe Zhou. *Handbook of MRI Pulse Sequences*. Elsevier Inc., 9 2004.

[13] G. Biglino, D. Cosentino, J. A. Steeden, L. De Nova, M. Castelli, H. Ntsinjana, G. Pennati, A. M. Taylor, and S. Schievano. Using 4d cardiovascular magnetic resonance imaging to validate computational fluid dynamics: A case study. *Frontiers in Pediatrics*, 3:107, 2015.

[14] Malenka M. Bissell, Aaron T. Hess, Luca Biasiolli, Steffan J. Glaze, Margaret Loudon, Alex Pitcher, Anne Davis, Bernard Prendergast, Michael Markl, Alex J. Barker, Stefan Neubauer, and Saul G. Myerson. Aortic dilation in bicuspid aortic valve disease. *Circulation: Cardiovascular Imaging*, 6(4):499–507, jul 2013.

[15] J. Bittoun, O. Jolivet, A. Herment, E. Itti, E. Durand, E. Mousseaux, and J.P. Tasu. Multidimensional MR mapping of multiple components of velocity and acceleration by fourier phase encoding with a small number of encoding steps. *Magnetic Resonance in Medicine*, 44(5):723–730, 2000.

[16] J. Bittoun, J. Taquin, and M. Sauzade. A computer algorithm for the simulation of any Nuclear Magnetic Resonance (NMR) imaging method. *Magnetic Resonance Imaging*, 2(2):113 – 120, 1984.

[17] F. Bloch. Nuclear induction. *Phys. Rev.*, 70:460–474, Oct 1946.

[18] J. Bock, B. W. Kreher, J. Henning, and M. Markl. Optimized pre-processing of time-resolved 2D and 3D Phase Contrast mri. In *Proc. Intl. Soc. Mag. Reson. Med.*, 2007.

[19] Loic Boussel, Vitaliy Rayz, Alastair Martin, Gabriel Acevedo-Bolton, Michael T. Lawton, Randall Higashida, Wade S. Smith, William L. Young, and David Saloner. Phase-contrast magnetic resonance imaging measurements in intracranial aneurysms in vivo of flow patterns, velocity fields, and

wall shear stress: Comparison with computational fluid dynamics. *Magnetic Resonance in Medicine*, 61(2):409–417, feb 2009.

[20] Loic Boussel, Vitaliy Rayz, Charles McCulloch, Alastair Martin, Gabriel Acevedo-Bolton, Michael Lawton, Randall Higashida, Wade S. Smith, William L. Young, and David Saloner. Aneurysm growth occurs at region of low wall shear stress. *Stroke*, 39(11):2997–3002, nov 2008.

[21] Anthony R. Brady, Simon G. Thompson, F. Gerald R. Fowkes, Roger M. Greenhalgh, and Janet T. Powell. Abdominal aortic aneurysm expansion. *Circulation*, 110(1):16–21, jul 2004.

[22] Robert W. Brown, Yu-Chung N. Cheng, E. Mark Haacke, Michael R. Thompson, and Ramesh Venkatesan, editors. *Magnetic Resonance Imaging*. John Wiley & Sons Ltd, apr 2014.

[23] Julia Busch, Daniel Giese, Lukas Wissmann, and Sebastian Kozerke. Reconstruction of divergence-free velocity fields from cine 3d phase-contrast flow measurements. *Magnetic Resonance in Medicine*, 69(1):200–210, mar 2012.

[24] F. M. Callaghan, J. Karkouri, K. Broadhouse, M. Evin, D. F. Fletcher, and S. M. Grieve. Thoracic aortic aneurysm: 4d flow MRI and computational fluid dynamics model. *Computer Methods in Biomechanics and Biomedical Engineering*, 18(sup1):1894–1895, aug 2015.

[25] William D Campbell and John C Slattery. Flow in the Entrance of a Tube. *Journal Of Basic Engineering*, 1963.

[26] Belen Casas, Jonas Lantz, Petter Dyverfeldt, and Tino Ebbers. 4d flow mri-based pressure loss estimation in stenotic flows: Evaluation using numerical simulations. *Magnetic Resonance in Medicine*, 75(4):1808–1821, 2016.

[27] Juan R. Cebral, Marcelo A. Castro, James E. Burgess, Richard S. Pergolizzi, Michael J. Sheridan, and Christopher M. Putman. Characterization of cerebral aneurysms for assessing risk of rupture by using patient-specific computational hemodynamics models. *American Journal of Neuroradiology*, 26(10):2550–2559, 2005.

[28] Alexander Chernobelsky, Oleg Shubayev, Cindy R. Comeau, and Steven D. Wolff. Baseline correction of phase contrast images improves quantification of blood flow in the great vessels. *Journal of Cardiovascular Magnetic Resonance*, 9(4):681–685, jul 2007.

[29] C. Chnafa, O. Brina, V.M. Pereira, and D.A. Steinman. Better than nothing: A rational approach for minimizing the impact of outflow strategy on

cerebrovascular simulations. *American Journal of Neuroradiology*, 39(2):337–343, 2017.

[30] C. Chnafa, S. Mendez, R. Moreno, and F. Nicoud. *Using Image-based CFD to Investigate the Intracardiac Turbulence*, pages 97–117. Springer International Publishing, Cham, 2015.

[31] C. Chnafa, S. Mendez, and F. Nicoud. Image-based large-eddy simulation in a realistic left heart. *Computers & Fluids*, 94(Supplement C):173 – 187, 2014.

[32] C. Chnafa, S. Mendez, and F. Nicoud. Image-based simulations show important flow fluctuations in a normal left ventricle: What could be the implications? *Annals of Biomedical Engineering*, 44(11):3346–3358, Nov 2016.

[33] Alexandre J. Chorin and Jerrold E. Marsden. *A Mathematical Introduction to Fluid Mechanics*. Springer New York, 1993.

[34] Alexandre Joel Chorin. Numerical solution of the navier-stokes equations*. *Mathematics of Computation*, 22:745–762, 1968.

[35] M. Cibis, W. V. Potters, F. J. H. Gijsen, H. Marquering, E. vanBavel, A. F. W. van der Steen, A. J. Nederveen, and J. J. Wentzel. Wall shear stress calculations based on 3D cine phase contrast MRI and computational fluid dynamics: a comparison study in healthy carotid arteries. *NMR in Biomedicine*, 27(7):826–834, 2014. NBM-13-0300.R2.

[36] Jay N. Cohn, Arshed A. Quyyumi, Norman K. Hollenberg, and Kenneth A. Jamerson. Surrogate markers for cardiovascular disease. *Circulation*, 109(25 suppl 1):IV–31–IV–46, 2004.

[37] Paolo Crosetto, Philippe Reymond, Simone Deparis, Dimitrios Kontaxakis, Nikolaos Stergiopulos, and Alfio Quarteroni. Fluid–structure interaction simulation of aortic blood flow. *Computers & Fluids*, 43(1):46–57, apr 2011.

[38] Guillaume Daviller, Maxence Brebion, Pradip Xavier, Gabriel Staffelbach, Jens-Dominik Müller, and Thierry Poinsot. A mesh adaptation strategy to predict pressure losses in LES of swirled flows. *Flow, Turbulence and Combustion*, 99(1):93–118, mar 2017.

[39] W.R. Dean. XVI.note on the motion of fluid in a curved pipe. *The London, Edinburgh, and Dublin Philosophical Magazine and Journal of Science*, 4(20):208–223, jul 1927.

[40] W.R. Dean. LXXII.the stream-line motion of fluid in a curved pipe(second paper). *The London, Edinburgh, and Dublin Philosophical Magazine and Journal of Science*, 5(30):673–695, apr 1928.

[41] Anagha Deshmane, Vikas Gulani, Mark A. Griswold, and Nicole Seiberlich. Parallel MR imaging. *Journal of Magnetic Resonance Imaging*, 36(1):55–72, June 2012.

[42] Fabrizio Donati, C. Alberto Figueroa, Nicolas P. Smith, Pablo Lamata, and David A. Nordsletten. Non-invasive pressure difference estimation from PC-MRI using the work-energy equation. *Medical Image Analysis*, 26(1):159–172, dec 2015.

[43] F. Durst, S. Ray, B. Unsal, and O. A. Bayoumi. The Development Lengths of Laminar Pipe and Channel Flows. *J. Fluids Eng.*, 127(6):1154, 2005.

[44] Petter Dyverfeldt, Malenka Bissell, Alex J. Barker, Ann F. Bolger, Carl-Johan Carlhäll, Tino Ebbers, Christopher J. Francios, Alex Frydrychowicz, Julia Geiger, Daniel Giese, Michael D. Hope, Philip J. Kilner, Sebastian Kozerke, Saul Myerson, Stefan Neubauer, Oliver Wieben, and Michael Markl. 4d flow cardiovascular magnetic resonance consensus statement. *Journal of Cardiovascular Magnetic Resonance*, 17(1), aug 2015.

[45] Petter Dyverfeldt, John-Peder Escobar Kvitting, Andreas Sigfridsson, Jan Engvall, Ann F. Bolger, and Tino Ebbers. Assessment of fluctuating velocities in disturbed cardiovascular blood flow: In vivo feasibility of generalized phase-contrast mri. *Journal of Magnetic Resonance Imaging*, 28(3):655–663, 2008.

[46] T. Ebbers, L. Wigstrom, A. F. Bolger, B. Wranne, and M. Karlsson. Noninvasive measurement of time-varying three-dimensional relative pressure fields within the human heart. *Journal of Biomechanical Engineering*, 124(3):288, 2002.

[47] Tino Ebbers and Gunnar Farnebäck. Improving computation of cardiovascular relative pressure fields from velocity MRI. *Journal of Magnetic Resonance Imaging*, 30(1):54–61, jul 2009.

[48] Tino Ebbers, Lars Wigström, Ann F. Bolger, Jan Engvall, and Matts Karlsson. Estimation of relative cardiovascular pressures using time-resolved three-dimensional phase contrast MRI. *Magnetic Resonance in Medicine*, 45(5):872–879, 2001.

[49] W. A. Edelstein, Paul A. Bottomley, and Leah M. Pfeifer. A signal-to-noise calibration procedure for NMR imaging systems. *Medical Physics*, 11(2):180–185, mar 1984.

[50] Ahmad Falahatpisheh, Carsten Rickers, Dominik Gabbert, Ee Ling Heng, Aurelien Stalder, Hans-Heiner Kramer, Philip J. Kilner, and Arash Kheradvar. Simplified bernoulli's method significantly underestimates pulmonary transvalvular pressure drop. *Journal of Magnetic Resonance Imaging*, 43(6):1313–1319, 2015.

[51] DMITRY A. FEDOSOV, BRUCE CASWELL, ALEKSANDER S. POPEL, and GEORGE EM KARNIADAKIS. Blood flow and cell-free layer in microvessels. *Microcirculation*, 17(8):615–628, nov 2010.

[52] Dmitry A. Fedosov, Ming Dao, George Em Karniadakis, and Subra Suresh. Computational biorheology of human blood flow in health and disease. *Annals of Biomedical Engineering*, 42(2):368–387, oct 2013.

[53] Luca Formaggia, Alfio Quarteroni, and Alessandro Veneziani. *Cardiovascular Mathematics*, volume 3. 2009.

[54] Alexandre Fortin, Stéphanie Salmon, Joseph Baruthio, Maya Delbany, and Emmanuel Durand. Flow MRI simulation in complex 3D geometries: Application to the cerebral venous network. *Magn. Reson. Med.*, 80(4):1655–1665, April 2019.

[55] Y. C. Fung Fung Yuan-Cheng. *Biomechanics*. Springer New York, 2010.

[56] D Garcia, J C del Álamo, D Tanné, R Yotti, C Cortina, É Bertrand, J C Antoranz, E Pérez-David, R Rieu, F Fernández-Avilés, and J Bermejo. Two-dimensional intraventricular flow mapping by digital processing conventional color-doppler echocardiography images. *IEEE Transactions on Medical Imaging*, 29(10):1701–1713, oct 2010.

[57] Damien Garcia, Philippe Pibarot, Jean G. Dumesnil, Frédéric Sakr, and Louis-Gilles Durand. Assessment of aortic valve stenosis severity. *Circulation*, 101(7):765–771, 2000.

[58] Peter D. Gatehouse, Marijn P. Rolf, Martin J. Graves, Mark BM Hofman, John Totman, Beat Werner, Rebecca A. Quest, Yingmin Liu, Jochen von Spiczak, Matthias Dieringer, David N. Firmin, Albert van Rossum, Massimo Lombardi, Juerg Schwitter, Jeanette Schulz-Menger, and Philip J. Kilner. Flow measurement by cardiovascular magnetic resonance: a multi-centre multi-vendor study of background phase offset errors that can compromise

the accuracy of derived regurgitant or shunt flow measurements. *Journal of Cardiovascular Magnetic Resonance*, 12(1):5, Jan 2010.

[59] F. P. Glor, J. J M Westenberg, J. Vierendeels, M. Danilouchkine, and P. Verdonck. Validation of the coupling of magnetic resonance imaging velocity measurements with computational fluid dynamics in a U bend. *Artificial Organs*, 26(7):622–635, 2002.

[60] Gerald Greil, Tal Geva, Stephan E. Maier, and Andrew J. Powell. Effect of acquisition parameters on the accuracy of velocity encoded cine magnetic resonance imaging blood flow measurements. *Journal of Magnetic Resonance Imaging*, 15(1):47–54, 2002.

[61] Philip M. Gresho and Robert L. Sani. On pressure boundary conditions for the incompressible navier-stokes equations. *International Journal for Numerical Methods in Fluids*, 7(10):1111–1145, oct 1987.

[62] Sascha Gross-Hardt, Fiete Boehning, Ulrich Steinseifer, Thomas Schmitz-Rode, and Tim A. S. Kaufmann. Mesh sensitivity analysis for quantitative shear stress assessment in blood pumps using computational fluid dynamics. *Journal of Biomechanical Engineering*, 141(2):021012, dec 2018.

[63] HáKon Gudbjartsson and Samuel Patz. The rician distribution of noisy mri data. *Magnetic Resonance in Medicine*, 34(6):910–914, 1995.

[64] Hojin Ha, Jonas Lantz, Magnus Ziegler, Belen Casas, Matts Karlsson, Petter Dyverfeldt, and Tino Ebbers. Estimating the irreversible pressure drop across a stenosis by quantifying turbulence production using 4d flow mri. *Scientific Reports*, 7:46618, April 2017.

[65] E.M. Haacke, R.W. Brown, M.R. Thompson, and R. Venkatesan. *Magnetic Resonance Imaging: Physical Principles and Sequence Design*. Wiley, 1999.

[66] Craig A Hamilton, Jennifer H Jordan, Robert A Kraft, and W Gregory Hundley. Noninterleaved velocity encodings for improved temporal and spatial resolution in phase-contrast magnetic resonance imaging. *Journal of computer assisted tomography*, 34(4):570—574, July 2010.

[67] Arijit Hazra, Gert Lube, and Hans-Georg Raumer. Numerical simulation of Bloch equations for dynamic magnetic resonance imaging. *Applied Numerical Mathematics*, 123:241 – 255, 2018.

[68] X He and D N Ku. Unsteady entrance flow development in a straight tube. *Journal of biomechanical engineering*, 116:355–360, 1994.

[69] Xiaoyi He, David N. Ku, and James E. Moore. Simple calculation of the velocity profiles for pulsatile flow in a blood vessel using mathematica. *Annals of Biomedical Engineering*, 21(1):45–49, 1993.

[70] Soroush Heidari Pahlavian, Alexander C. Bunck, Francis Loth, Shane R. Tubbs, T. I. Yiallourou, J. R. Kröger, Walter Heindel, and B. A. Martin. Characterization of the discrepancies between four-dimensional phase-contrast magnetic resonance imaging and in-silico simulations of cerebrospinal fluid dynamics. *Journal of Biomechanical Engineering*, 137(5):051002–051002–8, 2015.

[71] Berthold K. P. Horn, Hugh M. Hilden, and Shahriar Negahdaripour. Closed-form solution of absolute orientation using orthonormal matrices. *Journal of the Optical Society of America A*, 5(7):1127, jul 1988.

[72] Kartik Jain, Jingfeng Jiang, Charles Strother, and Kent-André Mardal. Transitional hemodynamics in intracranial aneurysms — comparative velocity investigations with high resolution lattice boltzmann simulations, normal resolution ansys simulations, and mr imaging. *Medical Physics*, 43(11):6186–6198, 2016.

[73] Gábor Janiga. Large eddy simulation of the fda benchmark nozzle for a reynolds number of 6500. *Comput. Biol. Med.*, 47(C):113–119, April 2014.

[74] Thies H. Jochimsen, Andreas Schäfer, Roland Bammer, and Michael E. Moseley. Efficient simulation of magnetic resonance imaging with bloch–torrey equations using intra-voxel magnetization gradients. *Journal of Magnetic Resonance*, 180(1):29–38, may 2006.

[75] L.D. Jou and D. Saloner. A numerical study of magnetic resonance images of pulsatile flow in a two dimensional carotid bifurcation: A numerical study of MR images. *Medical Engineering & Physics*, 20(9):643 – 652, 1998.

[76] Krzysztof Jurczuk, Marek Kretowski, Jean-Jacques Bellanger, Pierre-Antoine Eliat, Hervé Saint-Jalmes, and Johanne Bézy-Wendling. Computational modeling of mr flow imaging by the lattice Boltzmann method and Bloch equation. *Magnetic Resonance Imaging*, 31(7):1163 – 1173, 2013.

[77] Iman Khodarahmi, Mostafa Shakeri, Melanie Kotys-Traughber, Stefan Fischer, M. Keith Sharp, and Amir A. Amini. In vitro validation of flow measurement with phase contrast MRI at 3 tesla using stereoscopic particle image velocimetry and stereoscopic particle image velocimetry-based computational fluid dynamics. *Journal of Magnetic Resonance Imaging*, 39(6):1477–1485, oct 2013.

[78] J. Kim and P. Moin. Application of a fractional-step method to incompressible navier-stokes equations. *Journal of Computational Physics*, 59(2):308 – 323, 1985.

[79] Artur Klepaczko, Piotr Szczypiński, Grzegorz Dwojakowski, Michał Strzelecki, and Andrzej Materka. Computer simulation of magnetic resonance angiography imaging: Model description and validation. *PLOS ONE*, 9(4):1–15, 04 2014.

[80] A. N. Kolmogorov. The local structure of turbulence in incompressible viscous fluid for very large reynolds numbers. *Proceedings: Mathematical and Physical Sciences*, 434(1890):9–13, 1941.

[81] M. Kraushaar. *Application of the compressible and low-mach number approaches to large-eddy simulation of turbulent flows in aero-engines*. PhD thesis, Institut National Polytechnique de Toulouse, 2011.

[82] Sebastian B.S. Krittian, Pablo Lamata, Christian Michler, David A. Nordsletten, Jelena Bock, Chris P. Bradley, Alex Pitcher, Philip J. Kilner, Michael Markl, and Nic P. Smith. A finite-element approach to the direct computation of relative cardiovascular pressure from time-resolved MR velocity data. *Medical Image Analysis*, 16(5):1029–1037, jul 2012.

[83] Z. Kulcsár, Á. Ugron, M. Marosfői, Z. Berentei, G. Paál, and I. Szikora. Hemodynamics of cerebral aneurysm initiation: The role of wall shear stress and spatial wall shear stress gradient. *American Journal of Neuroradiology*, 32(3):587–594, feb 2011.

[84] Jihoon Kweon, Dong Hyun Yang, Guk Bae Kim, Namkug Kim, MunYoung Paek, Aurelien F. Stalder, Andreas Greiser, and Young-Hak Kim. Four-dimensional flow mri for evaluation of post-stenotic turbulent flow in a phantom: comparison with flowmeter and computational fluid dynamics. *European Radiology*, 26(10):3588–3597, Oct 2016.

[85] John F LaDisa, Lars E Olson, Douglas A Hettrick, David C Warltier, Judy R Kersten, and Paul S Pagel. *BioMedical Engineering OnLine*, 4(1):59, 2005.

[86] Pablo Lamata, Alex Pitcher, Sebastian Krittian, David Nordsletten, Malenka M. Bissell, Thomas Cassar, Alex J. Barker, Michael Markl, Stefan Neubauer, and Nicolas P. Smith. Aortic relative pressure components derived from four-dimensional flow cardiovascular magnetic resonance. *Magn. Reson. Med.*, 72(4):1162–1169, March 2014.

[87] Jonas Lantz, Tino Ebbers, Jan Engvall, and Matts Karlsson. Numerical and experimental assessment of turbulent kinetic energy in an aortic coarctation. *Journal of Biomechanics*, 46(11):1851 – 1858, 2013.

[88] Adrian T. Lee, G. Bruce Pike, and Norbert J. Pelc. Three-point phase-contrast velocity measurements with increased velocity-to-noise ratio. *Magnetic Resonance in Medicine*, 33(1):122–126, 1995.

[89] A. Leonard. Energy cascade in large-eddy simulations of turbulent fluid flows. In *Turbulent Diffusion in Environmental Pollution, Proceedings of a Symposium held at Charlottesville*, pages 237–248. Elsevier, 1975.

[90] Andrea S. Les, Shawn C. Shadden, C. Alberto Figueroa, Jinha M. Park, Maureen M. Tedesco, Robert J. Herfkens, Ronald L. Dalman, and Charles A. Taylor. Quantification of hemodynamics in abdominal aortic aneurysms during rest and exercise using magnetic resonance imaging and computational fluid dynamics. *Annals of Biomedical Engineering*, 38(4):1288–1313, feb 2010.

[91] D. K. Lilly. A proposed modification of the germano subgrid-scale closure method. *Physics of Fluids A: Fluid Dynamics*, 4(3):633–635, mar 1992.

[92] Ramona Lorenz, Jelena Bock, Jeff Snyder, Jan G. Korvink, Bernd A. Jung, and Michael Markl. Influence of eddy current, Maxwell and gradient field corrections on 3D flow visualization of 3D CINE PC-MRI data. *Magnetic Resonance in Medicine*, 72(1):33–40, 2014.

[93] Sylvie Lorthois, Jenn Stroud-Rossman, Stanley Berger, Liang-Der Jou, and David Saloner. Numerical simulation of magnetic resonance angiographies of an anatomically realistic stenotic carotid bifurcation. *Annals of Biomedical Engineering*, 33(3):270–283, Jan 2005.

[94] Michael Lustig, David Donoho, and John M. Pauly. Sparse MRI: The application of compressed sensing for rapid MR imaging. *Magnetic Resonance in Medicine*, 58(6):1182–1195, 2007.

[95] W. H. Lyne. Unsteady viscous flow in a curved pipe. *Journal of Fluid Mechanics*, 45(1):13–31, jan 1971.

[96] Dan Ma, Vikas Gulani, Nicole Seiberlich, Kecheng Liu, Jeffrey L. Sunshine, Jeffrey L. Duerk, and Mark A. Griswold. Magnetic resonance fingerprinting. *Nature*, 495(7440):187–192, mar 2013.

[97] Mathias Malandain, Nicolas Maheu, and Vincent Moureau. Optimization of the deflated conjugate gradient algorithm for the solving of elliptic equations on massively parallel machines. *Journal of Computational Physics*, 238(Supplement C):32 – 47, 2013.

[98] Richard A. Malinauskas, Prasanna Hariharan, Steven W. Day, Luke H. Herbertson, Martin Buesen, Ulrich Steinseifer, Kenneth I. Aycock, Bryan C. Good, Steven Deutsch, Keefe B. Manning, and Brent A. Craven. Fda benchmark medical device flow models for cfd validation. *ASAIO Journal*, 63(2), 2017.

[99] M. Markl, S. Schnell, C. Wu, E. Bollache, K. Jarvis, A. J. Barker, J. D. Robinson, and C. K. Rigsby. Advanced flow MRI: emerging techniques and applications. *Clinical Radiology*, 71(8):779–795, 8 2016.

[100] Michael Markl, Frandics P. Chan, Marcus T. Alley, Kris L. Wedding, Mary T. Draney, Chris J. Elkins, David W. Parker, Ryan Wicker, Charles A. Taylor, Robert J. Herfkens, and Norbert J. Pelc. Time resolved three dimensional phase contrast MRI. *Journal of Magnetic Resonance Imaging*, 18(3):396–396, 2003.

[101] Michael Markl, Alex Frydrychowicz, Sebastian Kozerke, Mike Hope, and Oliver Wieben. 4d flow MRI. *Journal of Magnetic Resonance Imaging*, 36(5):1015–1036, oct 2012.

[102] David Marlevi, Bram Ruijsink, Maximilian Balmus, Desmond Dillon-Murphy, Daniel Fovargue, Kuberan Pushparajah, Cristóbal Bertoglio, Massimiliano Colarieti-Tosti, Matilda Larsson, Pablo Lamata, C. Alberto Figueroa, Reza Razavi, and David A. Nordsletten. Estimation of cardiovascular relative pressure using virtual work-energy. *Scientific Reports*, 9(1), feb 2019.

[103] Ian Marshall. Computational simulations and experimental studies of 3d phase-contrast imaging of fluid flow in carotid bifurcation geometries. *Journal of Magnetic Resonance Imaging*, 31(4):928–934, 2010.

[104] Johannes Mauer, Simon Mendez, Luca Lanotte, Franck Nicoud, Manouk Abkarian, Gerhard Gompper, and Dmitry A. Fedosov. Flow-induced transitions of red blood cell shapes under shear. *Physical Review Letters*, 121(11), sep 2018.

[105] D. J. McConalogue and R. S. Srivastava. Motion of a Fluid in a Curved Tube. *Proceedings of the Royal Society A: Mathematical, Physical and Engineering Sciences*, 307(1488):37–53, 1968.

[106] S. Mendez, C. Chnafa, E. Gibaud, J. Siguenza, V. Moureau, and F. Nicoud. YALES2BIO: a Computational Fluid Dynamics Software Dedicated to the Prediction of Blood Flows in Biomedical Devices. *International Federation for Medical and Biological Engineering*, 2015.

[107] S. Mendez and F. Nicoud. Large-eddy simulation of a bi-periodic turbulent flow with effusion. *Journal of Fluid Mechanics*, 598:27–65, feb 2008.

[108] Simon Mendez and Manouk Abkarian. In-plane elasticity controls the full dynamics of red blood cells in shear flow. *Physical Review Fluids*, 3(10), oct 2018.

[109] Rodrigo Méndez Rojano, Simon Mendez, and Franck Nicoud. Introducing the pro-coagulant contact system in the numerical assessment of device-related thrombosis. *Biomechanics and Modeling in Mechanobiology*, 17(3):815–826, Jun 2018.

[110] H. Meng, V.M. Tutino, J. Xiang, and A. Siddiqui. High wss or low wss? complex interactions of hemodynamics with intracranial aneurysm initiation, growth, and rupture: Toward a unifying hypothesis. *American Journal of Neuroradiology*, 35(7):1254–1262, 2014.

[111] Shohei Miyazaki, Keiichi Itatani, Toyoki Furusawa, Teruyasu Nishino, Masataka Sugiyama, Yasuo Takehara, and Satoshi Yasukochi. Validation of numerical simulation methods in aortic arch using 4d flow mri. *Heart and Vessels*, 32(8):1032–1044, Aug 2017.

[112] Parviz Moin and Krishnan Mahesh. Direct numerical simulation: A tool in turbulence research. *Annual Review of Fluid Mechanics*, 30(1):539–578, 1998.

[113] P. R. Moran. A flow velocity zeugmatographic interlace for nmr imaging in humans. *Magnetic Resonance Imaging*, 1:197–203, 1982.

[114] U. Morbiducci, R. Ponzini, D. Gallo, C. Bignardi, and G. Rizzo. Inflow boundary conditions for image-based computational hemodynamics: Impact of idealized versus measured velocity profiles in the human aorta. *Journal of Biomechanics*, 46(1):102 – 109, 2013.

[115] Victoria L. Morgan, Robert J. Roselli, and Christine H. Lorenz. Normal three-dimensional pulmonary artery flow determined by phase contrast magnetic resonance imaging. *Annals of Biomedical Engineering*, 26(4):557–566, Jul 1998.

[116] G. B. D. 2015 Mortality and Causes of Death Collaborators. Global, regional, and national life expectancy, all-cause mortality, and cause-specific mortality for 249 causes of death, 1980-2015: a systematic analysis for the global burden of disease study 2015. *Lancet (London, England)*, 388(27733281):1459–1544, October 2016.

[117] V. Moureau, P. Domingo, and L. Vervisch. Design of a massively parallel CFD code for complex geometries. *Comptes Rendus Mécanique*, 339(2):141 – 148, 2011. High Performance Computing.

[118] F. Nicoud and F. Ducros. *Flow, Turbulence and Combustion*, 62(3):183–200, 1999.

[119] Franck Nicoud, Hubert Baya Toda, Olivier Cabrit, Sanjeeb Bose, and Jungil Lee. Using singular values to build a subgrid-scale model for large eddy simulations. *Physics of Fluids*, 23(8):085106, 2011.

[120] J. Nikuradse and J. Nikuradse. Laws of flow in rough pipes. *VDI Forschungsheft*, page 361, 1933.

[121] S. Ohtsuki and M. Tanaka. The flow velocity distribution from the doppler information on a plane in three-dimensional flow. *Journal of Visualization*, 9(1):69–82, mar 2006.

[122] Magnus B. E. Olsson, Ronnie Wirestam, and Bertil R. R. Persson. A computer simulation program for MR imaging: application to rf and static magnetic field imperfections. *Magnetic Resonance in Medicine*, 34(4):612–617, 1995.

[123] T. J. Pedley. *The Fluid Mechanics of Large Blood Vessels*. Cambridge University Press, 1980.

[124] Norbert J. Pelc, Matt A. Bernstein, Ann Shimakawa, and Gary H. Glover. Encoding strategies for three-direction phase-contrast mr imaging of flow. *J. Magn. Reson. Imaging*, 1(4):405–413, January 2019.

[125] Sven Petersson, Petter Dyverfeldt, and Tino Ebbers. Assessment of the accuracy of MRI wall shear stress estimation using numerical simulations. *Journal of Magnetic Resonance Imaging*, 36(1):128–138, feb 2012.

[126] Sven Petersson, Petter Dyverfeldt, Roland Gårdhagen, Matts Karlsson, and Tino Ebbers. Simulation of phase contrast mri of turbulent flow. *Magnetic Resonance in Medicine*, 64(4):1039–1046, 2010.

[127] Stephen B. Pope. *Turbulent Flows*. Cambridge University Press, 2000.

[128] Wouter V. Potters, Pim Ooij, Henk Marquering, Ed vanBavel, and Aart J. Nederveen. Volumetric arterial wall shear stress calculation based on cine phase contrast MRI. *Journal of Magnetic Resonance Imaging*, 41(2):505–516, 2015.

[129] I. I. Rabi, J. R. Zacharias, S. Millman, and P. Kusch. A new method of measuring nuclear magnetic moments. *Physical Review*, 53:318, 1938.

[130] Vitaliy L. Rayz, Loic Boussel, Gabriel Acevedo-Bolton, Alastair J. Martin, William L. Young, Michael T. Lawton, Randall Higashida, and David Saloner. Numerical simulations of flow in cerebral aneurysms: Comparison of cfd results and in vivo mri measurements. *Journal of Biomechanical Engineering*, 130(5):051011–051011–9, August 2008.

[131] Dietmar Rempfer. On boundary conditions for incompressible navier-stokes problems. *Applied Mechanics Reviews*, 59(3):107–125, may 2006.

[132] Vinicius C. Rispoli, Jon F. Nielsen, Krishna S. Nayak, and Joao L. A. Carvalho. Computational fluid dynamics simulations of blood flow regularized by 3d phase contrast MRI. *BioMedical Engineering OnLine*, 14(1), nov 2015.

[133] C. Rocchini and P. Cignoni. Generating random points in a tetrahedron. *Journal of Graphics Tools*, 5(4):9–12, jan 2000.

[134] Partho P. Sengupta, Gianni Pedrizzetti, Philip J. Kilner, Arash Kheradvar, Tino Ebbers, Giovanni Tonti, Alan G. Fraser, and Jagat Narula. Emerging trends in CV flow visualization. *JACC: Cardiovascular Imaging*, 5(3):305–316, mar 2012.

[135] Anou Sewonu. *Développements méthodologiques et techniques pour le contrôle qualité en Imagerie par Résonance Magnétique*. PhD thesis, Université de Lorraine, 2014.

[136] Pavel Shkarin and Richard G. S. Spencer. Time domain simulation of fourier imaging by summation of isochromats. *International Journal of Imaging Systems and Technology*, 8(5):419–426, 1997.

[137] J. H. Siggers and Sarah L. Waters. Steady flows in pipes with finite curvature. *Physics of Fluids*, 17(7):1–18, 2005.

[138] J. Sigüenza, S. Mendez, D. Ambard, F. Dubois, F. Jourdan, R. Mozul, and F. Nicoud. Validation of an immersed thick boundary method for simulating fluid-structure interactions of deformable membranes. *Journal of Computational Physics*, 322:723 – 746, 2016.

[139] S. Moon-Ho Song, S. Napel, N.J. Pelc, and G.H. Glover. Phase unwrapping of MR phase images using poisson equation. *IEEE Transactions on Image Processing*, 4(5):667–676, may 1995.

[140] Samuel M. Song, Sandy Napel, Gary H. Glover, and Norbert J. Pelc. Noise reduction in three-dimensional phase-contrast mr velocity measurements. *Journal of Magnetic Resonance Imaging*, 3(4):587–596, 1993.

[141] S.M. Song, R.M. Leahy, D.P. Boyd, B.H. Brundage, and S. Napel. Determining cardiac velocity fields and intraventricular pressure distribution from a sequence of ultrafast CT cardiac images. *IEEE Transactions on Medical Imaging*, 13(2):386–397, jun 1994.

[142] Julio Sotelo, Jesus Urbina, Israel Valverde, Cristian Tejos, Pablo Irarrazaval, Marcelo E. Andia, Sergio Uribe, and Daniel E. Hurtado. 3d quantification of wall shear stress and oscillatory shear index using a finite-element method in 3d CINE PC-MRI data of the thoracic aorta. *IEEE Transactions on Medical Imaging*, 35(6):1475–1487, jun 2016.

[143] Julio Sotelo, Jesús Urbina, Israel Valverde, Cristian Tejos, Pablo Irarrázaval, Daniel E. Hurtado, and Sergio Uribe. Quantification of wall shear stress using a finite-element method in multidimensional phase-contrast MR data of the thoracic aorta. *Journal of Biomechanics*, 48(10):1817–1827, jul 2015.

[144] A.F. Stalder, M.F. Russe, A. Frydrychowicz, J. Bock, J. Hennig, and M. Markl. Quantitative 2d and 3d phase contrast MRI: Optimized analysis of blood flow and vessel wall parameters. *Magnetic Resonance in Medicine*, 60(5):1218–1231, nov 2008.

[145] G. De Stefano, F. M. Denaro, and G. Riccardi. High-order filtering for control volume flow simulation. *International Journal for Numerical Methods in Fluids*, 37(7):797–835, 2001.

[146] David A. Steinman, C. Ross Ethier, and Brian K. Rutt. Combined analysis of spatial and velocity displacement artifacts in phase contrast measurements of complex flows. *Journal of Magnetic Resonance Imaging*, 7(2):339–346, 1997.

[147] Daniel Stucht, K. Appu Danishad, Peter Schulze, Frank Godenschweger, Maxim Zaitsev, and Oliver Speck. Highest resolution in vivo human brain mri using prospective motion correction. *PloS one*, 10(26226146):e0133921–e0133921, July 2015.

[148] Tony Stöcker, Kaveh Vahedipour, Daniel Pflugfelder, and N. Jon Shah. High-performance computing mri simulations. *Magnetic Resonance in Medicine*, 64(1):186–193, 2010.

[149] Sivaprasad Sukavaneshvar, Gesse M. Rosa, and Kenneth A. Solen. Enhancement of stent-induced thromboembolism by residual stenoses: Contribution of hemodynamics. *Annals of Biomedical Engineering*, 28(2):182–193, feb 2000.

[150] Ronald M. Summers, Leon Axel, and Solomon Israel. A computer simulation of nuclear magnetic resonance imaging. *Magnetic Resonance in Medicine*, 3(3):363–376, 1986.

[151] Charles Taylor, Christopher Cheng, Leandro A Espinosa, Beverly T Tang, David Parker, and Robert Herfkens. In vivo quantification of blood flow and wall shear stress in the human abdominal aorta during lower limb exercise. *Annals of Biomedical Engineering*, 30:402–8, 04 2002.

[152] Per Thunberg, Lars Wigstrom, Bengt Wranne, Jan Engvall, and Matts Karlsson. Correction for acceleration-induced displacement artifacts in phase contrast imaging. *Magnetic Resonance in Medicine*, 43(5):734–738, may 2000.

[153] Brahim Timité, Cathy Castelain, and Hassan Peerhossaini. Pulsatile viscous flow in a curved pipe: Effects of pulsation on the development of secondary flow. *International Journal of Heat and Fluid Flow*, 31(5):879–896, 2010.

[154] Hubert Baya Toda, Olivier Cabrit, Karine Truffin, Gilles Bruneaux, and Franck Nicoud. Assessment of subgrid-scale models with a large-eddy simulation-dedicated experimental database: The pulsatile impinging jet in turbulent cross-flow. *Physics of Fluids*, 26(7):075108, jul 2014.

[155] H. C. Torrey. Bloch equations with diffusion terms. *Physical Review*, 104(3):563–565, 1956.

[156] K. Valen-Sendstad and D.A. Steinman. Mind the gap: Impact of Computational Fluid Dynamics solution strategy on prediction of intracranial aneurysm hemodynamics and rupture status indicators. *American Journal of Neuroradiology*, 35(3):536–543, 2014.

[157] P. van Ooij, J.J. Schneiders, H.A. Marquering, C.B. Majoie, E. van Bavel, and A.J. Nederveen. 3d cine phase-contrast mri at 3t in intracranial aneurysms compared with patient-specific computational fluid dynamics. *American Journal of Neuroradiology*, 34(9):1785–1791, 2013.

[158] Pim van Ooij, Wouter V. Potters, Annetje Guédon, Joppe J. Schneiders, Henk A. Marquering, Charles B. Majoie, Ed vanBavel, and Aart J. Nederveen. Wall shear stress estimated with phase contrast mri in an in vitro and in vivo intracranial aneurysm. *Journal of Magnetic Resonance Imaging*, 38(4):876–884, 2013.

[159] Stijn Vantieghem. *Numerical simulations of quasi-static magnetohydrodynamics using an unstructured finite volume solver: development and applications*. PhD thesis, Université Libre de Bruxelles, 2011.

[160] S. Weinbaum and K. H. Parker. The laminar decay of suddenly blocked channel and pipe flows. *Journal of Fluid Mechanics*, 69(4):729–752, jun 1975.

[161] J.H Williamson. Low-storage runge-kutta schemes. *Journal of Computational Physics*, 35(1):48–56, mar 1980.

[162] Jiyuan Tu; Kiao Inthavong; Kelvin Kian Loong Wong. *Computational Hemodynamis-Theory, Modelling and Applications*, volume 53. 2015.

[163] Kelvin Kian Loong Wong, Sherman Chi Pok Cheung, William Yang, and Jiyuan Tu. Numerical simulation and experimental validation of swirling flow in spiral vortex ventricular assist device. *The International Journal of Artificial Organs*, 33(12):856–867, jan 2010.

[164] C. G. Xanthis, I. E. Venetis, A. V. Chalkias, and A. H. Aletras. Mrisimul: A gpu-based parallel approach to mri simulations. *IEEE Transactions on Medical Imaging*, 33(3):607–617, March 2014.

[165] Christos G. Xanthis, Ioannis E. Venetis, and Anthony H. Aletras. High performance mri simulations of motion on multi-gpu systems. *Journal of cardiovascular magnetic resonance : official journal of the Society for Cardiovascular Magnetic Resonance*, 16(24996972):48–48, July 2014.

[166] Guang-Zhong Yang, Philip J. Kilner, Nigel B. Wood, S. Richard Underwood, and David N. Firmin. Computation of flow pressure fields from magnetic resonance velocity mapping. *Magnetic Resonance in Medicine*, 36(4):520–526, oct 1996.

[167] T.L. Yearwood and K.B. Chandran. Physiological pulsatile flow experiments in a model of the human aortic arch. *Journal of Biomechanics*, 15(9):683–704, 1982.

[168] Theresia I. Yiallourou, Jan Robert Kröger, Nikolaos Stergiopulos, David Maintz, Bryn A. Martin, and Alexander C. Bunck. Comparison of 4d

phase-contrast mri flow measurements to computational fluid dynamics simulations of cerebrospinal fluid motion in the cervical spine. *PLOS ONE*, 7(12):1–14, 12 2012.

[169] Akira Yoshizawa and Kiyosi Horiuti. A statistically-derived subgrid-scale kinetic energy model for the large-eddy simulation of turbulent flows. *Journal of the Physical Society of Japan*, 54(8):2834–2839, 1985.

[170] Kelly A. Young, James A. Wise, Peter DeSaix, Dean H. Kruse, Brandon Poe, Eddie Johnson, Jody E. Johnson, Oksana Korol, J. Gordon Betts, and Mark Womble. *Anatomy & Physiology*. OpenStax College, 2013.

[171] Chun Yuan, Grant T. Gullberg, and Dennis L. Parker. The solution of bloch equations for flowing spins during a selective pulse using a finite difference method. *Medical Physics*, 14(6):914–921, nov 1987.

[172] Vladeta Zmijanovic, Simon Mendez, Vincent Moureau, and Franck Nicoud. About the numerical robustness of biomedical benchmark cases: Interlaboratory FDA's idealized medical device. *International Journal for Numerical Methods in Biomedical Engineering*, 33(1):e02789–n/a, 2017. e02789 cnm.2789.

Abstract

Hemodynamics (blood flow dynamics) is now recognized as a key marker in the onset and evolution of many cardiovascular disorders such as aneurysms, stenoses, or blood clot formation. As it provides a comprehensive access to blood flows in-vivo, time-resolved 3D phase-contrast magnetic resonance imaging (or 4D Flow MRI) has gained an increasing interest over the last years and stands out as a highly relevant tool for diagnosis, patient follow-up and research in cardiovascular diseases. On top of providing a non-invasive access to the 3D velocity field in-vivo, this technique allows retrospective quantification of velocity-derived hemodynamic biomarkers such as relative pressure or shear stress, which are pertinent for medical diagnosis but difficult to measure in practice. However, several acquisition parameters (spatio-temporal resolution, encoding velocity, imaging artifacts) might limit the expected accuracy of the measurements and potentially lead to erroneous diagnosis. Moreover, the intrinsic complexities of the MRI acquisition process make it generally difficult to localize the sources of measurement errors.

This thesis aims at developing a methodology for the assessment of 4D Flow MRI measurements in complex flow configuration. A well-controlled experiment gathering an idealized in-vitro flow phantom generating flow structures typical of that observed in the cardiovascular system is designed. The flow is simultaneously predicted by means of a high-order Computational Fluid Dynamics (CFD) solver and measured with 4D flow MRI. By evaluating the differences between the two modalities, it is first shown that the numerical solution can be considered very close to the ground truth velocity field. The analysis also reveals the typical errors present in 4D flow MRI images, whether relevant to the velocity field itself or to classical derived quantities (relative pressure, wall shear stress). Finally, a 4D Flow MRI simulation framework is developed and coupled with CFD to reconstruct the synthetic MR images of the reference flow that correspond to the acquisition protocol, but exempted from experimental measurement errors. Thanks to this new capability, the sources of the potential errors in 4D Flow MRI (hardware, software, sequence) can be identified.

Keywords : hemodynamics, Computational Fluid Dynamics, 4D Flow MRI, MRI simulation.

Résumé

L'hémodynamique (la manière dont le sang coule) est aujourd'hui considérée par la communauté médicale comme un marqueur prépondérant dans l'apparition et dans l'évolution de certaines pathologies cardiovasculaires (formation d'un caillot sanguin, anévrisme, sténose...). Les récents progrès technologiques ont permis d'adapter l'Imagerie par Résonance Magnétique (IRM) à l'exploration vélocimétrique 3D du système cardiovasculaire grâce à l'IRM de flux 4D. En plus d'être non invasive et non ionisante, cette technique ouvre l'accès à l'évaluation de quantités dérivées du champ de vitesse telles que la pression ou le frottement pariétal, pertinentes lors des diagnostics médicaux, mais difficilement accessibles par imagerie. Néanmoins, les contraintes technologiques (temps d'acquisition, résolution spatiale, dépendance aux vitesses d'encodages) limitent la précision des mesures. De plus, les complexités intrinsèques au processus d'acquisition en IRM rendent difficilement identifiables les sources d'erreurs de mesures.

Cette thèse à pour but de développer une méthodologie standardisée permettant l'évaluation systématique des mesures par IRM de flux 4D dans un régime d'écoulement complexe. Dans ce but, un fantôme IRM compatible capable de générer un écoulement typique de ceux observés dans la circulation thoracique (crosse aortique, bifurcation, anévrisme) est conçu et intégré à un banc d'essai expérimental. L'écoulement est prédit par simulation numérique (Mécanique des fluides Numérique) et simultanément mesuré par IRM de flux 4D. Grâce à une évaluation rigoureuse des différences entre ces deux modalités, on montre que la simulation numérique peut être considérée comme une représentation fidèle du champ de vitesse réel. L'analyse met aussi en lumière d'une part des erreurs typiques de mesures du champ de vitesse par IRM de flux 4D, ainsi que des erreurs relatives au calcul de quantités dérivées (pression et le frottement pariétal). Enfin, une méthodologie de simulation du processus d'acquisition en IRM est développée. Couplée avec la MFN, celle-ci permet de reconstruire des images IRM synthétiques correspondant à l'écoulement de référence mesuré par un protocole d'acquisition donné, mais exemptes de toutes erreurs expérimentales. La capacité à produire des images in silico permet notamment d'identifier les sources d'erreurs (matériel, logiciel, séquence) en IRM de flux 4D.

Mots-clefs : hémodynamique, Mécanique des fluides numérique, IRM de flux 4D, simulation d'IRM.